

CONTROLLED GROWTH AND PROPERTY STUDY OF ONE-DIMENSIONAL
AND TWO-DIMENSIONAL LAYERED NANOSTRUCTURES OF MOLYBDENUM
OXIDE

by

Soheil Razmyar

A dissertation submitted to the faculty of
The University of North Carolina at Charlotte
In partial fulfillment of the requirements
For the degree of Doctor of Philosophy in
Mechanical Engineering

Charlotte

2019

Approved by:

Dr. Haitao Zhang

Dr. Quiming Wei

Dr. Edward P. Morse

Dr. Aixi Zhou

Dr. Srinivas Pulugurtha

©2019
Soheil Razmyar
ALL RIGHTS RESERVED

ABSTRACT

SOHEIL RAZMYAR. Controlled growth and property study of one-dimensional and two-dimensional layered nanostructures of molybdenum oxide. (Under the direction of DR. HAITAO ZHANG)

Molybdenum trioxide (MoO_3) is a versatile semiconductor material with a wide range of potential applications in photocatalysis, electrochromism/photochromism, sensing, and energy storage. Its highly anisotropic layered structure with weak van der Waals interactions makes it easy to form one-dimensional (1D) and two-dimensional (2D) layered nanostructures. This dissertation focuses on realizing the controlled growth of MoO_3 nanostructures with tunable structures, exploring the corresponding growth mechanisms, and studying the resulting properties. It is composed of four major research themes, including (1) study of catalyst effects of alkali metal-based catalysts on the morphologies of MoO_3 nanostructures, (2) low temperature growth of MoO_3 nanoribbons with uniform shapes, (3) synthesis of 1D ITO (indium tin oxide)- MoO_3 core-shell nanostructures with different morphologies, and (4) photocatalytic investigation of 2D MoO_3 nanoflakes with enhanced low-temperature protonation performance and tunable plasmonic properties.

As the core part of this dissertation, the last theme (chapter 5) covers material synthesis and processing, structure characterization and optical property measurement, and photothermal study of reaction mechanism. Formation of MoO_3 nanoflakes was realized using a facile liquid exfoliation of MoO_3 whiskers from chemical vapor deposition (CVD). A low-temperature protonation reaction of MoO_3 nanoflakes with pure alcohol under visible light irradiation was discovered. The reaction is initiated by the visible light

absorption from sub-bandgap defects and expedited by photothermal heating. The low reaction temperature provides a new low-cost method to produce substoichiometric semiconductors with tunable plasmonic behaviors. The reaction mechanism can be extended to other photocatalytic processes of MoO_3 nanostructures to improve their efficiencies in utilizing solar energy.

For the first theme (chapter 2), the growth resulted in different morphologies (*e.g.*, rectangular fork-end nanoplates, long nano/micro-belts, and microtowers) and highly uniform millimeter long nanobelts were successfully synthesized across the entire substrate.

During the second theme (chapter 3), high density and uniform growth of $\alpha\text{-MoO}_3$ rectangular nanoribbons (sharp edges) with the length ranging from 7 to 10 μm , typical thickness of 60-130 nm, and width around 350-800 nm was successfully established at the relatively low temperature of 350-550°C with a minimum amount of source materials (as low as 6 mg).

For the third theme (chapter 4), growth mechanisms of ITO nanowires (NWs) was discussed for specific temperature zones (high to low) inside the (CVD) reaction chamber. After successful growth of ITO NWs, shell layer materials (MoO_3) were deposited on the ITO core by altering different growth parameters. Deposition of shell materials on ITO NWs led to three distinguished morphologies of longitudinal, transverse, and needle shaped structures. It was concluded that ultra-thin (50 nm) 1D core-shell nanostructures (ITO/MoO_3) were successfully synthesized. Under this condition, as-synthesized ITO NWs were fully covered with a thin layer of shell materials.

DEDICATION

To my parents for their self-sacrifice, unconditional love and support.

To my lovely wife for her patience, her faith, her love and support.

ACKNOWLEDGMENTS

I would like to express my sincere gratitude to my graduate advisor, Dr. Haitao Zhang for his fundamental role in my doctoral work. I cannot express my appreciation enough for his continuous support, patience, motivation, and immense knowledge. This work would not have been possible without his continuous guidance and dedicated support. I would like to thank Dr. Terry Xu for the unlimited support and allowing me access to her laboratories and research facilities. I am grateful to Dr. Quiming Wei, Dr. Edward Morse, Dr. Aixi Zhou, and Dr. Srinivas Pulugurtha for agreeing to be on my doctoral committee and generously sharing their valuable feedback on my work. I would like to express my appreciation for the financial support of GASP at UNC Charlotte and the teaching assistantship from the Department of MEES. I am thankful to Dr. Garry Hodgins who selected me to be the Instrumentation and Materials labs TA for several semesters, providing me the opportunities to learn numerous valuable skills and experiences that at the end guided me to start my career at the Materials and Joining Center Lab at Siemens Energy. I am thankful to Dr. Kevin Lawton for his trust in my knowledge and skills by selecting me to instruct the “Introduction to Engineering Materials” course for several semesters. I would also like to thank Tao Sheng for his time to train me with lab facilities during the start of my research work.

TABLE OF CONTENTS

LIST OF FIGURES	xi
LIST OF TABLES.....	xxi
LIST OF ABBREVIATIONS.....	xxii
CHAPTER 1. INTRODUCTION AND PROBLEM STATEMENT	1
1.1. Background and Motivation	1
1.2. Technologies for Converting Sunlight.....	2
1.2.1. Photovoltaics	2
1.2.2. Thin-film Photovoltaics.....	3
1.2.3 Photoelectrolysis	3
1.3. Mechanisms of Photoelectrochemical Activity	4
1.4. Photoelectrode Materials and Limitations	6
1.5. Approaches to Improve Photoelectrochemical Activity	9
1.5.1 Single Bandgap Photo-active Materials	10
1.5.2 Multi Bandgap Photo-active Materials	13
1.5.3 Hetero-structures	15
1.5.4 Co-catalyst Modification.....	16
1.5.5 Plasmonic Effects.....	17
1.6. One-dimensional Nanostructures: Properties and Applications	17
1.6.1 One-dimensional Nanostructures Photocatalysts.....	18
1.7 Molybdenum Trioxide (MoO ₃): An Important Catalytic, Electrochromic, Photochromic, Thermochromic Semiconductor Material.....	18
1.8 Vapor-Liquid-Solid: Growth Mechanisms of One-dimensional Nanostructures	22
1.8.1 A Reliable Growth Process to Synthesize Nanostructures and Microstructures	22

1.8.2 Metal Catalysts: Potential Candidates for Vapor-Liquid-Solid Mechanism	22
1.8.3 Kinetics of Vapor-Liquid-Solid Mechanism	23
1.8.4 Size Limitation of Metal Catalysts	24
1.8.5 Major Challenge Faced by Conventional Metal Catalysts	25
CHAPTER 2. MECHANISM STUDY OF CATALYST-ASSISTED GROWTH ..	26
2.1 Introduction.....	26
2.2 Experimental Procedure.....	27
2.2.1 Synthesis Techniques and Equipment.....	27
2.2.2 Substrate Preparation and Growth Parameters (CVD furnace setup)	31
2.3 Results and Discussion	32
2.3.1 Distribution of Catalyst (One Droplet).....	32
2.3.2 Distribution of Catalyst (Three Droplets)	40
2.3.3 Growth Morphology Study (Single Substrate).....	41
2.3.4 Growth Improvement by Additional Source of Catalyst	46
2.3.5 Growth Reactions Summary	55
CHAPTER 3. LOW TEMPERATURE GROWTH OF MOLYBDENUM TRIOXIDE NANOSTRUCTURE.....	58
3.1 Experimental Setup, Results and Discussion.....	58
3.1.1 Tube Residue Induces Low Temperature Growth of MoO ₃	58
3.1.2 Residue Induced Growth.....	59
3.1.3 Residue Induced Growth-Mechanism Study.....	62

3.1.4 Low Temperature Growth of Uniform Nanoribbons.....	68
3.1.5 Mechanism Analysis of Growth:	80
3.1.6 Source Consumption: Powders vs. Whiskers	82
CHAPTER 4. ONE DIMENSIONAL NANO-CABLE HETEROSTRUCTURE....	85
4.1 Introduction.....	85
4.2 Experimental Setup.....	87
4.2.1 Substrates Preparation.....	87
4.2.2. Synthesis Techniques, and Characterization Methods.....	87
4.3 Result and Discussion	89
4.3.1 Effects of Oxygen Flow Rate on Growth of ITO Nanowires	89
4.3.2 Catalyst Formation on SiO ₂ /Si Substrate by Annealing	100
4.3.3 Effects of Uniform Heating Zone (Thermal Insulator) on Improving Uniformity of ITO Nanowires	111
4.3.4 Growth of ITO Nanowires on ITO/glass Substrate	113
4.3.5 One-dimensional Core-Shell Nanostructures of ITO-MoO ₃	120
CHAPTER 5. LOW-TEMPERATURE PHOTOCATALYTIC PROTONATION OF MoO ₃ NANOFLAKES WITH ALCOHOL: MECHANISM AND OPTICAL PROPERTY STUDY.....	127
5.1 Introduction.....	127
5.2 Experimental Section.....	129
5.2.1 Synthesis of MoO ₃ Whisker.....	129
5.2.2 Exfoliation.....	130
5.2.3 Light irradiation and UV-vis-NIR spectrometry.....	131

5.3 Results and Discussion	132
5.3.1 Morphology and Structure Characterization.....	132
5.3.2 Optical Property Measurement	135
5.3.3. Mechanism Discussion and Photothermal Analysis	152
CHAPTER 6. SUMMARY AND CONCLUSION.....	160
REFERENCES.....	165

LIST OF FIGURES

Figure 1-1. Schematic diagram of a photoelectrochemical cell for water splitting, right: oxygen is generated with an n-type semiconductor photoanode, left: hydrogen is produced via photocathode materials (Pt sheet) [16].	5
Figure 1-2. Half-cell oxidation and reduction reactions for two water molecules [18].	6
Figure 1-3. Suggested solutions for improvement PEC efficiency for water splitting by Chen <i>et. al.</i> [9].	10
Figure 1-4. (A) narrowing of bandgap; (B) creation of localized states above valence band (VB); (C): formation of localized states below the conduction band (CB),[25]	12
Figure 1-5. α -MoO ₃ crystal structure; A and B are the atomic layers stacked along [001] direction [46]	20
Figure 1-6. Summary of VLS mechanism kinetic stages; (1) mass transportation of vaporized reactant materials, (2) initiation of chemical reaction at vapor-liquid interface, (3) diffusion of reacted materials into the liquid phase, (4) incorporation of diffused atoms into the crystal lattice [76]	23
Figure 2-1. Home-built low-pressure chemical vapor deposition system CVD	28
Figure 2-2. Detailed components of the CVD system, where C1-2: Ar and O ₂ ; MFC: mass flow controllers; V1-4: needle valves; H1-2: ceramic heater; A1: quartz tube; V5-7: butterfly valves; B1: bubbler; E1: mechanical pump; P1: pressure gauge	28
Figure 2-3. Temperature profile of home-built CVD system in ambient environment	29
Figure 2-4. Change in temperature profile across the reaction chamber	30
Figure 2-5 Schematic of catalytic substrate before (left) and after (right) growth: 30 μ L of 0.01M NaOH drop-casted on SiO ₂ /Si substrate.	32
Figure 2-6. One droplet experiment: catalytic effects of sodium hydroxide on growth morphology of molybdenum oxide. (a) before growth, 30 μ L of 0.01M NaOH drop-casted on SiO ₂ /Si substrate and air dried overnight, (b) after growth, schematic of growth coverage on and around the catalytic droplet, (c) optical microscope image of drop-casted catalyst before growth, (d) obtained SEM image from growth morphology across the substrate, (d ₁) not catalytically affected area; thick density growth of MoO ₃ semi-circle microplates, (d ₂) lower density growth of MoO ₃ semi-circle microplates (d ₃) growth of long triangle end nanobelts at the droplet's right outer boundary, (d ₄) no growth in boundary area between the center and outer region of droplet, (d ₅) formation of short fork end microplates at the center of the droplet, (d ₆) formation of long fork end microplates at the droplet's left inner boundary, (d ₇) formation of thick fork end microplates at the droplet's left outer boundary,	

(d₈) reappearance of thick density growth of MoO₃ semi-circle microplates, not catalytically affected area. 33

Figure 2-7. SEM images of selected locations within the right boundary of the 30 μ L catalytic droplet before and after the growth. Before growth: (a - a₁) low and high magnification SEM images of innermost region of the droplet boundary, (b - b₁) low and high magnification SEM images of outermost region of the droplet boundary, (c - c₁) low and high magnification SEM images outside the droplet boundary. After growth: a₂ - a₃) low and high magnification SEM images of innermost region of the droplet boundary, (b₂ - b₃) low and high magnification SEM images of outermost region of the droplet boundary, (c₂ - c₃) low and high magnification SEM images outside the droplet boundary 35

Figure 2-8. SEM images were captured from the center of the catalytic droplet before and after the growth, images (a - b) are low and high magnification SEM images of NaOH crystal branches before the growth, images (c - d) are low and high magnification SEM images of obtained growth at the center of catalytic droplet. 36

Figure 2-9. SEM images of selected locations within the left boundary of the 30 μ L catalytic droplet before and after the growth. Before growth: (a - a₁) low and high magnification SEM images of the outermost region of the droplet boundary, (b - b₁) low and high magnification SEM images of middle region of the droplet boundary, (c - c₁) low and high magnification SEM images of innermost area of the droplet boundary. After growth: (a₂ - a₃) low and high magnification SEM images of the outermost region of the droplet boundary, (b₂ - b₃) low and high magnification SEM images of middle region of the droplet boundary, (c₂ - c₃) low and high magnification SEM images of innermost area of the droplet boundary 37

Figure 2-10. (1) Drop-casted sodium hydroxide catalytic droplet (1 μ L) on SiO₂/Si substrate before growth, (b) catalyst- assisted growth of MoO₃ (after growth)..... 38

Figure 2-11. SEM images of the NaOH catalytic droplet before and after growth: (a - b), SEM images from right and left boundaries of the drop-casted NaOH catalyst on bare SiO₂/Si substrate before growth: (c-d), SEM images of the catalyst-assisted growth of MoO₃ with different morphologies on right and left boundaries of the catalytic droplet after growth. 38

Figure 2-12. SEM images of selected locations within the right boundary of the catalytic droplet before and after growth. Before growth: (a) is the innermost region of the right droplet boundary; (b) is the middle region of the right droplet boundary; (c) is the outermost region of right droplet boundary. After growth: (a₁, a₂) are high magnification SEM images of obtained growth from the innermost region. (b₁, b₂) are high magnification SEM images of obtained growth from the middle region. (c₁, c₂) are high magnification SEM images of obtained growth from the outermost region..... 39

Figure 2-13. SEM images of selected locations within the left boundary of the catalytic droplet before and after growth. Before growth: (a) is the outermost region of the right droplet boundary; (b) is the middle region of the right droplet boundary; (c) is the innermost

region of right droplet boundary. After growth: (a₁, a₂) are high magnification SEM images of obtained growth from outermost region; (b₁, b₂) are high magnification SEM images of obtained growth from the middle region; (c₁, c₂) are high magnification SEM images of obtained growth from the innermost region..... 40

Figure 2-14. Three droplets experiment: catalytic effects of sodium hydroxide on the growth morphology of molybdenum oxide; (a-j) schematic of growth coverage on and around the catalytic droplet: (a) rectangular microplates at the center of droplet, (b) semi-circle microplates within droplet boundary, (c) long triangular-end nanobelts appeared outside of droplets boundaries, (d) semi-circle microplates within droplet boundary, (e) rounded fork-end rectangular plates at the center of droplet, (f) sharp fork- end rectangular microplates within the droplet boundary, (g) high density of semi-circle microplates outside droplet boundary, (h) round end rectangular microplates within droplet boundary, (i) fork-end rectangular microplates at innermost droplet boundary, (j) fork-end rectangular microplates at the center of the droplet..... 41

Figure 2-15. SEM images of the effect of the sodium hydroxide catalyst on the morphology of MoO₃ (at the right side of catalytic droplet): (a) low magnification SEM image of MoO₃ with different morphology grown with the NaOH catalyst (from upstream side of the substrate toward the right side of the of catalytic droplet boundary), (b) low density growth of MoO₃ microplatelets, (c) high density growth of MoO₃ microplatelets (d) mixed growth of MoO₃ platelets (underneath) and nanobelts (on top) at the droplet boundary..... 42

Figure 2-16. SEM images of the effect of the sodium hydroxide catalyst on the morphology of MoO₃ (at the center of catalytic droplet): (a-b) SEM images of low and high magnification of round-end rectangular microplates, (c-d) SEM images of low and high magnification of fork-end rectangular microplates..... 43

Figure 2-17. SEM images of the effects of the sodium hydroxide (NaOH) catalyst on the morphology of MoO₃ (at the left side of catalytic droplet): (a) low magnification SEM image of MoO₃ with different morphology grown with the NaOH catalyst (from left side of the catalytic droplet boundary toward the downstream side of the substrate), (b) growth morphology on the left boundary of the catalytic droplet, (c) thick and high density growth of semi-circle microplates, (d) appearance of very few long nanobelts on top of the semi-circle microplates..... 44

Figure 2-18. Front back position; back: SiO₂/Si substrate with extra source of Na, 30 µl 1M NaOH, located at 585-742°C. Front: target substrate with NaOH catalytic droplet, 10 µl 0.01M NaOH, placed at 280-585°C..... 46

Figure 2-19. Front-back position: SEM images obtained from different MoO₃ morphologies grown by providing an extra source of catalytic materials (right side of the catalytic droplet on the target substrate): (a) low magnification SEM image of growth (from the upstream side of the substrate toward the right side of the of the catalytic droplet boundary), (b) low density growth parallel to the substrate, (c) appearance of semi-circle microplatelets, (d) mixed growth; underneath: MoO₃ platelets below and long triangle nanobelts on top..... 47

Figure 2-20. SEM images obtained from different MoO_3 morphologies grown by providing an extra source of catalytic materials (the left side of the catalytic droplet on the target substrate): (a) Low magnification SEM image of growth (extending from droplet's left boundary toward downstream), (b) continuation of MoO_3 rectangular fork-end microplates from the center of the droplet, (c) end of fork-end microplate morphology and the reappearance of semi-circle microplates (underneath) and long triangular nanobelts (on top), (d) increase in growth density of long triangular nanobelts, (e) appearance of tower-like structure, (f) high magnification of the MoO_3 micro-tower structure 48

Figure 2-21. Side-by-side position: SiO_2/Si substrate with an extra source of Na, 30 μl 1M NaOH, was placed next to the target substrate, the substrate with 10 μl 0.01M NaOH, and at temperature range of 585-742°C..... 49

Figure 2-22. Obtained SEM images from the side-by-side position experiment, where different MoO_3 morphologies were observed around the catalytic substrate by using extra catalytic materials, (a) low temperature growth at the droplet's left boundary, (b) medium temperature growth at the center of the droplet, (c) high temperature growth at the droplet's right boundary, (d-f) high magnification SEM images from left, center, and right sides of the catalytic droplet, respectively. 50

Figure 2-23. Effects of extra catalytic source on growth of long triangular nanobelts, (a & b); SEM images from high density growth of MoO_3 long nanobelts at the right side of the catalytic droplet boundary at low and high magnification, respectively (c & d); SEM images of low density growth of long nanobelts at the left side of the catalytic droplet boundary, at low and high magnification, respectively 51

Figure 2-24. XRD patterns of nanobelts grown at three different locations (temperatures) on the target substrate. 52

Figure 2-25. Repeating the side-by-side experiment, the target substrate, without the catalytic droplet, was positioned next to the catalytic substrate which has 30 μl 1M NaOH at the temperature range of 280-585°C..... 52

Figure 2-26. Effects of the catalytic droplet on the target substrate's increased growth zone of nanobelts (a & b); SEM images from high density growth of MoO_3 long nanobelts at a temperature range of 327-449°C, at low and high magnification, respectively (c & d); SEM images of low density growth of long nanobelts at a temperature range of 280-327°C, at low and high magnification, respectively 53

Figure 2-27. XRD spectra of MoO_3 nanobelts performed on the growth zone of 280°C (12mm center, 041415)..... 54

Figure 2-28. up and down position; top: 20 mm by 25 mm piece of SiO_2/Si substrate with an extra source of Na, 30 μl 1M NaOH underneath: bare target substrate without the catalytic droplet, both substrates were placed at 280-585°C. 54

Figure 2-29. Effects of the extra catalytic source on the growth of long triangular nanobelts in the up and down position (a & b); SEM images from high density growth of MoO_3 long

nanobelts at the temperature range of 517-530°C, at low and high magnification, respectively (c & d); SEM images of low density growth of long nanobelts at a temperature range of 435-517°C, at low and high magnification, respectively. 55

Figure 2-30. Reproduced diagram phase of $\text{Na}_2\text{MoO}_4\text{-MoO}_3$ by Tao et al. [83] from ref. [85]. 56

Figure 3-1. Residue (thin white layer of molybdenum trioxide) formed on quartz tube within the low temperature area. 58

Figure 3-2. CVD system growth set up for residue induced growth on glass substrate ... 59

Figure 3-3. Schematic of glass substrate after growth on SEM plate (copper tape underneath); white deposition on right side (low temperature area), no deposition on left side (high temperature area). 60

Figure 3-4. SEM images from different morphologies of obtained growth (at different temperature zones) across glass substrate. Growth was induced by deposited residue (from previous experiments) on quartz tube walls, Zone I: high temperature zone with little or no growth, Zone II & III: medium temperature zone appearance of sharp/round end rectangular nanoribbons, Zone IV: low temperature zone non-uniform growth (mostly in the form of rods). 61

Figure 3-5. Schematic set up of residue production experiment on quartz substrate 62

Figure 3-6. Deposited molybdenum oxide on quartz substrate; SEM images of deposition morphology at different temperature zones, zone I: no or limited deposition, zone II: high density deposition in the form of semi-circle platelets, zone III: reduction in deposition density due to temperature reduction. 63

Figure 3-7. Mimicking residue effects, growth source: a quartz substrate with molybdenum oxide deposition located on top of the boat, target: bare glass substrate located underneath 64

Figure 3-8. Mimicking residue effect: induced growth on a glass substrate located underneath a quartz substrate with molybdenum oxide deposition. 64

Figure 3-9. Mimicking residue effect: SEM images of induced growth on glass, (a) high temperature zone (449-585°C) with no or little growth, (b & c) appearance of uniform rectangular nanoribbons at medium temperature zone, (d) less uniform nanoribbon in the form of fork-end rectangular, (e & f) non-uniform growth with mix growth at low temperature side of glass substrate. 65

Figure 3-10. SEM images from morphology change of deposited molybdenum oxide on a quartz substrate before and after inducing growth on a glass substrate located underneath the quartz, (a) before growth; continuous thick film of deposition in the form of small platelets positioned at high temperature, (b) majority portion of thick film is evaporated and contribute to growth, (c, e, g) before growth: molybdenum oxide deposition in the form

of semi-circle platelets extended from medium to low temperature, (d, f, h) after growth, no significant change in morphology of deposition, minor decomposition and growth of tiny nanowire on top of platelets..... 66

Figure 3-11. SEM images of mimicking the residue effect while using SiO_2/Si substrate as growth source (on top) and a glass substrate as the target (underneath). (a) high temperature zone with no or limited growth, (b-d) appearance of nanoribbons with low to high density growth, respectively, (e-f) mixed and non-uniform growth with no or very few nanoribbons..... 67

Figure 3-12. SEM images from morphology change of deposited residue on SiO_2/Si substrate before and after the experiment for mimicking the residue effects. 68

Figure 3-13. Uniformity of heating zone at center versus end of reaction chamber: (blue oval) center of reaction chamber with uniform heating, (red oval) end of reaction chamber with significant temperature gradient across substrate 69

Figure 3-14. Distribution of temperature profile across the reaction chamber at 600°C .. 70

Figure 3-15. SEM images of obtained growth using a small amount of powders ordered from high to low temperature (left to right), (1st raw: a-d) growth source: 3 mg MoO_3 , (2nd raw: e-h) growth source: 6 mg MoO_3 , (3rd raw: i-l) growth source: 12 mg MoO_3 72

Figure 3-16. Summarized growth morphologies and density in respect to temperature zone using low amount of growth source..... 72

Figure 3-17. SEM images of obtained growth using large amount of powders ordered from high to low temperature (left to right), (1st raw) growth source: 25 mg MoO_3 , (2nd raw) growth source: 50 mg MoO_3 , (3rd raw) growth source: 100 mg MoO_3 73

Figure 3-18. Summarized growth morphologies and density in respect to temperature zone using a large amount of growth source. 74

Figure 3-19. CVD system set up for growth of MoO_3 nanoribbons on a glass substrate by using synthesized MoO_3 whiskers 75

Figure 3-20. As-synthesized MoO_3 whiskers..... 75

Figure 3-21. SEM images of obtained growth using small amount of MoO_3 whiskers ordered from high to low temperature (left to right) , (1st raw: a-d) 3 mg MoO_3 whiskers, (2nd raw: e-h) 6 mg MoO_3 whiskers, (3rd raw: i-l) 12 mg MoO_3 whiskers. 76

Figure 3-22. Summarized growth morphologies and density in respect to temperature zones using low amount of growth source (MoO_3 whiskers) 77

Figure 3-23. SEM images of obtained growth using large amount of whiskers ordered from high to low temperature (left to right) , (1st raw) 25 mg MoO_3 whiskers, (2nd raw) 50 mg MoO_3 whiskers, (3rd raw) 100 mg MoO_3 whiskers. 78

Figure 3-24. Summarized growth morphologies and density in respect to temperature zones using large amount of growth source (MoO_3 whiskers).	78
Figure 3-25. XRD pattern of the as-synthesized MoO_3 nanoribbons	79
Figure 3-26. Structural characterization of as-synthesized $\alpha\text{-MoO}_3$ nanoribbons. (a) Low-magnification TEM image and (b) HRTEM image of nanoribbon. Inset shows the selected area electron diffraction (SAED) patterns.	80
Figure 3-27. SEM images of MoO_3 powder particles (left) and whiskers (right)	82
Figure 3-28. Comparison of growth source consumption using different types of growth source (powders vs whiskers).	83
Figure 4-1. SEM images of few ITO NWs grown on bare SiO_2/Si substrates (high temp. heating zone: $740\text{-}780^\circ\text{C}$) with 0.1 sccm oxygen flow rate	90
Figure 4-2. SEM images of ITO NWs grown on bare SiO_2/Si substrate (medium temp. heating zone: $585\text{-}740^\circ\text{C}$ with 0.1 sccm oxygen flow rate.....	91
Figure 4-3. EDX spectrum acquired from tip of NWs (grown within medium temp. heating zone: $585\text{-}740\text{-}585^\circ\text{C}$	92
Figure 4-4. SEM images of non-uniform micro-trees grown on bare SiO_2/Si substrate (low temp. heating zone: $280\text{-}585^\circ\text{C}$ with 0.1 sccm oxygen flow rate	93
Figure 4-5. SEM images of NWs grown on bare SiO_2/Si substrates (high temp. heating zone: $740\text{-}780^\circ\text{C}$) with 0.5 sccm oxygen flow rate.....	94
Figure 4-6. SEM images of NWs grown on bare SiO_2/Si substrates (medium temp. heating zone: $740\text{-}585^\circ\text{C}$) with 0.5 sccm oxygen flow rate	94
Figure 4-7. SEM images of NWs grown on bare SiO_2/Si substrates (low temp. heating zone: $280\text{-}585^\circ\text{C}$) with 0.5 sccm oxygen flow rate.	95
Figure 4-8. SEM images of NWs grown on bare SiO_2/Si substrates (high temperature heating zone: $740\text{-}780^\circ\text{C}$) with 1.5 sccm oxygen flow rate.	96
Figure 4-9. SEM images of nucleation and growth of ITO NWs on SiO_2/Si substrate with 1.5 sccm oxygen flow.	97
Figure 4-10. SEM images of mixed in-plane and out-of-plane growth of NWs on SiO_2/Si substrate (medium temp. heating zone: $585\text{-}740^\circ\text{C}$) with 1.5 sccm oxygen flow.	98
Figure 4-11. SEM images of mixed in-plane and out-of-plane growth of ITO NWs on SiO_2/Si substrate (low temp. heating zone: $280\text{-}585^\circ\text{C}$) with 1.5 sccm oxygen flow.	99
Figure 4-12. SEM images of growth morphologies resulting under the conditions of 0.1 (a-c), 0.5 (d-f), and 1.5 (g-i) sccm oxygen flow rate.	100

- Figure 4-13. SEM images of Au nanoclusters after annealing at (750°C for 1 h); deposited Au film thickness (a) 5; (b) 10; (c) 15 ; and (d) 20 nm..... 101
- Figure 4-14. SEM images of ITO NWs (800°C for 30 min) grown on annealed SiO₂/Si substrate with Au films thickness of 5 nm, 10 nm, and 15 nm..... 102
- Figure 4-15. Reported EDS spectra (M. Terauchi et al) on (In O₃)_{1-x} (Sn O₂)_x (x=0.05 ~ 0.1) obtained using MLC grating system (red) and conventional EDS (blue line) [99]. 103
- Figure 4-16. SEM images of performed EDX ITO NWs grown on SiO₂/Si substrate with different Au film thickness; white cross sign indicates the locations where EDX spectrums captured from the tip of NWs 104
- Figure 4-17. Enlargement of emission spectra from Figure 4-16- b showing detailed Sn peaks for self-catalyzed VLS growth mechanism 104
- Figure 4-18. SEM image of ITO NWs grown at various oxygen flow rates of (a-c) 0.1 sccm; (d-f) 0.2 sccm; (g-i) 0.3 sccm; (j-l) 0.5 sccm within temperature zone of 750-800 °C..... 106
- Figure 4-19. EDX spectra (heating zone 750-800°C) of ITO NWs grown on SiO₂/Si substrate under different oxygen flow rate of (a) 0.1 sccm; (b) 0.2 sccm; (c) 0.3 sccm; (d) 0.5 sccm; white cross sign indicates the locations where EDX spectrums captured from the tip of NWs..... 107
- Figure 4-20. SEM image of ITO NWs grown at various oxygen flow rates of (a-c) 0.1 sccm; (d-f) 0.2 sccm; (g-i) 0.3 sccm; (j-l) 0.5 sccm within temperature zone of 600-750 °C..... 108
- Figure 4-21. EDX spectra (heating zone:600-750°C) of ITO NWs grown on SiO₂/Si substrate under different oxygen flow rate of (a & b) 0.1 sccm; (c & d) 0.2 sccm; (e) 0.3 sccm; (f) 0.5 sccm; white cross sign indicates the locations where EDX spectrums were obtained from the tip of NWs. 110
- Figure 4-22. SEM image of microtree (a and b); nanotrees (c & d) branched morphology under 0.1-0.5 sccm oxygen flow rate within the temperature window of 500-585°C. ... 111
- Figure 4-23. SEM images of ITO NWs grown on SiO₂/Si substrate in a temperature window of (750-800 °C); (a-c) without thermal insulator; (d-f) thermal insulator was installed on both sides of CVD reaction chamber. 112
- Figure 4-24. SEM images of ITO NWs grown on SiO₂/Si substrate in a temperature window of (600-750 °C); (a-c) without thermal insulator; (d-f) thermal insulator was installed on both sides of CVD reaction chamber. 113
- Figure 4-25. SEM images of Au nanoclusters on ITO/glass substrate; annealing performed at 750°C for 1 h for substrates with (a) 5 nm; (b) 10 nm; and (c) 15 nm thick Au films.114

Figure 4-26. SEM images of ITO NWs grown on annealed ITO/glass substrates with Au films thickness of ; (a-b) 5 nm, (c-d) 10 nm, and (e-f) 15 nm; growth performed at 800°C for 30 min and substrates were place within temperature window of 700-740°C. 115

Figure 4-27. EDX spectra of ITO NWs grown on annealed ITO/glass substrates with Au films thicknesses of ; (a) 5 nm, (b) 10 nm, and (c) 15 nm; growth performed at 800°C for 30 min and substrates were place within temperature window of 700-740°C. 116

Figure 4-28. SEM images of ITO NWs grown on annealed ITO/glass substrates with Au films thicknesses of ; (a-b) 5 nm, (c-d) 10 nm, and (e-f) 15 nm; growth performed at 800°C for 30 min and substrates were place within temperature window of 585-700°C. 117

Figure 4-29. SEM images of growth performed using ; (a) zero; (b) 2 sccm argon flow; (c) resulting in formation of ITO NWs with diameter as small as 150 nm. 118

Figure 4-30. XRD patterns of synthesized ITO NWs grown on ITO/glass substrate..... 119

Figure 4-31. SEM images of (a & b) ITO NWs with no shell layer (c & d) 1D core-shell nanostrcutres of ITO-MoO₃ with longitudinal shell morphology..... 121

Figure 4-32. EDX spectra of 1D core-shell nanostructure of ITO-MoO₃ with a longitudinal type of shell..... 122

Figure 4-33. SEM images of (a) ITO NWs with no shell layer (b) 1D core-shell nanostrcutres of ITO-MoO₃ with transverse shell morpholoy (c) EDX spectra on stem of 1D core-shell structure of ITO-MoO₃ with transverse shell morphology..... 123

Figure 4-34. SEM images of (a) ITO NWs with no shell layer (temperature zone 700°C), (b) 1D core-shell nanostrcutres of ITO-MoO₃ with longitudinal shell morphology (temperature zone 450°C)..... 124

Figure 4-35. SEM images of (a) ITO NWs with no shell layer (b) 1D core-shell nanostrcutres of ITO-MoO₃ with needle shape shell morpholoy (c) EDX spectra on stem of 1D core-shell structure of ITO-MoO₃ with needle shaped shell morphology. 125

Figure 4-36. SEM images of (a) ITO NWs with no shell layer (b) 1D core-shell nanostrcutres of ITO-MoO₃ with ultrathin longitudinal shell morphology (c) EDX spectra on stem of 1D core-shell structure of ITO-MoO₃ with ultrathin longitudinal shell morphology. 126

Figure 5-1. Demonstration of the steps of the liquid exfoliation process changing the CVD grown MoO₃ whiskers into MoO₃ nanoflakes suspended in IPA solutions. 130

Figure 5-2. Reflectivity spectrum of the dichroic cold beam turning mirrors. Model 66219 was used to reflect the light in the visible range. Adapted from Newport product information brochure [119]..... 131

Figure 5-3. (a-b) Photos of (a) the as-synthesized MoO_3 whiskers and (b) the whiskers twisted and rolled into a ball and (c) SEM image of the whiskers. 133

Figure 5-4. (a-c) Low magnification TEM images of the MoO_3 nanoflakes from liquid exfoliation in different IPA solutions: (a) 100% IPA, (b) 70 vol% IPA- H_2O , and (c) 50 vol% IPA- H_2O . (d) HRTEM image of a MoO_3 nanoflake and a SAED pattern (inset) showing its crystalline structure..... 135

Figure 5-5. UV-vis-NIR absorbance measurement demonstrating the effects of catalysts settling and remixing in the solution: (blue) right after photocatalytic reaction, the spectrum shows many large spikes at the UV region; (black) after setting in dark for 2h, most of the spikes disappear or diminish due to the settlement of the aggregated catalysts; and (red) the spikes reappear after the sediment was remixed with the solution by stirring and light ultrasonication. The spectra are plotted with a diagonally shift for a clear view. 136

Figure 5-6. UV-vis-NIR absorbance measurement of (a) MoO_3 -50IPA and (b) MoO_3 -100IPA suspensions with different durations of visible light irradiation. Insets are corresponding optical photos of MoO_3 nanoflake suspensions showing color changes before and after different light exposure durations. 138

Figure 5-7. Direct bandgap fittings of (a) MoO_3 -50IPA and (b) MoO_3 -100IPA suspensions at different durations of visible light irradiation. Inset in (a) shows the fitting of exciton edges and bandgaps..... 140

Figure 5-8. Indirect bandgap fittings of (a) MoO_3 -50% IPA and (b) MoO_3 -100% IPA solutions at different durations of visible light irradiation. Inset in (a) shows the fitting of exciton edges and bandgaps..... 141

Figure 5-9. Urbach defect tail fitting for (a) MoO_3 -50IPA and (b) MoO_3 -100IPA samples. 146

Figure 5-10. Peak fittings for the absorption bands of (a) MoO_3 -50IPA sample with irradiation durations of 1.5 min, 2.5 min, and 2hr; and (b) MoO_3 -100IPA sample with irradiation duration of 2hr..... 150

Figure 5-11. (a) Temperature profiles of different solutions during continuous light irradiation, and (b-c) repeating experiments of 30 min light irradiation with 15 min interval on a MoO_3 -100IPA sample: (b) temperature profile and (c) corresponding UV-vis-NIR absorption measurements..... 153

Figure 5-12. Temperature profiles (a-c) and corresponding UV-vis-NIR absorption measurements (d-f) of different heating and light exposure conditions for MoO_3 -100IPA samples: (a, d) dark heating at two plateau temperatures, (b, e) samples from (a,d) having light irradiation for 2.5 hr, and (c, f) dark heating at two plateau temperatures followed by immediate light exposure of 2.5 hr. Insets show typical photographs of the resulting suspensions. 155

LIST OF TABLES

Table 2-1. Range and resolution of the home-built CVD system.....	29
Table 2-2. Summary of MoO ₃ growth morphology at different temperature zones grown with NaOH catalyst.....	45
Table 3-1. Reactant information for production of residue on quartz tube	62
Table 3-2. Reactant information for improving the growth yield.....	70
Table 4-1. Summary of diameters and lengths of grown ITO NWs on SiO ₂ /Si substrate with different thicknesses of Au films catalyst.....	102
Table 4-2. Summary of diameter, length, and growth mechanism of grown ITO NWs at various oxygen flow rates within 750-800°C heating zone.....	106
Table 4-3. Summary of diameter, length, and growth mechanisms of grown ITO NWs at various oxygen flow rates within 600-750°C heating zone.....	108
Table 4-4. Diameters and lengths of ITO NWs grown on ITO/glass substrate with different Au films thicknesses and within temperature zone 700-740°C.....	115
Table 5-1. List of Bandgap and exciton edge values at different irradiation durations from the direct bandgap fittings.....	141
Table 5-2. List of Bandgap and exciton edge values at different irradiation durations from the indirect bandgap fittings.....	142
Table 5-3. Results from Urbach defect tail fitting.	148

LIST OF ABBREVIATIONS

CB	conduction band
CBM	conduction band minimum
CVD	chemical vapor deposition
DP	diffraction pattern
DFT	density functional theory
EDX	energy dispersive X-ray spectroscopy
HRTEM	high resolution TEM
IPA	isopropyl alcohol
IPCE	incident-photon-to-current-conversion efficiency
ITO	tin doped indium oxide
NWs	nanowires
OM	optical microscope
PEC	photo-electrochemical cell
PEC	photoelectrochemical
PV	photovoltaic cell
SEM	scanning electron microscopy
SAED	selected area electron diffraction
TEM	transmission electron microscopy
TCO	transparent conductive oxide
TMDC	transition metal dichalcogenide
TMO	transition metal oxide
UV	ultraviolet

VB	valence band
VBM	valence band maximum
VLS	vapor liquid solid
VS	vapor solid
XRD	X-ray diffraction

CHAPTER 1. INTRODUCTION AND PROBLEM STATEMENT

1.1. Background and Motivation

Increasing population, growing economies, and limited fossil fuel reserves demand a sustainable and eco-friendly form of energy. British Petroleum (BP) reported an additional 1.3 billion new energy consumers by 2030 [1]. A reported Energy Outlook by Exxon predicts an 85% increase in global electricity demand by 2040 [2]. More than 85% of today's energy demand is provided by fossil fuels and continued use of these resources has caused serious concerns regarding global warming, environmental pollution, and depleting natural resources [3]. As an example, many newly drilled gas wells produce 80-95% less gas after only 3 years. Considering the predicted lifespan of these wells is 40 years in order to keep up with current world energy demand, discovering and drilling 7200 gas wells per year is vital, which will cost 42 billion dollars [4]. Solar energy is considered a cheap, efficient, and carbon-neutral source of energy which might be a possible solution for all the mentioned challenges for generating clean, sustainable and zero-cost energy. Considering 36,000 terawatts (TW) of solar energy strike the earth and a solar cell with 25% efficiency, a solar cell farm as big as just 0.3% of the 9.4 million km² of Sahara Desert (~367 km by 367 km) can generate enough energy to supply the projected electricity demand [5-7]. In other words, total consumption of energy on planet earth during one year (4.1×10^{20} J) is less than the energy from sunlight striking the earth for only one hour (4.3×10^{20} J). However, currently less than 2% of the world's energy is being generated by solar energy, which is mostly due to technology limitation.

1.2. Technologies for Converting Sunlight

Solar fuels (photo-electrochemical cell or PEC), solar electricity (photovoltaic cell or PV), and solar thermal systems are three currently available technologies for harvesting sunlight energy. In PV cells, direct conversion of solar radiation to electrical energy happens via photovoltaic effect. Water splitting to oxygen and hydrogen in PEC cells converts the solar energy to chemical energy, and finally the solar energy is converted to thermal energy in solar thermal systems. Since both oxygen and hydrogen can be used directly as a fuel, the PEC technology has drawn much attention [8, 9].

1.2.1. Photovoltaics

As it was mentioned above, solar cells made via PV technology directly convert sunlight into electrical energy, which has a high potential for generating clean electrical power in large scale. The first state in generating electricity in PV technology is sunlight collection and stimulation of charge-separated state for generating an electron-hole pairs. The process of migration of excitons to a p-n junction occurs in silicon semiconductors and via photon absorption, which produces an electromotive force due to charge separation. Connection of the p-n junction to an external load generates power, which means a photo-current flows through the load and completes the process of photo-to-electricity conversion [10]. High production cost is one of the major challenges faced by PV technology, which is two to five times higher than energy generated from fossil fuels [11]. Crystalline silicon wafers, 180-300 μm in thickness, are the most common photo-materials used in fabrication of PV. However, both the materials and their fabrication process are expensive.

Emerging technologies such as organic PVs and dye-sensitized solar cells are fabricated from relatively cheap materials, compared with crystalline silicon wafers, and they show more absorption of visible light [9, 12, 13].

1.2.2. Thin-film Photovoltaics

The high cost of using silicon-based photo active materials in photovoltaics are reduced in thin-film technology, which only uses 1-2 μm in thickness of photo-active films on substrates such as plastic, stainless steel or glass. In this method, the expensive conventional crystalline silicon is substituted with thin-film solar cells made of GaAs, CdTe, CuInSe₂, and amorphous/polycrystalline silicon, which can improve the photoconversion efficiency (PE) [9, 11].

1.2.3 Photoelectrolysis

In this method, the energy of sunlight is utilized for splitting water via a solid photoelectrode for generating chemical energy. Hydrogen is the ultimate form of green energy since it can be used in fuel cells and other applications. However, currently, hydrogen is mostly generated through the steam forming process, which requires burning fossil fuels and generating carbon dioxide as a byproduct [14]. In photoelectrolysis, no byproduct is generated after splitting water into hydrogen and oxygen. However, the low performance of photoelectrodes have resulted in lower conversion efficiency in photoelectrolysis in comparison with photovoltaic technologies.

The water splitting method was first discovered back in 1972 using TiO₂ photoelectrodes under ultraviolet (UV) illumination [15]. During this process, the generation of both electrons and holes occurred when the semiconductor electrode (TiO₂) was exposed to UV light. Hydrogen was formed on a Pt counter-electrode via reduction of

water molecules by photo-generated electrons. Also, the oxidation of water molecules by holes resulted in the formation of oxygen on the surface of TiO₂-based electrodes. However, due to the wide band gap of TiO₂ (~ 3.0 eV) and low percentage of UV radiation in the solar spectrum (only 5%) the efficiency was limited. Considering that visible light counts for the majority of the solar spectrum (~46%), substantial efforts have been made in research on visible-light effective photoelectrode materials. Long-term stability, rapid charge transfers at the semiconductor/electrolyte interface, and efficient harvesting of a wide range of the solar spectrum are some of the most important features for candidate semiconductor materials in a PEC. Over the past decades, much research has been focused on semiconductor materials to develop PECs and photocatalysts. However, no breakthroughs on either materials' stability or design for photoelectrode applications have been achieved [9].

In nanotechnology, nanomaterials offer outstanding properties due to their large surface area and small feature size and it is believed that they could be promising materials for fabrication of novel photoelectrodes. Tailoring the band gap of semiconductors, quantum dot sensitization, plasmonic effects, and domination of crystal facets are all beneficial effects of photoelectrodes with nano-structures [9].

1.3. Mechanisms of Photoelectrochemical Activity

Conversion of one molecule of H₂O into hydrogen (H₂) and oxygen (1/2 O₂), under standard conditions, requires 272.2 kJ mol⁻¹ change in Gibbs free energy (ΔG), which is equal to an electrolysis cell voltage (ΔE^0) of 1.23 V per electron transfer. A photoelectrochemical cell is shown in Figure 1-1. The photoanode electrode is made of semiconducting or photoactive materials and will be exposed to sunlight. The cathode is a

counter electrode known as a photocathode and is not irradiated by sunlight. This cell reaction can only occur if the amount of absorbed irradiated light by photoactive materials on the photoanode is high enough to generate an electrode potential higher than 1.23 V (wavelength of 1000 nm) for both oxidation and reduction of the water molecule to form O_2 and (H^+) on photoanode and H_2 at the cathode, respectively.

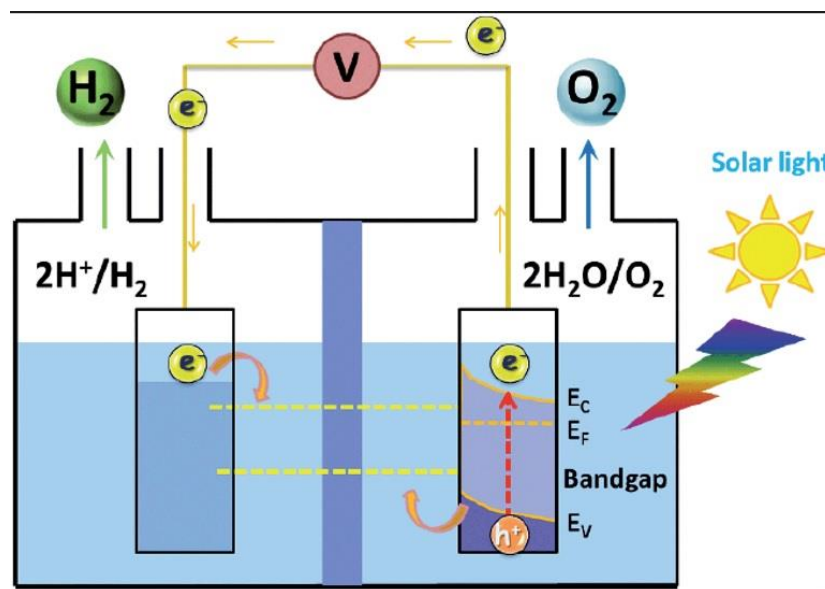


Figure 1-1. Schematic diagram of a photoelectrochemical cell for water splitting, right: oxygen is generated with an n-type semiconductor photoanode, left: hydrogen is produced via photocathode materials (Pt sheet) [16]

During the cell reaction, most of the energy loss happens at the photoanode/electrolyte interface, which is due to the slow kinetics of water splitting. The required energy for photoelectrolysis is assumed to be 1.7-2.4 eV for producing four electron-hole pairs for oxygen generation. Considering the potential loss, the photoelectrochemical splitting of a water cell requires at least 1.7-1.9 eV of minimum thermodynamic energy (wavelength of 730 nm). Due to the intensity drop in the solar spectrum below 350 nm, the upper limit bandgap is about 3.5 eV. In conclusion, semiconductor candidate materials for electrochemical water splitting cells should have a

bandgap in the range of 1.9-3.5 eV, which is within the visible range of the solar spectrum [9]. Based on the bandgap of semiconductor material, the solar spectrum and various losses, reports have predicted a maximum efficiency of 27.5% for the solar photons flux in the wavelength range from 680 – 280 nm (1.8 eV- 4.4 eV) [17]. The cell half-reactions are summarized in Figure 1-2.

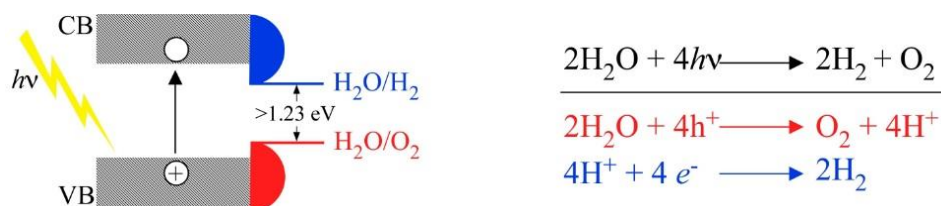


Figure 1-2. Half-cell oxidation and reduction reactions for two water molecules [18].

The electrons of the valence band of photoactive materials can be excited into the conduction band, then the absorbed energy of irradiated photoanodes (from sunlight) is greater than the photoactive material bandgap (E_{BG}). During this process, holes remain in the valence band and at the photoanode to oxidize (H_2O) (O^{2-}) for oxygen production (O_2).

Besides the bandgap condition of photoactive materials, the band level's condition should be considered for the capability of a semiconductor for water splitting. This means that nominated semiconductors for water splitting must have conduction band energy (E_{C}) higher than that of reduction potential $E_{\text{red}}(\text{H}_2/\text{H}^+)$, and a valence band energy (V_{C}) lower than that of oxidation potential $E_{\text{ox}}(\text{H}_2\text{O}/\text{O}_2)$.

1.4. Photoelectrode Materials and Limitations

Several factors should be considered for candidate semiconductor materials in a photoelectrochemical cell for water splitting purposes. For example, the kinetics of the carrier transportation of a photoelectrochemical cell can be improved by some modification of co-catalyst materials. Co-catalysts such as RuO_2 and Pt nanoparticles are able to provide

active sites on the surface of photoactive materials which could be helpful for hydrogen and oxygen evolution. Rapid carrier transportation on n-type semiconductor/electrolyte interface is an important factor since it prevents accumulation of electron-holes on the surface of photoanode.

Chemical stability and resistance to photocorrosion is another critical factor that needs to be considered for selecting photocatalytic materials. The instability of the majority of semiconductor materials results in photocorrosion and/or anodic photodecomposition, which means oxidation of photoactive materials by photogenerated holes rather than water. This chemical instability will result in either the dissolving of semiconductor materials or the formation of a thin oxide layer on their surface which prevents electron transfer between semiconductor/electrolyte interfaces. Some semiconductor materials such as TiO_2 and SnO_2 are highly stable over a wide range of electrolyte pH.

Also it should be noted that the pH value of the electrolyte solution can change and shift the band level of semiconductor materials which consequently will affect the redox potential of the PEC cell. Higher pH of the electrolyte solution while measuring the photocurrent, shift the voltage to lower region [19]. Photocorrosion and/or anodic decomposition phenomena can be limited or stopped if transferring of photogenerated electrons through the interface happens faster than any competing reaction. Other factors such as charge separation, charge mobility and the lifetime of photogenerated electron-hole pairs must be considered for photo activity of semiconductor materials. Also generation and separation of electron-hole pairs is strongly dependent on the structure and electronic properties of co-catalyst materials on the surfaces of the photoelectrodes. Any defect could act as a recombination's site for photogenerated electron-holes resulting in lowering the

cell's efficiency. Therefore, highly crystalline materials with low density of defects could improve the efficiency of the water splitting reaction. The incident-photon-to-current-conversion efficiency (IPCE) can be calculated from Eqn. 1-1 which represents photoresponse based on the wavelength of the incident light:

$$IPCE(\%) = \frac{1240J}{\lambda \times I} \times 100\% \quad \text{Eqn. 1-1}$$

Where λ is wavelength of the incident light (nm), I is the intensity of the incident light (mW cm^{-2}), and J is the photo current density (mA cm^{-2}). It should be noted that at the end, overall efficiency of solar energy conversion is the most important factor need to be considered and can be calculated from Eqn. 1-2

$$\% = J \frac{E_{rex}^0 - |E_{means} - E_{aoc}|}{I} \times 100\% \quad \text{Eqn. 1-2}$$

where η is the overall efficiency of solar energy conversion, J is the photocurrent density (mA cm^{-2}), I is the intensity of the incident light (mW cm^{-2}), E_{rex}^0 is the required potential for water splitting (normally 1.23 eV for water splitting reaction), E_{means} is the electrode potential for the working electrode under illumination, and E_{aoc} is also the electrode potential of the working electrode but at open circuit conditions and under the same illumination as E_{rex}^0 [20]. One of the limitations of this equation is usage of sacrifice reagents such as alcohol, sulfide ions and silver, which act as electron donors or holes which is a common method for evaluation of photocatalytic activity of water splitting. Addition of these reagents is due to the limitation of the majority of the semiconductor materials to straddle their band level for covering both the reduction and oxidation potential of water. In this case, the calculation of energy conversion efficiency is not accurate to estimate the photocatalytic activity since photogenerated electron-holes will react with injected electron donors or holes instead of water. Therefore, photoactivity of PEC cell is

calculated based on photocurrent instead of conversion efficiency [9]. In conclusion, an ideal photo-active material for photoelectrode fabrication and for water splitting applications should exhibit all the following properties at the same time:

- Small semiconductor bandgap to cover most of the solar spectrum
- A valence/conduction band which is able to straddle water redox potentials
- Photocorrosion and/or anodic decomposition stability
- High conversion efficiency
- Low cost

It should be noted that a photoelectrode made of single-component photo-active material is not able to possess all the above requirements together. Therefore, it cannot yield the required photocurrent or conversion efficiency which is needed to satisfy the energy demand of our daily life. Below lists the critical limitations of current photoelectrode materials:

- Low absorbance in the range of visible light
- Poor charge-carrier transportation
- Low or limited chemical stability in electrolyte solution and under illumination

1.5. Approaches to Improve Photoelectrochemical Activity

Proposed solutions to tailor the PEC structure for improving the photoactivity of water splitting cells are summarized in Figure 1-3. Research is mostly focused on methods to improve either the sunlight absorption or carrier transportation.

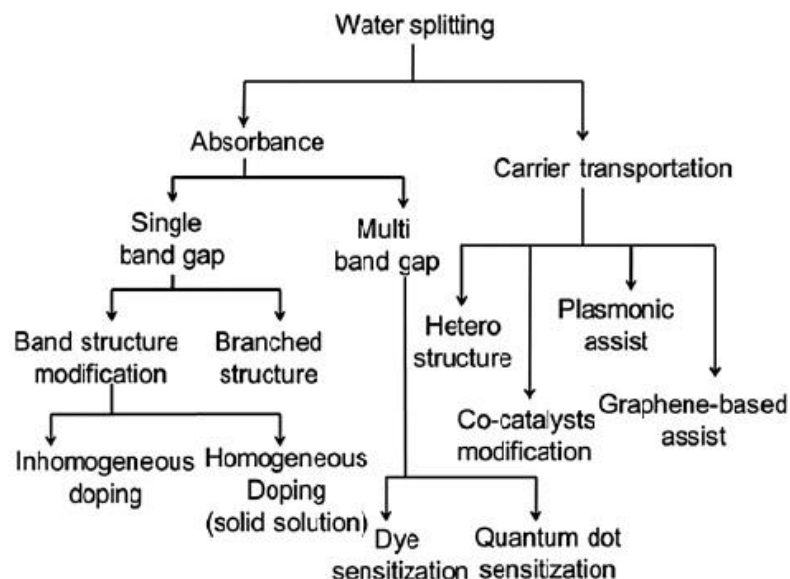


Figure 1-3. Suggested solutions for improvement PEC efficiency for water splitting by Chen *et. al.* [9].

1.5.1 Single Bandgap Photo-active Materials

A branched structure semiconductor has a large absorption cross-section, which can absorb many photons and improves sunlight absorption to extend the solar absorption spectrum range. Doping (the injection of ions or cations to semiconductor bandgap) is one method to alter the band structure of photo-active materials resulting in stretching the absorption level of the solar spectrum to higher wavelengths and therefore more absorption of solar light. In general, doping is one of the methods to improve the electrical and optical properties of semiconducting materials [9].

1.5.1.1 Branched structure

Morphology control of nanomaterials is one of the most important factors for optimizing their optical properties for semiconductor photomaterials. Nanomaterials' morphology defines their crystal facets and their related properties such as heterogeneous reactivity. Also heterogeneous reactivity of nanomaterials is related to surface atomic

pattern and their neighboring bonding, which are both related to crystalline facets. For example, the [1] facet of TiO_2 anatase crystals, in comparison with {101} and {010}, shows less reactivity in photooxidation for generating hydrogen by production of OH radicals [21].

Early research was focused on developing semiconductor nanoparticle films due to their high surface area to volume ratio. However, electron-hole recombination is a major limiting factor for these types of materials, causing huge loss and reducing their performance. The electron-hole recombination is mostly due to very slow electron mobility, which occurs because of electron trapping/scattering at grain boundaries. In nanoparticle film electron mobility is about two orders of magnitude in comparison with bulk single crystals [22].

The probability of electron-hole recombination is higher in two-dimensional (2D) nanostructure, such as nanoparticle films, due to the existence of defects and grain boundaries, which could act as trapping and recombination centers for the electron-hole recombination process. Recently, one-dimensional (1D) nanostructures such as nanotubes, nanorods, and nanowires have attracted attention due to their outstanding properties in charge separation/transportation and light absorption, which is due to their lower defect density. In conclusion a branched structure semiconductor material is able to improve photo-activity property by providing, [9]:

- A more conductive and rapid charge transfer (1D channel) pathway for charge collection
- A higher surface area, which expedites the electron-hole reaction at electrolyte interface

1.5.1.2 Tailoring band structure by inhomogeneous and homogeneous doping

One of the limitations of branched nanostructures' photo-active materials is their wide bandgaps, which limit their ability to absorb the solar spectrum only in the ultraviolet (UV) region. Non-metal doping is one of the methods for narrowing the bandgap of semiconductor materials to improve their absorption in the visible light spectrum. In this method, oxygen or carbon are doped to semiconductor materials with wide bandgaps such as TiO_2 and ZnO . The exact mechanism(s) of bandgap reduction by doping still is (are) not defined.

For example Asahi *et al.* [23] proposed mechanisms for bandgap reduction in N-doped TiO_2 was mixing of the two energy states of O 2p and N 2p, nitrogen atoms from doping, in newly formed valence band. Irie *et al.* [24] suggested that formation of isolated N 2p states on top of the TiO_2 valence band as the reason for bandgap reduction and visible-light absorption. In other studies, localized states of oxygen efficiency, created during the nitrogen doping process rather than N dopant, is identified as the bandgap reduction mechanism for N-doped TiO_2 [25]. Figure 1-4 summarizes the described mechanisms for visible light absorption band of N-doped TiO_2 .

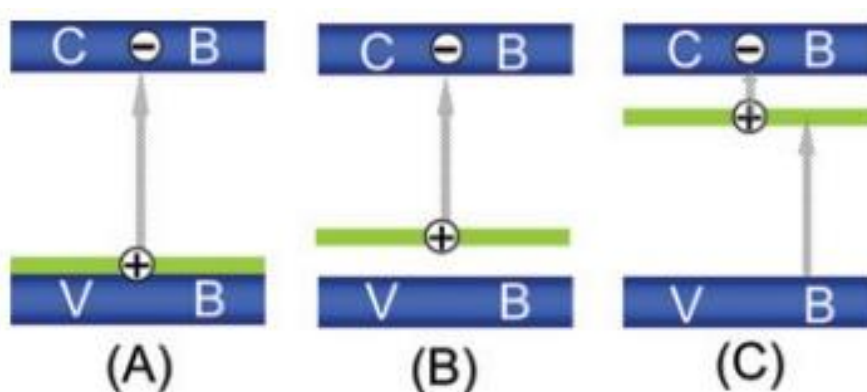


Figure 1-4. (A) narrowing of bandgap; (B) creation of localized states above valence band (VB); (C): formation of localized states below the conduction band (CB),[25]

It should be noted that photocatalytic activity does not always improve by increasing the amount of dopants. Crystallinity is sacrificed by increasing the dopants' concentration resulting in more defects and less carrier mobility, which increases the chance of electron-hole recombination.

Homogeneous doping could be a solution for improving both carrier mobility and increasing the visible light absorption. This method is suggested to solve the problem of dopant short diffusion length.

Employing nanomaterials for homogeneous doping, due to their high surface area and their small dimensions, which is less than dopants diffusion length, is recommended. Solid solution is a form of homogeneous doping for modifying the conduction band by increasing the number of unoccupied states, resulting in transition from valence band to conduction band, which could increase the PEC cells' response in visible-light range [9].

1.5.2 Multi Bandgap Photo-active Materials

Light absorbance of semiconductor materials for PEC cell applications can be improved by described methods such as synthesis branched nanostructures (higher surface areas) and modification of band structures by doping. However, these methods resulted in only a slight change for improving the conversion efficiency, which is attributed to low effectiveness of the dopant in shifting the wavelength to visible-light range. Wider range absorption of the solar spectrum could be possible by using multi-bandgap materials. Using multi-bandgap materials could increase the photoactivity more than band modification since complementary light is absorbed, in addition to the light absorbed by primary semiconductor [9].

1.5.2.1 Dye Sensitization

In a dye-sensitized solar cell, dye molecules, with a high capability of light absorption, are sputtered on an inorganic electron conducting film with high surface area. This type of solar cell is the most efficient type of excitonic cell [26]. For PEC cells, the dye monolayer performs application, light absorption, water oxidization and transferring electrons to semiconductor.

Dye molecules are normally attached to high surface area nanoparticle film made of TiO_2 , SnO_2 , or ZnO (in several micrometer thickness), which are coated with semiconductor materials (photoanodes). Both dye concentration and film thickness have strong effects on PEC cells' performance. For example, higher dye concentration results in more light absorption and optimum film thickness is required to maximize the length of incident light traveling distance and also causes more light absorption by dye.

It should be noticed that a thicker film could have some negative impacts on PEC cell performance by introducing more grain boundaries, reducing electron transport and increasing the probability of electron-hole recombination. The low chemical stability of organic dye is the major drawback of this type of the PEC cells, which is mostly due to dye degradation in electrolyte materials and if the degradation rate is higher than the amount of photogenerated holes from semiconductor materials [9].

1.5.2.2 Quantum Dots Sensitization

Semiconductor nanocrystals known as quantum dots (QDs) are able to overcome the degradation issue of photosensitive dyes and also increase the visible-light absorption of photoanodes. QDs absorption spectrum can be modified and matched with the solar spectrum by altering the size of their nanoparticles. Generation of multiple electron-hole

pairs per photon is another advantage of QDs [27]. Although QDs indicate high chemical resistibility against photo-oxidation in aqueous solutions, photodecomposition and photocorrosion are the two major drawback of these materials, resulting in reducing their photoactivity. This problem might be due to the transferring of photogenerated electrons or holes to their neighboring QDs and reacting to each other rather than water [9].

1.5.3 Hetero-structures

Besides light absorption and charge generation/separation, carrier transportation is another critical factor with high impact on photocatalytic activity. For example, recombination of charges can be prevented or reduced by facilitating the transportation of charge carriers.

In other words, during the irradiation of photoelectrodes, two mechanisms of electron-hole recombination and photoinduction of charge-separation are involved and compete with each other, that is the probability of charge recombination could be reduced by improving the photoinduction of the charge-separation step. With respect to this, short carrier diffusion length is a critical factor causing difficulty for the collection of photogenerated carriers. Possible proposed solutions for increasing carrier diffusion length could be doping or reduction of dimension by changing the morphology [28]. A one-dimensional (1D) array of nanowires or nanorods, with high crystallinity and high surface area, could provide networks of connected channels with high conductivity, which could substantially accelerate carriers' separation and collection.

Fabrication of PEC cells with hetero-structured photoelectrodes is carried out by coating an array of nanowires/rods, for example Si nanowires, with photoactive materials. Due to the high conductivity of 1D arrays of nanowire, carriers' transportation improves,

resulting in a substantial increase in efficiency of water splitting. In order to reduce the creation of impedance during transportation of photogenerated carriers from photoactive materials to arrays of 1D nanowire semiconductor, a thin, uniform, and defect free coating of photoactive materials on the surface of nanowires is required [9].

1.5.4 Co-catalyst Modification

Co-catalyst materials, such as platinum nanoparticles, are commonly used in photocatalytic systems due to their ability to trap and collect the photogenerated electrons from semiconductors, which later produce hydrogen by reacting with protons (hydrogen evolution).

Co-catalysts can also be used for oxygen evolution without applying any external bias. Kanan *et al.* [29] reported an anodic electrochemical deposition method for oxygen evolution.

In their method, Co^{+2} oxidizes to a Co^{+3} ion and it precipitates out on surface of, for example, an n-type semiconductor photoanode as either Co oxide or hydroxide products. This deposited Co-based co-catalyst causes the reaction of photogenerated holes with water without applying any external bias. The advantage of this system could be reducing the production cost, by combining this PEC cell with a solar cell and an electrolyzer in a single device. The mechanism for fabrication of Co-based co-catalyst on the surface of a photoanode and for oxygen evolution can be explained such that Co^{+2} ions start oxidizing to Co^{+3} ions, using photogenerated holes, only if the valence band edge of the semiconductor materials is more positive than the oxidation potential of the Co^{+2} ions. This facilitates the evolution of oxygen and prevents the blocking of the semiconductor [30].

1.5.5 Plasmonic Effects

Plasmonic materials can provide beneficial effects for photoelectrochemical reactions and substantially improve their photo response to solar water splitting. This occurs by three methods, (1) enhancing the charges transportation between metal/semiconductor, also called "hot" electron-hole pairs, (2) induced electromagnetic field, and (3) plasmonically induced heating. Some reports explain the mechanism of plasmonic photogeneration such that, upon irradiation of metal nanoparticles such as gold, an electron in the valence band of semiconductor materials can be injected to the conduction band by a plasmon-induced electromagnetic field that exists on the surface of nanoparticles, resulting in the creation of a hole [9].

1.6. One-dimensional Nanostructures: Properties and Applications

One-dimensional nanostructured materials such as nanobelts, nanoribbons, and nanowires have attracted a great deal of interest due to their unique electronic, photonic, and electrochemical properties, which makes them great candidates to be incorporated in electronic, photonic, photovoltaic, and photoelectrochemical devices [31, 32]. In order to achieve high quality single-crystalline materials with controlled morphology (dimension, length), composition, and phase, their synthesis process should be carefully controlled. The outstanding properties of 1D nanostructures can be attributed to (1) their high surface-to-volume ratio, compared with their bulk version, which substantially increases their chemical reactivity (2) the large aspect ratio of these 1D nanostructures provides a fast-transport-path for photons, phonons, and electrons [32].

1.6.1 One-dimensional Nanostructures Photocatalysts

Photocatalysis refers to the process that utilizes light to advance chemical transformations on either organic or inorganic substrates, which are penetrable at the irradiated wavelength range [32, 33]. Upon light absorption, photocatalytic materials get excited, resulting in electron-transfer reaction, which provides the required driving force for chemical reactions. Photocatalysis' limitations include (1) inability to efficiently harvest the visible light, (2) low quantum efficiency, and (3) photo-degradation of the photocatalytic materials. However, 1D nanostructures photocatalysts can be promising candidates to overcome the mentioned barriers. The photocatalysis can be substantially enhanced due to 1D nanostructures' unique features, including (1) fast and long electron transport thanks to large aspect ratio, (2) greater surface-to-volume ratio and pore volume, and (3) enhanced light absorption/scattering ability due to their high length-to-diameter ratio [32]. Employing 1D nanostructures photocatalysts can substantially increase the efficiency of photocatalysis.

1.7 Molybdenum Trioxide (MoO_3): An Important Catalytic, Electrochromic, Photochromic, Thermochromic Semiconductor Material

The fairly wide band gap (>2.7 eV) n-type semiconductor, molybdenum trioxide, is an electrochromic and photochromic material [34, 35] with poor ionic and electric conductivity that is widely used as a catalyst and in devices like field effect transistors and photodetectors [36].

Transition metal oxide is a compound of oxygen atoms bonded to transition metals and are mainly known for their semi-conductive properties [37]. Due to the high thermal and chemical stability as well as multiple valance states, Molybdenum trioxide (MoO_3) is

considered an important transition metal oxide and is suitable for application in photovoltaic energy conversion [38, 39] and electrochemical storage [40, 41]. A variety of surface structures as well as the coordination of the metal cation and oxygen anion in transition metal oxides affects the surface energy and chemical properties of these compounds [37].

Molybdenite has three different thermodynamically stable anhydrous crystalline polymorphs: orthorhombic α -MoO₃, metastable monoclinic β -MoO₃ with a rhenium trioxide (ReO₃)-type structure, hexagonal γ -MoO₃, and metastable high pressure phase MoO₃-II [42]. At the temperature range of 370°C to 400°C, monoclinic β -MoO₃ transforms into a layered α -MoO₃ which is the most thermodynamically stable phase with an anisotropic crystal structure [42, 43].

The Anisotropic α -MoO₃ phase is a double-layered orthorhombic arrangement in the [010] direction shown in Figure 1-5 [44]. Each layer possesses two sublayers, linked by a corner-sharing octahedral along the [001] and [100] directions with strong covalent bonding [44]. A weak van der Waals coupling holds the layered sheets vertically in the [010] direction [42, 43]. Lattice constants of α -MoO₃ (space group *Pbnm*) are $a = 3.962$ Å, $b = 13.855$ Å, and $c = 3.699$ Å [45].

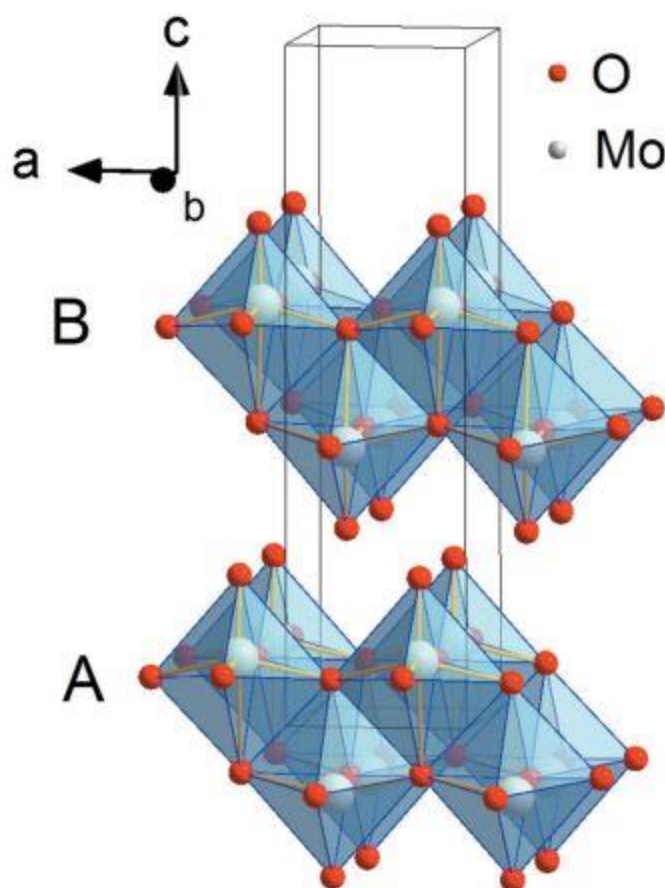


Figure 1-5. α -MoO₃ crystal structure; A and B are the atomic layers stacked along [001] direction [46]

Due to its multifaceted structure that facilitates adding different donor ions into the free spaces, α -MoO₃ exhibits photochromic [34] and thermochromic [47] and electrochromic [48] properties and is a popular choice as an electrochromic material [49-52]. Electrochromic, thermochromic and photochromic properties refer to the reversible change in optical properties caused by the electrochemical oxidation/reduction of electrons and ions, temperature change, and photon absorption respectively [48]. Improving the coloration performance of photochromic materials has been an interest for many researchers.

The nanostructured form of α -MoO₃ offers high surface to volume ratio (> 200) that leads to higher catalytic [2, 53, 54], sensing [55], and charge collection [56] efficiencies. Due to different synthetic techniques and experiment routes, different morphologies of molybdenum trioxide crystals are formed, such as molybdenum trioxide nano-rods [57], nano-tubes [58, 59], hollow MoO₃ nano-spheres and mesostructured toroids, [60, 61], and molybdenum trioxide fibers or nano-belts [62-64]. MoO₃ nano-belts with uniform structure and a high conductive electron pathway show higher electrochemical performance and better cycle ability over bulk α -MoO₃ [43].

Despite the wide bandgap of α -MoO₃, different approaches such as hydrogen intercalation into the crystal lattice, thermal treatment, UV irradiation and photochemical deposition followed by annealing can be adopted to achieve the aforementioned structural changes [65-68] and can tune the bandgap to a desired numbers. Sha et al. [69] performed detailed studies on using density functional theory (DFT) to narrow the α -MoO₃ bandgap by adsorption of H atoms into the α -MoO₃ crystal lattice.

Induction of the hydrogen adsorption happens by either decomposition of the gas phase H₂ onto the MoO₃ surface or diffusion of the H⁺ ions in liquid media and MoO₃ lattice [45, 70]. Hydrogen adsorption into the MoO₃ lattice leads to the formation of hydrogen molybdenum bronzes (H_x MoO₃). Due to the bonding of the hydrogen and oxygen and the formation of the open oxygen vacancies reduces the bandgap of MoO₃ [45, 70]. The reduction in the bandgap is highly dependent on the H₂ exposure time. The longer the MoO₃ is exposed to the H₂, the narrower the bandgap will be [45, 65]. Optical properties of the 2D materials such as MoO₃ are layer dependent. Reducing the crystal thicknesses to one layer widens the bandgaps and the bandgap type transforms from indirect to direct

[45]. Thermal conductivity of layered materials is an isotropic property and the fairly high thermal conductivity along the plane direction drops to a much smaller value for the out of plane direction [71]. Lattice mismatches caused by exfoliation and restacking of the layers reduces this thermal conductivity and therefore, promotes phonon scattering [45, 72].

1.8 Vapor-Liquid-Solid: Growth Mechanisms of One-dimensional Nanostructures

1.8.1 A Reliable Growth Process to Synthesize Nanostructures and Microstructures

The vapor-liquid solid (VLS) mechanism was first reported by S. Wagner in 1964 when Si whiskers were grown with wire-like structure with diameters ranging from hundreds of nanometers to microns [73]. Through this process, reactant species, which were vaporized at high temperatures, are deposited on metal catalysts (*e.g.*, Au and Pt) forming liquid alloy droplets at lower temperatures. As absorption of vapor components continues on liquid alloy droplets, the alloy reaches its supersaturation point.

The system tends to reduce its energy and reaches minimum free energy, which causes precipitation of reactant materials at the liquid-solid interface. The precipitation results in one dimensional crystal growth which continues as long as reactant materials are provided and absorb on the surface of alloy droplets. Due to vapor (vaporized reactant materials), liquid (catalyst alloy), and solid (precipitated 1D structure) phases, the mechanism is known as the VLS. The diameter and position of a catalyst droplet has significant impact on the final morphology of grown 1D structures, which is mostly due to precipitation of solid phase at the confined area of liquid alloy droplet [74].

1.8.2 Metal Catalysts: Potential Candidates for Vapor-Liquid-Solid Mechanism

It should be noted that the candidate metal catalysts should be able (1) to alloy (form a liquid solution) with reactant materials (vaporized in the form of solid phase) and

(2) to form a eutectic alloy, which has a lower melting point compared with two other participant materials in the reactions [75]. Also, (3) when comparing the solubility limit of the liquid phase (C_l) versus the solubility of a solid phase (C_s); the relation $K=C_s/C_l < 1$ should be satisfied. (4) It is required that a metal catalyst has low vapor pressure (V_p), compared with formed liquid alloy, which prevent its evaporation during the growth process. (5) No intermediate phase should be formed during reaction since it hinders the catalytic properties [73].

1.8.3 Kinetics of Vapor-Liquid-Solid Mechanism

Kinetics and rate-determining steps involved in the vapor-liquid-solid (VLS) mechanism have been summarized and discussed by Redwing, Miao [76]. Figure 1-6 illustrates the kinetics of VLS mechanism, which includes four major stages (1) evaporation of reactant materials at high temperatures followed by their transportation in the form of gas phase, (2) deposition (condensation) of transported materials at lower temperatures and their reaction at the vapor-liquid interface, (3) diffusion of reacted materials into the liquid phase, (4) incorporation of diffused atoms into the crystal lattice [77, 78].

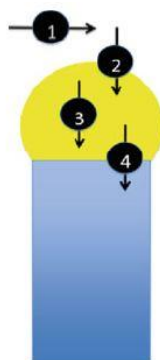


Figure 1-6. Summary of VLS mechanism kinetic stages; (1) mass transportation of vaporized reactant materials, (2) initiation of chemical reaction at vapor-liquid interface,

(3) diffusion of reacted materials into the liquid phase, (4) incorporation of diffused atoms into the crystal lattice [76]

1.8.4 Size Limitation of Metal Catalysts

Due to thermodynamic limitations, there are some limits on reducing the diameter of grown 1D structures from nanometer-sized metal catalysts. With unlimited size reduction of metal catalyst droplets, the diameter of grown 1D structures decreases, but will be limited at certain values [76]. This can be explained through the Eqn. 1-3 and Eqn. 1-4 as below:

$$R_m = \frac{2V_1}{RT \ln(S)} \sigma_{lv} \quad \text{Eqn. 1-3}$$

Where R_m is the minimum radius of a liquid metal droplet, V_l is the molar volume of the droplet, σ_{lv} is the liquid-vapor surface energy, and s is the degree of supersaturation of the vapor [79]. From Eqn. 1-4, reduction in the diameter of the catalytic droplet, increases the rate of supersaturation. On the other hand, the relationship between the chemical potential of a catalytic droplet component and the radius of its curvature should also be taken into account, which is indicated through the Gibbs-Thompson effect:

$$\Delta\mu = \frac{2\gamma}{r} \quad \text{Eqn. 1-4}$$

$\Delta\mu$ shows the chemical potential difference of component in a liquid droplet, γ is the surface energy, r denotes the radius of droplet curvature [76]. Eqn. 1-4 implies that as the radius of droplet curvature reduces, the amount of chemical potential energy of the component in the catalytic liquid alloy increases, which is undesirable. At this stage, reaching supersaturation states becomes complicated and suppressing the growth of nanowires becomes difficult [76].

Reported by Redwing, Miao [76], nanoparticle agglomeration and Ostwald ripening are two factors that hinder the process of downsizing the metal catalyst droplets. Nanoparticles agglomerate and turn into clusters, which is due to their strong van der Waals attractive force. Also at higher temperatures (a required driving force for diffusion of the metal component) and through the Ostwald ripening phenomena, nanoparticles tend to transform into larger particles to reduce the overall energy of the system. Therefore, it is essential to carefully control the parameters involved in the downsizing process of metal catalysts, for example, annealing sputtered Au gold thin film on Si substrate.

1.8.5 Major Challenge Faced by Conventional Metal Catalysts

The VLS growth mechanism has been widely used in the semiconductor industry for the growth of many nanowires such as Si, Ge, ZnO, GaN and GaAs. Many of these nanowires are synthesized by employing Au as the metal catalyst. However Au contamination of the nanowires is one of the major challenges facing this process. This is mostly due to the direct contact of liquid Au (at high temperatures) with the semiconductor, which introduces more impurities to the band gap of the semiconductor materials, altering their optical properties to lower values [80]. In another example, few successful efforts have been reported growth of Si nanowires using Al as metal catalyst, which is mostly due to the quick oxidation of Al [81, 82].

CHAPTER 2. MECHANISM STUDY OF CATALYST-ASSISTED GROWTH

2.1 Introduction

As discussed, molybdenum trioxide, with an orthorhombic crystal structure (α - MoO_3), has received intensive attention due to its anisotropic layered structure suitable for a wide range of applications such as electrochromism, photochromism, lubricants, photocatalysts, gas sensors, and Li-ion or Na-ion batteries [83]. Also the (VLS) mechanism was introduced as the commonly used growth mechanism for one-dimensional (1D) nanostructures and microstructures, using well-known metal catalysts such as Pt or Au. It is worth noting that the major drawback of metal catalysts can be explained by their high temperature reaction with target materials, which produces intermetallic compounds and contamination, and negatively affects the overall electrical and optical properties of synthesized nanostructures [84]. Unlike the common metal catalyst, Tao et al. reported the synthesis of MoO_3 1D structures by utilizing alkali metal based catalysts. Using either catalytic compounds of sodium (e.g., hydroxide, halides, and carbonate) or substrates consisting of alkali metal (e.g., glass), Tao et al. have reported the synthesis of MoO_3 1D nanostructures and microstructures with different morphologies such as rectangular fork-end nanoplates, long nano/micro-belts, and microtowers [83]. However, in order to obtain high density and uniform growth of these nano/microstructures, it is essential to carefully study methods of distributing catalysts on the target substrate.

Using sodium hydroxide, an alkali metal based catalyst, this research is focused on investigating the effects of different ways of providing catalysts to the target substrate, which can substantially control and improve the growth quality (density and uniformity) of MoO_3 1D nanobelts.

During this study, a catalyst was introduced to the target substrate using two different methods. First, a certain amount of sodium catalyst (30 μ l and 10 μ l) was directly drop-cast on the target substrate to investigate its effects on inducing the growth of nano/microstructures inside, outside, and within the droplet boundaries. Second, in order to improve the density and uniformity of the growth, the catalyst was separately drop-cast on another substrate until it fully covers the entire substrate. Then the substrate was placed at different positions (side-by-side, front-back, up-down) close to the target substrate.

2.2 Experimental Procedure

2.2.1 Synthesis Techniques and Equipment

A home-made hot wall chemical vapor deposition (CVD) system was utilized to carry out all the synthesis processes (Figure 2-1). A thermal furnace and a fused silica tube are the major components of the reaction chamber. A 1 inch diameter quartz tube (Quartz Sci, Inc) is fitted into two semi-cylindrical ceramic fiber heaters (WATLOW, Inc), with power density ranging from 0.8 to 4.6 W cm⁻². The reaction chamber is connected to a mechanical pump (Alcatel Adixen 2010SD), labeled downstream, to sustain the low pressure (as low as 20 mTorr) environment inside the chamber. The total length of the furnace is 8 inches, and consists of 6 inches for the heating zone and 2 inches for the cooling zone (1 inch lengthened on each side). Argon (Ar) and oxygen (O₂) gases are introduced from the side labeled upstream as carrier and reactant gases, respectively. Gases are regulated at both low and high flows using flow controllers (Sierra Instruments, Inc). Detailed components of the CVD system are shown in Figure 2-2.

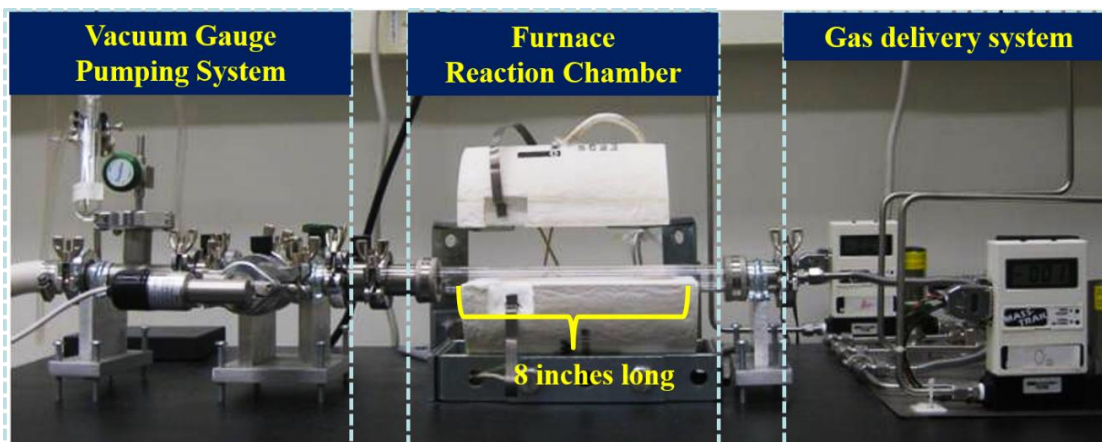


Figure 2-1. Home-built low-pressure chemical vapor deposition system CVD

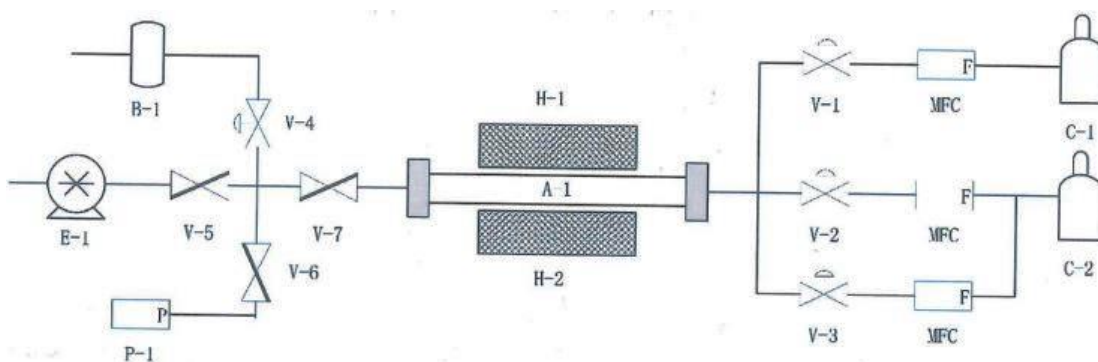


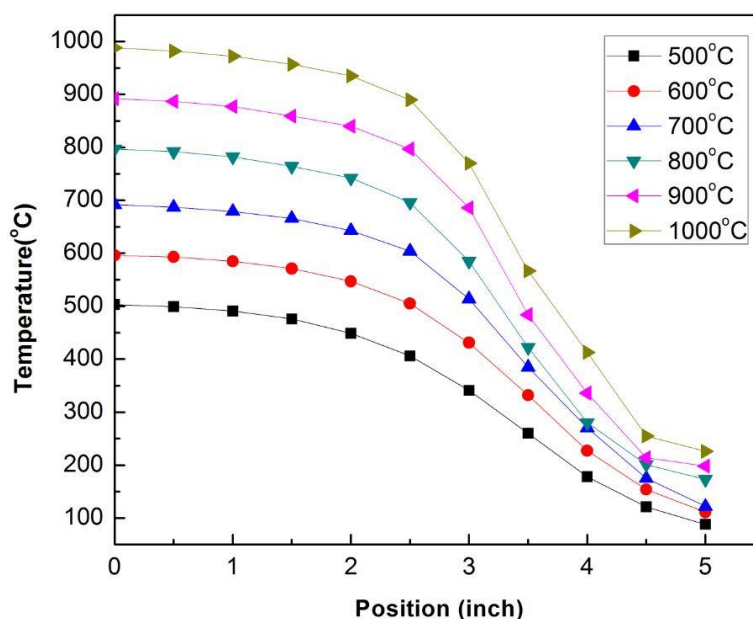
Figure 2-2. Detailed components of the CVD system, where C1-2: Ar and O₂; MFC: mass flow controllers; V1-4: needle valves; H1-2: ceramic heater; A1: quartz tube; V5-7: butterfly valves; B1: bubbler; E1: mechanical pump; P1: pressure gauge

Except the heating rate (30°C/ min) and cooling rate (60°C/ min), which are kept constant for all the experiments, the time, central heating temperature, the absolute gas flow, amount of source materials, and the location of substrates are the controllable variables of this CVD system. The ranges and resolutions for both temperature and gas flows (Ar and O₂) are summarized in Table 2-1.

Table 2-1. Range and resolution of the home-built CVD system

	Temperature	Pressure	Flow	
			Ar	O ₂
	°C	mTorr	sccm	sccm
Range	Room Temp-1100	10 mTorr-1 atm	0-100	0.08-4
Resolution	±1%			

The temperature calibration of the CVD system was carried out by setting up different temperatures (500-1000°C) in the ambient environment, and recording the actual temperature using a thermocouple (Omega, CN8200-DC1-FH2). Figure 2-3 indicates the obtained calibrated temperature profile. The center of the CVD system presents a uniform heating zone about one and a half inches long. The uniformity of the heating zone decreases slightly when reaching either 2 inch point and then rapidly falls afterward.

**Figure 2-3.** Temperature profile of home-built CVD system in ambient environment

The ability to adjust and control growth parameters such as time and temperature is the most important advantage of the above CVD system. Source and substrate can be placed at different locations across the heating chamber in order to control the growth

conditions or the source heating conditions. During this project the 0 inch point is referred to as the center of heating chamber (uniform heating zone), and the 4 inch point is referred to as the downstream heating zone connected to mechanical pump (Figure 2-4). For each growth experiment, the source materials (molybdenum powders or molybdenum trioxide powders/whiskers) are placed in the center of the heating zone (0 inch point) and the CVD system is set for a specific time and temperature.

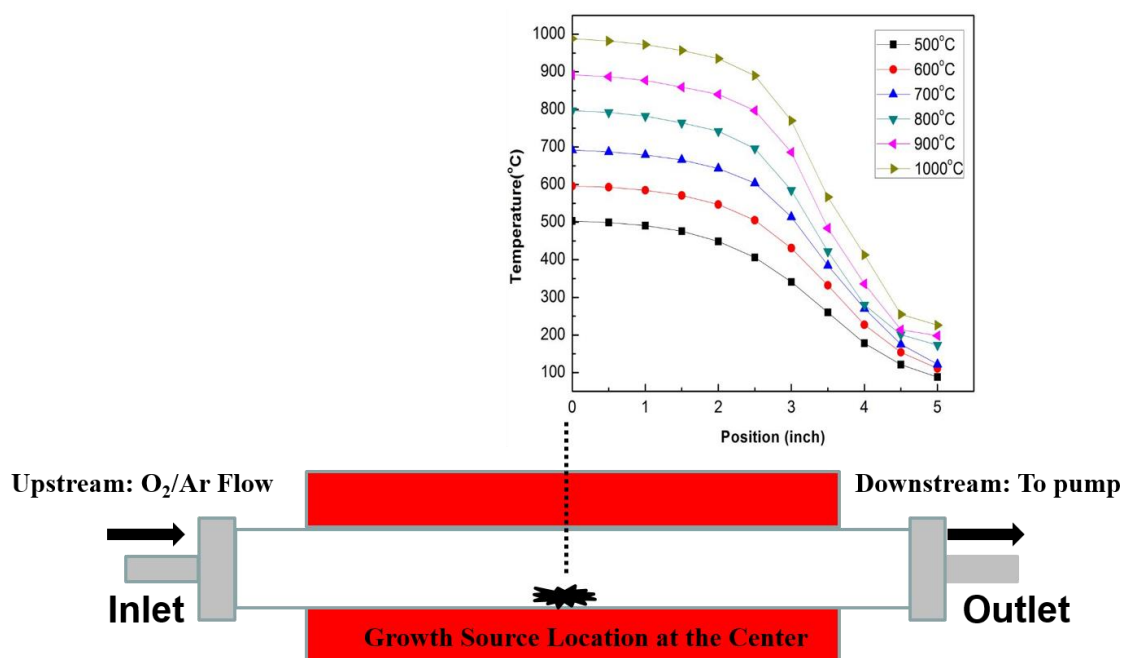


Figure 2-4. Change in temperature profile across the reaction chamber

In presence of oxygen flow, and once the heating chamber reaches the target temperature, oxidation and evaporation of source materials' species are initiated. The transportation of growth species from source materials to target substrate is carried out by carrier gas (Ar). Upon reduction in temperature, the deposition process is initiated, leading to bombarding of the substrate and chamber wall by growth species. Detailed growth conditions and mechanisms will be discussed in the following chapters.

2.2.2 Substrate Preparation and Growth Parameters (CVD furnace setup)

A silicon (100) substrate (1 μm SiO₂/Si, p-type, University Wafers) was cut into 10 mm by 25 mm rectangular pieces and then washed in an ultrasound cleaner (Branson 1510R-MTH) using acetone and alcohol solutions for 15 minutes and were dried by nitrogen gas.

For some experiments, oxygen plasma cleaning (Plasma-Preen 862, Kurt J Lesker) was employed to achieve a hydrophilic surface for uniform distribution of catalytic materials on the silicon substrate. Sodium hydroxide powders (NaOH, Fisher Scientific, 99.98%) were dissolved in DI water to prepare a 0.01M solution of sodium hydroxide (NaOH) as the catalytic materials. This solution was drop-casted (30 μL) on the center of the silicon substrate and air dried in a chemical fume hood. Here we use the term “target or bare substrate” for a silicon substrate with no catalytic materials, and the term “catalytic substrate” for the drop-casted silicon substrate (30 μL of 0.01M NaOH) which was either treated or untreated with oxygen plasma. For all the experiments, the CVD system target temperature/time was set at 800°C for 30 minutes with a 10 sccm oxygen flow as the reactant gas, and a 10 sccm UHP Ar (99.999%) as a carrier gas. The reactant and carrier gases were introduced to the CVD reaction chamber. One gram of molybdenum powders (Mo, Alfa Aesar, 99.9%) were placed at the center of the reaction chamber at 800°C as the growth source. For all the experiments, the target substrates (substrates with or without the catalytic droplet) remained in the same position. These target substrates were placed at the downstream (extending from 7 inches to 8 inches) inside the reaction chamber and in a temperature range of 280-585-°C. Depending on the experiment, the position of an

additional catalytic substrate, which was used for providing an extra source of Na to the target substrate, was changed for each experiment.

2.3 Results and Discussion

2.3.1 Distribution of Catalyst (One Droplet)

The prepared catalytic substrate (Figure 2-5) was placed in the downstream area (heating zone of 280-585°C) inside the CVD reaction chamber. The growth was carried out according to the conditions mentioned in the experimental section. Substrate schematics for before and after growth are shown in Figure 2-5. The before growth condition indicates the drop-casted catalytic droplet at the center of the substrate. The after growth condition shows white covered areas that represent the region that underwent growth during this experiment. The purple color represents the high temperature areas with no growth.

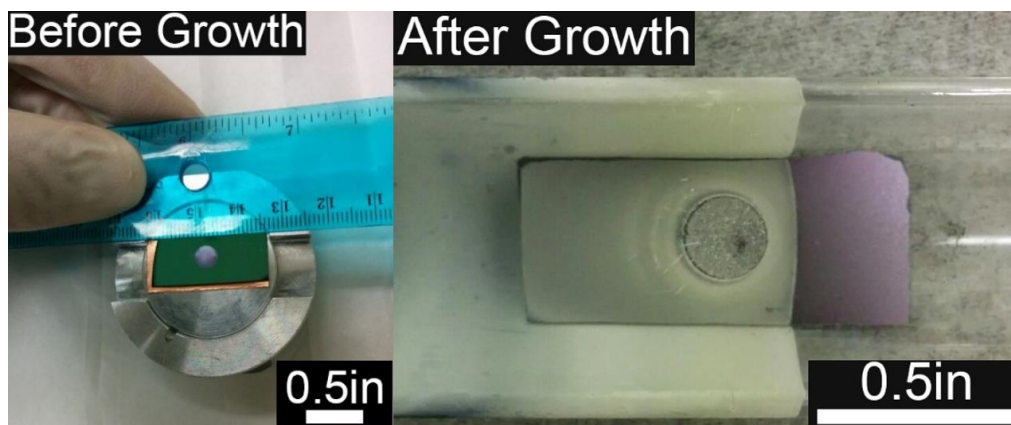


Figure 2-5 Schematic of catalytic substrate before (left) and after (right) growth: 30 μL of 0.01M NaOH drop-casted on SiO_2/Si substrate

Before growth, the morphology of the drop-casted sodium hydroxide droplet was examined using an optical microscope (OM), and scanning electron microscope (SEM) techniques were utilized to investigate the white areas covering the substrate at the end of

the experiment. Figure 2-6 (a and b) illustrates the substrate condition before and after the experiment.

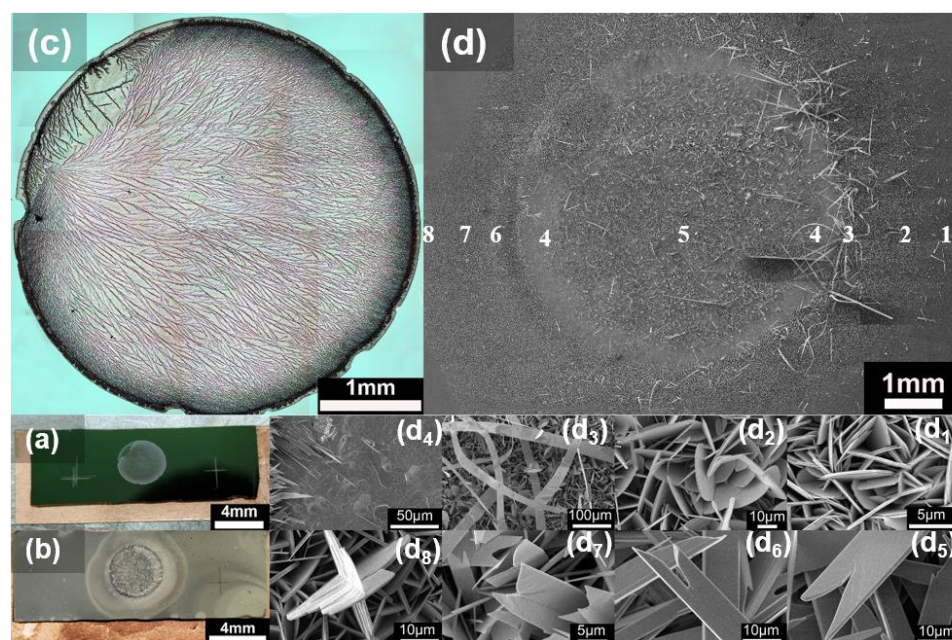


Figure 2-6. One droplet experiment: catalytic effects of sodium hydroxide on growth morphology of molybdenum oxide. (a) before growth, 30 μL of 0.01M NaOH drop-casted on SiO_2/Si substrate and air dried overnight, (b) after growth, schematic of growth coverage on and around the catalytic droplet, (c) optical microscope image of drop-casted catalyst before growth, (d) obtained SEM image from growth morphology across the substrate, (d₁) not catalytically affected area; thick density growth of MoO_3 semi-circle microplates, (d₂) lower density growth of MoO_3 semi-circle microplates (d₃) growth of long triangle end nanobelts at the droplet's right outer boundary, (d₄) no growth in boundary area between the center and outer region of droplet, (d₅) formation of short fork end microplates at the center of the droplet, (d₆) formation of long fork end microplates at the droplet's left inner boundary, (d₇) formation of thick fork end microplates at the droplet's left outer boundary, (d₈) reappearance of thick density growth of MoO_3 semi-circle microplates, not catalytically affected area.

Before growth, the catalytic droplet indicated a uniform and wide range of branch-type structures linked together through the entire droplet (Figure 2-6-c). Figure 2-6-d shows the white coverage on the substrate under SEM. The numbers are ordered from high temperature to low temperature region corresponding to different morphologies. Semi-circle platelets (Figure 2-6-d₁ - d₂), long belts (Figure 2-6-d₃), fork-end rectangular plates (Figure 2-6 d₅- d₇) are the typical observed morphologies outside and inside of the catalytic

droplet. A no growth zone (Figure 2-6- d₄) was also observed. In order to accurately investigate the growth mechanism, this study is focused on results obtained from experiments with one catalytic droplet.

2.3.1.1 Growth Inside and Outside of Droplet (30 ul Sodium Hydroxide)

In order to examine the growth dependence of the MoO₃ differing morphologies in respect to location of catalytic droplet boundaries, two experiments were performed. First, we analyzed the growth boundaries' regions of the catalytic droplet, with 30 μ L before and after growth. Later on, the results were verified by repeating the experiment for a 1 μ L catalytic droplet.

For this purpose, and for both right and left droplet boundaries, three locations were selected within the droplet boundaries.

Figure 2-7 summarizes the selected locations within the right boundary of the catalytic droplet. The locations were chosen from innermost, outermost, and outside of the droplet boundary, respectively (Figure 2-7 a-c). Low and high magnification SEM images of the candidate locations were captured and are shown in Figure 2-7 a-c and Figure 2-7 a₁-c₁, respectively. Also, Figure 2-7 a₂-c₂ and Figure 2-7 a₃-c₃ indicate the high and low magnification SEM images of the same locations after growth. By comparing the SEM images before and after growth, it is concluded the distance between the innermost and outermost points of the droplet boundary Figure 2-7 a-c), which is around 100 μ m, defines the right limit of droplet boundary after the growth (Figure 2-7 a₃-c₃) where the growth of triangular nanobelts initiates.

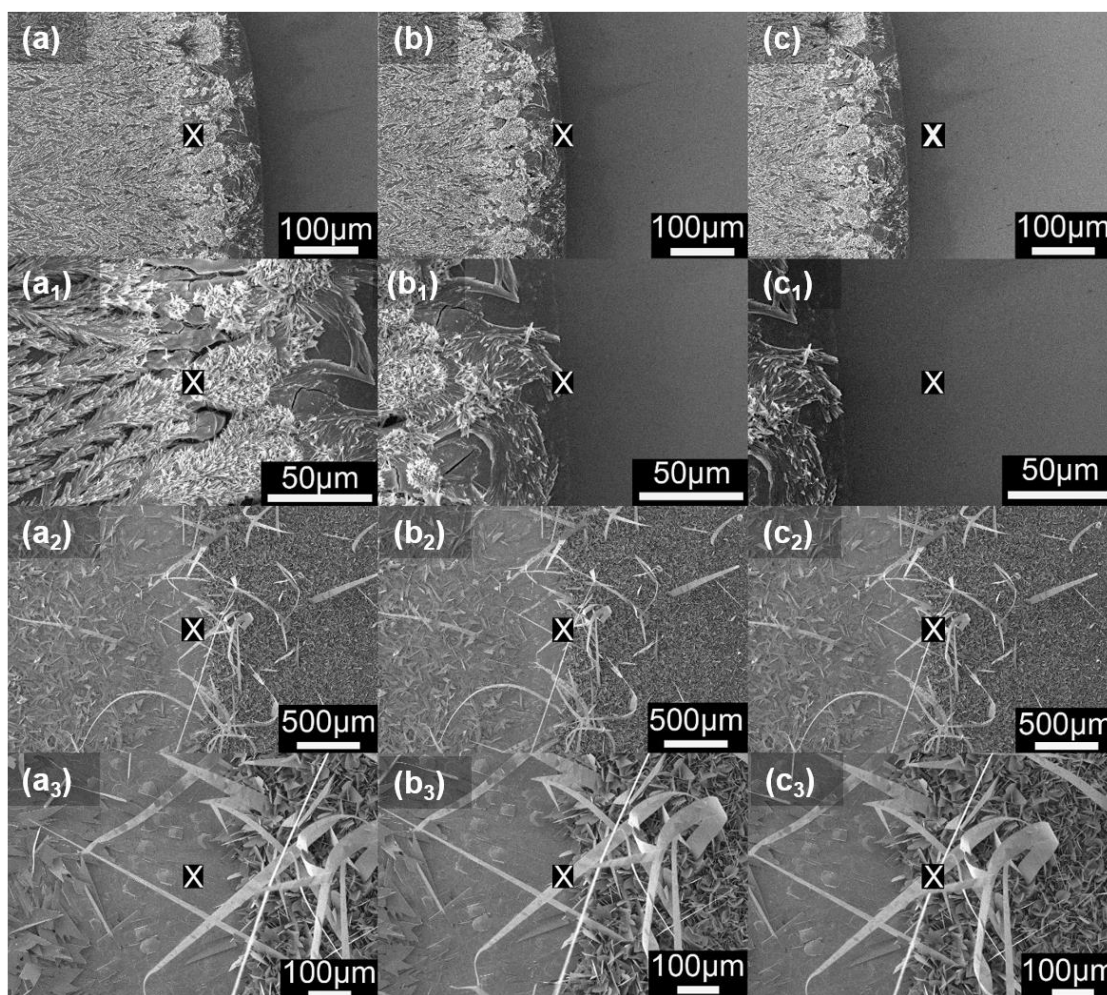


Figure 2-7. SEM images of selected locations within the right boundary of the 30 μL catalytic droplet before and after the growth. Before growth: (a - a₁) low and high magnification SEM images of innermost region of the droplet boundary, (b - b₁) low and high magnification SEM images of outermost region of the droplet boundary, (c - c₁) low and high magnification SEM images outside the droplet boundary. After growth: a₂ - a₃) low and high magnification SEM images of innermost region of the droplet boundary, (b₂ - b₃) low and high magnification SEM images of outermost region of the droplet boundary, (c₂ - c₃) low and high magnification SEM images outside the droplet boundary

Crystalline branches of drop-casted sodium hydroxide at the center of the droplet are shown at low and high magnification (Figure 2-8 a-b). The obtained growth, mostly in fork-end rectangular microplates, are also shown in Figure 2-8 c-d. This is the typical type of growth coverage at the center of the catalytic droplet which mostly extends to both right and left boundaries.

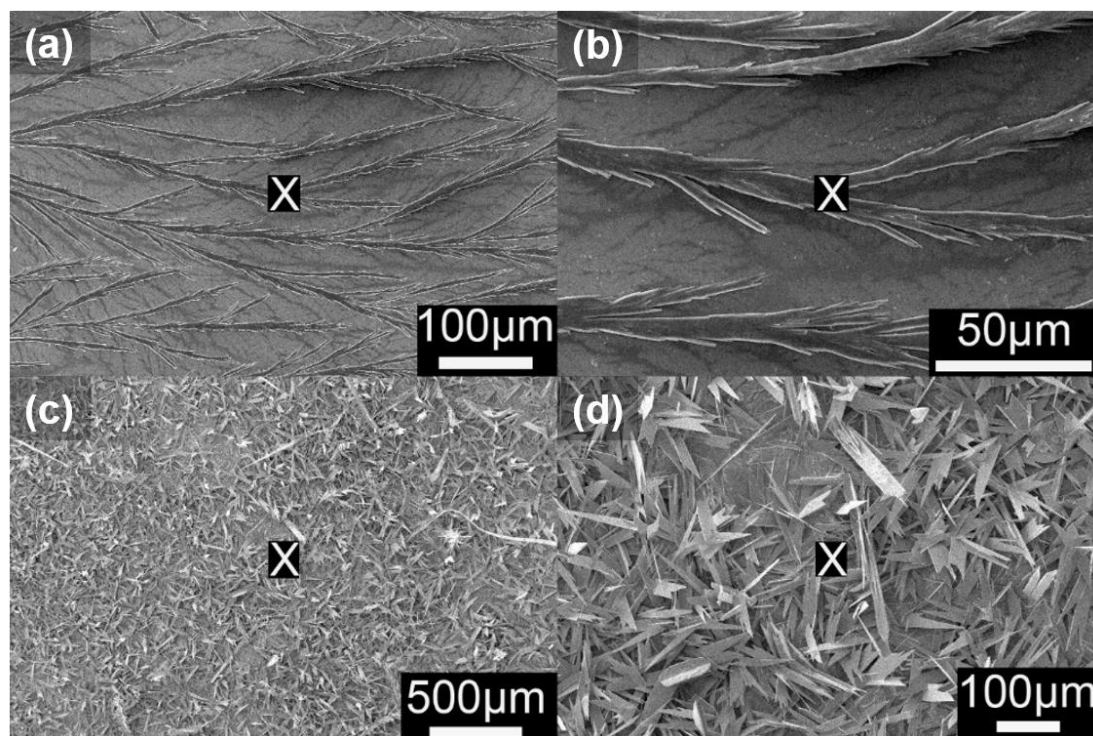


Figure 2-8. SEM images were captured from the center of the catalytic droplet before and after the growth, images (a - b) are low and high magnification SEM images of NaOH crystal branches before the growth, images (c - d) are low and high magnification SEM images of obtained growth at the center of catalytic droplet.

Figure 2-9 summarizes the selected locations within the left boundary of the catalytic droplet. The locations were chosen from the outermost, the middle, and the innermost areas of the droplet's left boundary, respectively (Figure 2-9 a-c). Low and high magnification SEM images of the selected locations were captured and are shown in Figure 2-9 a-c and Figure 2-9 a₁-c₁, respectively. Also Figure 2-9 a₂-c₂ and Figure 2-9 a₃-c₃ indicate the high and low magnification SEM images of the same spots after growth.

SEM images comparison of locations before and after growth verify a similar conclusion as the right droplet boundary, which means the 100 μm distance between selected location (Figure 2-9 a-c) shows no sign of growth and this is the area where the left droplet boundary comes to an end. Different growth morphology, in comparison with

the right droplet boundary, shows that long fork-end rectangular microplates started appearing right after this location.

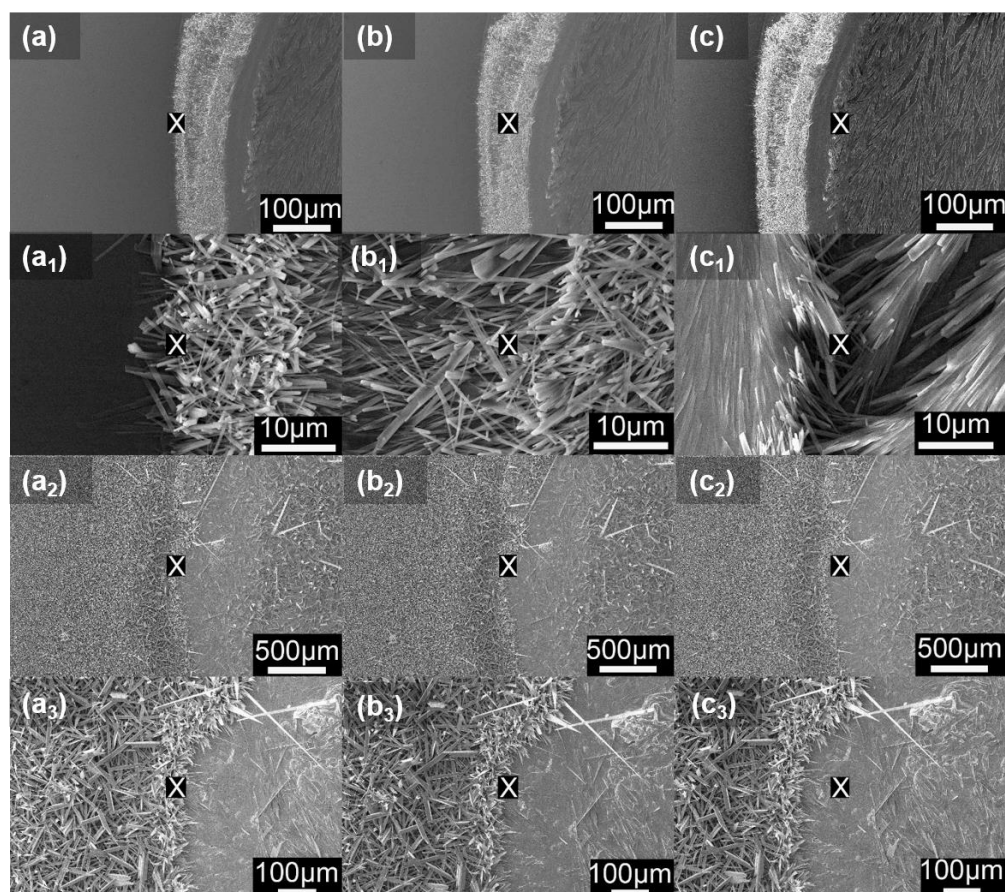


Figure 2-9. SEM images of selected locations within the left boundary of the 30 μL catalytic droplet before and after the growth. Before growth: (a - a₁) low and high magnification SEM images of the outermost region of the droplet boundary, (b - b₁) low and high magnification SEM images of middle region of the droplet boundary, (c - c₁) low and high magnification SEM images of innermost area of the droplet boundary. After growth: (a₂ - a₃) low and high magnification SEM images of the outermost region of the droplet boundary, (b₂ - b₃) low and high magnification SEM images of middle region of the droplet boundary, (c₂ - c₃) low and high magnification SEM images of innermost area of the droplet boundary

2.3.1.2 Growth Inside and Outside of Droplet (10 μL Sodium Hydroxide)

Figure 2-10, shows SEM images of the catalytic droplet boundaries before and after growth that were obtained and compared (Figure 2-10).

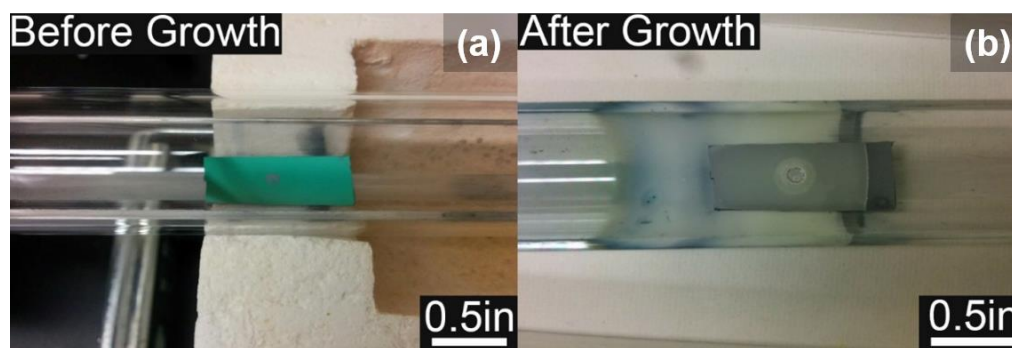


Figure 2-10. (1) Drop-casted sodium hydroxide catalytic droplet (1 μ L) on SiO₂/Si substrate before growth, (b) catalyst- assisted growth of MoO₃ (after growth)

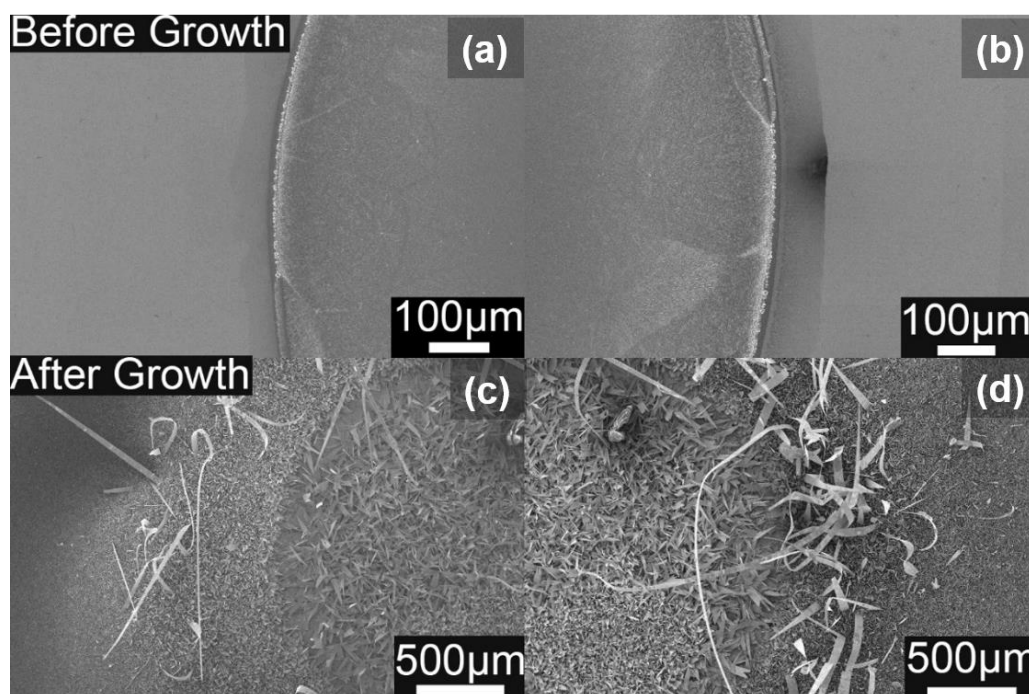


Figure 2-11. SEM images of the NaOH catalytic droplet before and after growth: (a - b), SEM images from right and left boundaries of the drop-casted NaOH catalyst on bare SiO₂/Si substrate before growth: (c-d), SEM images of the catalyst-assisted growth of MoO₃ with different morphologies on right and left boundaries of the catalytic droplet after growth.

Three locations were chosen within both the right and left boundaries of the catalytic droplet, and the SEM images of the chosen locations were obtained before and after growth (Figure 2-12 and Figure 2-13). Before growth, and from the right droplet boundary region, locations were chosen from the innermost, middle, and outermost areas within the boundary zone, respectively (Figure 2-12 a-c). By comparing the obtained SEM

images before and after growth, Figure 2-12 (a1-a2, b1-b2, and c1-c2), it is concluded that, before growth, the distance between the chosen outermost and innermost points defines the boundary between two different morphologies of MoO_3 after growth.

That is where growth of long nanobelts (on top of the semi-circle microplates) comes to an end, and the formation of fork-end rectangular microplates begins.

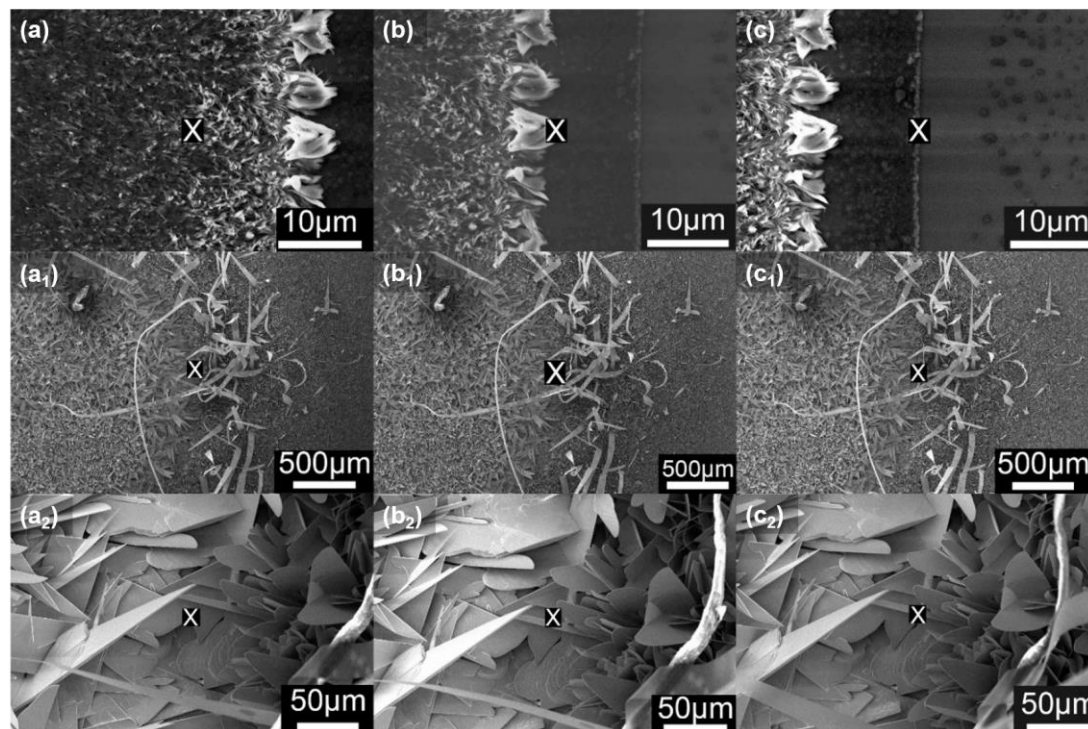


Figure 2-12. SEM images of selected locations within the right boundary of the catalytic droplet before and after growth. Before growth: (a) is the innermost region of the right droplet boundary; (b) is the middle region of the right droplet boundary; (c) is the outermost region of right droplet boundary. After growth: (a₁, a₂) are high magnification SEM images of obtained growth from the innermost region. (b₁, b₂) are high magnification SEM images of obtained growth from the middle region. (c₁, c₂) are high magnification SEM images of obtained growth from the outermost region.

Similar to right droplet boundary, before growth, and from the left droplet boundary, three locations were chosen from the outermost, middle, and innermost areas within the boundary zone, respectively (Figure 2-13 a-c). By comparing the obtained SEM images before and after growth (Figure 2-13 (a₁-a₂, b₁-b₂, and c₁-c₂), it is concluded that,

before the growth, the distance between the chosen outermost and innermost points ($\sim 25\mu\text{m}$) specifies the boundary between two different morphologies of MoO_3 after the growth. That is where the growth of fork-end rectangular microplates comes to an end and a high density of semi-circle microplates starts appearing again. Also it is concluded that rectangular fork-end microplates are the dominant MoO_3 morphology type within the catalytic droplet.

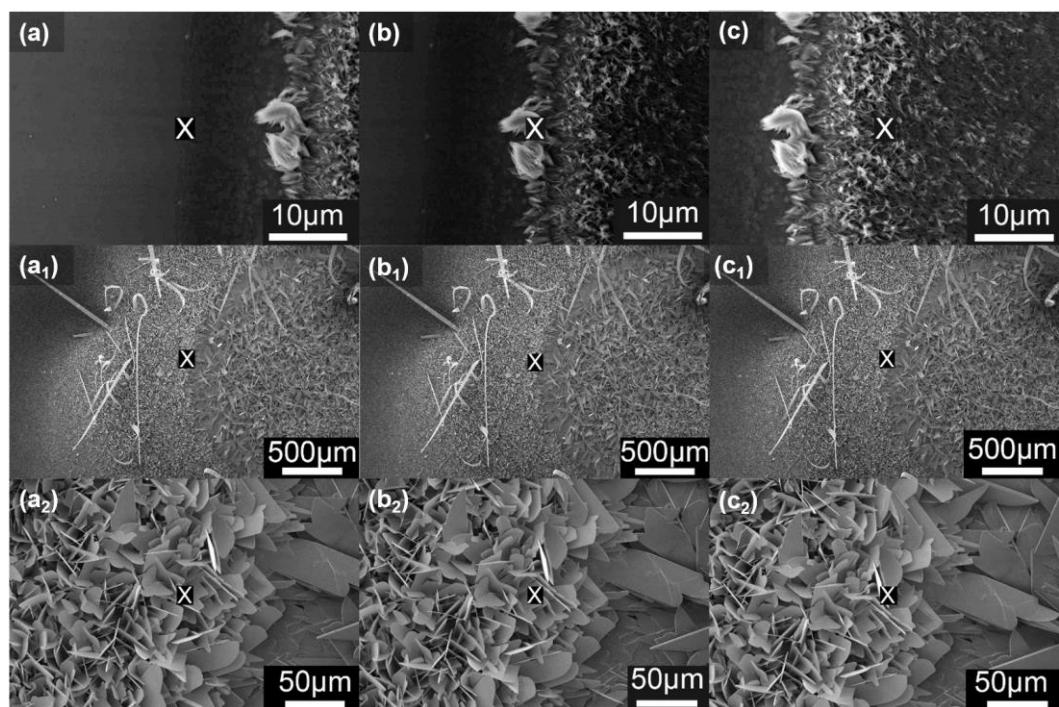


Figure 2-13. SEM images of selected locations within the left boundary of the catalytic droplet before and after growth. Before growth: (a) is the outermost region of the right droplet boundary; (b) is the middle region of the right droplet boundary; (c) is the innermost region of right droplet boundary. After growth: (a₁, a₂) are high magnification SEM images of obtained growth from outermost region; (b₁, b₂) are high magnification SEM images of obtained growth from the middle region; (c₁, c₂) are high magnification SEM images of obtained growth from the innermost region.

2.3.2 Distribution of Catalyst (Three Droplets)

Under the same growth conditions, a similar experiment was repeated with a SiO_2/Si substrate which had three catalytic droplets (each droplet contained $30\ \mu\text{L}$ of 0.01M NaOH). Figure 2-14 a-j summarizes several different types of morphologies that

emerged under this growth condition. Besides rectangular, rounded, fork-end, and semi-circle microplate morphologies, which were mostly forming inside the droplet's boundaries, a few long nanobelts (this research's focus) were observed between the catalytic droplets.

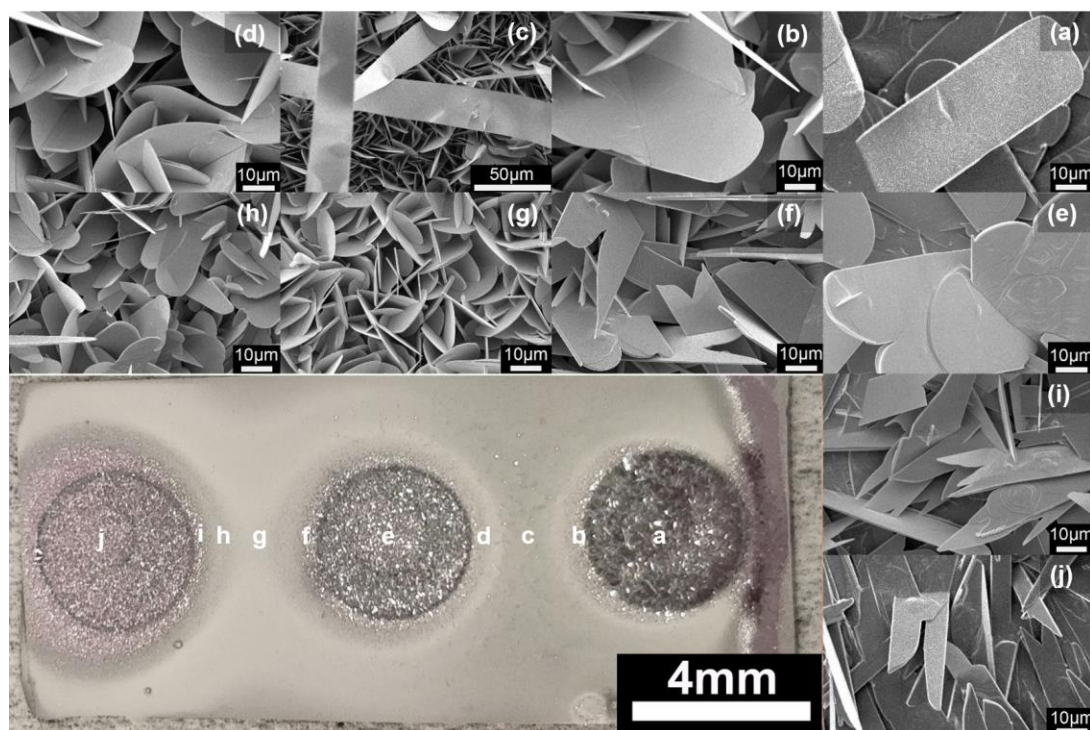


Figure 2-14. Three droplets experiment: catalytic effects of sodium hydroxide on the growth morphology of molybdenum oxide; (a-j) schematic of growth coverage on and around the catalytic droplet: (a) rectangular microplates at the center of droplet, (b) semi-circle microplates within droplet boundary, (c) long triangular-end nanobelts appeared outside of droplets boundaries, (d) semi-circle microplates within droplet boundary, (e) rounded fork-end rectangular plates at the center of droplet, (f) sharp fork-end rectangular microplates within the droplet boundary, (g) high density of semi-circle microplates outside droplet boundary, (h) round end rectangular microplates within droplet boundary, (i) fork-end rectangular microplates at innermost droplet boundary, (j) fork-end rectangular microplates at the center of the droplet.

2.3.3 Growth Morphology Study (Single Substrate)

Here we divide the growth region into three sections of right, center, and left sides of the catalytic droplet and the growth morphologies are discussed in detail below.

2.3.3.1 High Temperature Zone (Right side of Catalytic Droplet)

Using SEM techniques, we carefully study the effects of the sodium hydroxide catalyst on the morphology of MoO_3 deposition at high ($462\text{--}585^\circ\text{C}$), medium ($410\text{--}462^\circ\text{C}$) and low ($280\text{--}410^\circ\text{C}$) temperature zones across the SiO_2/Si substrate. Figure 2-15 a-d, shows the SEM images obtained from growth of MoO_3 at the right side of catalytic droplet with different morphology. At higher temperatures ($462\text{--}585^\circ\text{C}$), low and poor density growth of MoO_3 semi-circle microplatelets ($40\mu\text{m}$ long) was observed (Figure 2-15 b). Further reduction of temperature across the substrate leads to high density growth of MoO_3 microplatelets (Figure 2-15 c). Growth of a few long nanobelts (a few millimeters long) was observed on top of the MoO_3 microplatelets at the right side of the catalytic droplet boundary (Figure 2-15 d).

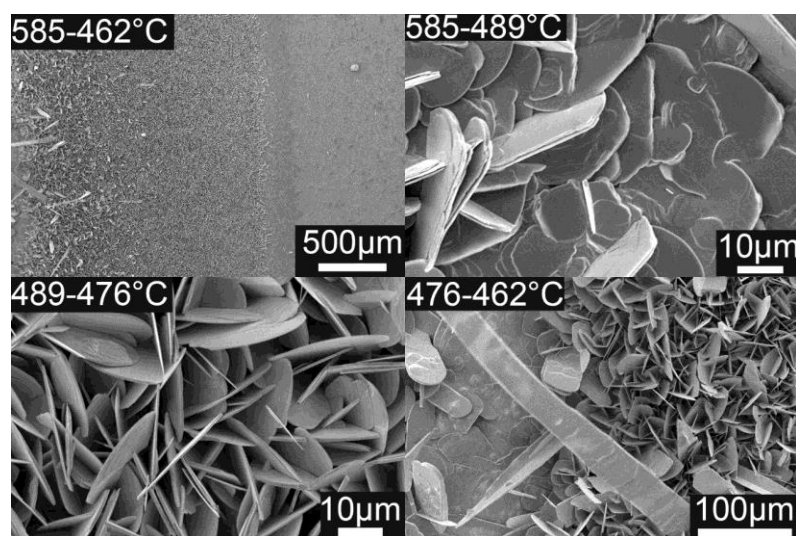


Figure 2-15. SEM images of the effect of the sodium hydroxide catalyst on the morphology of MoO_3 (at the right side of catalytic droplet): (a) low magnification SEM image of MoO_3 with different morphology grown with the NaOH catalyst (from upstream side of the substrate toward the right side of the of catalytic droplet boundary), (b) low density growth of MoO_3 microplatelets, (c) high density growth of MoO_3 microplatelets (d) mixed growth of MoO_3 platelets (underneath) and nanobelts (on top) at the droplet boundary.

2.3.3.2 Mid-temperature Zone (Center of Catalytic Droplet)

Figure 2-16 indicates the catalytic effect of NaOH droplet on growth morphology of MoO_3 at the center of the droplet. In the temperature zone of $462\text{--}410^\circ\text{C}$, two different types of morphology were observed: round-end rectangular microplates (up to $200\text{ }\mu\text{m}$ long), mostly parallel to the substrate (Figure 2-16 a-b), and fork-end rectangular microplates ($100\text{--}200\text{ }\mu\text{m}$ long), which also were parallel to the substrate.

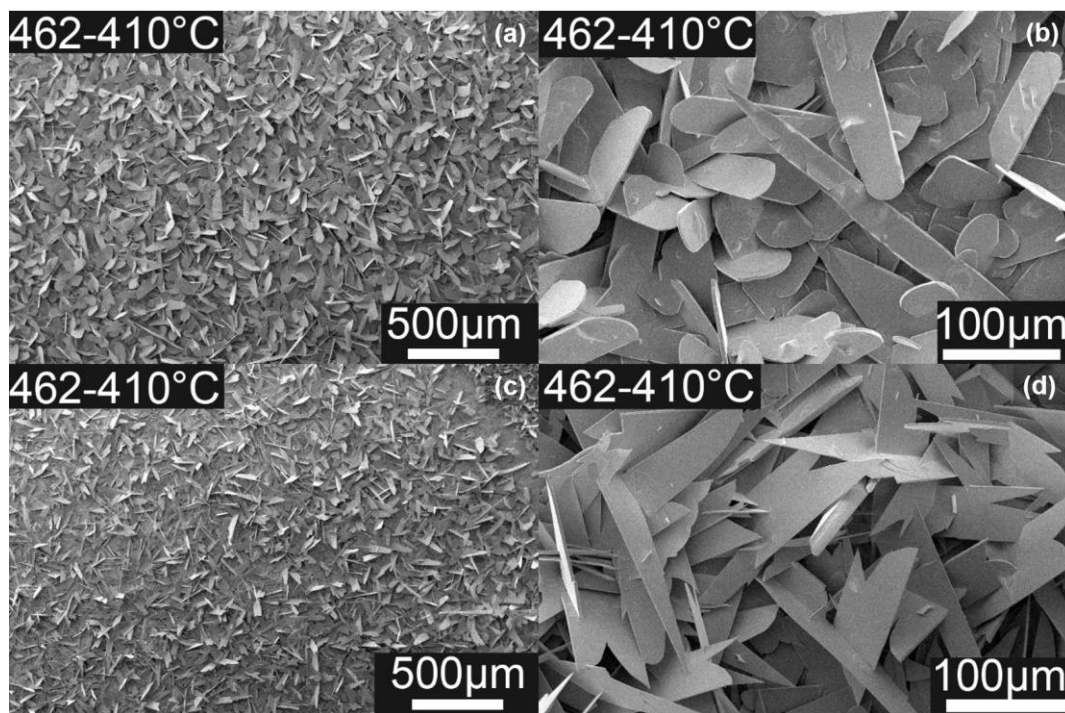


Figure 2-16. SEM images of the effect of the sodium hydroxide catalyst on the morphology of MoO_3 (at the center of catalytic droplet): (a-b) SEM images of low and high magnification of round-end rectangular microplates, (c-d) SEM images of low and high magnification of fork-end rectangular microplates.

2.3.3.3 Low Temperature Zone (Left Side of Catalytic Droplet)

Thick, high density, and mostly uniform growth of semi-circle microplates was observed at the left side of the catalytic droplet boundary in the $280\text{--}410^\circ\text{C}$ temperature zone (Figure 2-17 a), which is very similar to the growth morphology at the high temperature zone of $476\text{--}489^\circ\text{C}$. Growth of fork-end rectangular microplates comes to end

at the left boundary of the catalytic droplet (Figure 2-17 b). Although semi-circle microplates of MoO_3 are the dominant growth morphology at the left side of the catalytic droplet (Figure 2-17c), very few long (millimeter) nanobelts were observed on top of them (Figure 2-17 d).

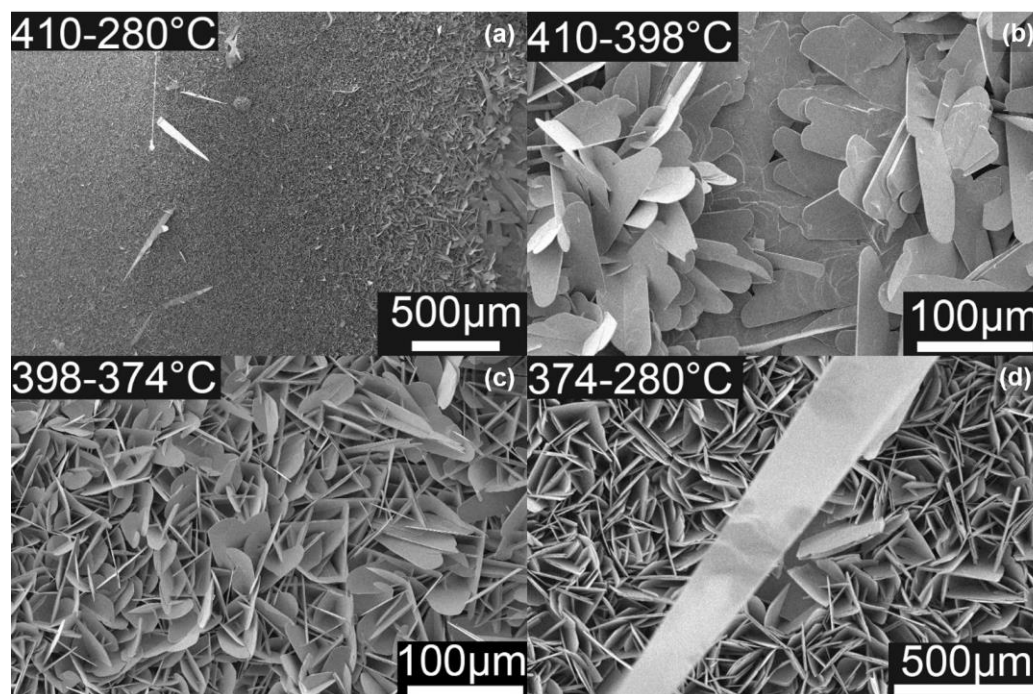


Figure 2-17. SEM images of the effects of the sodium hydroxide (NaOH) catalyst on the morphology of MoO_3 (at the left side of catalytic droplet): (a) low magnification SEM image of MoO_3 with different morphology grown with the NaOH catalyst (from left side of the catalytic droplet boundary toward the downstream side of the substrate), (b) growth morphology on the left boundary of the catalytic droplet, (c) thick and high density growth of semi-circle microplates, (d) appearance of very few long nanobelts on top of the semi-circle microplates.

Table 2-2 summarizes obtained MoO_3 morphologies at different temperature zones and locations around the catalytic NaOH droplet.

Table 2-2. Summary of MoO₃ growth morphology at different temperature zones grown with NaOH catalyst

High Temp. Zone.	585-489°C	489-476°C	476-462°C
MoO ₃ Growth Morphology	No growth, (few semi-circle microplates)	High density of semi-circle microplatelets	Droplet right boundary : few long nanobelts
Medium Temp. Zone.	462-410°C		
Growth Morphology	round-end rectangular microplates and fork-end rectangular microplates		
Low Temp. Zone.	410-398°C	398-374°C	374-280°C
Growth Morphology	Droplet left boundary: end of fork-end rectangular microplates, start of semi-circle microplatelets	High density of Semi-circle microplatelets	Underneath : high density of semi-circle microplatelets, On top: few long nanobelts

Here we performed a series of experiments which investigated the effects of how the growth morphology of MoO₃ changes when providing additional catalytic materials to the target substrate.

For this purpose, a plasma cleaned SiO₂/Si substrate was cut and cleaned, as discussed in the experimental section, and was drop-casted with 30 µL (3 droplets) of 1M sodium hydroxide (NaOH). The substrate was placed at different locations around the target substrate. The selected position for both substrates were chosen as “front-back”, “side-by-side”, and “up-and-down”. As it was explained before, no change was made to the location of the target substrate.

2.3.4 Growth Improvement by Additional Source of Catalyst

2.3.4.1 Front-Back Position:

The prepared additional substrate, with an additional source of Na, was placed behind the target substrate and inside the reaction chamber (extending from 6 inches to 7 inches with a temperature range of 585-742°C, (Figure 2-18).

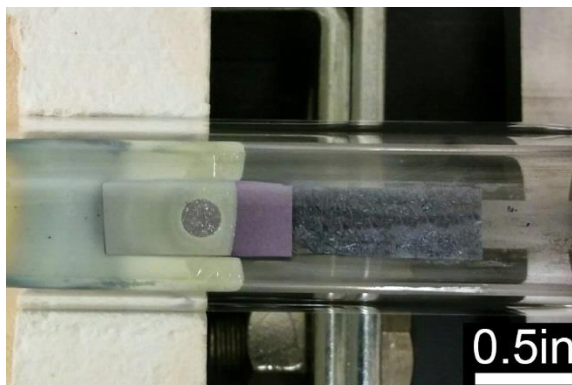


Figure 2-18. Front back position; back: SiO_2/Si substrate with extra source of Na, 30 μl 1M NaOH, located at 585-742°C. Front: target substrate with NaOH catalytic droplet, 10 μl 0.01M NaOH, placed at 280-585°C.

No change was made to the experimental conditions and the experiment was performed at 800°C for 30 min while introducing 10 sccm oxygen and Ar gasses to the reaction chamber. Growth results, from the right side of the catalytic droplet, are summarized in Figure 2-19 a-c. No major change was observed in type of MoO_3 growth morphology in comparison to the experiment conducted without the additional source of Na. However, the growth density of long triangle nanobelts was substantially improved (Figure 2-19d).

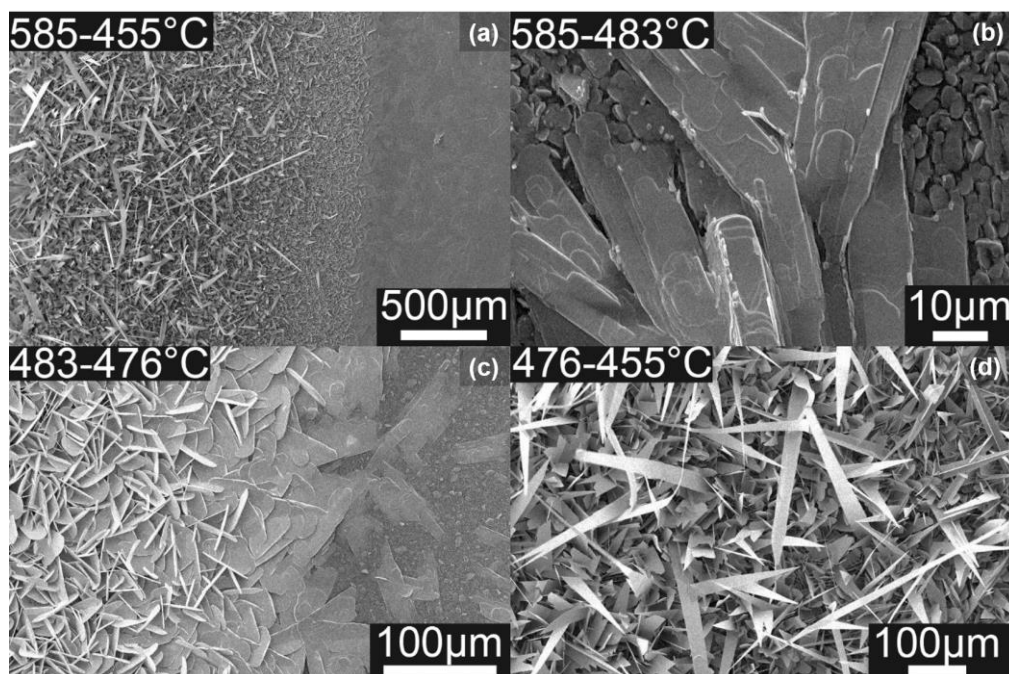


Figure 2-19. Front-back position: SEM images obtained from different MoO_3 morphologies grown by providing an extra source of catalytic materials (right side of the catalytic droplet on the target substrate): (a) low magnification SEM image of growth (from the upstream side of the substrate toward the right side of the of the catalytic droplet boundary), (b) low density growth parallel to the substrate, (c) appearance of semi-circle microplatelets, (d) mixed growth; underneath: MoO_3 platelets below and long triangle nanobelts on top.

The MoO_3 morphologies obtained from the left side of the catalytic droplet, are shown in Figure 2-20 a-f. In comparison with the experiment without extra catalytic substrate (Figure 2-17), few changes were observed in the growth morphologies of MoO_3 . First, the growth of semi-circle microplates were not observed at the end of the droplet boundary; instead, the growth of rectangular fork-end microplates continued from the center of the droplet (Figure 2-20b). However, this covered a small area (1mm) and growth of semi-circle microplates restarted after this zone (Figure 2-20c). Second, a substantial increase in growth of long triangle nanobelts was noticed (Figure 2-20d), which was similar to what was observed on the droplet's right boundary.

Finally, a new tower structure of MoO_3 morphology was identified (Figure 2-20e). The microtowers are made of stacks of MoO_3 platelets with low density growth (Figure 2-20 f).

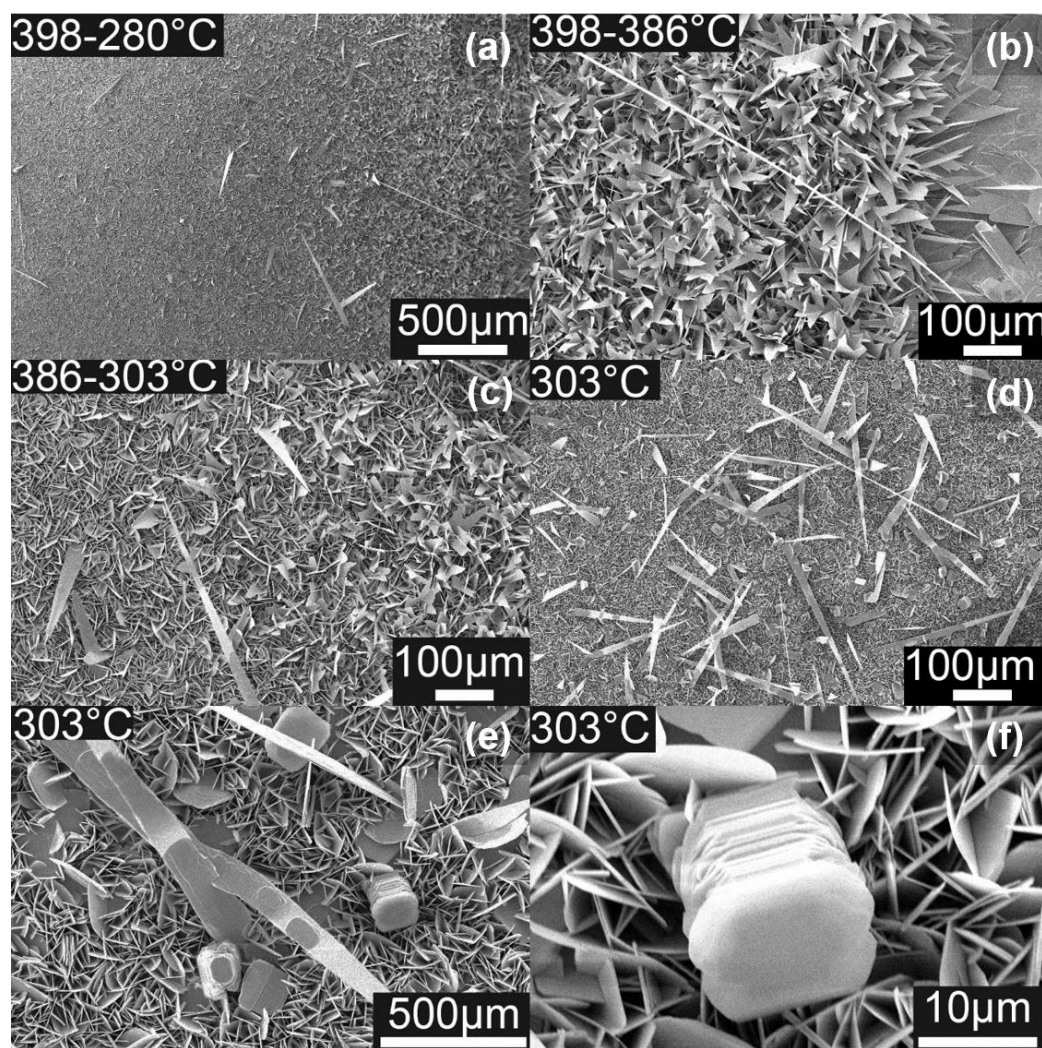


Figure 2-20. SEM images obtained from different MoO_3 morphologies grown by providing an extra source of catalytic materials (the left side of the catalytic droplet on the target substrate): (a) Low magnification SEM image of growth (extending from droplet's left boundary toward downstream), (b) continuation of MoO_3 rectangular fork-end microplates from the center of the droplet, (c) end of fork-end microplate morphology and the reappearance of semi-circle microplates (underneath) and long triangular nanobelts (on top), (d) increase in growth density of long triangular nanobelts, (e) appearance of tower-like structure, (f) high magnification of the MoO_3 micro-tower structure

2.3.4.2 Side-by-Side Position (Catalytic Droplet on the Target Substrate)

Unlike the previous experiment, here the extra catalytic substrate was placed next to the target substrate (Figure 2-21), and at the temperature range of 585-742°C.

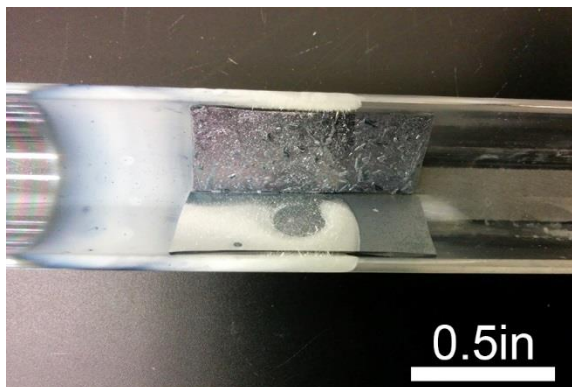


Figure 2-21. Side-by-side position: SiO₂/Si substrate with an extra source of Na, 30 μ l 1M NaOH, was placed next to the target substrate, the substrate with 10 μ l 0.01M NaOH, and at temperature range of 585-742°C.

SEM images obtained from different morphologies of MoO₃ are summarized in Figure 2-22 a-c (low magnification), and Figure 2-22 d-f (high magnification). Similar to previous experiments, no major difference was observed in the type of MoO₃ growth morphologies. In the low temperature area, in the droplet's left boundary, semi-circle microplates appeared underneath while long triangle nanoribbons were on top (Figure 2-22 a & d). The flat rectangular fork-end microplates covered most of the center of the catalytic droplet (Figure 2-22 b & e). Finally, in the high temperature area, at the droplet's right boundary, growth morphologies were in the form of semi-circle microplates underneath and long nanobelts on top (Figure 2-22 c & f).

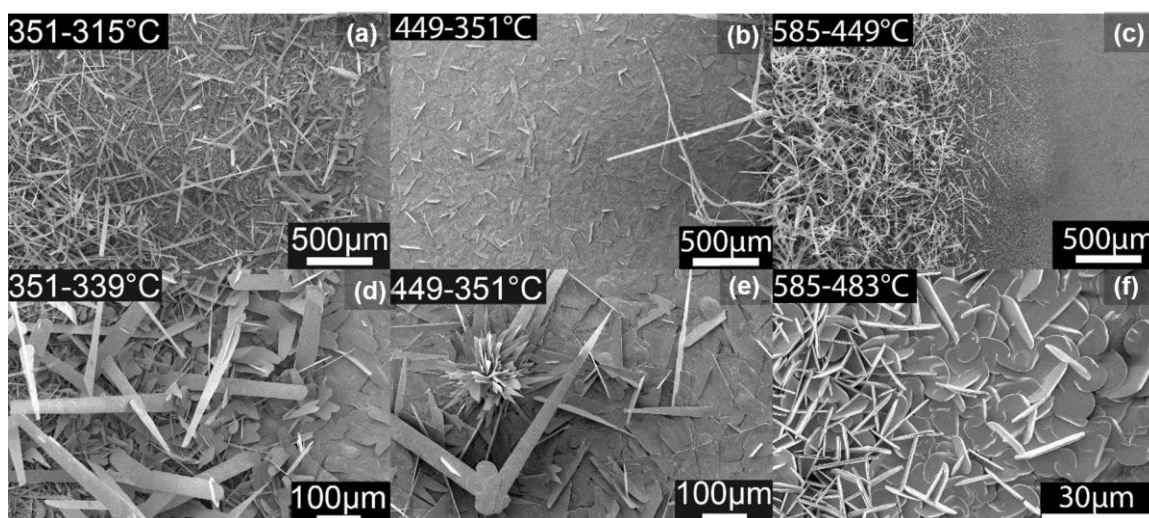


Figure 2-22. Obtained SEM images from the side-by-side position experiment, where different MoO_3 morphologies were observed around the catalytic substrate by using extra catalytic materials, (a) low temperature growth at the droplet's left boundary, (b) medium temperature growth at the center of the droplet, (c) high temperature growth at the droplet's right boundary, (d-f) high magnification SEM images from left, center, and right sides of the catalytic droplet, respectively.

Although using an extra catalytic source does not affect the type of MoO_3 morphologies, it greatly changes the growth density of long nanobelts (Figure 2-23). As it is shown in (Figure 2-23 a & b), the growth density of triangular nanobelts has substantially increased and a large area at the right droplet boundary has been covered. An increase in the growth density of nanobelts was also observed at the left side of the droplet boundary (low temperature zone). However, the growth density of nanobelts was slightly lower in comparison with the droplet's right boundary (Figure 2-23 c & d). This indicates the positive effects of providing an additional source of catalytic to significantly improve the growth of nanobelts.

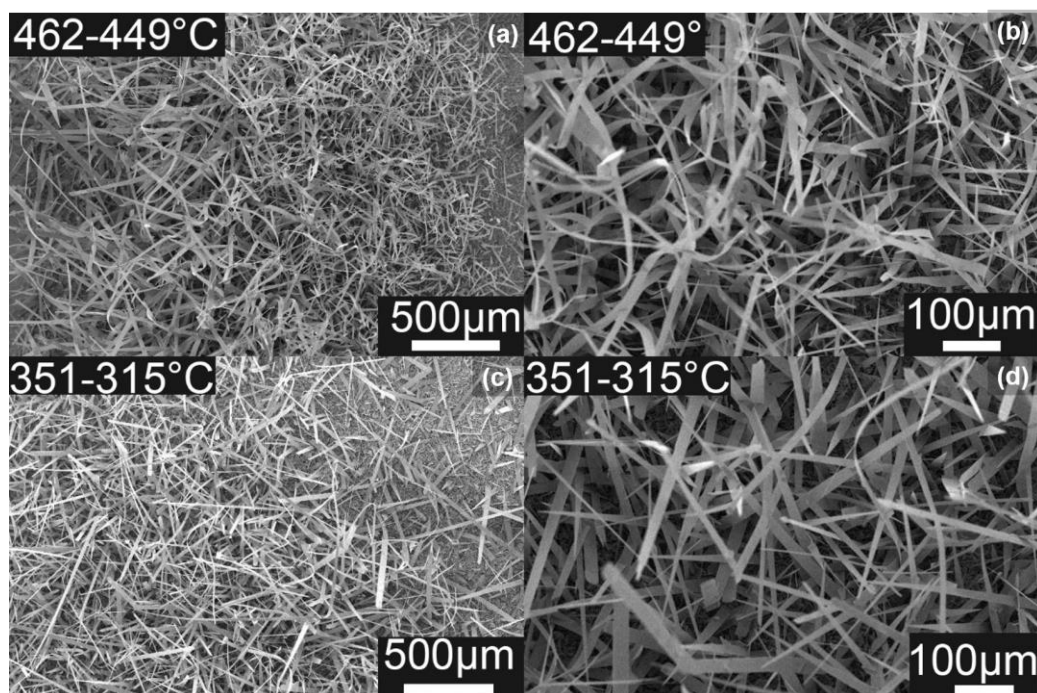


Figure 2-23. Effects of extra catalytic source on growth of long triangular nanobelts, (a & b); SEM images from high density growth of MoO_3 long nanobelts at the right side of the catalytic droplet boundary at low and high magnification, respectively (c & d); SEM images of low density growth of long nanobelts at the left side of the catalytic droplet boundary, at low and high magnification, respectively

Crystallographic information of the nanobelts was investigated using the X-ray powder diffraction (XRD) method. Figure 2-24 displays a set of XRD patterns associated with three different locations on the target substrate with MoO_3 nanobelt morphology. The XRD spectrums closely match the orthorhombic phase of MoO_3 (ICDD PDF 05-0508, $a=3.9628 \text{ \AA}$, $b=13.855 \text{ \AA}$, $c=3.6964 \text{ \AA}$). The XRD patterns indicate dominant diffraction peaks, (020), (040), (060), and (0100) and crystal faces at 2θ of 12.8° , 25.7° , 39.09° , and 67.57° , respectively. The strong intensities of the reflection peaks reveal the strong preferred orientation (highly anisotropic) of α - MoO_3 nanobelts along the [001] crystallography direction.

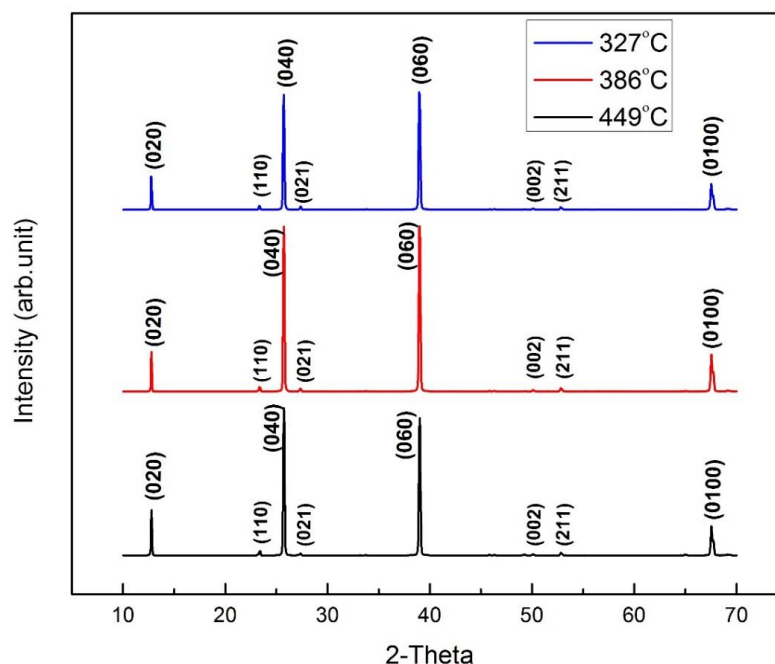


Figure 2-24. XRD patterns of nanobelts grown at three different locations (temperatures) on the target substrate.

2.3.4.3 Side-by-Side (without Catalytic Droplet on The Target Substrate)

In order to increase the growth zone of nanobelts, the side-by-side experiment was repeated without drop-casting the catalytic droplet on the center of the target substrate (Figure 2-25).



Figure 2-25. Repeating the side-by-side experiment, the target substrate, without the catalytic droplet, was positioned next to the catalytic substrate which has 30 μl 1M NaOH at the temperature range of 280-585°C.

Obtained SEM images from growth demonstrates the positive effects of removing the catalytic droplet from the target substrate, which led to extending the growth zones of nanobelts (Figure 2-26). The growth zones of nanobelts is divided into two sections, the high density (Figure 2-26 a-b) and low density zones (Figure 2-26 c-d).

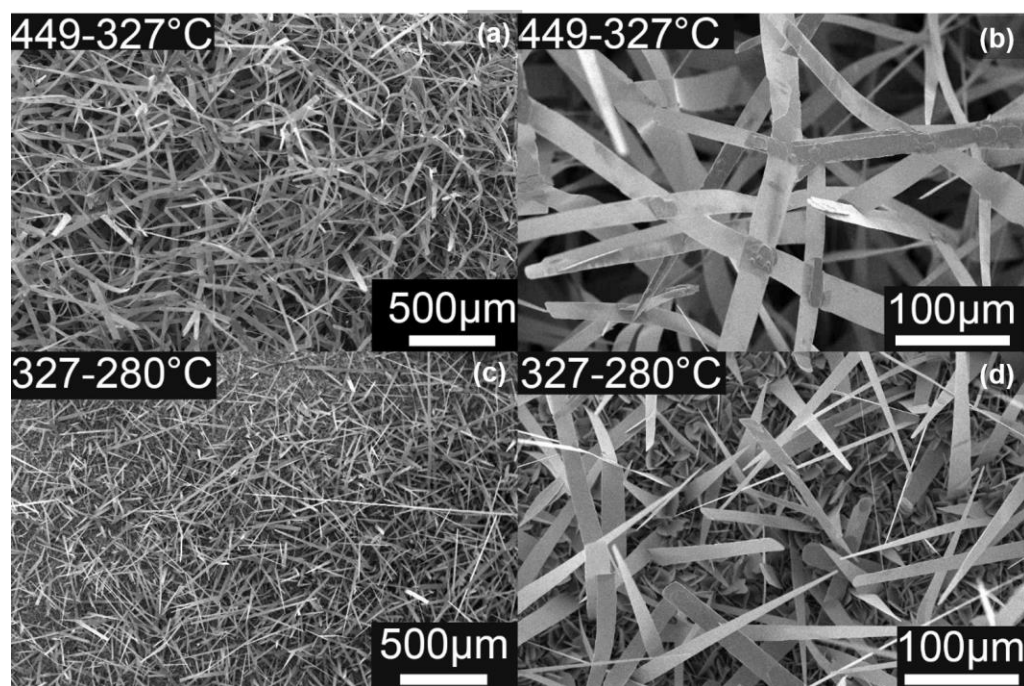


Figure 2-26. Effects of the catalytic droplet on the target substrate's increased growth zone of nanobelts (a & b); SEM images from high density growth of MoO_3 long nanobelts at a temperature range of 327-449°C, at low and high magnification, respectively (c & d); SEM images of low density growth of long nanobelts at a temperature range of 280-327°C, at low and high magnification, respectively

The crystal structures of the synthesized nanobelts were examined using the X-ray diffraction (XRD) technique (Figure 2-27). From the XRD results, synthesized nanobelts showed highly anisotropic growth in the (010) direction, with a highly crystalline structure. Also the peaks were well indexed as MoO_3 orthorhombic phase (PDF# 05-0508).

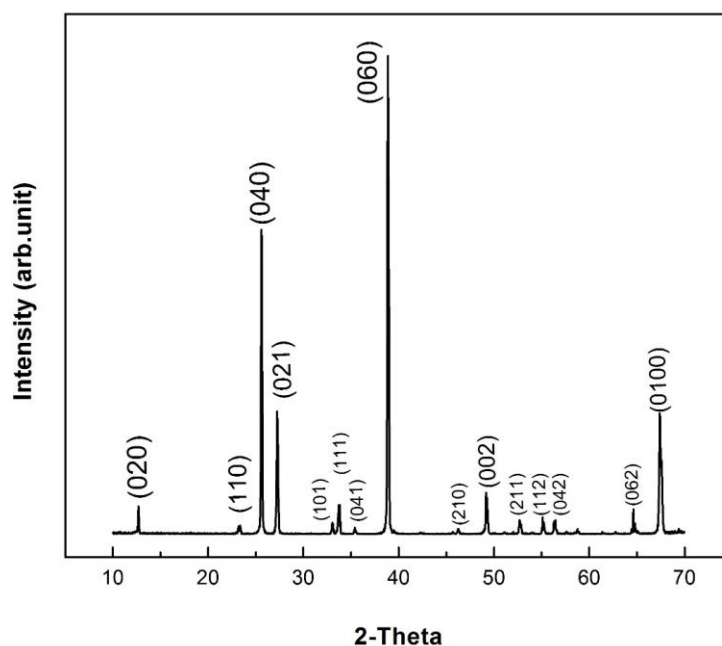


Figure 2-27. XRD spectra of MoO_3 nanobelts performed on the growth zone of 280°C (12mm center, 041415)

2.3.4.4 Up and Down position

One more experiment was conducted in order to find the optimum location of the catalytic substrate. The catalytic substrate was placed above the target substrate in the same temperature range of 280 - 585°C (Figure 2-28)

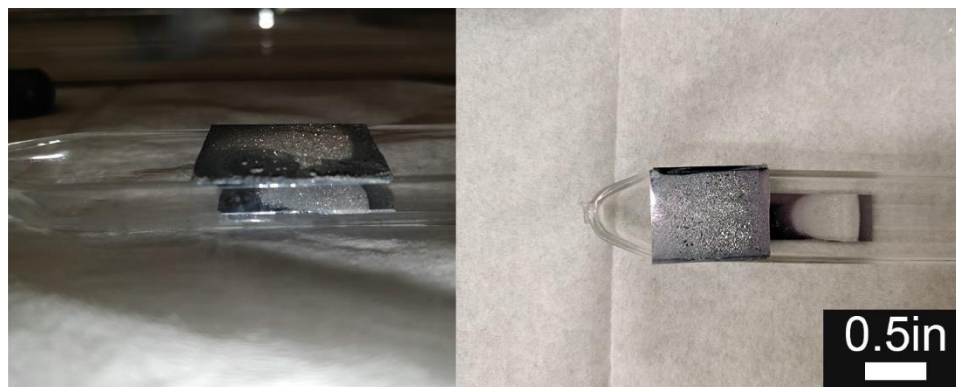


Figure 2-28. up and down position; top: 20 mm by 25 mm piece of SiO_2/Si substrate with an extra source of Na, $30\ \mu\text{l}$ 1M NaOH underneath: bare target substrate without the catalytic droplet, both substrates were placed at 280 - 585°C .

Figure 2-29 presents the SEM images obtained of the growth of MoO_3 nanobelts. No significant change in growth of MoO_3 nanobelts were observed, and the growth zone was reduced in comparison with the side-by-side experiment. Also, unlike the side-by-side experiment, the growth of nanobelts was only observed at high temperature zone.

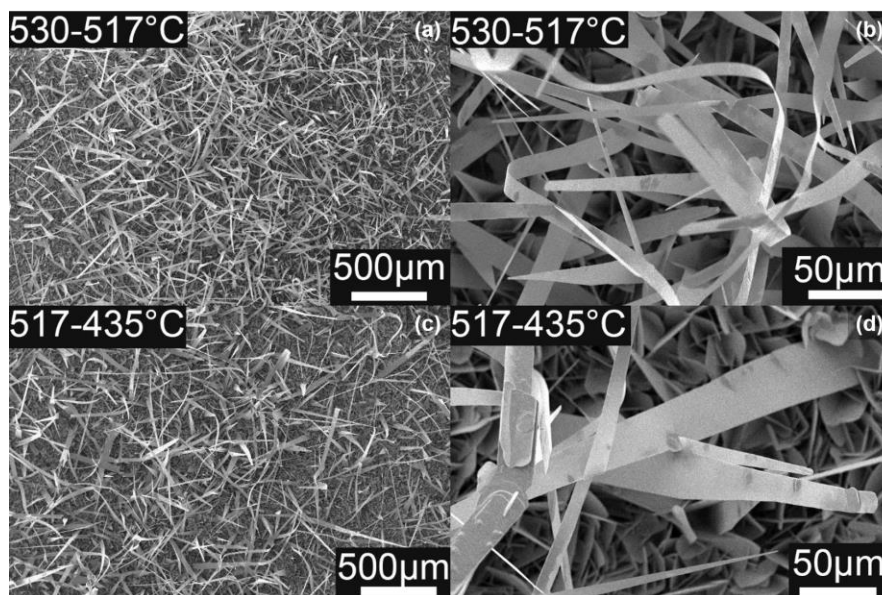


Figure 2-29. Effects of the extra catalytic source on the growth of long triangular nanobelts in the up and down position (a & b); SEM images from high density growth of MoO_3 long nanobelts at the temperature range of 517-530°C, at low and high magnification, respectively (c & d); SEM images of low density growth of long nanobelts at a temperature range of 435-517°C, at low and high magnification, respectively.

2.3.5 Growth Reactions Summary

In order to analyze the growth mechanism of synthesized 1D nano/micro-structures, first we referred to the reproduced $\text{Na}_2\text{MoO}_4\text{-MoO}_3$ phase diagram and overall reaction (Eqn. 2-1 and Eqn. 2-2) reported in Tao et al. (Figure 2-30). In summary, Mo powders are oxidized by introducing oxygen gas to the reaction chamber. The molybdenum trioxide (MoO_3) produced is transported (via the carrier gas, Ar) to the target substrate and reacts with the already deposited sodium hydroxide catalyst [83].

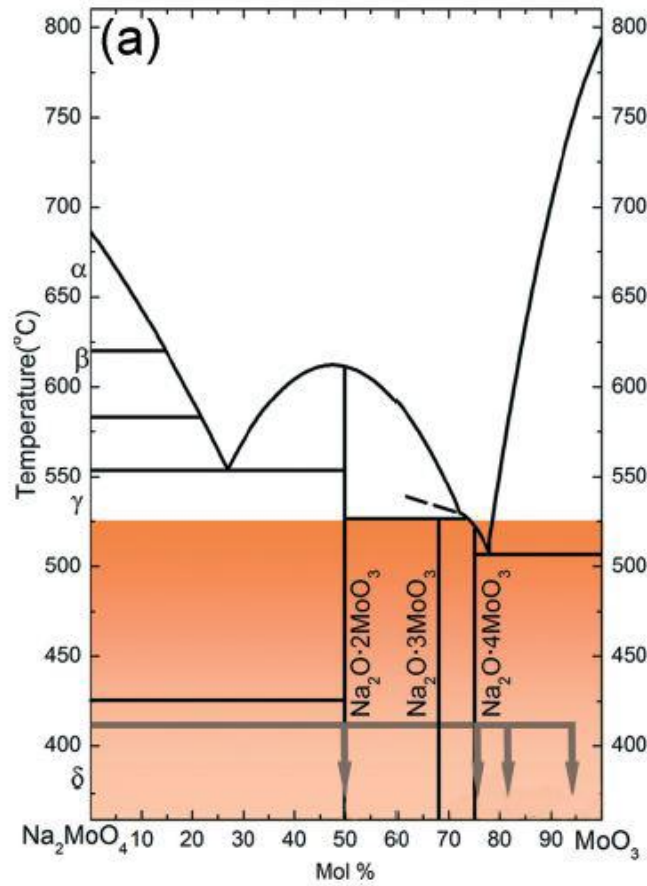
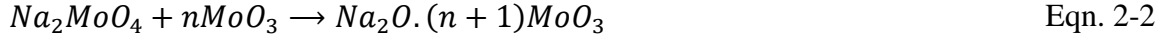
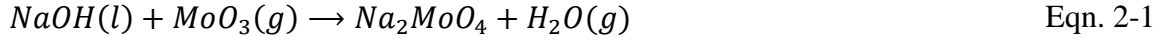


Figure 2-30. Reproduced diagram phase of Na_2MoO_4 - MoO_3 by Tao et al. [83] from ref. [85].

As mentioned earlier, the target substrate was located at the downstream (extending from 7 inches to 8 inches) inside the reaction chamber and in the temperature range of 280-585°C. Also from the Na_2MoO_4 - MoO_3 phase diagram, we realize that the lowest eutectic point occurs at 507°C. All liquid phase in compound will solidify upon passing this point and reaching lower temperatures. Having said that, the growth mechanism can be explained

as vapor-solid-solid (VSS), which is similar to the VLS mechanism while the phase of catalyst particles is mostly solid. It should be noted that the plotted temperature profile of reactions was measured in ambient pressure. Therefore, due to pressure differences during the growth and thermal conduction on the Si/SiO₂ substrate, the actual growth temperature on the substrate is higher compared with the measured one in open air [86]. This demonstrate the involvement of VLS mechanism in addition to VSS.

CHAPTER 3. LOW TEMPERATURE GROWTH OF MOLYBDENUM TRIOXIDE NANOSTRUCTURE

3.1 Experimental Setup, Results and Discussion

3.1.1 Tube Residue Induces Low Temperature Growth of MoO_3

Residue is a thin white layer of molybdenum oxide deposition formed on top of the quartz tube, which comes from previous droplet experiments. It forms in a very small amount within the low temperature zone of the reaction chamber (Figure 3-1).

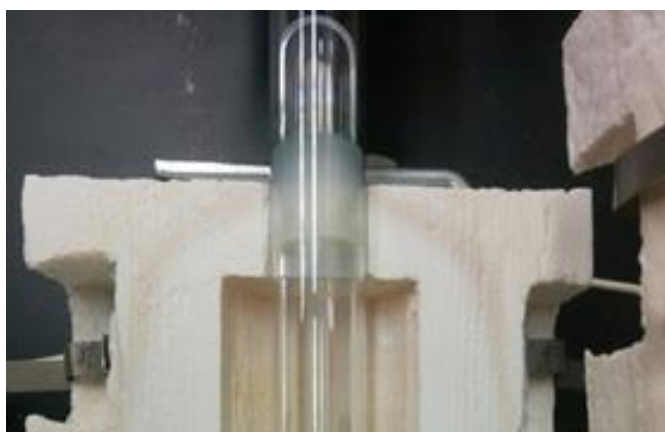


Figure 3-1. Residue (thin white layer of molybdenum trioxide) formed on quartz tube within the low temperature area

It is suggested that tube residue could promote low cost and highly efficient growth of molybdenum trioxide nanostructures on a transparent substrate, e.g. glass at low temperatures using a small amount of source materials. In order to test this idea, an experiment was designed to investigate the residue effects on promoting growth of molybdenum trioxide nanostructures on a glass substrate.

For the growth source a quartz tube with residue from previous droplet experiments was selected and placed inside the reaction chamber. A glass substrate was placed at the downstream area underneath the tube residue extending from 3 inches to 4 inches, which is within a temperature range of 280-585°C. The reaction chamber was sealed and pumped

down to 20 mTorr. The carrier (10 sccm Ar) and reactant (1 sccm O₂) gases were introduced to the chamber consecutively. The reaction chamber heating rate, target heating temperature (at the center 4 inch mark), and dwell time were set as 30°C/min, 800°C, and 15 min, respectively. At the end of the dwell time, the furnace power was switched off and the reaction chamber naturally cooled to room temperature. The CVD system setup and detailed temperature profile (at 800°C) across the 1 inch long glass substrate are shown in Figure 3-2.

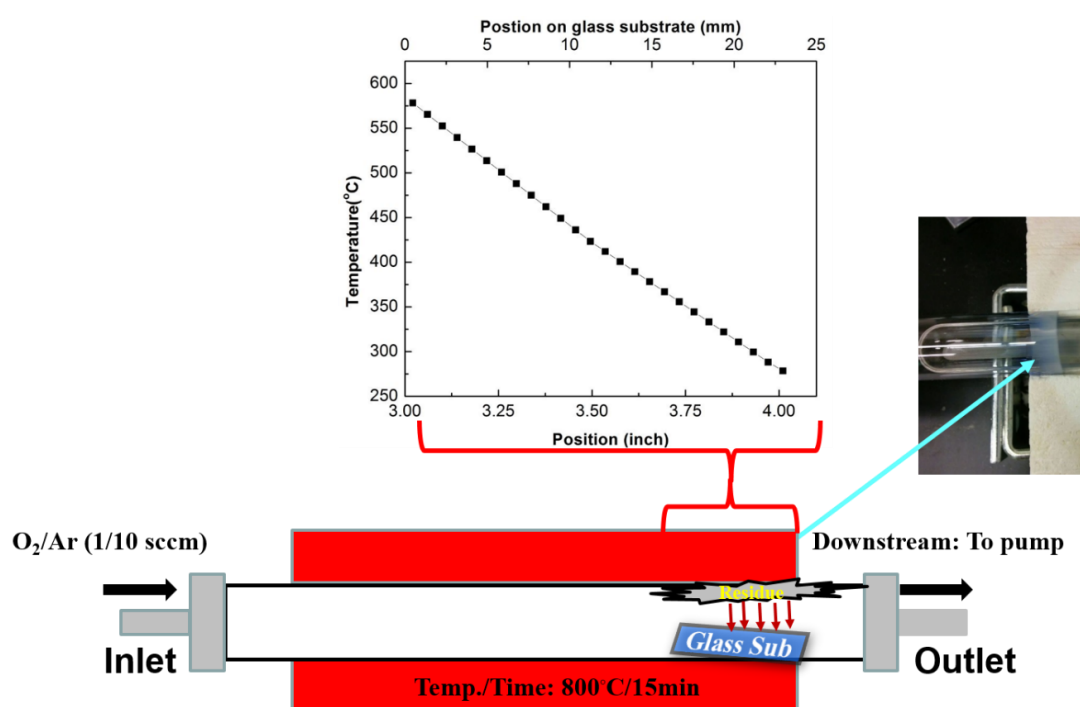


Figure 3-2. CVD system growth set up for residue induced growth on glass substrate

3.1.2 Residue Induced Growth

The deposited white layer on the glass substrate (Figure 3-3) was analyzed using SEM techniques and the results are shown in Figure 3-3.



Figure 3-3. Schematic of glass substrate after growth on SEM plate (copper tape underneath); white deposition on right side (low temperature area), no deposition on left side (high temperature area).

Due to the temperature gradient across the substrate, four different temperature zones (Figure 3-4) were identified, which resulted in growth with different densities and morphologies. At the high temperature zone (zone I, 404-585°C), growth is poor or very limited, and no or very few α -MoO₃ nanoribbons were observed. As the temperature reduced (zone II, 386-398°C), low density growth of the α -MoO₃ rectangular nanoribbons (mostly rounded end) was observed. Further reduction in temperature (zone III, 362-386°C), resulted in high density and uniform growth of the α -MoO₃ rectangular nanoribbons (sharp edges) with length ranging from 7 to 10 μ m, a typical thickness of 60-130 nm, and width from 350-800 nm (d-f). These results are satisfying and proves growth of α -MoO₃ rectangular nanoribbons, which have very ordered structures, with a small amount of source material and at relatively low temperatures.

Towards the low temperature side of the glass substrate (zone IV, 280-327°C), the density of the α -MoO₃ rectangular nanoribbons is reduced and formation of thick fork ribbons was observed. At this point, the majority of the growth source was consumed and deposited at Zones II and III. Therefore, fewer materials will be delivered to this region causing a reduction in the nucleation rate. No sign of the α -MoO₃ rectangular nanoribbons was observed at the end of the low temperature zone and growth there was non-uniform thick rods.

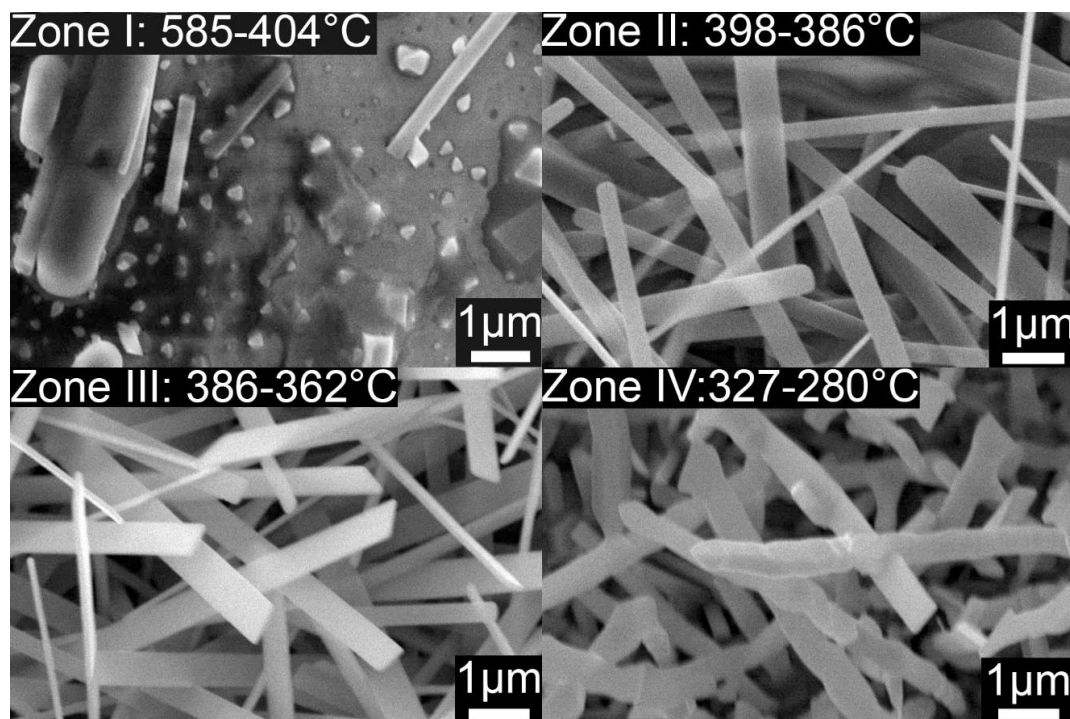


Figure 3-4. SEM images from different morphologies of obtained growth (at different temperature zones) across glass substrate. Growth was induced by deposited residue (from previous experiments) on quartz tube walls, Zone I: high temperature zone with little or no growth, Zone II & III: medium temperature zone appearance of sharp/round end rectangular nanoribbons, Zone IV: low temperature zone non-uniform growth (mostly in the form of rods).

We concluded that residue in the tube can induce growth of α - MoO_3 rectangular nanoribbons, instead of fork-end ribbons or micro-tower structures. These nanoribbons can be used for device applications. In order to improve growth quality, such as growth density, it is necessary to conduct a thorough study of this phenomena by analyzing the growth source's (residue) morphology. However, since it would be a difficult task to collect the residue from tube walls of CVD systems, an experiment was designed to simulate the formation of residue on a quartz substrate, which is the same material as the tubes inside the reaction chamber of the CVC system. The repeatability of this experiment was tested using a SiO_2/Si substrate.

3.1.3 Residue Induced Growth-Mechanism Study

3.1.3.1 Simulating Residue Deposition: Production and Morphology Study of MoO_3 Deposition

As previously discussed, for the purpose of morphology characterization, collection of deposited residue from a tube wall, due to risk of damaging and altering the original morphologies, would be a difficult task. Therefore, a simulating experiment was performed to produce deposition on a quartz substrate which is comparable with deposited residue on quartz tubes. For this purpose, a quartz substrate (Quartz Scientific, Inc.) was cut into 20 mm by 25 mm pieces, cleaned (according to the procedure stated in Sec. 2.1.1), and was placed at the downstream area (7 inches). The reactant information used in this study is listed in Table 3-1:

Table 3-1. Reactant information for production of residue on quartz tube

Material	Stock No.	LOT	Purity	Vendor
Molybdenum Powder	00932	I7S024	99.9%	Alfa Aesar

One gram (1g) molybdenum powders were weighed and placed at the center of the horizontal furnace. Thermal treatment was carried out at 800°C for 30 min using 10 sccm Ar (carrier gas) and 10 sccm O_2 (reactant gas). The schematic of the experiment set up is shown in Figure 3-5.



Figure 3-5. Schematic set up of residue production experiment on quartz substrate

Deposited molybdenum oxide (white residue) on a quartz substrate is shown in Figure 3-6 (transparent areas represent high temperature zones without a deposition). The morphologies of deposited molybdenum oxide layers was investigated at three temperature zones using SEM techniques. Zone I represents the high temperature side of the quartz substrate (449-585°C) with no or very limited deposition. As the temperature reduces in zone II (327-449°C), a dense deposition of molybdenum oxide (white layer) appears on the substrate. The typical observed morphology of deposition in this zone is semi-circle platelets. With further reduction in temperature in zone III (280-327°C), deposition density reduces while its morphology remains in the form of semi-circle platelets.

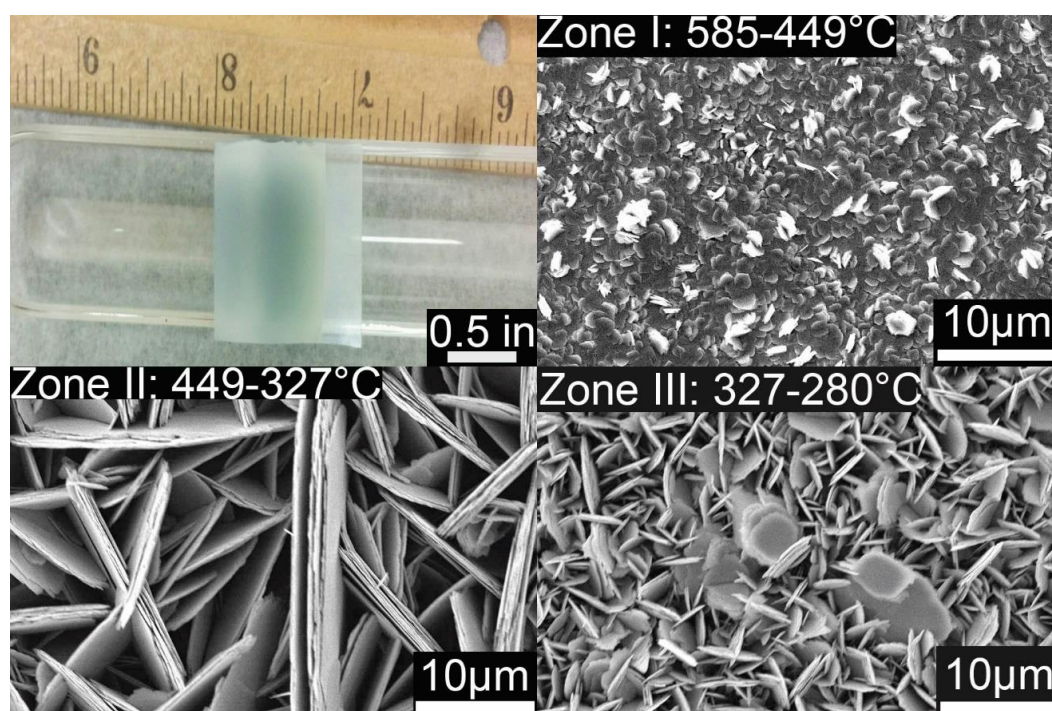


Figure 3-6. Deposited molybdenum oxide on quartz substrate; SEM images of deposition morphology at different temperature zones, zone I: no or limited deposition, zone II: high density deposition in the form of semi-circle platelets, zone III: reduction in deposition density due to temperature reduction.

3.1.3.2 Mimicking Residue Effect

In order to test whether the deposited molybdenum oxide on quartz substrate can induce the growth of MoO_3 nanoribbons, an experiment was designed as shown in Figure

3-7. It should be noted that deposition on quartz substrate, from the previous experiment, was the only growth source provided for this experiment. All experimental parameters were the same as the residue induce growth experiment. The experiment was performed at 800°C for 15 min using 10 sccm Ar (carrier gas) and 1 sccm O₂ (reactant gas).

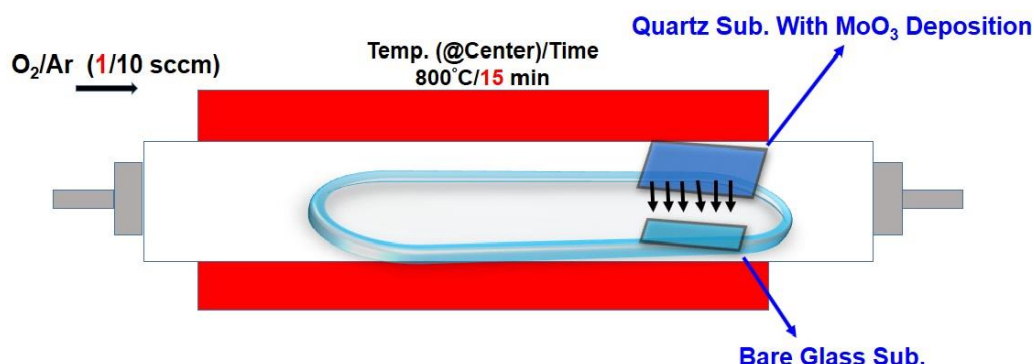


Figure 3-7. Mimicking residue effects, growth source: a quartz substrate with molybdenum oxide deposition located on top of the boat, target: bare glass substrate located underneath

At the end of the experiment, a white layer of deposition was observed across the glass substrate (Figure 3-8), which could be proof of inducing growth using deposition on a quartz substrate similar to residue effect on growth.

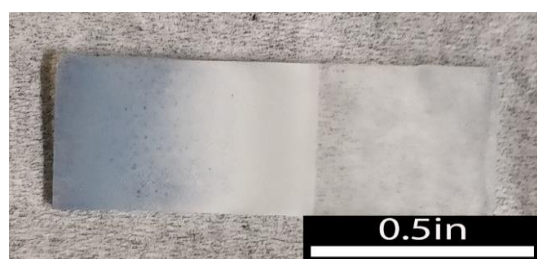


Figure 3-8. Mimicking residue effect: induced growth on a glass substrate located underneath a quartz substrate with molybdenum oxide deposition.

The deposited white layer on the glass substrate was investigated using SEM techniques. Depending on the temperature zone, different growth morphologies were observed (Figure 3-9). No or limited growth was observed at the high temperature zone (Figure 3-9-a). Uniform rectangular nanoribbons were observed by reduction in substrate (Figure 3-9 b & c). As the temperature drops, less uniform nanoribbons (fork-end

rectangular) were observed (Figure 3-9-d). Further reduction in temperature leads to mixed and non-uniform growth (Figure 3-9 e & f).

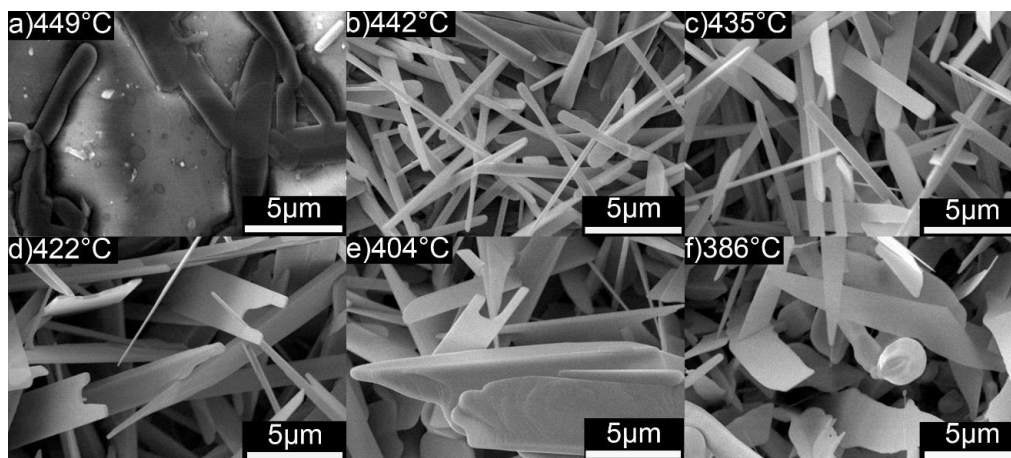


Figure 3-9. Mimicking residue effect: SEM images of induced growth on glass, (a) high temperature zone (449-585°C) with no or little growth, (b & c) appearance of uniform rectangular nanoribbons at medium temperature zone, (d) less uniform nanoribbon in the form of fork-end rectangular, (e & f) non-uniform growth with mix growth at low temperature side of glass substrate.

It is concluded that deposited molybdenum oxide on a quartz substrate can induce growth of nanoribbons on a glass substrate. Figure 3-10 compares the morphology changes of depositions at different temperature zones before and after inducing growth. Before growth, the high temperature side (Figure 3-10-a) shows a thick and continuous film of platelets which mostly evaporate during growth (Figure 3-10-b). However, as we move toward lower temperature zones, no significant change in morphology was observed. That is semi-circle morphology of deposition before (Figure 3-10 c-g) and after (Figure 3-10 d-h) growth almost remain intact. This indicates that the majority of the deposition, after the high temperature area, does not evaporate and high temperature areas (Figure 3-10-c) contribute to the growth. Due to performing the experiment at low oxygen flow (1scm), besides evaporation of molybdenum trioxide, platelets can decomposed and re-deposited on top of the deposition and in the form of non-crystalline or amorphous molybdenum

oxide (Figure 3-10-c). Due to higher nucleation density at lower temperature zone, formation of allen type growth and tiny nanowire were observed on top of the platelets, Figure 3-10-f and Figure 3-10-h, respectively.

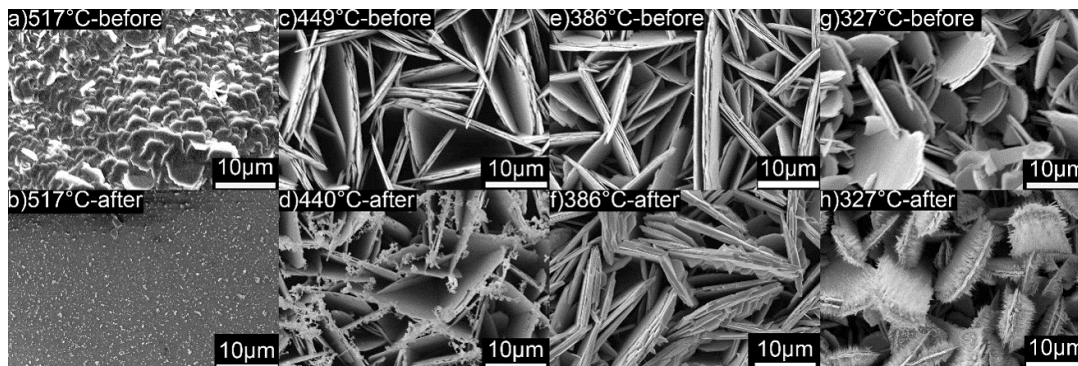


Figure 3-10. SEM images from morphology change of deposited molybdenum oxide on a quartz substrate before and after inducing growth on a glass substrate located underneath the quartz, (a) before growth; continuous thick film of deposition in the form of small platelets positioned at high temperature, (b) majority portion of thick film is evaporated and contribute to growth, (c, e, g) before growth: molybdenum oxide deposition in the form of semi-circle platelets extended from medium to low temperature, (d, f, h) after growth, no significant change in morphology of deposition, minor decomposition and growth of tiny nanowire on top of platelets.

We can conclude that a quartz substrate with molybdenum oxide deposition can act as a growth source, similar to the residue on the quartz tube, which induces growth of nanoribbons on a glass substrate located underneath.

Although the results from these two experiments, residue on a quartz tube versus deposition on a quartz substrate, do not match exactly, mostly due to source-target distance that alters the delivery of materials on the substrate, this proves that produced depositions are able to induce growth by locating and reheating then at relatively low temperatures

The repeatability of this experiment was tested using a SiO_2/Si substrate, instead of quartz as the growth source, while no change was applied to the rest of the test parameters. Below we represent the results:

The morphology of induced growth on the glass substrate is summarized in Figure 3-11. Similar to previous experiment, the induced growth is very limited in the high temperature area (Figure 3-11-a) showing no or limited signs of growth. With a temperature drop, a low density of protruded rectangular (mostly semi-circle end) ribbons appeared (Figure 3-11-b). A more uniform growth of MoO_3 rectangular nanoribbons was observed after a further reduction in temperature (Figure 3-11 c and d). However, the heat zone for uniform growth of rectangular nanoribbons is limited and none or very few nanoribbons were observed at the lowest temperature of the glass substrate (e and f).

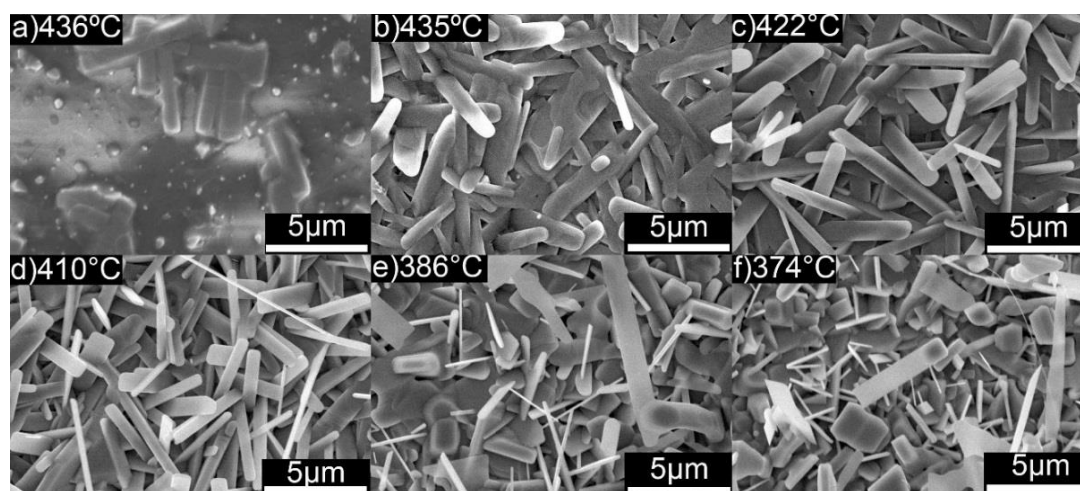


Figure 3-11. SEM images of mimicking the residue effect while using SiO_2/Si substrate as growth source (on top) and a glass substrate as the target (underneath). (a) high temperature zone with no or limited growth, (b-d) appearance of nanoribbons with low to high density growth, respectively, (e-f) mixed and non-uniform growth with no or very few nanoribbons.

As with the quartz substrate, SEM techniques were employed to investigate the change of deposition morphology on the SiO_2/Si substrate before and after growth (Figure 3-12). The morphology of deposition is very similar to what was obtained on the quartz substrate. The high temperature side of the substrate is covered with a thick film of molybdenum oxide platelets (Figure 3-12 a & c). This is the zone which contributes to the

growth of nanoribbons when a glass substrate is located underneath the quartz substrate. Figure 3-12 b & d indicate the evaporation of a thick film deposition from the high temperature side. Again, similar to the deposition on the quartz substrate, the low temperature side of the SiO_2/Si substrate (before growth) shows thin coverage of molybdenum oxide deposition in the form of semi-circle platelets (Figure 3-12 e & g). No significant change was observed when comparing the morphology of the deposition before and after contributing to the growth on the glass located underneath the substrate (Figure 3-12 e & d vs f & h).

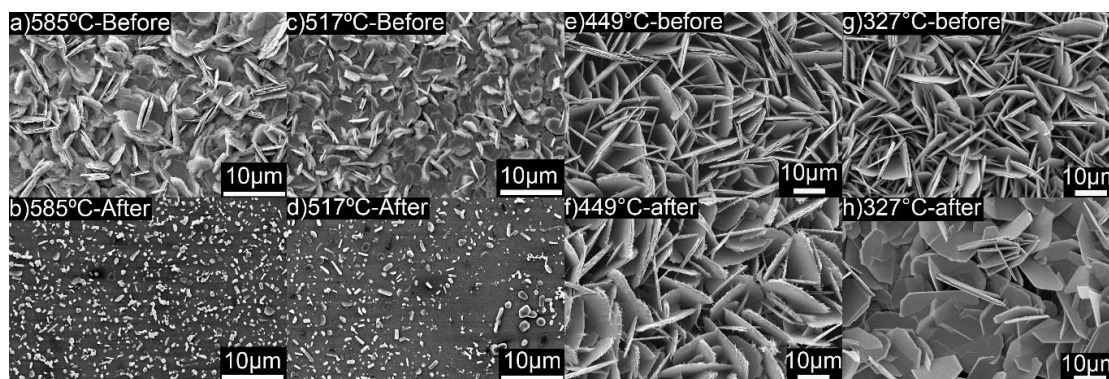


Figure 3-12. SEM images from morphology change of deposited residue on SiO_2/Si substrate before and after the experiment for mimicking the residue effects.

3.1.4 Low Temperature Growth of Uniform Nanoribbons

From the above experiments, we can conclude that low temperature growth of rectangular MoO_3 nanoribbons is possible when using small amounts of source materials. That is that both residue on tube walls and deposition on quartz or SiO_2/Si substrates can induce growth of nanoribbons. However, controlling the amount of source materials and the existence of high temperature gradients across the substrate (~ 300 degrees) are the major challenges that limit the growth zone.

In order to confront these challenges and increase the growth density, molybdenum trioxide powders (MoO_3) were chosen as the growth source because it is easily controlled.

Both the growth source and target substrate were moved to the central zone of the reaction chamber which has a more uniform heating zone.

Figure 3-13 summarizes the change in uniformity of the heating zone at the center and end of the reaction chamber. At the end of the reaction chamber (marked by a red oval in Figure 3-13), the temperature difference can vary up to 300 degrees across either the target substrate or the growth source. However, the maximum temperature change at the center of the reaction chamber (marked by a blue oval in Figure 3-13) is less than 50 degrees. In conclusion, the center of reaction chamber provides a large and uniform growth zone.

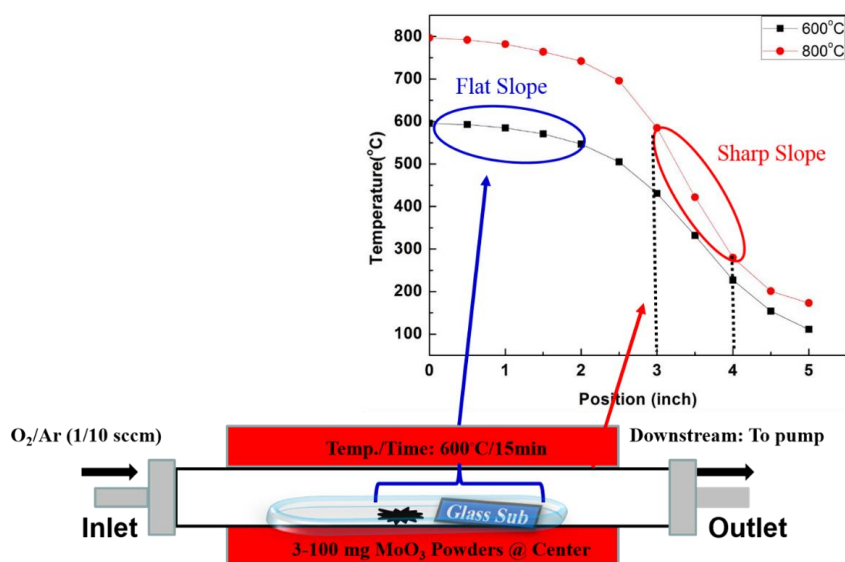


Figure 3-13. Uniformity of heating zone at center versus end of reaction chamber: (blue oval) center of reaction chamber with uniform heating, (red oval) end of reaction chamber with significant temperature gradient across substrate

For this purpose the glass substrate was moved toward the center of reaction chamber and a different amount of growth source (in the form of molybdenum trioxide

powders), ranging from 3 to 100 mg, was placed at the center of the reaction chamber (0 inch position in Figure 3-14). The reactant information is listed in Table 3-2.

Table 3-2. Reactant information for improving the growth yield

Material	Stock No.	LOT	Purity	Vendor
Molybdenum (VI) Oxide	11837	M28C037	99.95%	Alfa Aesar

The experiments were performed at 600°C for 15 minutes with no change made to the amount of oxidizer (O₂: 1 sccm), and carrier gases (Ar: 10 sccm). The temperature profile at 600°C, extending from center to downstream of the reaction chamber, is shown in Figure 3-14. The one inch long glass substrate was placed at 1.75 inches inside the reaction chamber, experiencing a temperature gradient from 474-559°C (Figure 3-14).

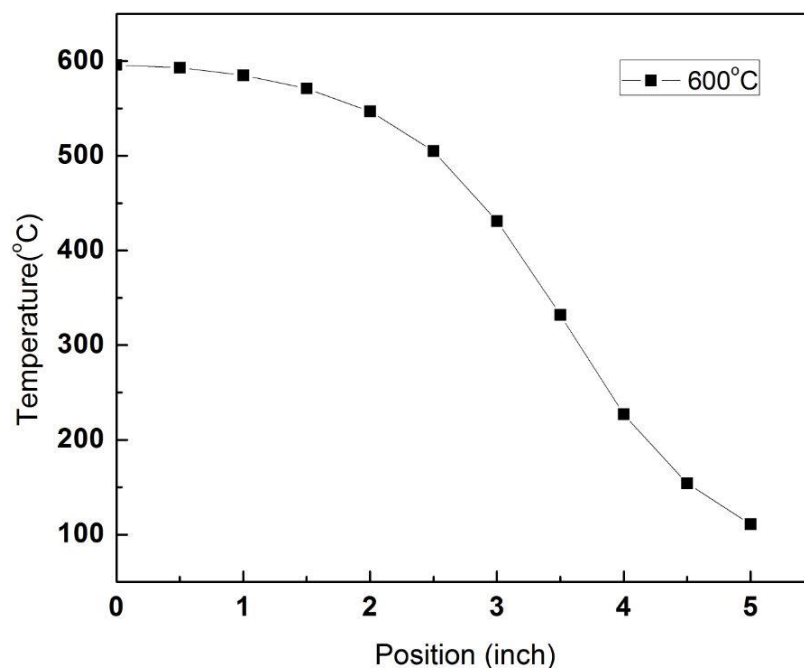


Figure 3-14. Distribution of temperature profile across the reaction chamber at 600°C

3.1.4.1 Effect of Amount of MoO₃ Powders

Here we discuss the effect of the growth source (in the form of powders) on growth morphology at different temperatures across the glass substrate. For ease of comparison we separately obtained results into two different categories:

3.1.4.1.1 Growth using a Small Amount of Powders (3 mg, 6 mg, 12 mg)

3.1.4.1.2 Growth using a Large Amount of Powders (25 mg, 50 mg, 100 mg)

SEM images from growth morphologies are summarized in Figure 3-15 and Figure 3-17. The amount of growth source and substrate temperature are the most important factors affecting the growth morphologies. At high temperatures, a low amount (3 mg) of growth source (Figure 3-15-a) results in no or poor growth. As the temperature reduces (Figure 3-15 b & c), growth density increases and a few nanoribbons start appearing. The majority of the evaporated source is delivered in these two regions causing less deposition at the lower end (Figure 3-15-f) with non-uniform growth. By increasing the amount of the growth source to 6 and 12 mg, formation of nanoribbons was observed at high temperature zones (Figure 3-15 e-i). Growth quality and density improved with a slight reduction in temperature (Figure 3-15 f & j). Further reduction in temperature decreased the growth density (Figure 3-15 g & h). Similar to growth with a 3 mg source, non-uniform and mixed growth were also observed at lower temperatures for these experiments (Figure 3-15 h & l).

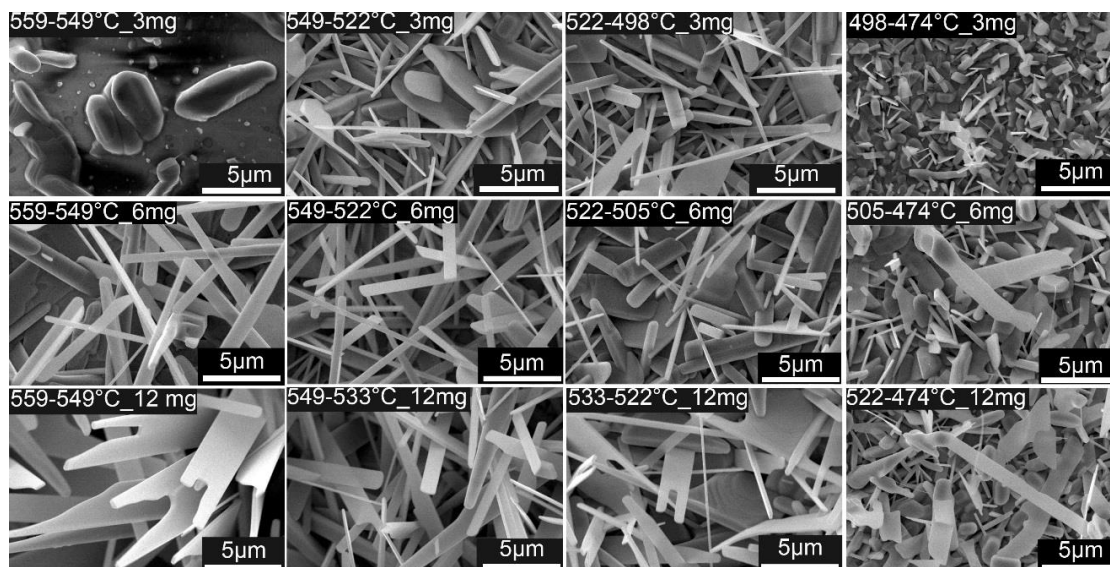


Figure 3-15. SEM images of obtained growth using a small amount of powders ordered from high to low temperature (left to right), (1st row: a-d) growth source: 3 mg MoO₃, (2nd row: e-h) growth source: 6 mg MoO₃, (3rd row: i-l) growth source: 12 mg MoO₃.

More details regarding growth morphologies in respect to temperature zone are summarized in Figure 3-16. High density growth of rectangular nanoribbons was most commonly observed in temperature zone 533-549°C when 6 or 12 mg of MoO₃ were used as the growth source.

3mg	559-549°C	549-522°C	522-498°C	498-474°C
	☒	Growth Starts	L ☑	☒
6mg	559-549°C	549-522°C	522-505°C	505-474°C
	M ☑	H ☑	L ☑	☒
12mg	559-549°C	549-533°C	533-522°C	522-474°C
	H ☑FR	H ☑	L ☑FR	☒

☑: Nanoribbons (rectangular or round-corner)

☒: No growth, limited or non-uniform growth zones

☑FR: Fork-end nanoRibbons

Growth Density: (L: Low) , (M: Medium) , (H: High)

Figure 3-16. Summarized growth morphologies and density in respect to temperature zone using low amount of growth source

In a similar way, higher amounts of growth source (25, 50, and 100 mg) were used to study effects of source amount on resulted morphologies. Observations made using SEM techniques about growth results are summarized in Figure 3-17. Increasing the amount of growth source caused significant change in growth density at the high temperature end of the substrate (Figure 3-17 a, e, and i). However, the growth morphology changed to wide platelets and no or very few ribbons were observed (Figure 3-17 a-c, e and f, I and j). Also, similar to previous conditions using a small amount of source, growth density reduced, with mixed and un-uniform growth once the temperature reduced. At this point, most of the growth source was consumed at the high temperature end and less was reaching downstream, causing non-uniform growth (Figure 3-17 c and d, g and h, k and l).

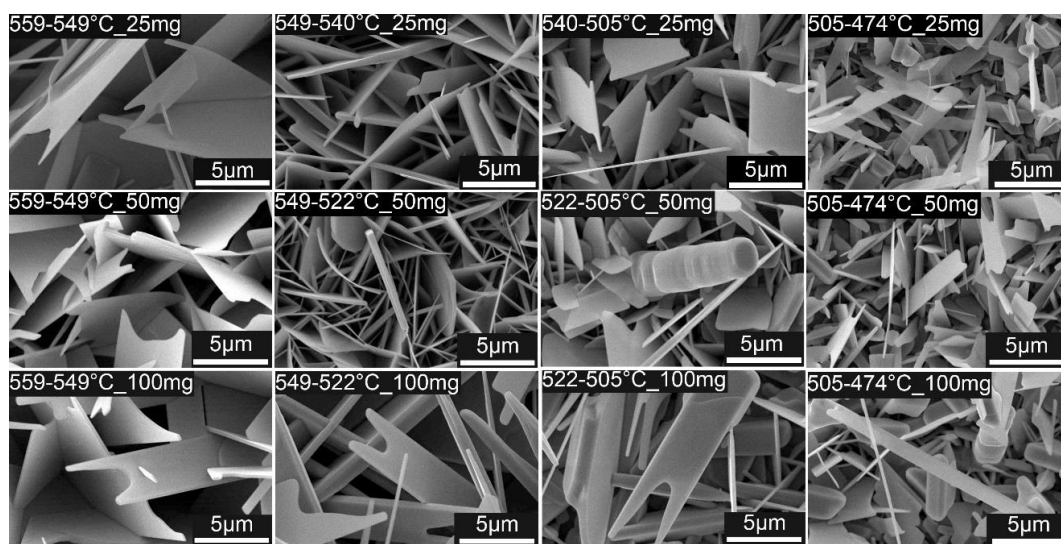



Figure 3-17. SEM images of obtained growth using large amount of powders ordered from high to low temperature (left to right), (1st row) growth source: 25 mg MoO₃, (2nd row) growth source: 50 mg MoO₃, (3rd row) growth source: 100 mg MoO₃


Figure 3-18 summarizes growth morphologies at different temperature zones. More non-uniform and mixed types of growth was observed in comparison with growth using a

small amount of source. Very few nanoribbons (mostly fork end) were observed and wide platelets were the dominant type of growth morphology.

25mg	559-549°C	549-540°C	540-505°C	505-474°C
	H 	HH 	L 	
50mg	559-549°C	549-522°C	522-505°C	505-474°C
	H 	HO 		
100mg	559-549°C	549-522°C	533-522°C	505-474°C
	L  + L 	H 		

FP: Fork-end wide nanoPlatelets, FR: Fork-end nanoRibbons

: Semi-circle nameplates

: limited and non-uniform growth zones

Growth Density: (L: Low) , (M: Medium) , (H: High)

Figure 3-18. Summarized growth morphologies and density in respect to temperature zone using a large amount of growth source.

Although using different amounts of MoO₃ powders as growth source resulted in the formation of rectangular nanoribbons, the growth density remained low. Therefore, this work performed a detailed study on the growth of nanoribbons using MoO₃ whiskers as the growth source. The experimental conditions to synthesize MoO₃ whiskers are explained below.

3.1.4.2 Synthesis of Molybdenum Trioxide Whisker as the growth Source

Whiskers of molybdenum trioxide (MoO₃) were prepared by placing one gram of molybdenum powders inside a quartz boat at the center of the reaction chamber (4 inches). The target temperature was set at 800°C for 2 hours. Once the reaction chamber was sealed and pumped down to 20 mTorr, it was vented to atmosphere pressure using Ar gas.

A constant flow of both carrier (Ar: 10 sccm) and reactant (O_2 : 10 sccm) gases was provided during the experiment. The schematic of experimental conditions is shown in Figure 3-19. As-synthesized whiskers are shown in Figure 3-20.

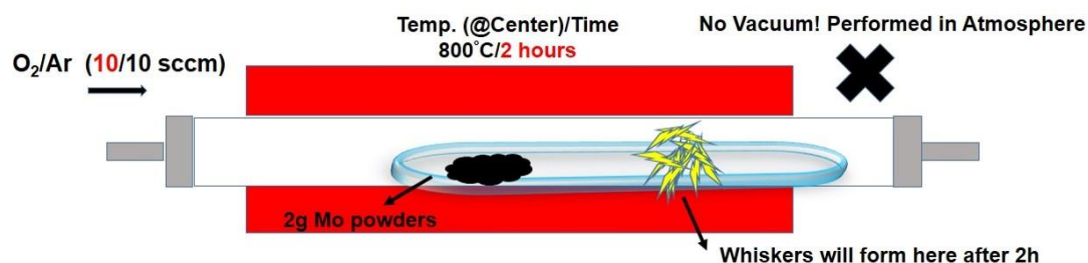


Figure 3-19. CVD system set up for growth of MoO_3 nanoribbons on a glass substrate by using synthesized MoO_3 whiskers



Figure 3-20. As-synthesized MoO_3 whiskers

Using the synthesized whiskers, previously performed experiments with MoO_3 powders were repeated to study the effect of whiskers amount as growth source on the formation of α - MoO_3 rectangular nanoribbons. No additional changes were made to other experimental conditions except the type of growth source (MoO_3 whiskers instead of powders).

3.1.4.2.1 Growth using Small Amounts of Whiskers (3 mg, 6 mg, 12 mg)

Figure 3-21 summarizes growth results using a low amount of whiskers. Low amounts of whiskers showed no growth at the high temperature end of the glass substrate

(Figure 3-21a). However, growth density greatly improved with a slight increase in growth source (Figure 3-21 e and i). Although growth coverage improves slightly when temperature drops (Figure 3-21 b-d), high density growth of rectangular nanoribbons were observed when the growth source is higher than 3 mg (Figure 3-21 f and g, j and k).

Regardless of the growth source, the low temperature end of the substrate displayed mixed and non-uniform growth, which is due to consumption of the growth source at high temperature zones (Figure 3-21 d, h, l)

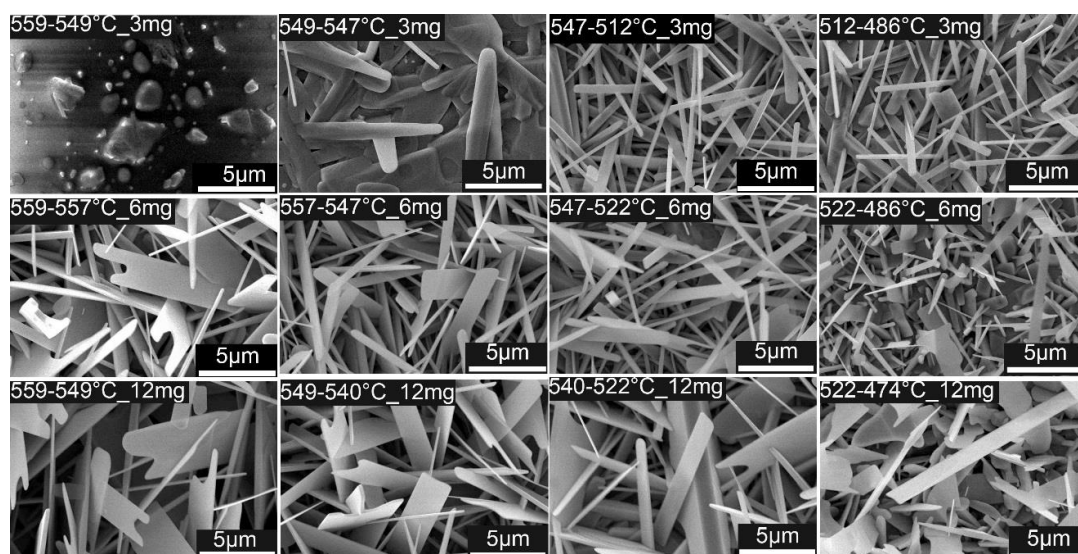


Figure 3-21. SEM images of obtained growth using small amount of MoO_3 whiskers ordered from high to low temperature (left to right) , (1st raw: a-d) 3 mg MoO_3 whiskers, (2nd raw: e-h) 6 mg MoO_3 whiskers, (3rd raw: i-l) 12 mg MoO_3 whiskers.

Detailed morphology analysis is summarized in Figure 3-22 which highlights the growth density and morphologies within different temperature zones.

3mg	559-549°C	549-547°C	547-512°C	512-486°C
	☒	Growth Starts	M ☑	L ☑
6mg	559-557°C	557-547°C	547-522°C	522-486°C
	H(☑FR+☑)	H ☑	M ☑	☒
12mg	559-549°C	549-540°C	540-522°C	522-474°C
	H ☑FR	H ☑ + (L☑FR)	L ☑ + (LL ☑FR)	☒

☑: Nanoribbons (rectangular or round-corner)

☒: No growth, limited or non-uniform growth zones

☑FR: Fork-end nanoRibbons

Growth Density: (L: Low) , (M: Medium) , (H: High)

Figure 3-22. Summarized growth morphologies and density in respect to temperature zones using low amount of growth source (MoO₃ whiskers)

3.1.4.2.2 Growth using Large Amount of Whiskers (25 mg, 50 mg, 100 mg)

Resultant growth with higher amounts of whiskers (25 mg, 50 mg, and 100 mg) are shown in Figure 3-23. Growth of nanoribbons, in the form of rectangular or fork-end, was observed most frequently when using 25 mg whiskers (Figure 3-23 a, b, c), and formation of wide platelets was observed by increasing the amount of growth source (Figure 3-23 e and f, I and j). Temperature drops across the substrate led to similar results and mixed/non-uniform growth appeared at the lower temperature end of the substrate Figure 3-23 d, g and h, k and l).

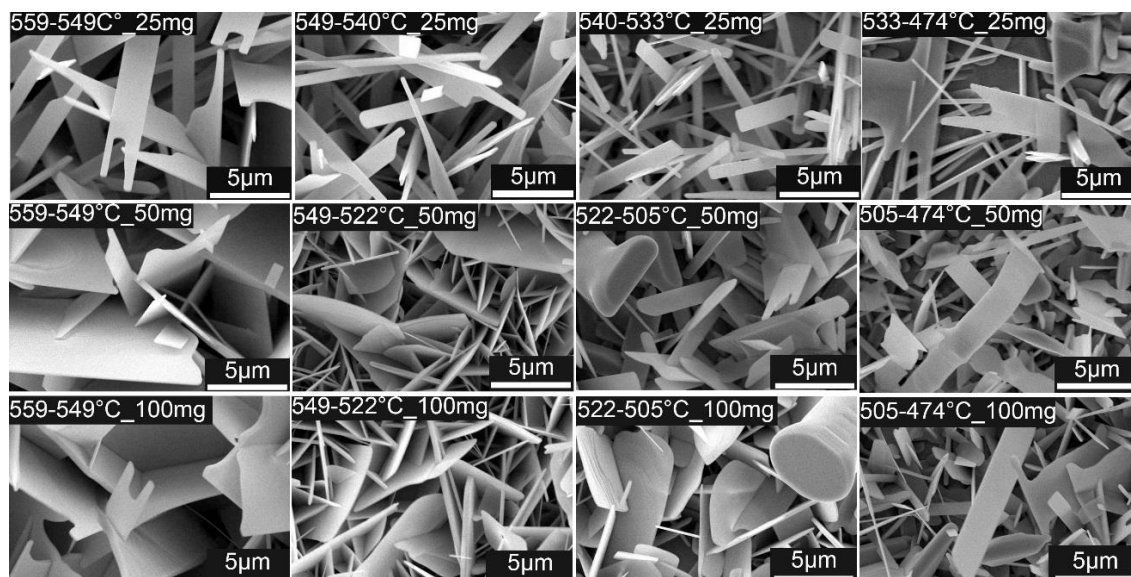


Figure 3-23. SEM images of obtained growth using large amount of whiskers ordered from high to low temperature (left to right), (1st row) 25 mg MoO₃ whiskers, (2nd row) 50 mg MoO₃ whiskers, (3rd row) 100 mg MoO₃ whiskers.

Detailed summary of growth density and morphologies (using a high amount of whiskers) are listed in Figure 3-24. As discussed, a higher amount of whiskers (>25 mg) does not show positive effect on the growth of nanoribbons.

25mg	559-549°C	549-540°C	540-533°C	533-474°C
	H ☑FR	H(☑FR + ☑)	M(☑FR + ☑)	☒
50mg	559-549°C	549-522°C	522-505°C	505-474°C
	H ☑FP	H ○	L(☑FR + ☑) + ☒	☒
100mg	559-549°C	549-522°C	522-505°C	505-474°C
	H ☑FP	H ○	☒	☒

☑FP: Fork-end wide Platelets, /☑FR: Fork-end nanoRibbons

○: Semi-circle nameplates

☒: limited and non-uniform growth zones

Growth Density: (L: Low) , (M: Medium) , (H: High)

Figure 3-24. Summarized growth morphologies and density in respect to temperature zones using large amount of growth source (MoO₃ whiskers).

Figure 3-25 shows obtained X-ray diffraction pattern of synthesized nanoribbon. The diffraction peaks were indexed to orthorhombic MoO_3 (JCPDS card no. 05-0508 space group: $pbnm$ (62), $a = 0.3962$ nm, $b = 1.3858$ nm, and $c = 0.3697$ nm). Appearance of a series of sharp and stronger density peaks at 12.7° , 25.7° , 39° , and 67.5° , which are attributed to $(0k0)$ facets of the orthorhombic $\alpha\text{-MoO}_3$, is indication of anisotropic growth of as-synthesized nanoribbons.

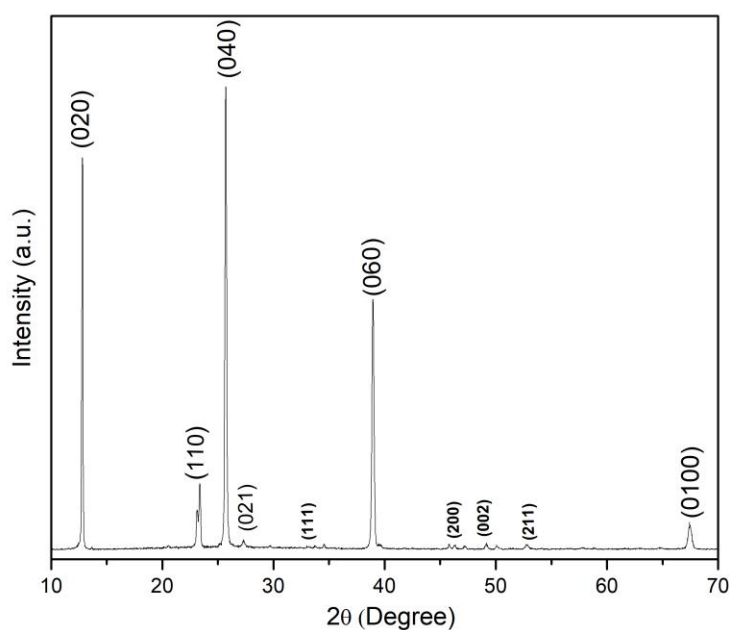


Figure 3-25. XRD pattern of the as-synthesized MoO_3 nanoribbons

Figure 3-26 shows a low-magnification TEM image of a fork-end rectangular nanoribbon and its selected area electron diffraction (SAED) (inset of Figure 3-26), which is collected perpendicular to the growth axis of the nanoribbon with $[010]$ zone axis. Fork-end rectangular nanoribbons have preferential growth along the c -axis $[001]$ direction indicating their high degree of crystallinity. Also, the interplanar spacing along $[100]$ and

[001] directions is determined as 0.37 nm and 0.39 nm, respectively. These are consistent with molybdenum trioxide orthorhombic phase which has d_{100} (0.37 nm) and d_{001} (0.39 nm).

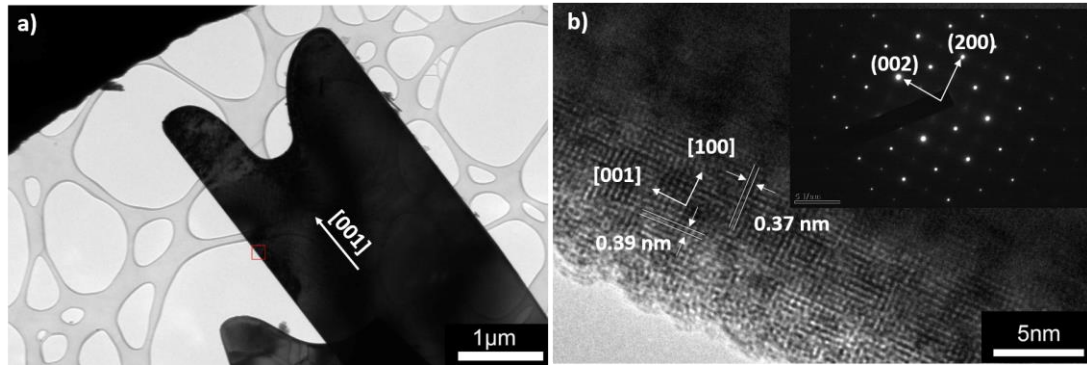


Figure 3-26. Structural characterization of as-synthesized α - MoO_3 nanoribbons. (a) Low-magnification TEM image and (b) HRTEM image of nanoribbon. Inset shows the selected area electron diffraction (SAED) patterns.

3.1.5 Mechanism Analysis of Growth:

Growth mechanism can be explained by heterogeneous nucleation theory as described in Zhang et al. [87], where ΔG is chemical free-energy change per unit volume of deposited materials from vapor phase to solid phase defined by Eqn. 3-1 :

$$\Delta G = -\frac{KT}{\Omega} \ln \frac{P_V}{P_S} = -\frac{KT}{\Omega} \ln(1 + S) \quad \text{Eqn. 3-1}$$

Where K is the Boltzmann constant, T is the growth temperature, Ω is the atomic volume, P_S is the vapor pressure above the solid or equilibrium vapor pressure, P_V is the pressure of the supersaturated vapor, and S is vapor supersaturation is determined by Eqn. 3-2:

$$S = \frac{P_V}{P_S} - 1 \quad \text{Eqn. 3-2}$$

Where P_V / P_S is the saturation ratio. Condensation and nucleation of MoO_3 vapor on glass substrate is possible when $\Delta G < 0$. Therefore, it is required that $S > 0$ for the vapor supersaturation for promoting deposition on the substrate.

It should be noted that the heating temperature of the growth source (T_h), here MoO_3 powders, was kept constant (600°C) for all the experiments. The growth temperature across the substrate (T_g) and the amount of growth source were the only two variable parameters affecting growth conditions. The three identified temperature zones were observed for the performed experiments: high temperature zone upstream (T_1 : $549\text{-}559^\circ\text{C}$), intermediate temperature zone (T_2 : $505\text{-}549^\circ\text{C}$), and low temperature zone downstream (T_3 : $505\text{-}747^\circ\text{C}$).

When using small amount of growth source on a glass substrate, (Figure 3-15-a and Figure 3-21-a), the areas in the T_1 zone experience similar temperatures to the growth source, which means $T_1 \cong T_g$.

Therefore, the MoO_3 equilibrium vapor pressure above the glass substrate (P_S^1) is close to or slightly smaller than the actual supersaturated MoO_3 vapor pressure (P_V^1), which means $P_V^1 \geq P_S^1$ leading to a very small vapor supersaturation ratio ($\frac{P_V^1}{P_S^1}$), thus producing little or no deposition. However, this equation changes to $P_V^1 > P_S^1$ once the amount of growth source increases ($\geq 6\text{mg}$) to within the high temperature zone upstream.

By further temperature reduction across the glass substrate and reaching the intermediate temperature zone (T_2 : $549\text{-}505^\circ\text{C}$), supersaturated MoO_3 vapor pressure (P_V^2) is much higher than the MoO_3 equilibrium vapor pressure above the glass substrate (P_S^2), that is $P_V^2 \gg P_S^2$ and $S \gg 0$ leading to a significant amount of deposition on the substrate. It is obvious that an increase in source growth in this temperature zone results in more deposition as the vapor supersaturation ratio continuously increases.

When reaching the low temperature zone downstream (T_3 : $505\text{-}747^\circ\text{C}$), significant reduction in supersaturated MoO_3 vapor pressure (P_V^3) occurs, which is due to consumption

of the majority of metal oxide vapors in the last two previous growth regions. This results in reduction in deposition leading to mixed and non-uniform type of growth at the low temperature end of the glass substrate.

3.1.6 Source Consumption: Powders vs. Whiskers

From the above observations, it can be said that growth density and its morphology vary across the substrate due to temperature drop and consumption of metal oxide vapors. However other factors such as different types of growth source may also show different evaporation rates which could also affect the growth results. A series of experiments were performed to investigate the effects of growth source type (in the form of powders versus whiskers) on evaporation rate. For this purpose, the different amounts of growth source varied from 3 to 100 mg. Besides the amount of growth source, no other change was made to the primary experimental condition.

Before further discussion on the evaporation rate of powders versus whiskers, it is necessary to study the morphology of powder particles and whiskers using SEM techniques. Molybdenum trioxide powder particles mainly have platelet morphology and they are a few microns long ($\sim 20\text{-}30\mu\text{m}$), while whiskers show millimeter- sized rectangular morphology (Figure 3-27).

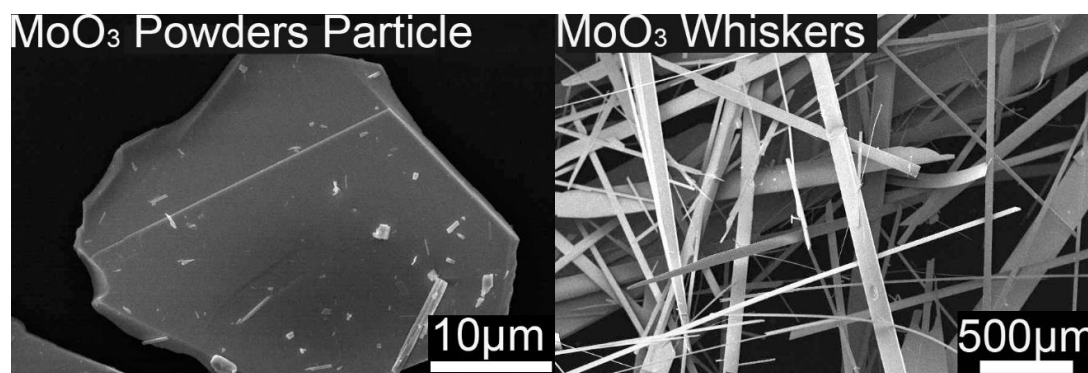


Figure 3-27. SEM images of MoO₃ powder particles (left) and whiskers (right)

The amount of growth source before and after the experiment was recorded and differences were plotted for source consumption versus source amount (Figure 3-28).

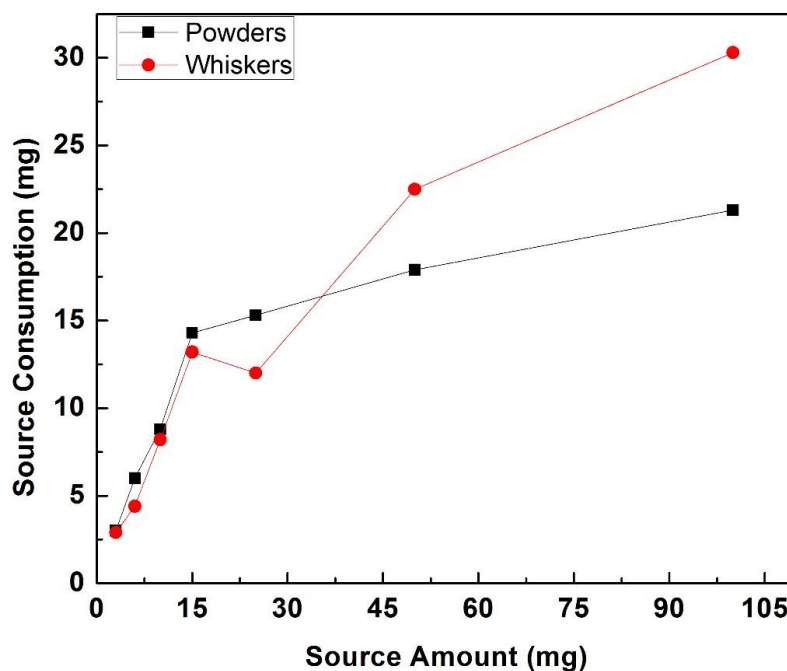


Figure 3-28. Comparison of growth source consumption using different types of growth source (powders vs whiskers).

Figure 3-28 shows three stages of the evaporation rate for powders versus whiskers. In the first stage when small amount of growth source (<15 mg) was used, the consumption rates of whiskers and powders are approximately equal. That is, a linear trend is observed between source amount and source consumption while the source amount is less than 15 mg. The majority of the growth source, regardless of its type, evaporates and contributes to growth of nanoribbons.

Considering equal mass and equal volume of growth source materials, the slight difference in consumption rate between powders and whiskers, for a growth source < 15 mg, could be related to their surface areas. Whiskers' evaporation is always slightly smaller

than powders due to its large crystal size. That is, whiskers have a smaller surface area and a lower evaporation rate. The low evaporation rate of whiskers, in comparison with powders, does not change for a source amount below 50 mg. As an example, when using a 25 mg growth source, the number of powder particles is much higher than the amount of whiskers. Also, the flat shape of powder particles provides a higher number of evaporation surfaces, leading to higher evaporation rate. However, the flat surface of platelet particles will not contribute to evaporation if the growth source increases and powder particles pile up on top of each other. This is the case when the growth source increases to an amount higher than 50 mg. In this case, the possibility of blockage increases, which means powder particles will pile up and block one another's flat surfaces. Therefore, the powder particle's edges contribute to evaporation during growth, reducing the evaporation rate due to lower surface area. The pile up or blockage effect is less likely to occur for whiskers due to their shape. Whiskers are long and their overlap cannot entirely cover each other's surfaces. Thus, the pile up effect does not occur for whiskers resulting in a higher rate of evaporation in comparison with powders when the source amount is more than 50 mg.

CHAPTER 4. ONE DIMENSIONAL NANO-CABLE HETEROSTRUCTURE

4.1 Introduction

Conversion of solar energy to electricity is mainly being carried out through the photocatalytic process. The process was first developed by Fujishima and Honda in the 1970s, by inventing world's first photoelectrochemical (PEC) cell, which was able to split water into its main components (H_2 and O_2) under ultraviolet light irradiation from illuminated TiO_2 by sun light [88]. PEC cells have received considerable attention over the past years due to their ability for developing a sustainable energy supply system. A PEC water splitting cell is able to produce hydrogen and oxygen by employing solar power and a water source, which are both abundant, renewable, and eco-friendly sources of energy. Also, recycling CO_2 , a greenhouse gas, is possible by generating hydrocarbon fuels through the chemical reaction between hydrogen and CO_2 in a PEC cell [89]. A highly efficient photocatalytic process depends on (1) strong solar light absorption and carrier conversion; (2) efficient carrier separation and fast carrier transport; and (3) efficient chemical oxidation/reduction reactions. Recently, the development of one-dimensional (1D) nanostructure photocatalysts and photoelectrodes has attracted significant attention due to their unique optical and electronic advantages over conventional thin-film-based photocatalysts and photoelectrodes. The 1D geometry provides a rapid and lengthy path for electron transport. Also, the high aspect ratio of 1D nanostructures greatly enhances light absorption and scattering properties [88]. The non-planar orientation of the 1D heterostructure arrays provides an exceptional opportunity to solve the dilemma of contradictory requirements of the length scales for photon absorption (micrometer scale)

and carrier transport (nanometer scale) in traditional semiconducting materials. The formation of nano-cable heterostructures with multiple heterojunctions will greatly facilitate carrier separation and expedite carrier transport, and hence, improve the overall efficiency of photoconversion.

One-dimensional (1D) nano-cable heterostructures are proposed in this project to realize enhanced photoactivities for high-efficiency solar energy harvesting. The nano-cable heterostructures are 1D core-shell nanostructures composed of semiconductor hetero-shells, MoO_3 and transparent conductive oxide (TCO) cores of tin doped indium oxide (ITO). This could be a promising design to achieve multiple functions together including strong light absorption, efficient photocarrier conversion and separation, and rapid carrier transport. Although several groups have reported growth of ITO nanowires (NWs) through the chemical vapor deposition method [90-93], there are no reports of formation of 1D Core-shell nanostructures of ITO/ MoO_3 .

It is essential to employ optimum growth parameters to successfully synthesize ITO NWs as the core structure. For this purpose, we have fully investigated the effects of (1) Au catalyst patterning, (2) different oxygen flow rates, (3) different Ar flow rates, and (4) employing thermal insulators (to provide a uniform growth heating zone), on morphology change of grown ITO NWs on both SiO_2/Si and ITO/glass substrates. Growth mechanisms of ITO NWs was discussed in detail for specific temperature zones (high to low) inside the CVD reaction chamber. Shell layer material (MoO_3) was deposited on ITO cores and their final morphologies were studied.

4.2 Experimental Setup

4.2.1 Substrates Preparation

ITO NWs were grown on both Silicon (100) substrate (p-type, 1 μm SiO_2/Si , University Wafers), and ITO substrate (600-1000 \AA thick ITO thin film on glass, $R_s = 15\text{--}30 \Omega/\text{sq}$, CG-61IN Delta Technologies). Substrates were cut into rectangular pieces with a size of 10 mm \times 25 mm and square pieces with a size of 20 mm \times 25 mm, which were cleaned in an ultrasound cleaner (Branson 1510R-MTH) using acetone and alcohol solutions for 15 min. Substrates were dried by nitrogen gas.

4.2.2. Synthesis Techniques, and Characterization Methods

A home-made hot wall CVD system was utilized to carry out the synthesis processes. The major components of the reaction chamber area thermal furnace and a fused silica tube. A 1 inch diameter quartz tube (Quartz Sci, Inc) was fitted into two semi-cylindrical ceramic fiber heaters (WATLOW, Inc), with power density to range from 0.8 to 4.6 W cm^{-2} . The reaction chamber was connected to a mechanical pump (Alcatel Adixen 2010SD), called downstream, to sustain the low pressure (as low as 20 mTorr) environment of inside the chamber. The total length of the furnace is 8 inches, and consists of 6 inches for the heating zone and 2 inches for the cooling zone (1 inch lengthened on each side). Argon (99.999%) and oxygen (O_2) gases were introduced from opposite sides of the vacuum pump as carrier and reactant gases, respectively. Gases were regulated at both low and high flows using flow controllers (Sierra Instruments, Inc). Except the heating rate (30°C/ min) and cooling rate (60°C/ min), which were kept constant during all the experiments, the time, central heating temperature, absolute gas flow, amount of source

materials, and the location of substrates were the controllable variables for this CVD system.

In a typical experiment for growth of ITO NWs, about 0.5 grams of ITO powders, indium (99.99%, -100 mesh, Alfa Aesar) and tin (99.995%, -100 mesh, Alfa Aesar) powders (Sn: In – 1:3, atomic ratio), were loaded into a quartz boat and were placed at the center of the quartz tube furnace. Target substrates (ITO or silicon) were placed apart from the growth source in different heating zones (580-780°C), which will be discussed in detail during the result section. The reaction chamber was pumped down to an ultimate vacuum pressure of ~ 20 mTorr and then brought up to 160 mTorr when the carrier gas (Ar) was added in at a constant 20 sccm (standard cubic centimeter per minute) flow. For the reactant gas, different rates of oxygen flow (0.1-1.5 sccm) were introduced into the reaction chamber (this will be discussed in results section).

The growth source was evaporated at 800°C during 30 min of reaction time. An accurate control on growth of ITO NWs was performed by sputtering different thicknesses of Au film (5nm, 10nm, 15nm, and 20 nm) on substrates using magnetron sputtering (Denton Vacuum Desk IV). Thermal annealing of the deposited Au film was performed at 750°C for 1 hour.

As-synthesized ITO NWs, on ITO/glass substrate, were employed to fabricate 1D core-shell nanostructures of ITO-MoO₃. One gram of Mo powders, molybdenum (99.9%, -250 mesh, Alfa Aesar), were loaded into a quartz boat and were placed at the center of the quartz tube furnace. Target substrates were placed apart from the growth source at two different heating zones, downstream (300-585°C), and upstream (550-650°C). The carrier

gas (Ar) was added at a constant 10 sccm flow for the target substrate located in the downstream zone.

The oxygen flow was introduced as the reactant gas at the rate of 1-2.5 sccm. No carrier gas was used for the shell layer deposition when the substrate was located on the upstream side. Also, no change was made for the growth condition (800°C during 30 min).

The morphological and compositional characterization of synthesized NWs were performed by scanning electron microscopy (SEM, JEOL JSM-6480), energy dispersive X-ray spectroscopy (EDS, Oxford Instrument INCA), and X-ray diffraction (XRD, PANalytical's X'pert Pro MRD with Cu K α radiation at $\lambda=1.5418$ Å).

4.3 Result and Discussion

4.3.1 Effects of Oxygen Flow Rate on Growth of ITO Nanowires

4.3.1.1 Growth on Bare 1 μ m SiO₂/Si Substrate under 0.1 sccm O₂

Three rectangular 10 mm \times 25 mm SiO₂/Si substrates were placed 1 inch, 2 inches, and 3 inches apart from the center of the growth source at the downstream end, and in the heating zones of 740-780°C, 585-740°C, and 280-585°C, respectively. When applying a 0.1 sccm oxygen flow rate, no or very few NWs are observed on the substrate located in the temperature range of 740-780°C (Figure 4-1). This can be explained by that the existence of surface contamination on the substrate that can act as nucleation sites, leading to sporadic growth across the substrate. However, due to the high temperature of the substrate, condensation of vapor species on the substrate is very limited, resulting in no growth.

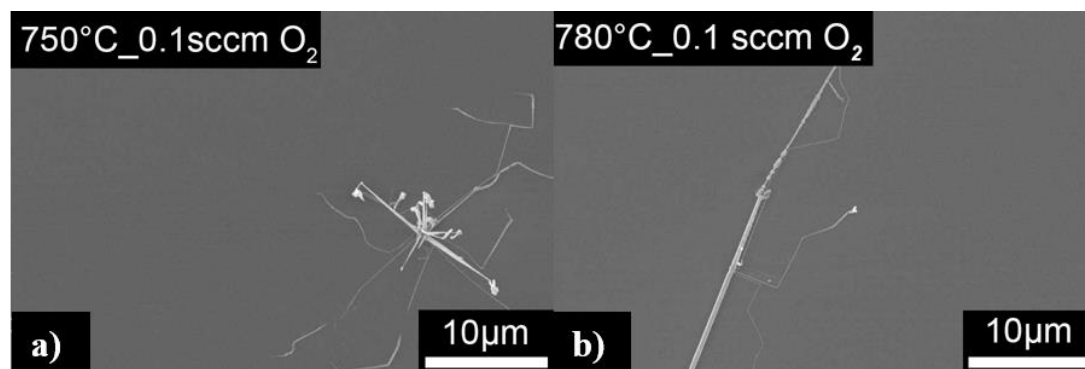


Figure 4-1. SEM images of few ITO NWs grown on bare SiO₂/Si substrates (high temp. heating zone: 740-780 °C) with 0.1 sccm oxygen flow rate

At a lower temperature range, 585-740°C (Figure 4-2), growth shows clusters of nanotrees with trunks and several branches. It is noted that a large area of the substrate still is uncovered in the background. The nanotrees structures may confirm a lack of nucleation sites on the substrate. Once the substrate temperature drops from the 740-780°C range to the 585-740°C range, more vaporized materials are condensed on the substrate.

Formation of nanotree structures occurs because once a nucleation site becomes available, which can be either contamination or a particle on the substrate, nucleation starts, and the main body or trunk of nanowire starts to grow out of the nuclei. The nanowires formed are also considered desired nucleation sites for more growth, and branches can grow on the region of the trunk exposed to flux. SEM images show that each branch can also act as additional potential sites for nucleation, therefore, the nanotree structure type is extended asymmetrically in three dimensions when absorbing more vapor species.

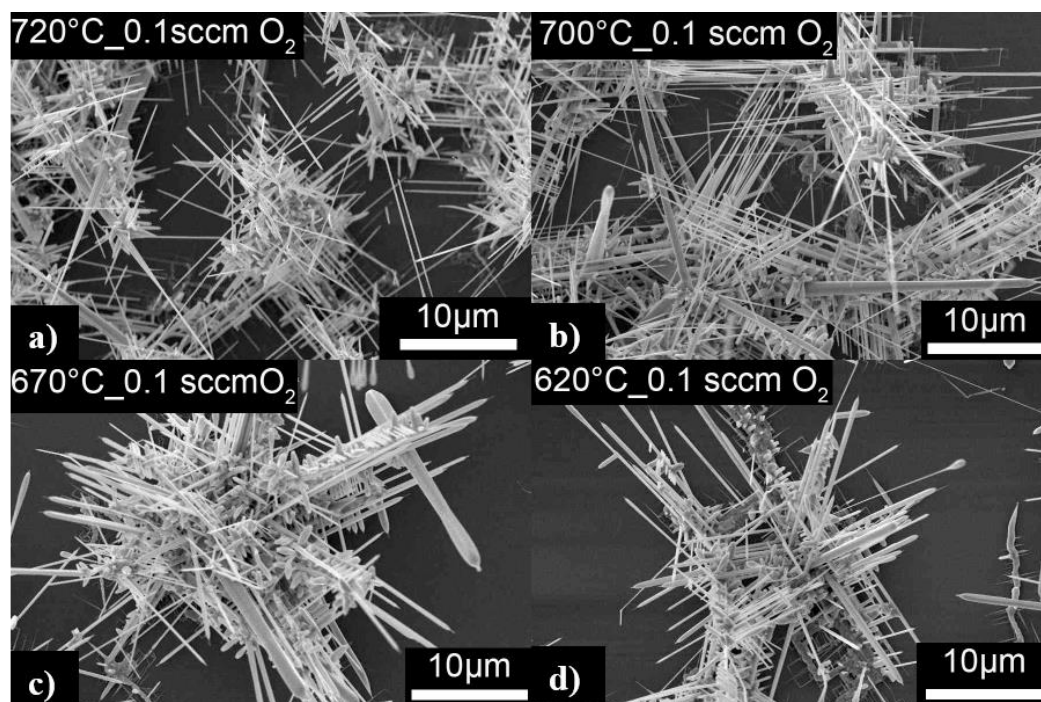


Figure 4-2. SEM images of ITO NWs grown on bare SiO₂/Si substrate (medium temp. heating zone: 585-740 °C with 0.1 sccm oxygen flow rate)

In conclusion, low density and nonuniform growth was observed across the substrate located at these temperature regions. The growth mechanism was found to be a vapor-solid (VS) process, which is a catalyst-free process including direct vaporization of reactant materials at higher temperatures, followed by their deposition on a substrate located in a lower temperature zone resulting in direct growth of NWs on solid particles [94]. Also, performing EDX analysis on the tip of NWs (Figure 4-3) reveals the involvement of another growth mechanism called self-catalytic VLS growth. Self-catalytic VLS growth mainly forms due to the formation of low eutectic temperature of the In-Sn alloy [95].

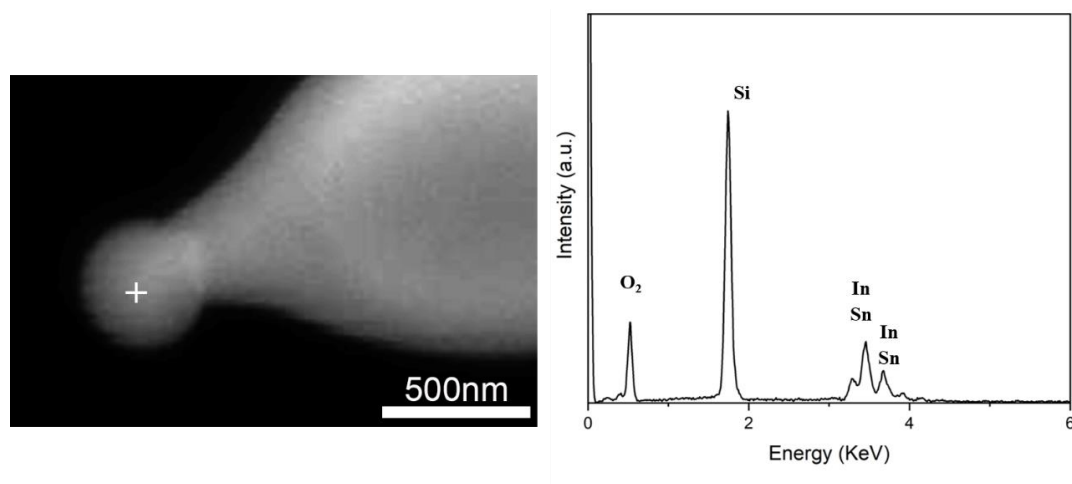


Figure 4-3. EDX spectrum acquired from tip of NWs (grown within medium temp. heating zone: 585-740-585°C).

Thick and non-uniform types of growth on SiO₂/Si substrates was observed (Figure 4-4) toward the downstream end of the reaction chamber and within the temperature range of 280-585°C. Micro-trees with several asymmetric branches were observed (Figure 4-4 b). The length of these micro trees is about 5μm and the diameter is about 1 μm. Formation of thick nanotrees can be explained such that the large reduction in temperature increased the condensation of vapor species on the substrate, leading to thick and non-uniform growth. This could be explained as; at the time of nucleation, branches mostly tend to grow on the regions of vertical micro trunk which are exposed to the flux at higher temperature end of the substrate (heating zone 585-515°C, Figure 4-4 a and b) [96]. Therefore, the majority of vapor species are absorbed to form these micro-trees with several branches, and less materials (vapor species) are delivered to downstream leading to very non-uniform growth.

It is expected that further reduction in temperature increases the formation of NWs with smaller diameters and more branches. This could be explained by the relationship between critical nuclei size and nucleation rate, which exponentially reduces to the power

of $(-1/KT)$. However, this is not the case here. At a lower temperature range (280-585°C), the required thermal energy to overcome the energy barrier of oxide formation is reduced, leading to a lower diffusion rate and less growth [97]. It was also noted that locations on the substrate which are closer to the downstream area of the CVD (heating zone 385-450°C, Figure 4-4 c and d), show flat growth with no vertical or micro-tree structures.

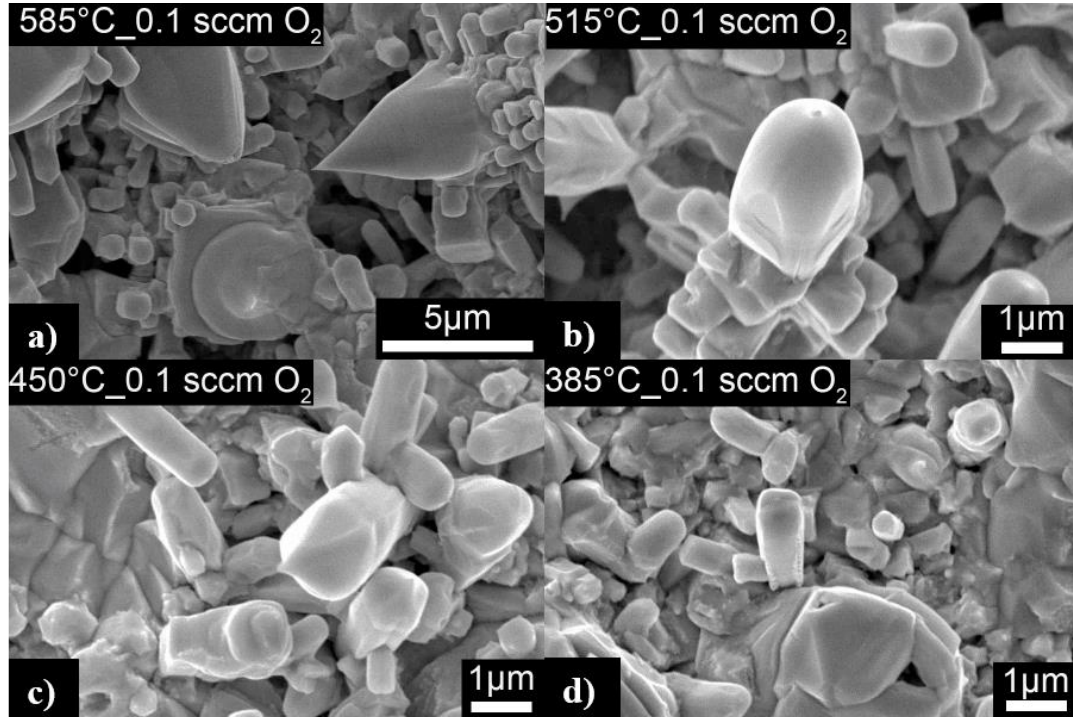


Figure 4-4. SEM images of non-uniform micro-trees grown on bare SiO₂/Si substrate (low temp. heating zone: 280-585°C with 0.1 sccm oxygen flow rate)

4.3.1.2 Growth on Bare 1µm SiO₂/Si Substrate under 0.5 sccm O₂

Figure 4-5 shows the resulting growth on SiO₂/Si substrate located at the high end of the temperature range (740-780°C) while the oxygen flow rate was increased up to 0.5 sccm. In an atmosphere with higher oxygen content, more of the source materials are oxidized and deposited on the substrate, leading to more growth compared with growth using 0.1 sccm O₂.

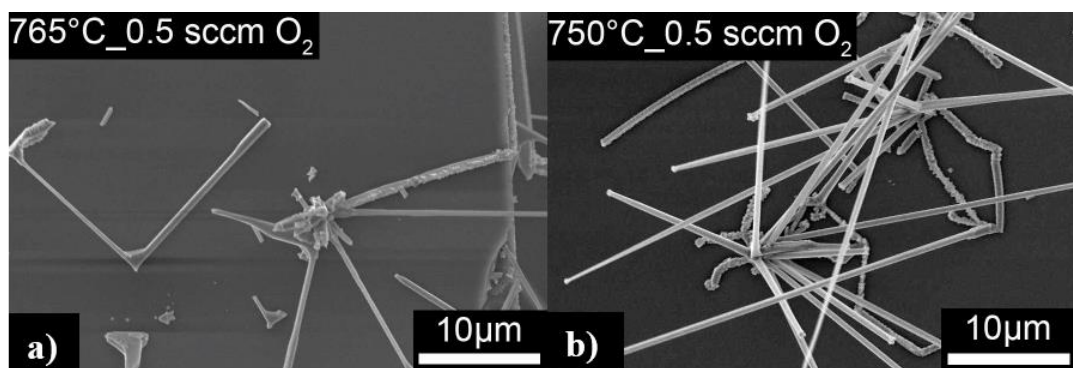


Figure 4-5. SEM images of NWs grown on bare SiO₂/Si substrates (high temp. heating zone: 740-780 °C) with 0.5 sccm oxygen flow rate

As we move toward the downstream and reach the medium temperature range 585-740°C, the formation of high density and uniform NWs were observed across the substrate (Figure 4-6). Improvement in density and the uniformity of NWs can be attributed to production of higher volume oxidized species (under 0.5 sccm O₂ flow), which leads to higher delivery and deposition of vapor species on the substrate (when compared to growth using 0.1 sccm O₂).

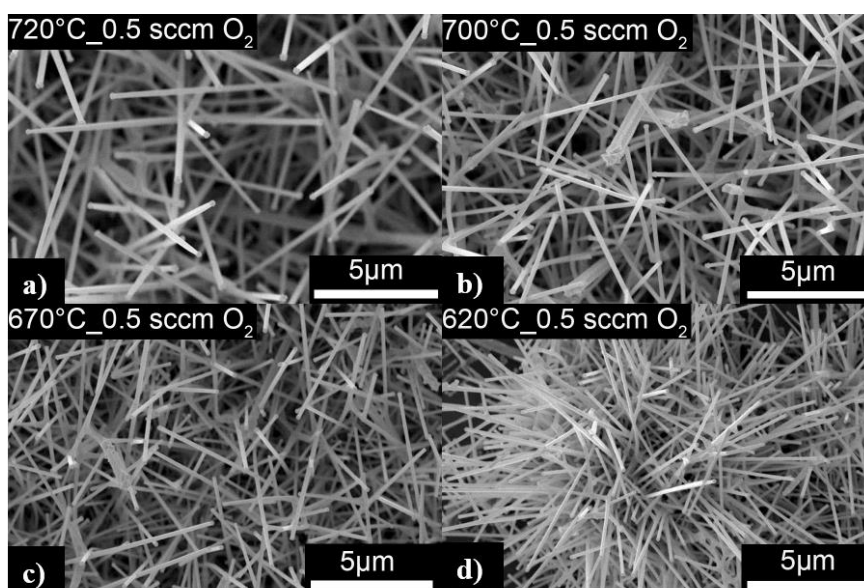


Figure 4-6. SEM images of NWs grown on bare SiO₂/Si substrates (medium temp. heating zone: 740-585 °C) with 0.5 sccm oxygen flow rate

Finally, when we reach the low temperature heating zone 280-585°C on the third SiO₂/Si substrate, we noticed formation of pine tree shaped nanotrees (Figure 4-7 a). As was discussed, higher oxygen flow (0.5 sccm) causes more oxidation of source materials, leading to the generation of a higher volume of oxidized vapor species, which is expected to increase the rate of vapor species' condensation and nucleation. However, the majority of evaporated growth source were delivered to substrate located at high and medium temperature zones, causing delivery of less materials into this region and resulting in growth of either few (Figure 4-7 b) or no NWs (Figure 4-7 c and d).

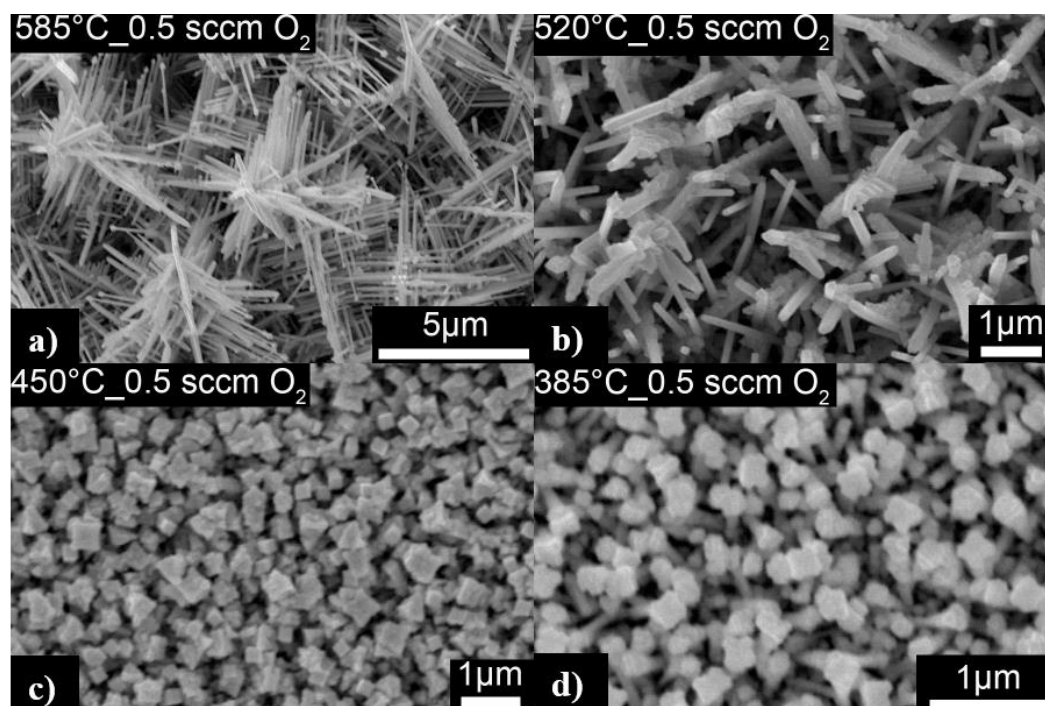


Figure 4-7. SEM images of NWs grown on bare SiO₂/Si substrates (low temp. heating zone: 280-585°C) with 0.5 sccm oxygen flow rate.

4.3.1.3 Growth on Bare 1μm SiO₂/Si Substrate under 1.5 sccm O₂

Figure 4-8 shows SEM images of resultant growth on SiO₂/Si substrate (heating zone: 780-740 °C) when the oxygen flow rate was raised to 1.5 sccm. Unlike the previous two experiments (performed under 0.5 and 1 sccm O₂), a white background was observed

on the substrate, which could be related to the creation of a thin film due to higher oxidation, evaporation, and deposition of growth source materials. Formation of this thin film can improve the growth density by acting as a continuous and uniform nucleation site across the substrate. This was not the case for previous experiments performed under lower oxygen flow rates, which showed little or no growth of NWs due to insufficient nucleation sites on the substrate.

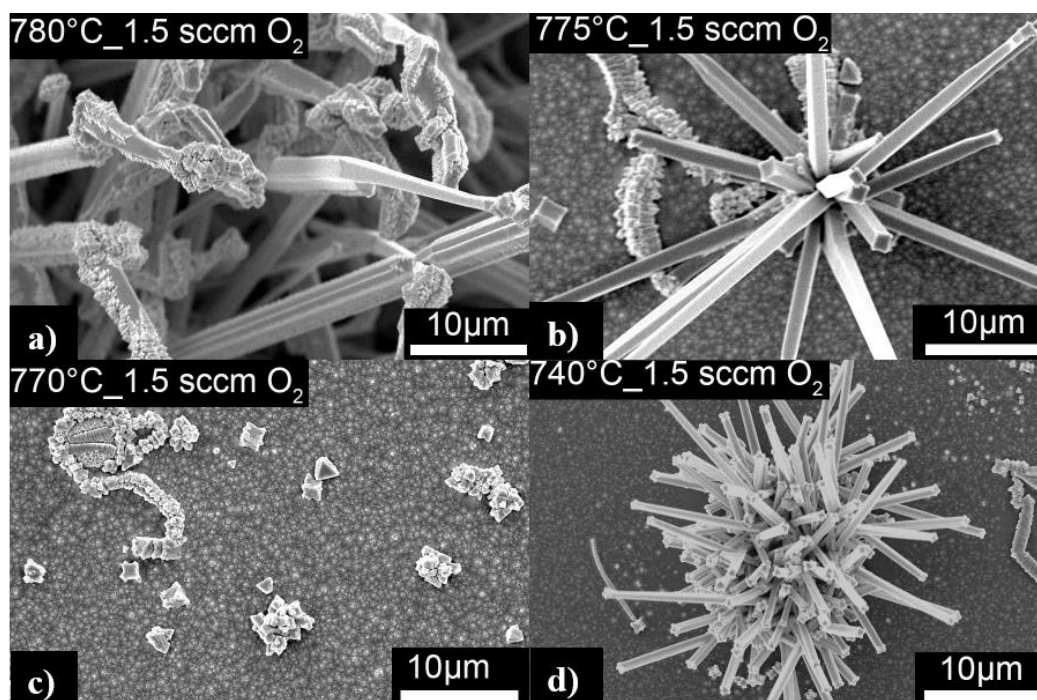


Figure 4-8. SEM images of NWs grown on bare SiO₂/Si substrates (high temperature heating zone: 740-780 °C) with 1.5 sccm oxygen flow rate.

Figure 4-9 shows the SEM images of nucleation and growth of out-of-plane ITO NWs. The SEM top-view images (Figure 4-9 a, c) suggest either a square or rectangular cross section as the nucleation sites. Depending on the nucleation site, growth can be in the form of a single (Figure 4-9 b) or a cluster of NWs (Figure 4-9 d).

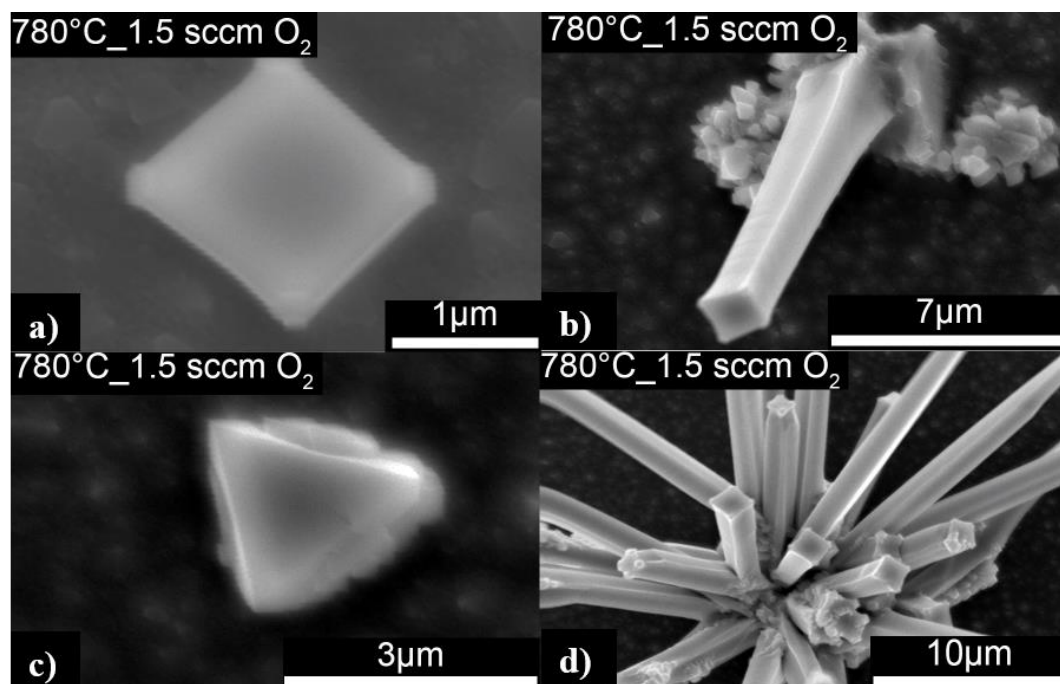


Figure 4-9. SEM images of nucleation and growth of ITO NWs on SiO₂/Si substrate with 1.5 sccm oxygen flow.

Figure 4-10 illustrates the SEM images of growth on SiO₂/Si substrate (medium temp. heating zone: 585-740°C) with an oxygen flow rate of 1.5 sccm. As the temperature drops (compared with Figure 4-8), the condensation rate of the vapor species on the substrate increases, leading to higher density growth. Growth at higher temperature zones (Figure 4-10 a and b), mainly follows an in-plane orientation with a horizontal direction parallel to the substrate. As the substrate is fully covered with horizontal growth, the appearance of vertical growth is observed (Figure 4-10 a). The origin of vertical growth is where the horizontal paths meet each other. Further reduction of temperature leads to either less vertical growth (Figure 4-10 b) or few or no in-plane growth of NWs (Figure 4-10 c and d, respectively).

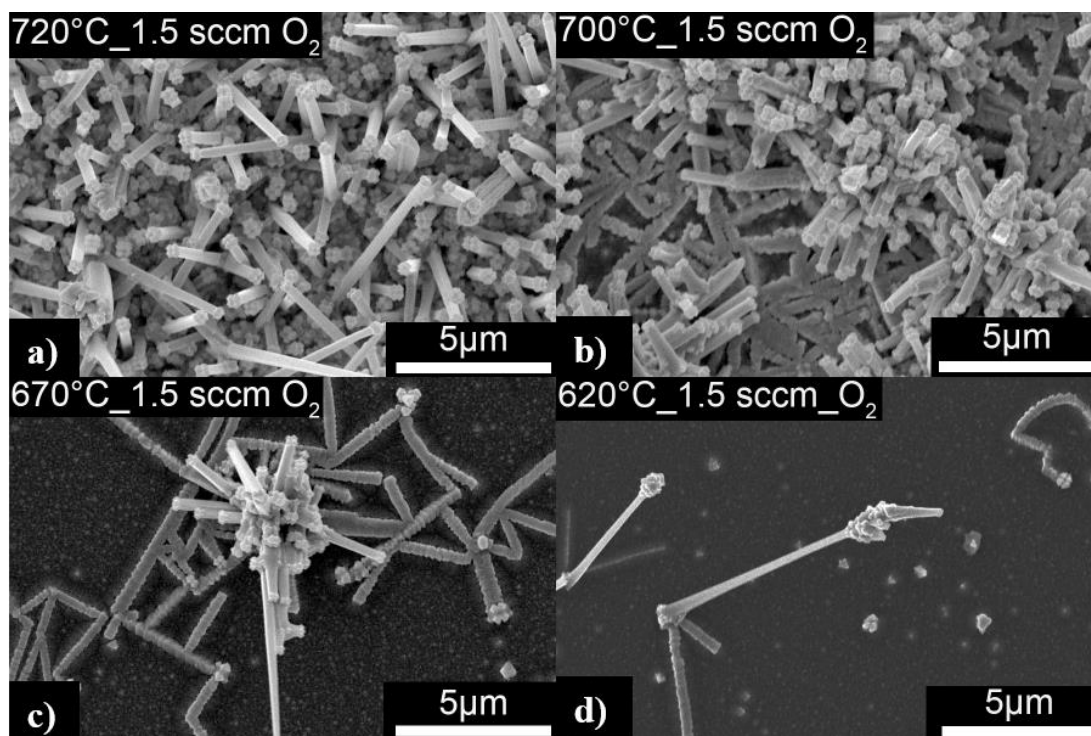


Figure 4-10. SEM images of mixed in-plane and out-of-plane growth of NWs on SiO₂/Si substrate (medium temp. heating zone: 585-740 °C) with 1.5 sccm oxygen flow.

Figure 4-11 illustrates the SEM images of growth on SiO₂/Si substrate (low temperature heating zone: 585-740°C) with an oxygen flow rate of 1.5 sccm. A substantial drop in temperature causes rapid condensation of remnant vapor species leading to thick and non-uniform growth (Figure 4-11 a). In addition to a major drop in temperature, consumption of the majority of the growth source leads to very limited or no deposition, and no growth of NWs (Figure 4-11 b, c, d).

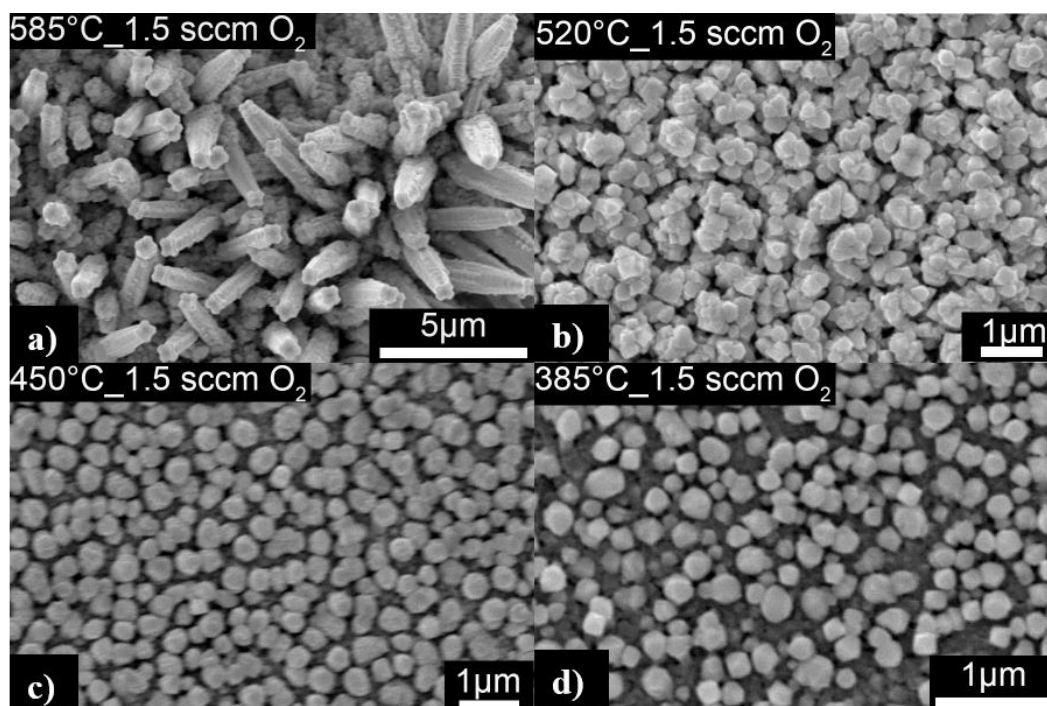


Figure 4-11. SEM images of mixed in-plane and out-of-plane growth of ITO NWs on SiO₂/Si substrate (low temp. heating zone: 280-585°C) with 1.5 sccm oxygen flow.

Figure 4-12 summarizes all obtained growth morphologies (at different heating zones) under different oxygen flow rates. It can be seen that, for the same temperature zone, mostly uniform growth of NWs was obtained within a 0.5 sccm oxygen flow rate. Also, under this growth condition, NWs showed the smallest diameter range from 161 to 526 nm with length up to 5 μm. With a 0.1 O₂ flow NWs were in a diameter range of 500 nm to 2.5 μm with a length of 20 μm, and with a 1.5 sccm O₂ flow, NWs were in a diameter range of 340 nm to 2 μm with length of 2 μm. It is concluded that the formation of ITO NWs, in the absence of a catalyst, is possible when growth parameters are carefully adjusted.

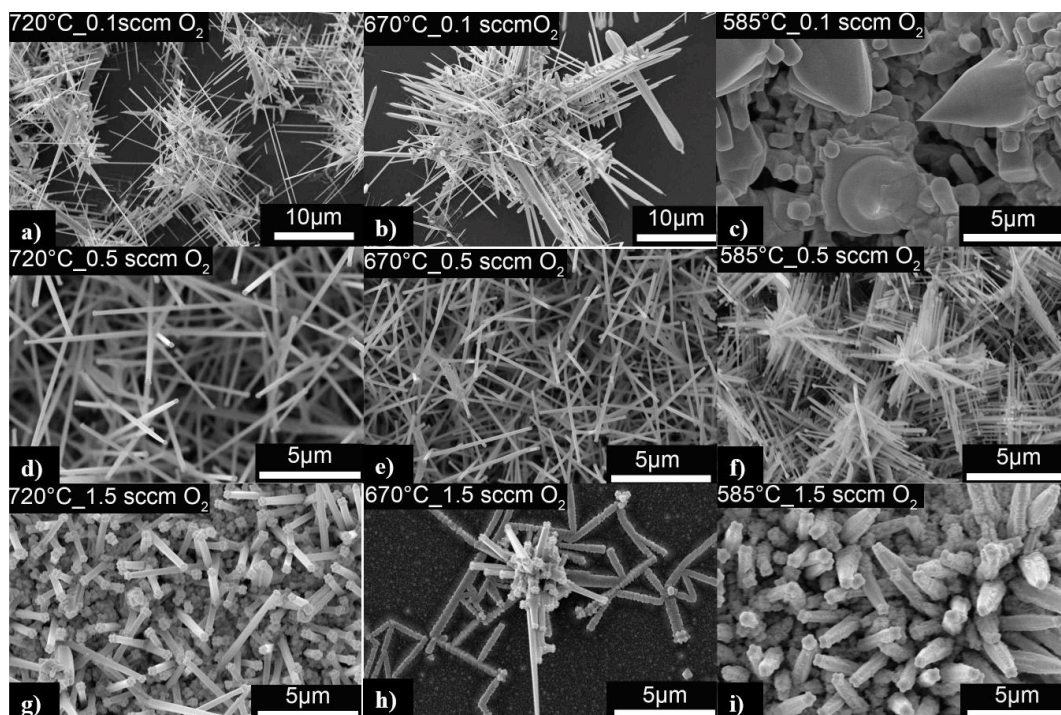


Figure 4-12. SEM images of growth morphologies resulting under the conditions of 0.1 (a-c), 0.5 (d-f), and 1.5 (g-i) sccm oxygen flow rate.

4.3.2 Catalyst Formation on SiO₂/Si Substrate by Annealing

In order to control the diameters of synthesized ITO NWs, a study was performed to investigate the thickness dependence of deposited Au film and the size of Au nanoclusters created by annealing. Figure 4-13 shows SEM images of annealed Au films (750°C for 1 h) deposited on SiO₂/Si substrate in different thicknesses. As is illustrated, an increase in the thickness of deposited Au film results in the formation of bigger nanoparticles with irregular geometry, which can be explained by the Ostwald ripening phenomena. Reduction in the surface energy of Au film is the driving force for this phenomena and takes place through surface diffusion and grain coarsening [98]. After annealing, the diameter of Au nanoclusters was in the range 35 nm, 180 nm, 400 nm, and 1μm for Au films with thickness of 5 nm, 10nm, 15 nm and 20 nm, respectively.

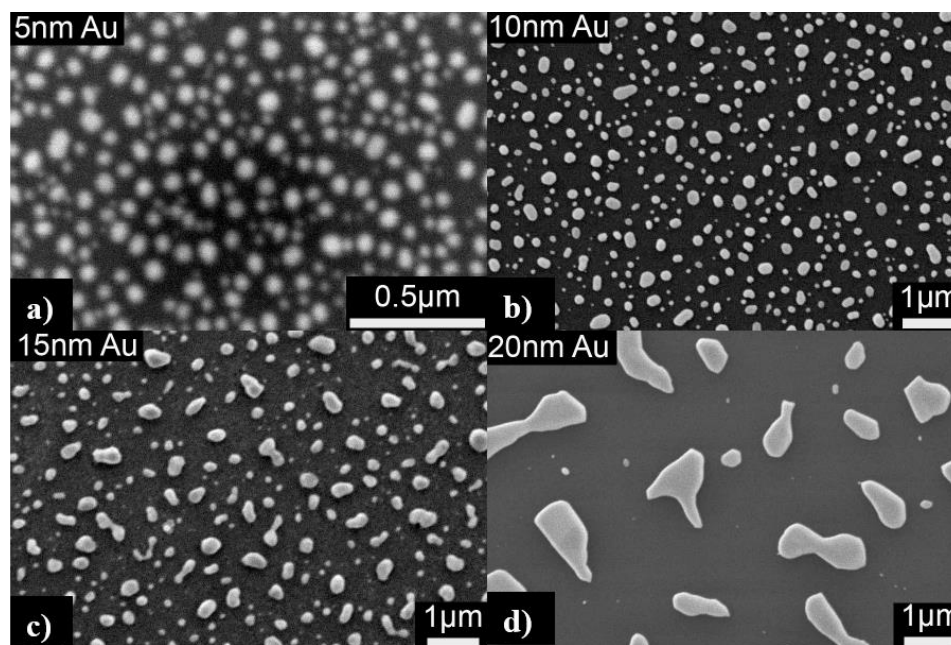


Figure 4-13. SEM images of Au nanoclusters after annealing at (750°C for 1 h); deposited Au film thickness (a) 5; (b) 10; (c) 15 ; and (d) 20 nm

4.3.2.1 Effects of Catalyst Patterning on Diameter-controlled Growth of ITO NWs on SiO₂/Si Substrate

Diameter-controlled growth of ITO NWs was studied using annealed substrates with different Au film thicknesses. Growth was performed at 800°C for 30 min with a 0.1 sccm oxygen flow. Figure 4-14 shows the SEM images of synthesized NWs on substrates with different sizes of Au nanoclusters. It is concluded that growth on a substrate with 5 nm of Au film (gold nanocluster diameters ~ 35 nm) leads to ITO NWs with a diameter of approximately 150-300 nm (Figure 4-14 a-d). Ten nanometers of gold film (gold nanocluster diameters ~ 180 nm) resulted in ITO NWs with a diameter of 550 nm (Figure 4-14 e-h). Finally, the diameters of grown ITO NWs on the substrate with 15 nm of Au film (nanoclusters size ~ 400 nm) were about 850 nm (Figure 4-14 i-l). The length of grown NWs were in the range 5-15 μm (for a substrate with 5 nm of Au film thickness) and 15-30 μm for substrates with 10 and 15 nm of Au films.

Table 4-1 summarizes the thicknesses of Au films, the corresponding diameters and lengths of grown ITO NWs.

Table 4-1. Summary of diameters and lengths of grown ITO NWs on SiO₂/Si substrate with different thicknesses of Au films catalyst

Thickness of deposited Au films (nm)	Diameter of Au nanoclusters	Diameter of ITO NWs (nm)	Length of ITO NWs (μm)
5	20-104 nm	150-300	5-30
10	33-400 nm	550	10-50
15	107-500 nm	850	10-50

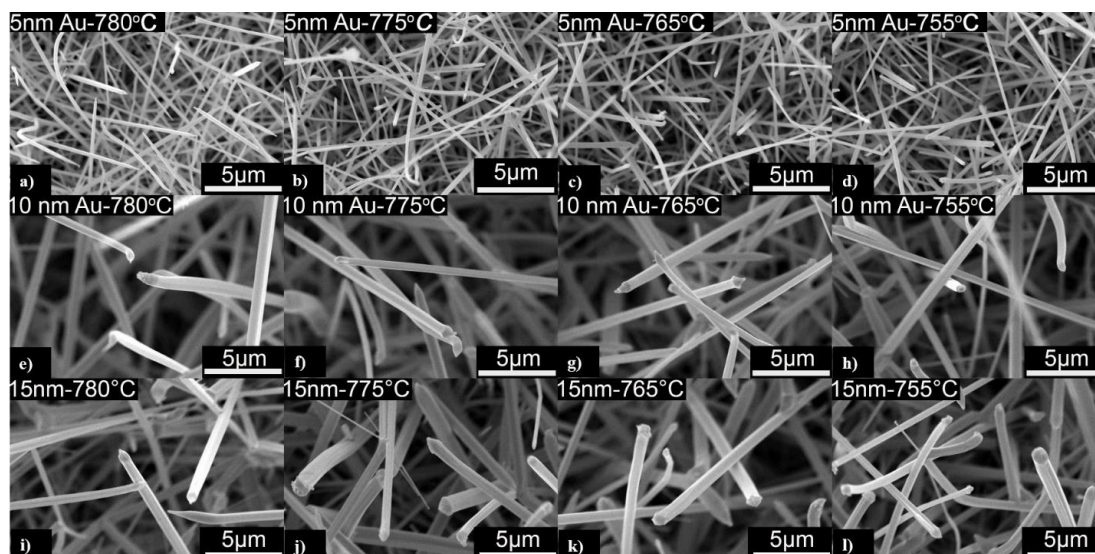


Figure 4-14. SEM images of ITO NWs (800°C for 30 min) grown on annealed SiO₂/Si substrate with Au films thickness of 5 nm, 10 nm, and 15 nm

Energy-dispersed X-ray spectrometry (EDX) was performed on the tips of grown ITO NWs (Figure 4-16) in order to study the growth mechanism. Before discussing the EDX results, it should be noted that due to neighboring of indium (In, Z=49) and tin (Sn, Z=50) in the periodic table, their L-emission energies are very close and very difficult to resolve. Using new multilayer coatings (MLCs) varied line spaced grating, M. Terauchi *et al* [99] were able to resolve Sn-L_α and In-L_{β1}. Figure 4-15 shows EDX spectra performed on (In O₃)_{1-x} (Sn O₂)_x (x=0.05 ~ 0.1) using MLC grating system (red curve) and a

conventional EDS (blue curve). This shows that resolving Sn-L α (electrons transfer from M $_{4,5}$ to L $_3$; 3444 eV) and In-L β_1 (electron transfer from M $_4$ to L $_2$; 3487 eV) peaks is very difficult using conventional EDS systems [99].

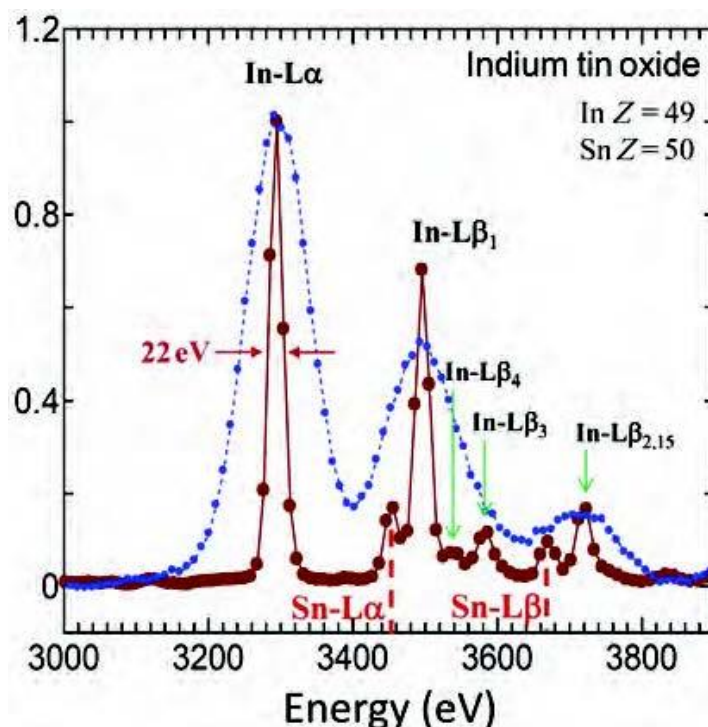


Figure 4-15. Reported EDS spectra (M. Terauchi et al) on (In O $_3$) $_{1-x}$ (Sn O $_2$) $_x$ ($x=0.05 \sim 0.1$) obtained using MLC grating system (red) and conventional EDS (blue line) [99]

EDX spectrums showed Au signals when targeting the tip of ITO NWs (Figure 4-16 a-c). EDX results showed either weak or no Au signals for growth with 5 nm thick Au film. The signals for the substrates with 10 and 15 nm thick Au film showed higher intensity for gold in comparison to 5 nm film. In addition to spotted Au droplets on top of the nanowires, no significant radial growth, along the length of nanowires, was observed. This was not the case for the majority of NWs grown on 5 nm thick Au film. That is, the growth on a substrate with 5 nm thick Au film is a combination of both VS and VLS mechanism [93]. Obtained EDX data (Figure 4-16-b) confirms both VLS (Au signals) and self-catalyzed VLS (Sn signals) as growth mechanisms for substrates with 10 nm Au film.

Growth on a substrate with a 15 nm thick Au film mainly involves the VLS mechanism (Figure 4-16-c). Also, detailed Sn signals representing self-catalyzed VLS growth are labeled in Figure 4-17.

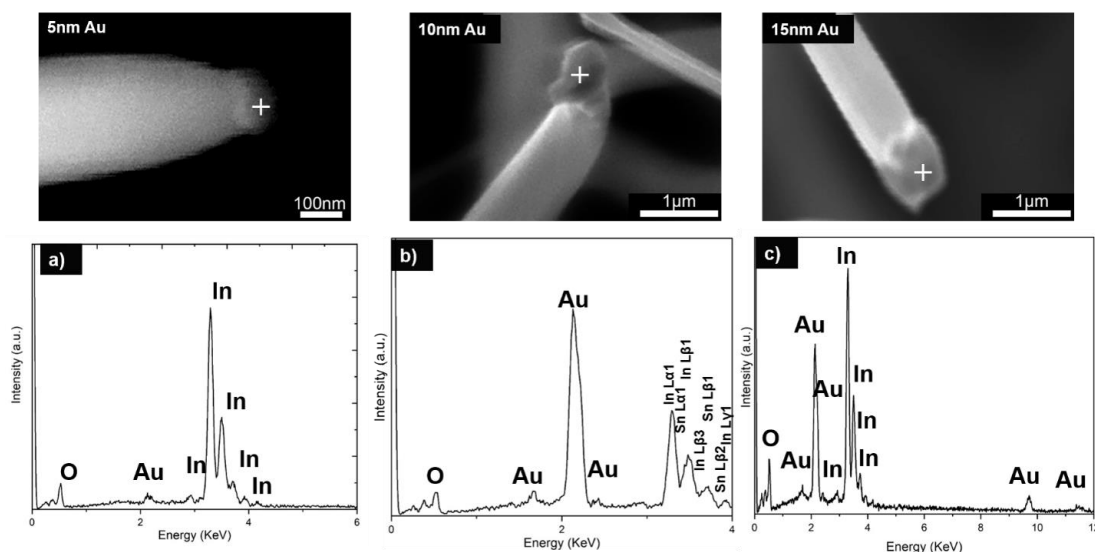


Figure 4-16. SEM images of performed EDX ITO NWs grown on SiO₂/Si substrate with different Au film thickness; white cross sign indicates the locations where EDX spectrums captured from the tip of NWs.

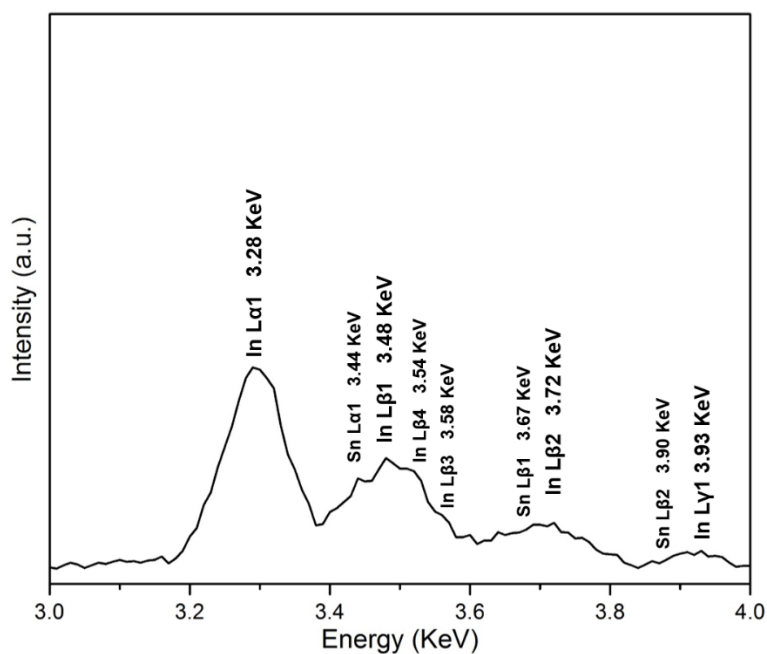


Figure 4-17. Enlargement of emission spectra from Figure 4-16- b showing detailed Sn peaks for self-catalyzed VLS growth mechanism

4.3.3 Effects of Oxygen Flow Increase on Growth of ITO NWs on SiO₂/Si Substrate

The impacts of a higher oxygen flow rate (0.2, 0.3, and 0.5 sccm) on growth of ITO NWs were carefully studied within the heating zone 600-800°C (Figure 4-18 and Figure 4-20). In order to get consistent results, no change was applied to previous growth condition (800°C for 30 min), and the 10 nm thick Au film (as the optimum catalytic thickness) was sputtered on all the SiO₂/ Si substrates. The only change was in oxygen flow rate. Figure 4-18 shows the morphology of NWs grown within heating zone 750-800°C. Diameter, length, and growth mechanism of these ITO NWs are summarized in Table 4-2. It can be seen that the increase in the rate of oxygen flow (from 0.1 to 0.5 sccm) reduces the length of NWs (Figure 4-18 a-c vs Figure 4-18 i-l). This is due to rapid oxidation of reactant materials before evaporation, which decreases the vapor pressure of precursor [93]. A successful growth procedure of ITO NWs can be explained by transportation of non-oxidized metal vapors (In and Sn metals) to gold nanoclusters, leading to formation of a liquid alloy and precipitation of ITO NWs at the bottom [100]. The low melting points of indium (156.6°C) and tin (213 °C), in relation to growth temperature (800°C), produces sufficient metallic vapor pressure for successful growth of ITO NWs. In a higher rate of oxygen flow, oxidation of reactant metals happens before evaporation. This produces In₂O₃ and SnO₂ with high melting points of 1912°C and 1630°C, respectively. In this case, less vapor pressure of the reactant metal is delivered to gold nanoclusters, leading to shorter length NWs.

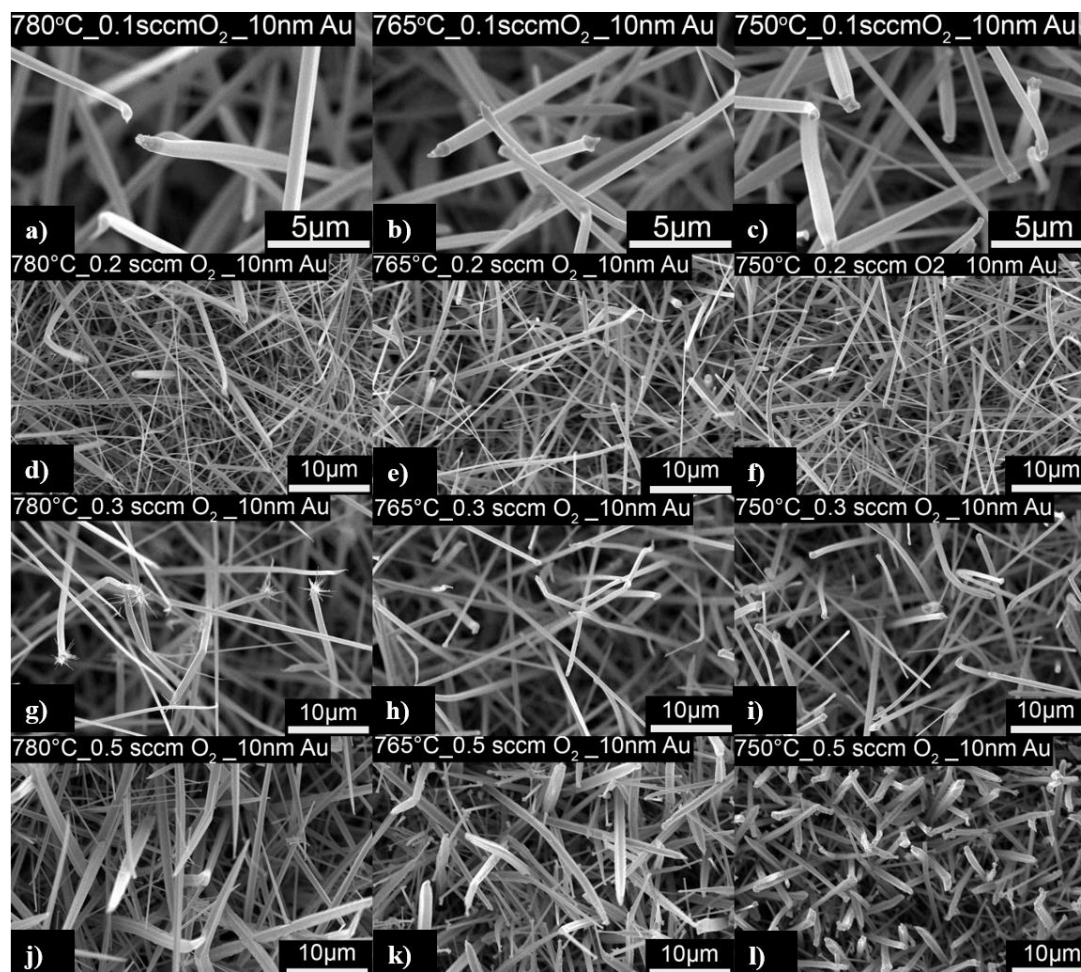


Figure 4-18. SEM image of ITO NWs grown at various oxygen flow rates of (a-c) 0.1 sccm; (d-f) 0.2 sccm; (g-i) 0.3 sccm; (j-l) 0.5 sccm within temperature zone of 750-800 °C.

Table 4-2. Summary of diameter, length, and growth mechanism of grown ITO NWs at various oxygen flow rates within 750-800°C heating zone.

Oxygen flow rate (sccm)	Diameters of ITO NWs	Length of ITO NWs (μm)	Growth Mechanism
0.1	300 nm -1 μm	10-50	VLS /self-catalyzed VLS
0.2	300 nm -1 μm	10-50	VLS only
0.3	500 nm -1 μm	10-50	VLS only
0.5	350 nm -1.7 μm	5-25	VS Only

The growth mechanism was studied by performing EDX analysis on the tips of grown ITO NWs (Figure 4-19). The appearance of a strong Au signal in EDX spectrums

for growth conditions under 0.1, 0.2, and 0.3 sccm oxygen flow confirms the existence of gold catalyst on top of the synthesized nanowires, indicating VLS as the dominant growth mechanism (Figure 4-19 a-c). In addition to the VLS growth mechanism, the appearance of tin signals the condition with 0.1 sccm O₂, this indicates the involvement of self-catalyzed VLS growth. For the growth condition with 0.5 sccm O₂, EDX spectra showed no trace of gold signals, proposing VS as the growth mechanism (Figure 4-19-d).

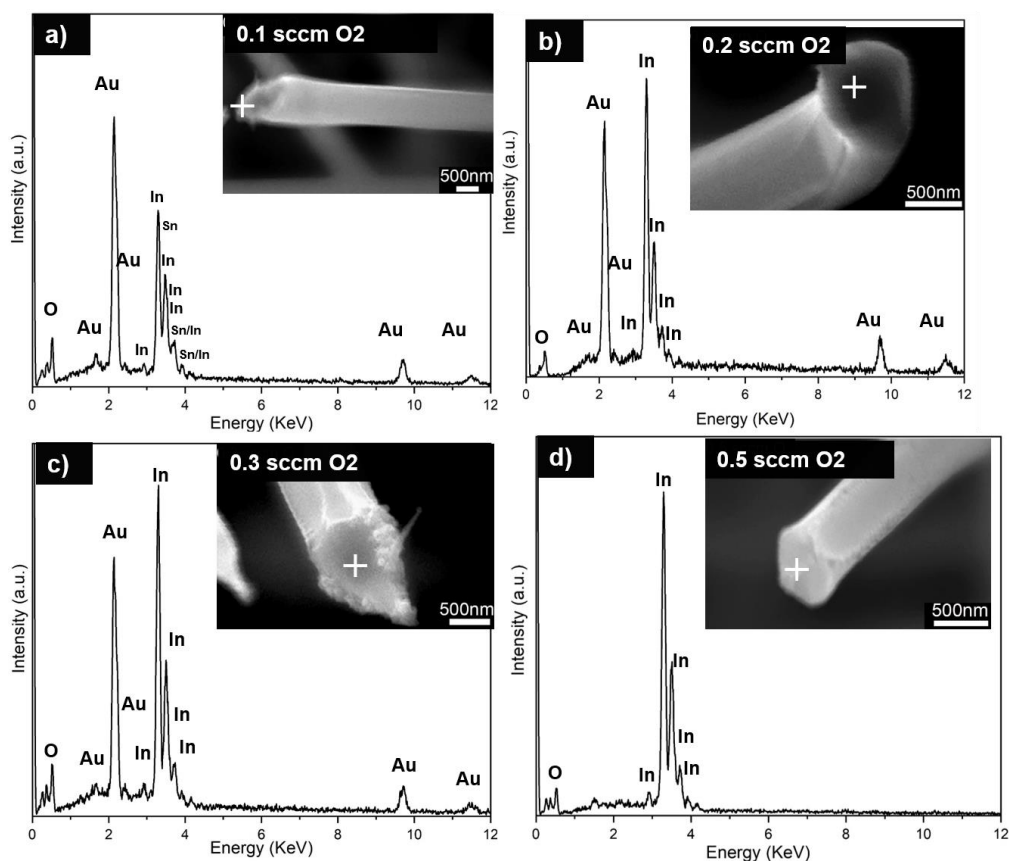


Figure 4-19. EDX spectra (heating zone 750-800°C) of ITO NWs grown on SiO₂/Si substrate under different oxygen flow rate of (a) 0.1 sccm; (b) 0.2 sccm; (c) 0.3 sccm; (d) 0.5 sccm; white cross sign indicates the locations where EDX spectrums captured from the tip of NWs.

Figure 4-20 shows the morphology of growth within heating zone 600-750°C. Diameter, length, and growth mechanism of grown ITO NWs are summarized in Table 4-3. Besides rapid oxidation of reactant metals, which leads to shorter NWs (5-25 μm),

reduction of temperature below 750°C substantially affects the uniformity of growth. For heating zone of 750-800°C, indium and tin have a vapor pressure of (10^{-4} - 10^{-3}) and (10^{-7} - 10^{-6}) Torr. This reduces to In 10^{-6} - 10^{-7} and Sn 10^{-9} - 10^{-7} Torr in the heating zone of 600-750°C [101] resulting shorter NWs.

Table 4-3. Summary of diameter, length, and growth mechanisms of grown ITO NWs at various oxygen flow rates within 600-750°C heating zone.

Oxygen flow rate (sccm)	Diameters of ITO NWs	Length of ITO NWs (μ m)	Growth Mechanism
0.1	200 nm -1 μ m	5-100	VS-VLS/self-catalytic
0.2	200-800 nm	5-20	VS-VLS/self-catalytic
0.3	200 nm -1.5 μ m	5-50	VS (dominant)-VLS
0.5	1 -5 μ m	5-25	VS Only

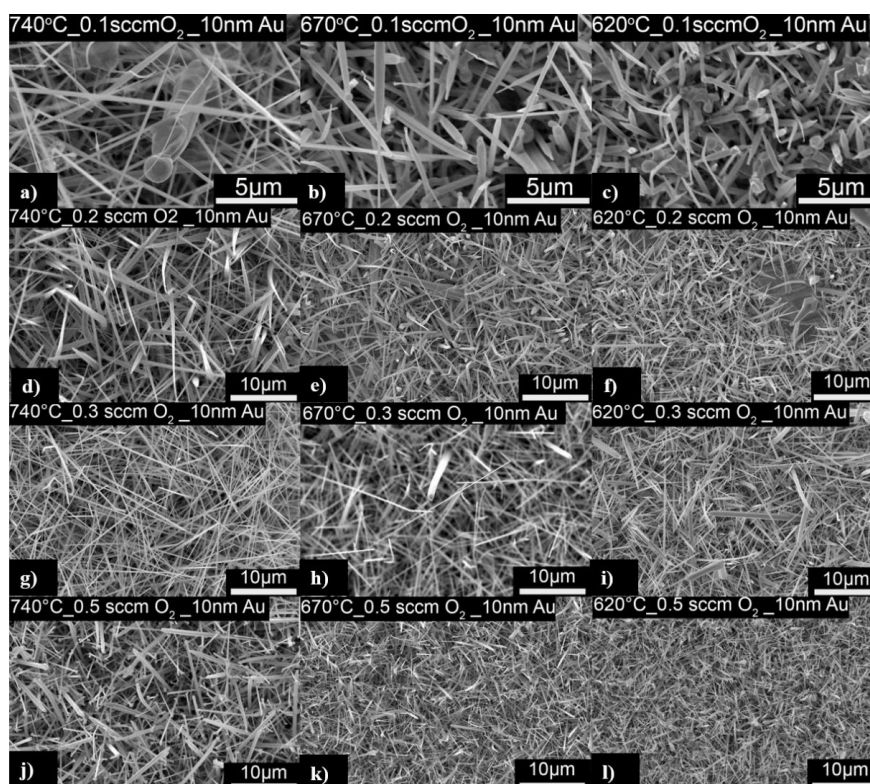


Figure 4-20. SEM image of ITO NWs grown at various oxygen flow rates of (a-c) 0.1 sccm; (d-f) 0.2 sccm; (g-i) 0.3 sccm; (j-l) 0.5 sccm within temperature zone of 600-750°C.

It can be seen from Figure 4-20 that, regardless of oxygen flow rate, all conditions show ITO NWs grown via VS growth mechanism. That is, no catalytic particles were observed at the end of NWs. However, a detailed growth mechanism study for this temperature zone (600-750°C) was studied by performing EDX analysis on the tips of grown ITO NWs (Figure 4-21). The appearance of both gold and tin signals in the EDX spectrums (Figure 4-21 a-d) confirms both VLS and self-catalyzed VLS as growth mechanisms for the conditions 0.1 and 0.2 sccm oxygen flow. It should be noted that self-catalyzed VLS growth happens at lower temperature zones (Figure 4-21 a-c) in comparison to the condition observed in (Figure 4-19 a-b) [102]. The existence of a gold catalyst on top of the synthesized nanowires indicates VLS as the dominant growth mechanism (Figure 4-21a, d, e). In addition to the VLS growth mechanism, tin signals were also observed for the condition with 0.1 sccm O₂, indicating the involvement of self-catalyzed VLS growth mechanisms for this condition. The increase of oxygen flow to 0.3 sccm leads to a Au-catalyzed VLS growth mechanism (Figure 4-21 e). For the growth condition under 0.5 sccm O₂, EDX spectra showed no trace of gold signal, suggesting VS as the growth mechanism (Figure 4-21-f). A higher rate of oxygen flow (0.5 sccm) accelerates the evaporation/condensation of reactant materials leading to solely VS mechanism.

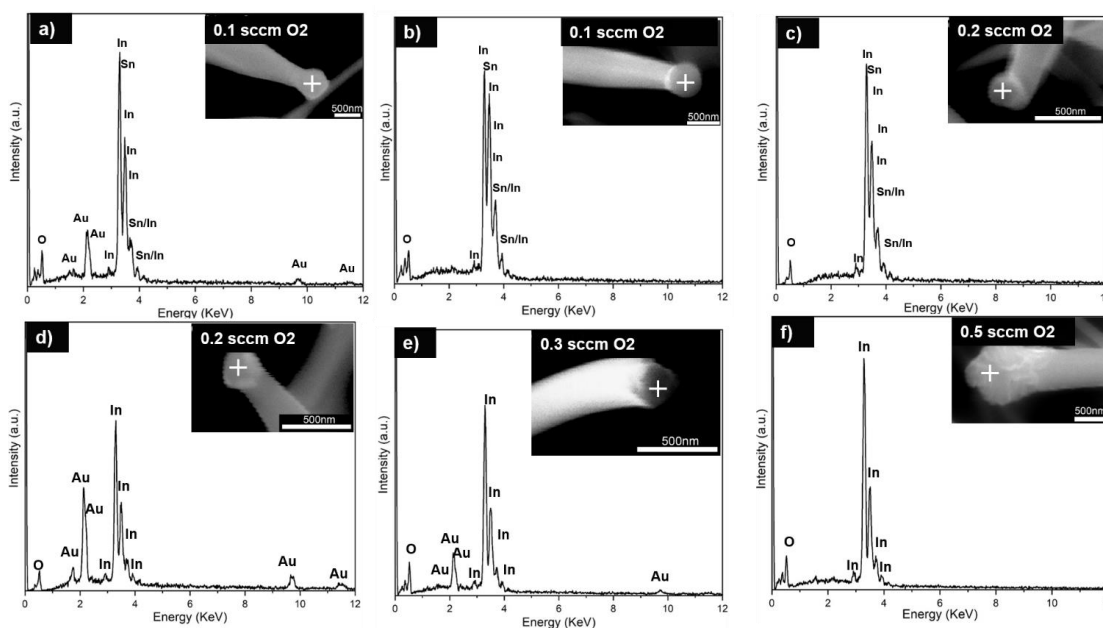


Figure 4-21. EDX spectra (heating zone:600-750°C) of ITO NWs grown on SiO₂/Si substrate under different oxygen flow rate of (a & b) 0.1 sccm; (c & d) 0.2 sccm; (e) 0.3 sccm; (f) 0.5 sccm; white cross sign indicates the locations where EDX spectrums were obtained from the tip of NWs.

Figure 4-22 shows the SEM micrographs of growth morphology for the substrates located in a temperature window of 500-585°C. Unlike the results seen under 0.1-0.3 sccm oxygen flow, which lead to asymmetric microtrees branch morphology (Figure 4-22 a-b), here uniform and symmetric nanotrees appeared once the oxygen flow rate was raised to 0.5 sccm (Figure 4-22 c-d). The formation of nanotrees at a higher rate of oxygen flow may be attributed to the rapid oxidation of reactant metal, leading to oxide coating. An oxide coating can act as a shield, limiting the evaporation of the metal reactant source. In this case, less vapor species of reactant materials are delivered, which provides a controlled nucleation and growth of nanobranches (Figure 4-22 c-d).

On the contrary, at a lower oxygen flow (0.1-0.3 sccm), a large amount of vapor species are transported to substrates located in the low temperature zone of 500-585°C, leading to uncontrolled and non-uniform growth (Figure 4-22 a-b).

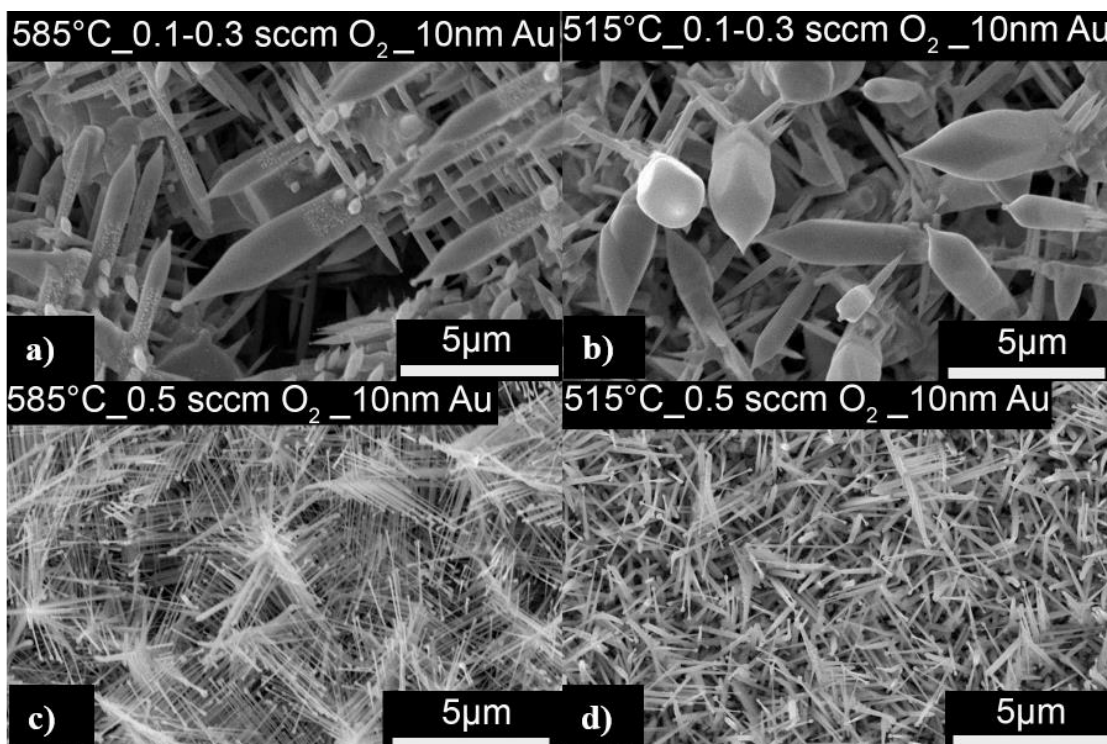


Figure 4-22. SEM image of microtree (a and b); nanotrees (c & d) branched morphology under 0.1-0.5 sccm oxygen flow rate within the temperature window of 500-585°C.

4.3.3 Effects of Uniform Heating Zone (Thermal Insulator) on Improving Uniformity of ITO Nanowires

In order to prevent negative effects of furnace heat loss on the uniformity of grown ITO NWs, two thermal insulators were installed at both the upstream and the downstream ends of the reaction chambers. All previous growth parameters were kept the same and growth was performed on an annealed SiO₂/Si substrate (10 nm thick Au film) at 800°C for 30 min. From Figure 4-23, it can be seen that the thermal insulators substantially improved the consistency of diameter of grown ITO NWs. Also, the maximum diameter of NWs (1μm) for these conditions without the thermal insulators (Figure 4-23 a-c), is smaller, at 700 nm, than the growth using the thermal insulators (Figure 4-23 d-f). The installed thermal insulators can increase the growth temperature by up to ten degrees.

Higher temperature increases the number of nucleation sites on the substrate, which leads to more nuclei sites and formation of NWs with smaller diameters. Two major changes were observed when using thermal insulators for growth in temperature window of 600-750 °C. First, from Figure 4-24 a, it can be seen that the mixed VS-VLS growth mechanism turns into only the VLS mechanism (Figure 4-24 d), which is more uniform. Secondly, the use of thermal insulators can greatly raise the temperature, by up to fifty degrees, which results in a substantial increase in the length of NWs (from 2.5 up to 10 μm) within the lower temperature zone (Figure 4-24 b-c vs e-f). This is due to the delivery of more reactant vapors to substrates located in the lower temperature zone.

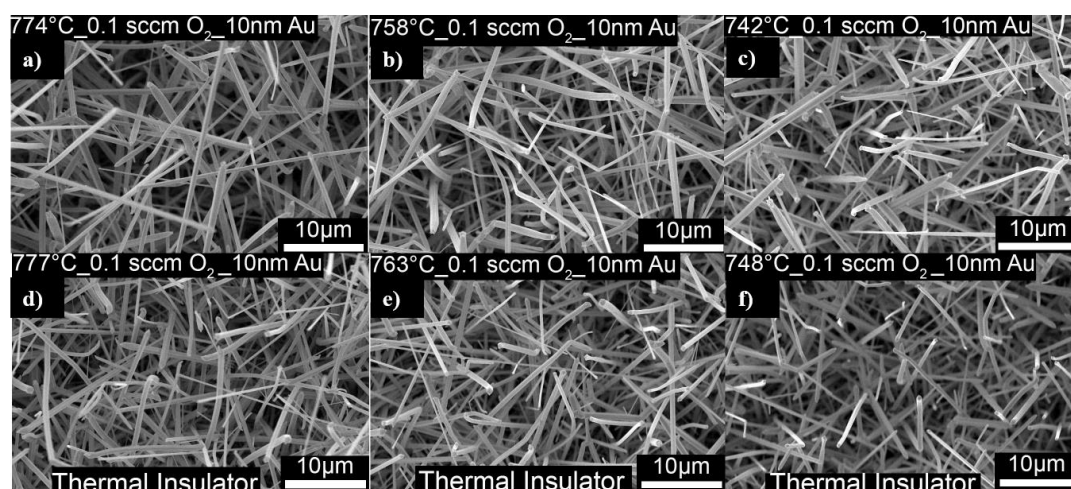


Figure 4-23. SEM images of ITO NWs grown on SiO_2/Si substrate in a temperature window of (750-800 °C); (a-c) without thermal insulator; (d-f) thermal insulator was installed on both sides of CVD reaction chamber.

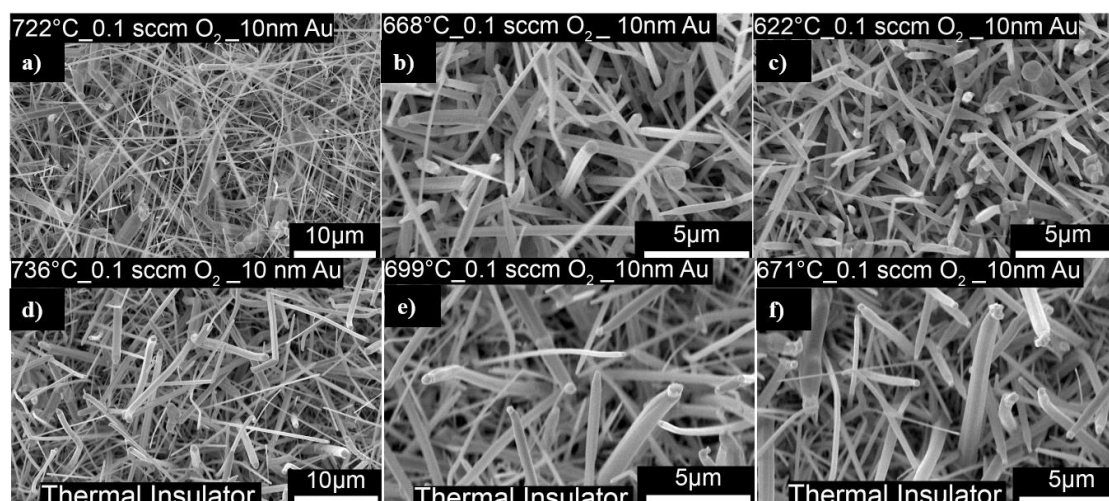


Figure 4-24. SEM images of ITO NWs grown on SiO₂/Si substrate in a temperature window of (600-750 °C); (a-c) without thermal insulator; (d-f) thermal insulator was installed on both sides of CVD reaction chamber.

4.3.4 Growth of ITO Nanowires on ITO/glass Substrate

4.3.4.1 Catalyst Formation on ITO/glass Substrate by Annealing

Similar to the catalyst formation process studied on the SiO₂/Si substrate, a study was carried out to investigate the relationship between the thickness dependence of deposited Au film and ITO NWs grown on ITO/glass substrate. Figure 4-25 shows SEM images of annealed Au films (750°C for 1 h) deposited on ITO/glass substrates with different thicknesses. As is illustrated, an increase in the thickness of deposited Au film results in the formation of bigger nanoparticles of irregular geometry. After annealing, the diameters of Au nanoclusters were in the range of 10-100 nm, 30-250 nm, and 140-550 nm for Au films with a thickness of 5nm, 10 nm and 15nm, respectively.

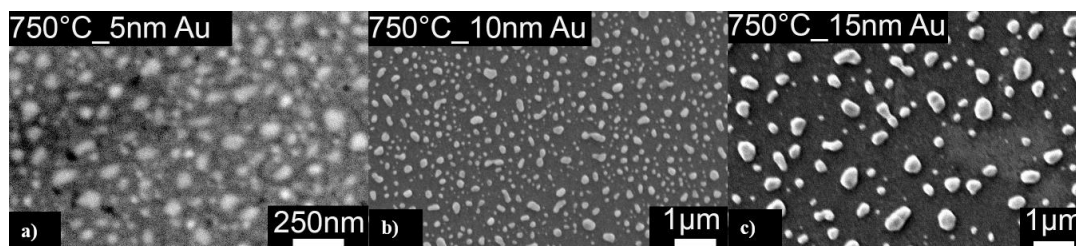


Figure 4-25. SEM images of Au nanoclusters on ITO/glass substrate; annealing performed at 750°C for 1 h for substrates with (a) 5 nm; (b) 10 nm; and (c) 15 nm thick Au films.

4.3.4.2 Effects of Catalyst Patterning on Diameter-controlled Growth of ITO NWs on ITO/glass Substrate

Diameter-controlled growth of ITO NWs on ITO/glass substrate was studied by employing annealed substrates with different thicknesses of Au films. Growth was performed at 800°C for 30 min with the optimum oxygen flow rate of 0.1 sccm obtained previously. The ITO/glass substrates were cut into two 10mm by 10mm pieces to prevent the heat effect on glass, which could bend the substrates at a size of 10mm by 25mm. The cut pieces were placed in temperature windows of 700-740°C and 585-700°C. Figure 4-26 shows the SEM images of growth results on ITO/glass substrates with Au film thickness in the range of 5-15 nm within heating zone 700-740°C. It is concluded that growth on a substrate with 5nm of Au film (gold nanocluster diameters ~ 10-100 nm) leads to ITO NWs with a diameter of approximately 130nm to 1.3μm (Figure 4-26 a-b). Ten nanometers of gold film (gold nanocluster diameters ~ 30-250 nm) resulted in ITO NWs with a diameter range 360 nm-1 μm (Figure 4-26 c-d). Finally the diameters of ITO NWs grown on the substrate with 15nm Au film (nanoclusters size ~ 140-550 nm) were 400 nm-1.2 μm (Figure 4-26 e-f). The length of grown NWs were in the range 5-30μm, 5-30 μm and 1-10μm for the substrate with 5, 10, and 15 nm thick Au films. Table 4-4 summarizes the

thickness of Au films and the corresponding diameters and lengths of ITO NWs grown on ITO/glass substrates.

Table 4-4. Diameters and lengths of ITO NWs grown on ITO/glass substrate with different Au films thicknesses and within temperature zone 700-740°C.

Thickness of deposited Au films (nm)	Diameter of Au nanoclusters	Diameter of ITO NWs	Length of ITO NWs (μm)	Growth Mechanism
5	10-100nm	130 nm-1.3 μm	5-30	VLS
10	30-250 nm	360 nm-1 μm	5-30	VLS
15	140-550 nm	400 nm-1.2 μm	1-10	VLS

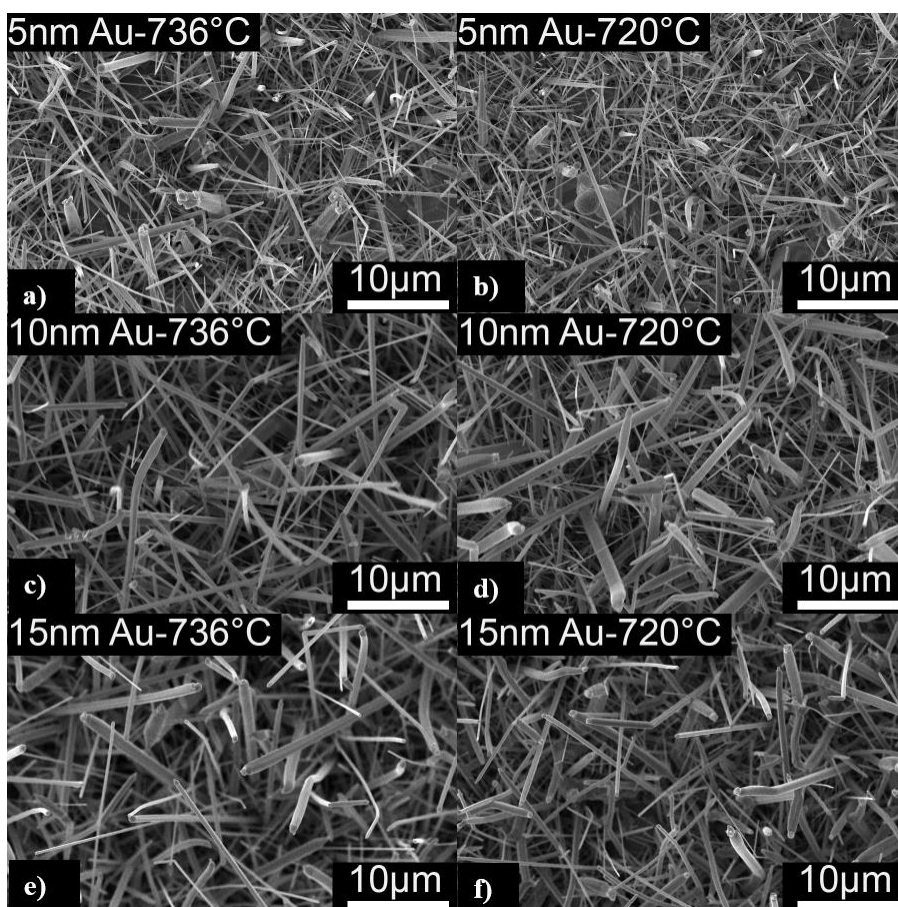


Figure 4-26. SEM images of ITO NWs grown on annealed ITO/glass substrates with Au films thickness of ; (a-b) 5 nm, (c-d) 10 nm, and (e-f) 15 nm; growth performed at 800°C for 30 min and substrates were place within temperature window of 700-740°C.

Acquired EDS spectrums from the tips of ITO NWs grown on ITO/glass substrate with different Au film thickness are shown in Figure 4-27 a-c. The appearance of a strong Au signal for all the conditions confirms VLS as the growth mechanism.

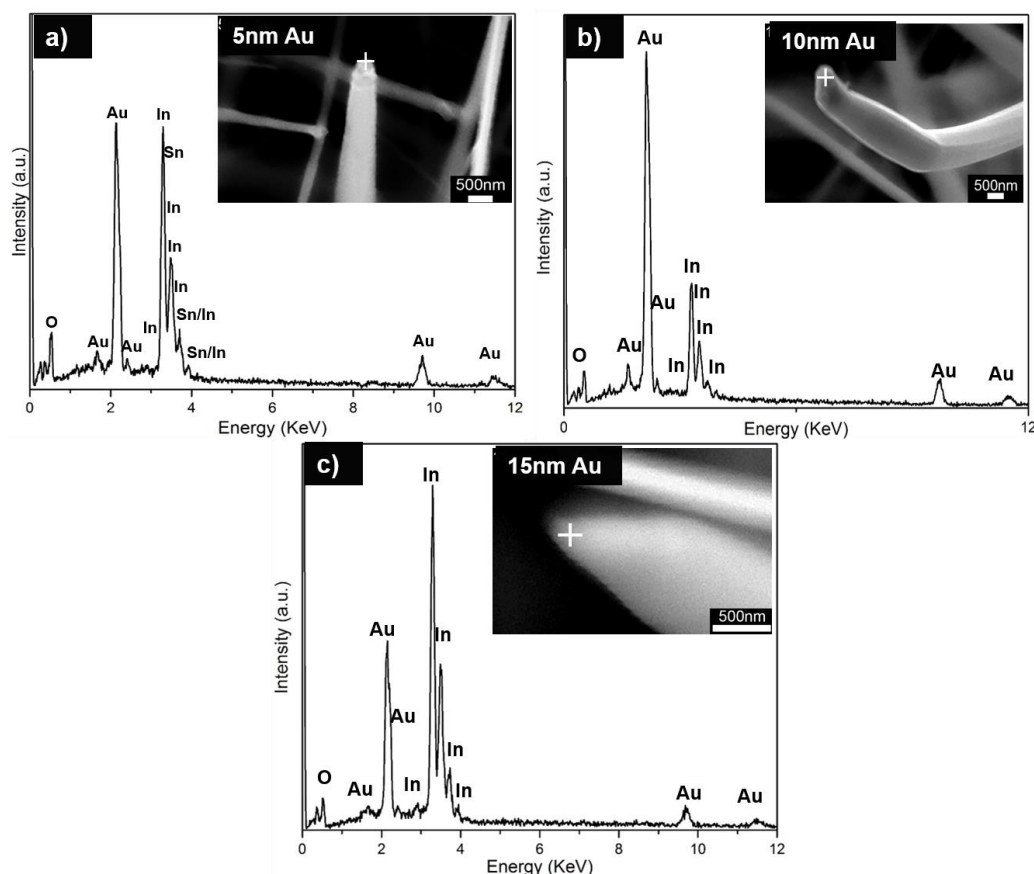


Figure 4-27. EDX spectra of ITO NWs grown on annealed ITO/glass substrates with Au films thicknesses of ; (a) 5 nm, (b) 10 nm, and (c) 15 nm; growth performed at 800°C for 30 min and substrates were place within temperature window of 700-740°C.

Figure 4-28 summarizes the distribution and uniformity of grown ITO NWs for temperature zone of 585-700°C. In general, growth uniformity, regardless of Au film thickness, substantially reduces.

For example, NWs with a width $> 5\mu\text{m}$ were observed on the substrate with 5 nm of Au film (Figure 4-28 a-b). Also, wide flat structures ($> 20\mu\text{m}$) were observed across the substrates which are not desired.

The sudden change in uniformity of growth might be attributed to temperature drop on the second half of the ITO/glass substrate. That is, as temperature reduces, critical nuclei size decreases exponentially to a power of $-1/KT$, which greatly increases the rate of nucleation. On the other hand, reduction in thermal energy reduces the diffusion rate, causing formation of thick and non-uniform growth [97].

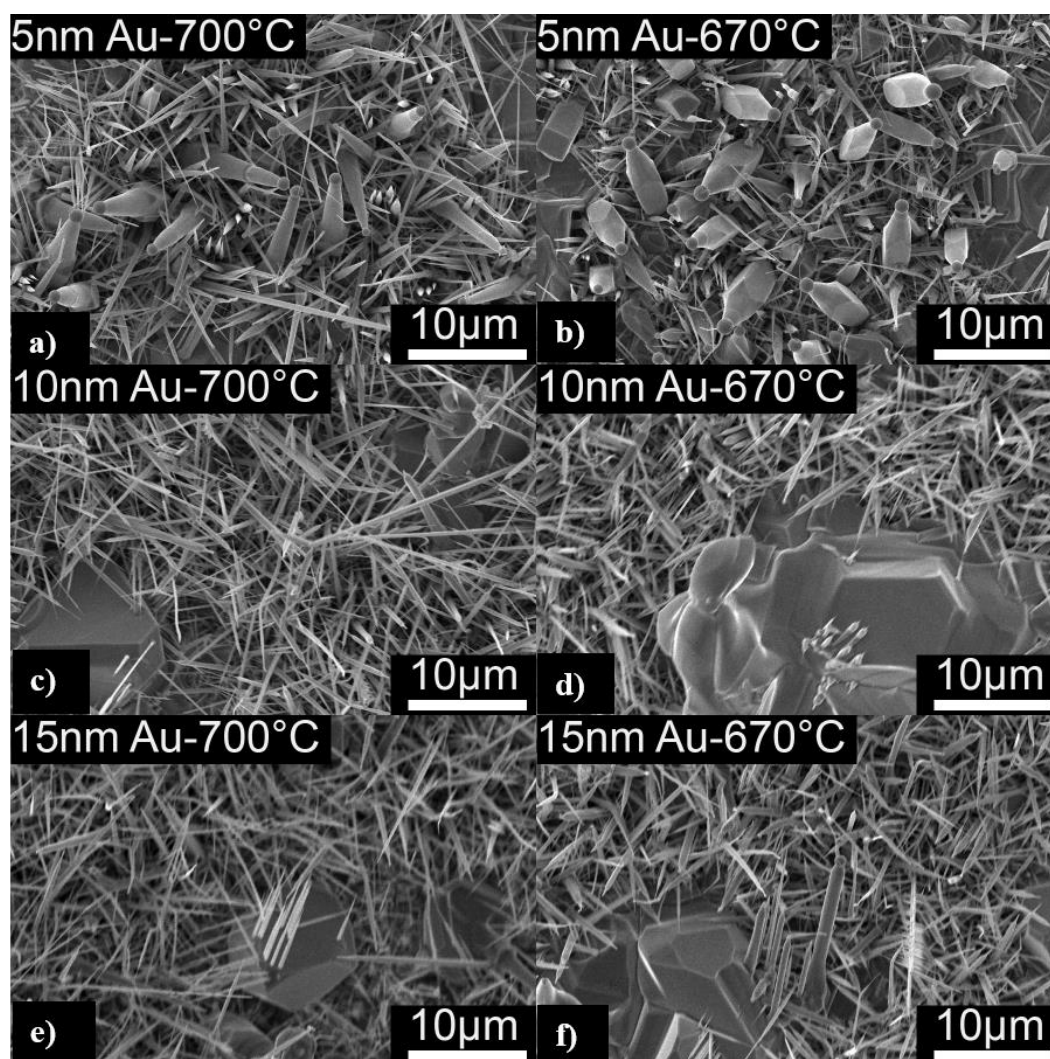


Figure 4-28. SEM images of ITO NWs grown on annealed ITO/glass substrates with Au films thicknesses of ; (a-b) 5 nm, (c-d) 10 nm, and (e-f) 15 nm; growth performed at 800°C for 30 min and substrates were place within temperature window of 585-700°C.

4.3.4.3 Effects of Carrier Gas Reduction on Growth of ITO NWs

By employing the obtained optimum parameters from earlier experiments, we studied the effects of change in the Ar flow rate on growth of ITO NWs. For this purpose, growth was performed on 20 mm by 25 mm ITO/glass substrates with 10 nm thick Au film, and under 0.1 sccm oxygen flow at 800°C for 30 minutes, using a thermal insulator at both ends of the reaction chamber. Introducing no (Figure 4-29 a) or a small (Figure 4-29 b) amount of Ar flow to the reaction chamber leads to the synthesis of ITO NWs with diameters as small as 150 nm (Figure 4-29 c) at a relatively low temperature of 585°C. The growth rate under 2 sccm of Ar flow led to longer NWs compared to zero argon condition.

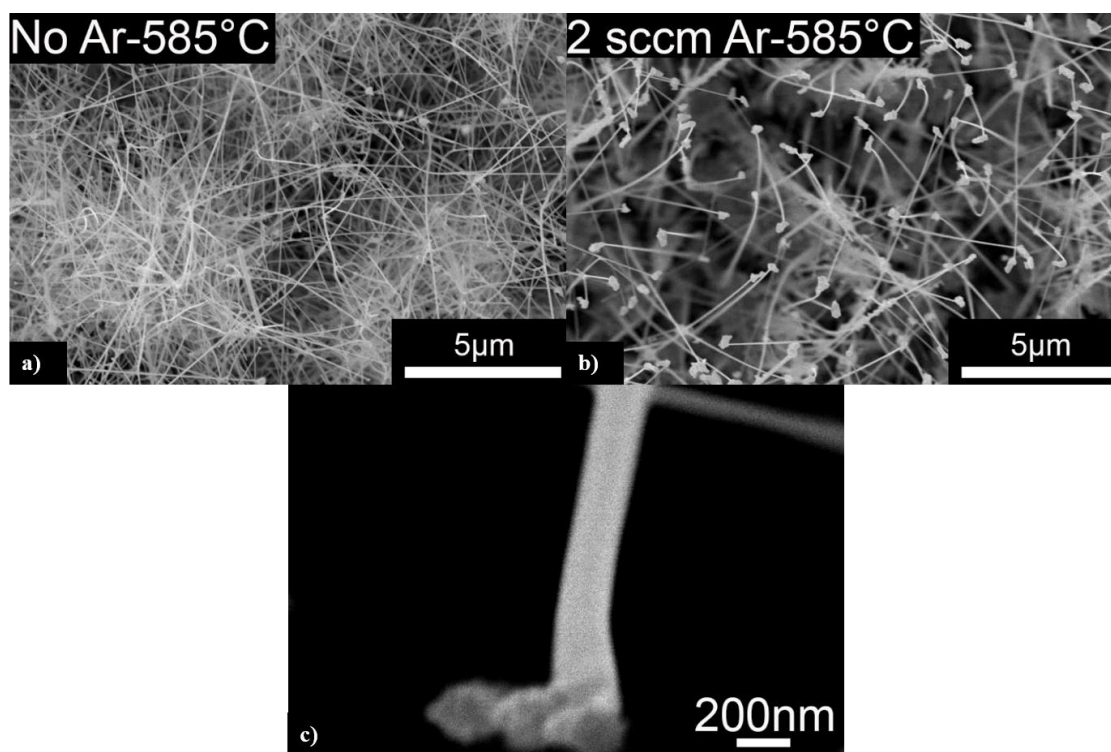


Figure 4-29. SEM images of growth performed using ; (a) zero; (b) 2 sccm argon flow; (c) resulting in formation of ITO NWs with diameter as small as 150 nm.

An X-ray diffraction (XRD) pattern was obtained to characterize the synthesized ITO NWs (Figure 4-30). The diffraction pattern is identified to be the In_2O_3 cubic bixbyite structure (JCPDS #17-2195). Although a small amount of precipitation of SnO_2 in In_2O_3 matrix (with rutile phase) was observed, the strong intensity of four major diffraction peaks corresponding to (222), (400), (440), and (622), compared to background, represents the high purity of synthesized ITO NWs. The precipitation of SnO_2 is related to the difference in Sn and In_2O_3 crystal structures, which hinder Sn doping into In_2O_3 . Besides the tetragonal structure of SnO_2 (less affinity when comparing to bixbyite In_2O_3), having high enthalpy ($60,980 \text{ J mol}^{-1}$) and entropy ($11.8 \text{ J mol}^{-1} \text{ K}^{-1}$), the 13.75 % difference in atomic radius between Sn^{+4} and In^{+3} makes the Sn doping process into In_2O_3 more complicated [103].

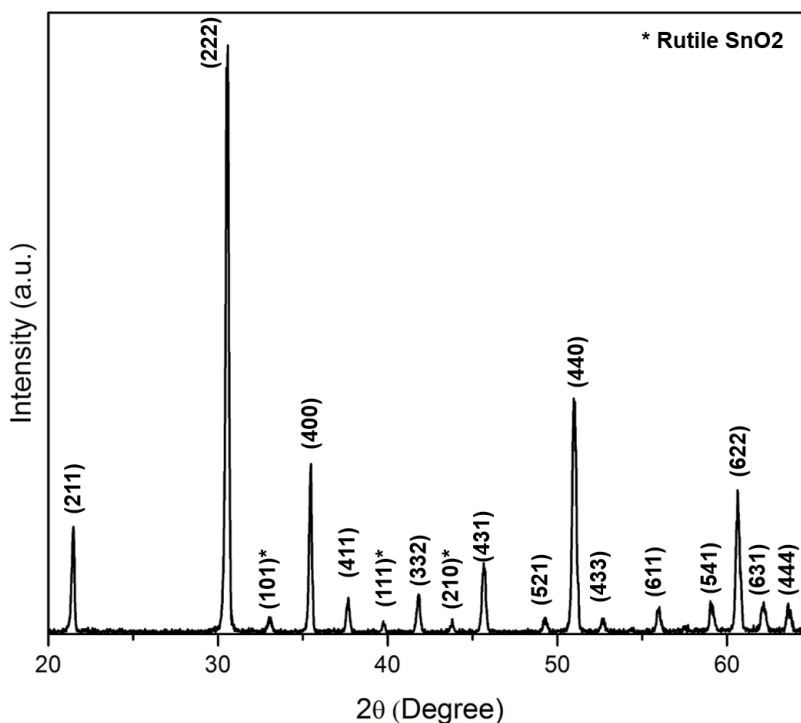


Figure 4-30. XRD patterns of synthesized ITO NWs grown on ITO/glass substrate.

4.3.5 One-dimensional Core-Shell Nanostructures of ITO-MoO₃

4.3.5.1 Morphology Study of Deposited Shell Layer

As-synthesized ITO NWs on ITO/glass substrate were employed to fabricate 1D core-shell nanostructures of ITO-MoO₃. The ITO/glass substrates were cut into two 10 mm by 10 mm pieces to prevent the heat effect on glass, which could bend the substrates at a size of 10 mm by 25 mm. The 15 nm thick Au film was sputtered on ultrasound cleaned (in accordance with Sec. 2.2.2) substrates. Thermal annealing was performed at 750°C for 1 hour. During annealing, substrates were placed at locations 5 inch and 5.5 inch inside the reaction chamber. For growth, about 0.5 grams of ITO powders were placed at the center of the quartz tube furnace. Thermal insulators were installed at both the upstream and the downstream ends of the reaction chambers. The already annealed substrates were placed in temperature windows of 710-750°C (6 inch point) and 650-710°C (6.5 inch point). The carrier gas (Ar) and reactant gas (O₂) were introduced to the reaction chamber at the rate of 20 sccm and 0.1 sccm, respectively. The growth source was evaporated at 800°C during 15 min of reaction time.

Deposition of a semiconductor shell layer of MoO₃ on as-synthesized ITO NWs was carried out by placing the ITO/glass substrates in the downstream heating zone with a temperature of 300-585°C (7 inch and 7.5 inch points). The carrier gas (Ar) and reactant gas (O₂) were introduced to the reaction chamber at the rate of 10 sccm and 2.5 sccm, respectively. One gram molybdenum powders were placed at the center of the reaction zone and growth was performed at 800°C for 15 min. Figure 4-31 (a and b) shows the SEM images of as-synthesized ITO NWs before deposition of a shell layer, 0 mm and 10 mm points corresponding to temperature zones 720-748°C, on 1st ITO/glass substrates. After

deposition of a shell layer, ITO NWs were covered with shell materials with a longitudinal structure (Figure 4-31 c and d), which was observed in the heating zone of 550-585°C.

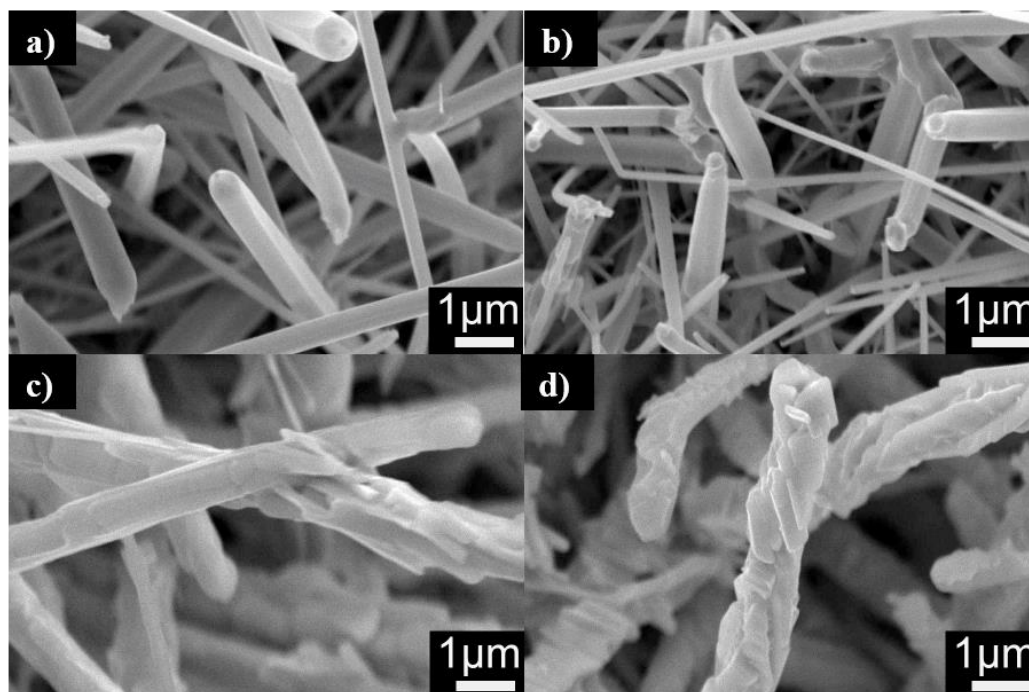


Figure 4-31. SEM images of (a & b) ITO NWs with no shell layer (c & d) 1D core-shell nanostructures of ITO-MoO₃ with longitudinal shell morphology.

EDX spectra from the synthesized ITO/MoO₃ core/shell nanostructures (Figure 4-32) shows strong molybdenum peaks revealing that the coating process is successfully completed and ITO NWs are fully covered with shell materials.

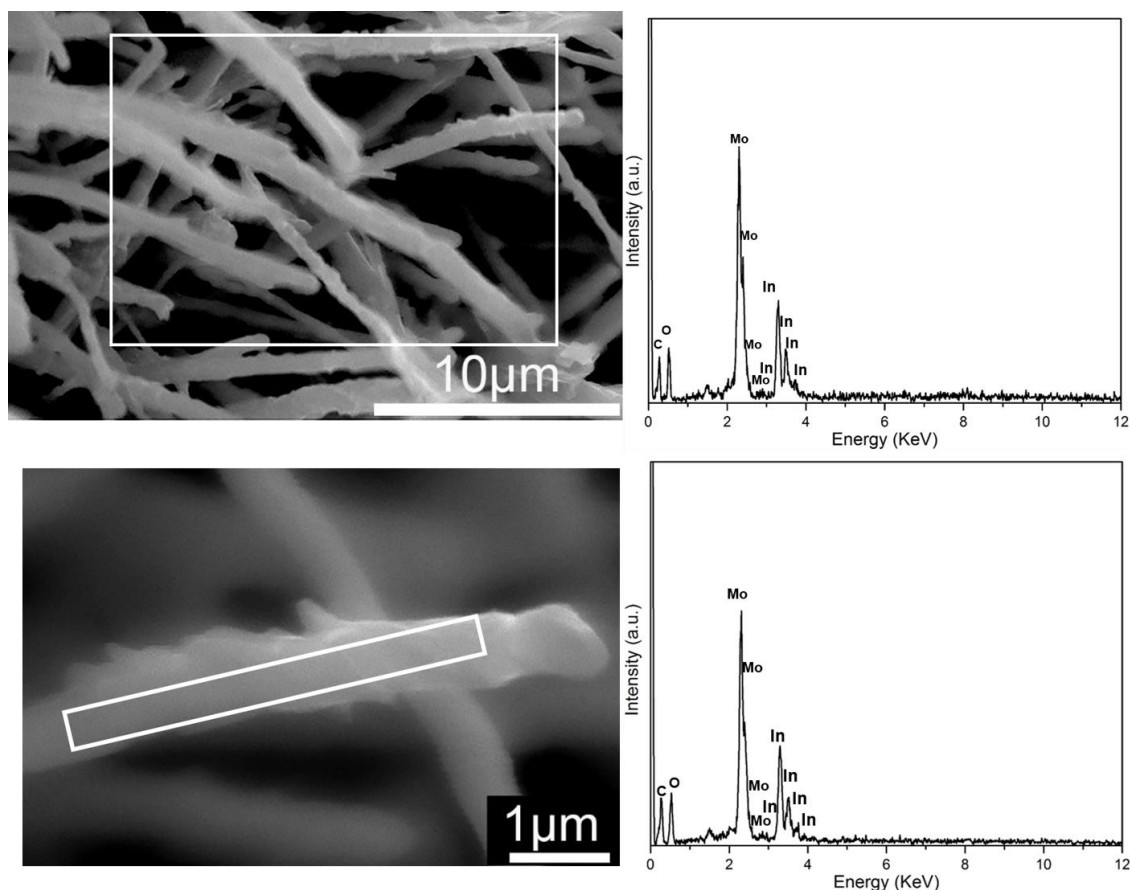


Figure 4-32. EDX spectra of 1D core-shell nanostructure of ITO-MoO₃ with a longitudinal type of shell

Figure 4-33 (a) represents the SEM image of as-synthesized ITO NWs on 2nd ITO/glass substrate corresponding to temperature zone 700°C before deposition of a shell layer. During deposition of the shell layer, the further reduction of temperature across the substrate (referring to 2nd ITO/glass substrate at 7.5 inch point, temperature zone 280-422°C) leads to the formation of shell layers with transverse morphologies (Figure 4-33 b), which is largely attributed to the acceleration in the condensation rate of vapor species. EDX spectra on the stem of covered NW shows a strong signal for Mo, indicating the NW is fully covered with deposited shell material. Also, it can be seen that an indium signal, compared with the In signal from longitudinal shell layer, is very weak. This is mostly due to deposition of thick layers of shell materials on the core structure.

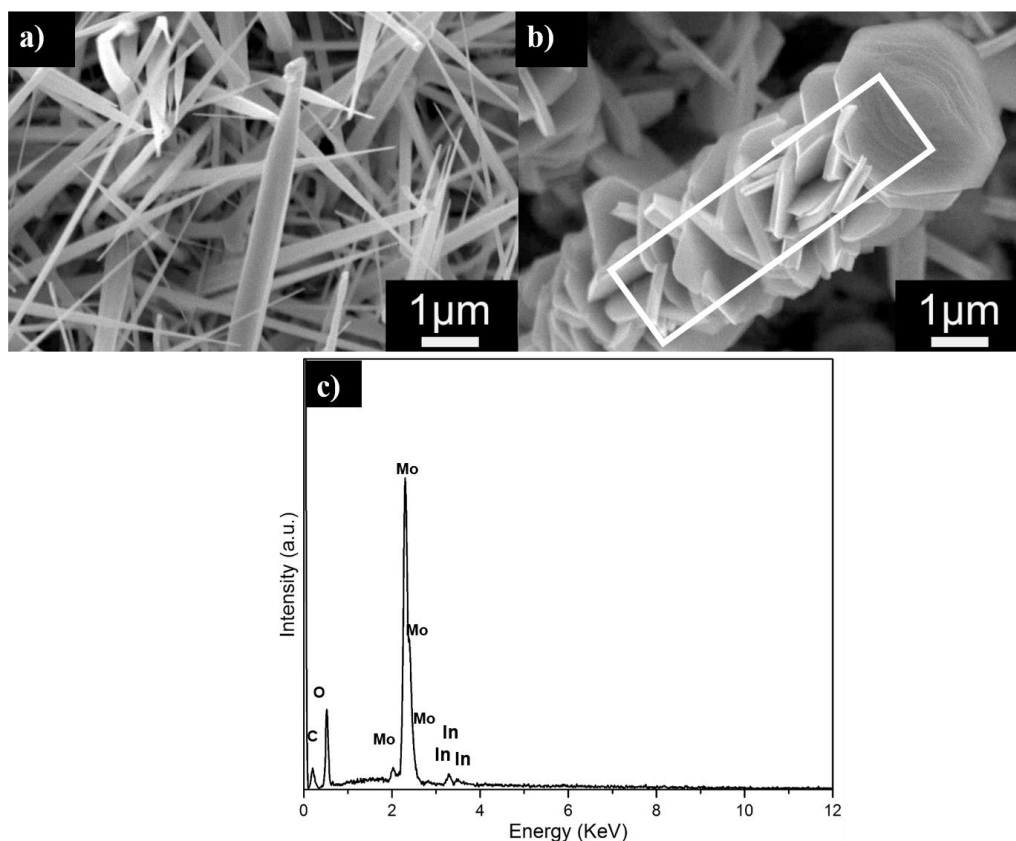


Figure 4-33. SEM images of (a) ITO NWs with no shell layer (b) 1D core-shell nanostructures of ITO-MoO₃ with transverse shell morphology (c) EDX spectra on stem of 1D core-shell structure of ITO-MoO₃ with transverse shell morphology.

In another attempt to deposit shell layer of MoO₃ on as-synthesized ITO NWs, ITO NWs were synthesized similar to previous growth conditions while 10 nm thick Au film sputtered on ultrasound cleaned (in accordance with Sec. 2.2.2) substrates and no thermal annealing was performed prior to growth. Also the reaction time increased to 30 min with no thermal insulators at both ends of the reaction chambers. Figure 4-34 (a) indicates the SEM image of as-synthesized ITO NWs on 1st ITO/glass substrate, corresponding to temperature zone 700°C. The shell layer with thin longitudinal structure was deposited on ITO NWs at temperature zone 422-585°C, when reactant gas (O₂) flow rate was reduced to a 1 sccm (Figure 4-34b). The intensity of the Mo signal on 1st substrate is significantly

lower compared to previously synthesized shell morphologies (longitudinal and transverse) which can be attributed to the reduction of oxygen flow.

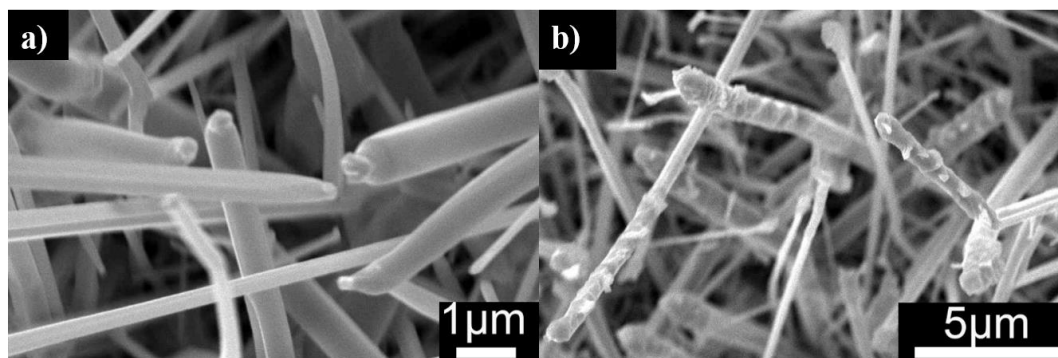


Figure 4-34. SEM images of (a) ITO NWs with no shell layer (temperature zone 700°C), (b) 1D core-shell nanostructures of ITO-MoO₃ with longitudinal shell morphology (temperature zone 450°C)

Figure 4-35 (a) indicates the SEM image of as-synthesized ITO NWs on 2nd ITO/glass substrate, corresponding to temperature zone 670°C. The shell layer with transverse needle structure was deposited on ITO NWs at temperature zone 280-422°C, when reactant gas (O₂) flow rate was reduced to a 1 sccm (Figure 4-35b). The reduction of reactant gas reduces the oxidation/evaporation rate of reactant materials, leading to less deposition on ITO NWs. The EDX spectra (Figure 4-35 c) reveals a strong signal for indium, indicating the thin layer of deposited shell material. The intensity of the Mo signal on 2nd substrate is minimal compared to previously synthesized shell morphologies (longitudinal and transverse) and the 1st substrate. That is, the surfaces of NWs are not fully coated by shell materials.

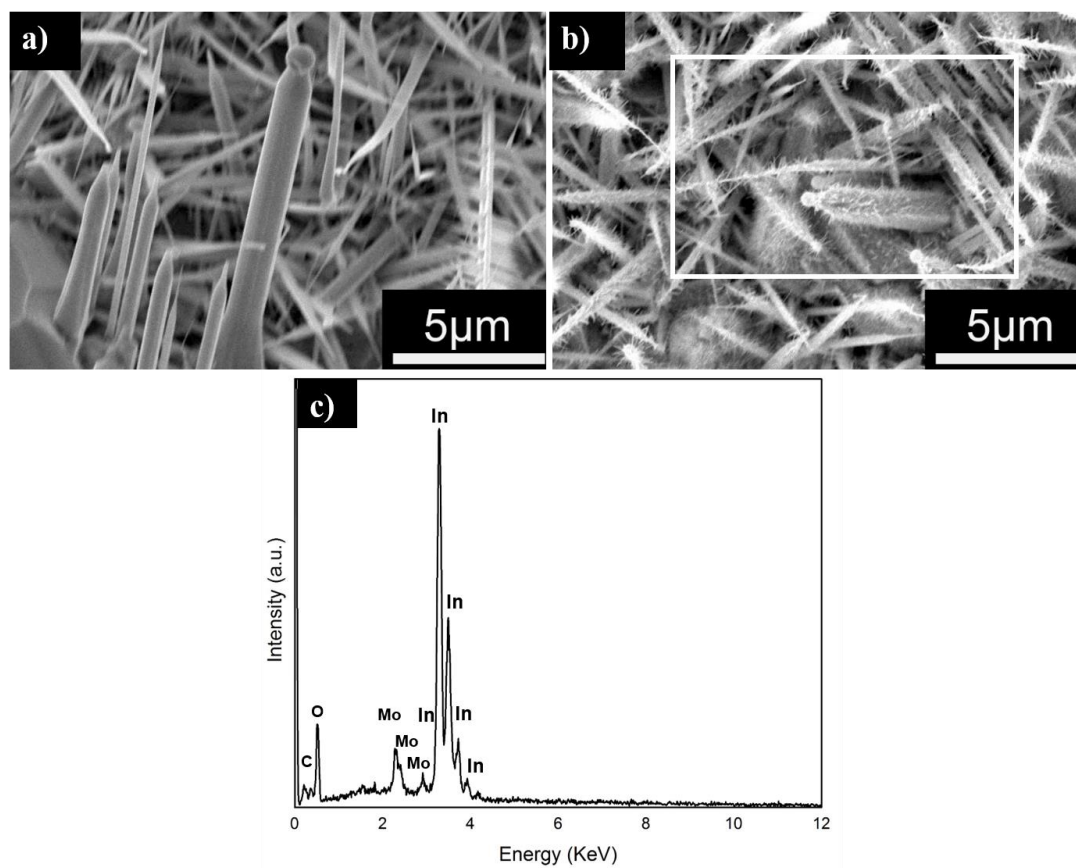


Figure 4-35. SEM images of (a) ITO NWs with no shell layer (b) 1D core-shell nanostructures of ITO-MoO₃ with needle shape shell morphology (c) EDX spectra on stem of 1D core-shell structure of ITO-MoO₃ with needle shaped shell morphology.

A final attempt was performed to deposit shell layer MoO₃ on none vertical ITO NWs as core. First the ITO/glass substrate was cut into two 10 mm by 10 mm piece. The 10 nm thick Au film was sputtered on ultrasound cleaned (in accordance with Sec. 2.2.2) substrates. The ITO/glass substrate was placed at locations 0.5 inch (upstream, temperature zone 550-650°C) inside the reaction chamber. About 0.7 grams of ITO powders were placed at the center of the quartz tube furnace. Thermal insulators were also installed at both the upstream and the downstream ends of the reaction chambers. The carrier gas (Ar) and reactant gas (O₂) were introduced to the reaction chamber at the rate of 2 sccm and 0.2 sccm, respectively. Growth was performed at 800°C for 30 min. As-synthesized ITO NWs are shown in Figure 4-36 a.

Deposition of a semiconductor shell layer of MoO_3 on as-synthesized ITO NWs was carried out by placing the ITO/glass substrate in the downstream heating zone with a temperature of $450\text{--}585^\circ\text{C}$ (7 inch points). The reactant gas (O_2) was introduced to the reaction chamber at the rate of 2 sccm with no carrier gas. One gram molybdenum powders were placed at the center of the reaction zone and growth was performed at 800°C for 30 min. A thin, continuous, and uniform coverage of shell materials deposited on ITO NWs (Figure 4-36 b). Both Mo and In shows comparable EDX signal intensity, which could be attributed to the optimum thickness of the deposited shell layer (Figure 4-36 c).

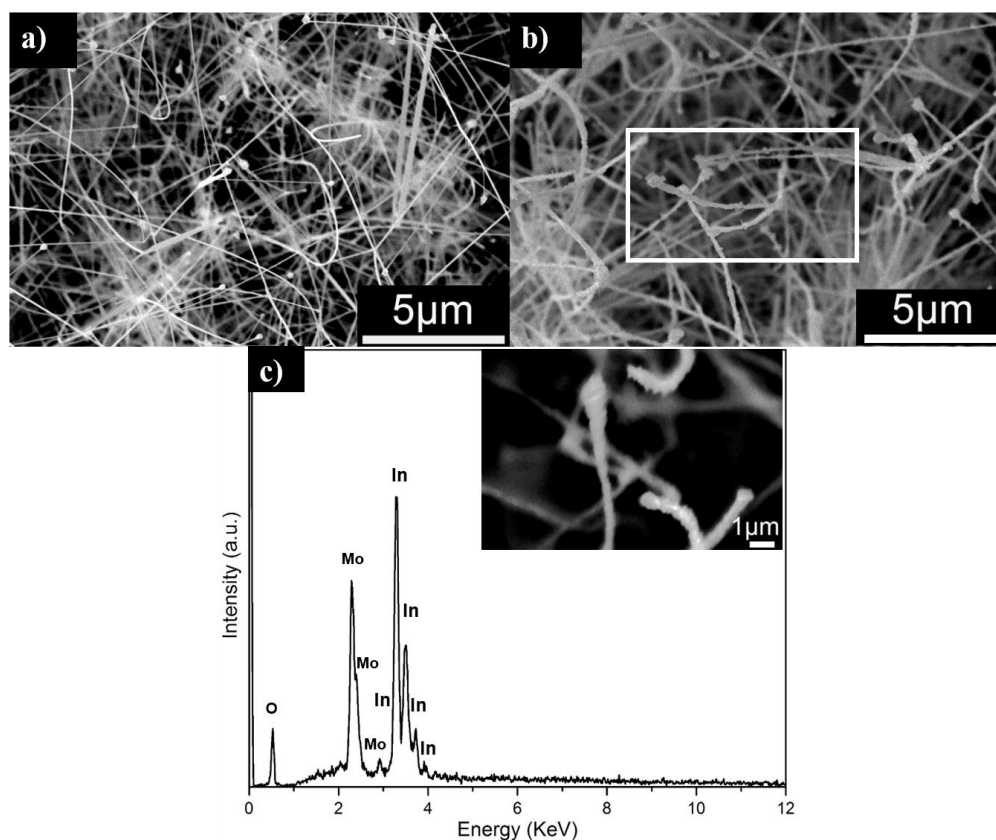


Figure 4-36. SEM images of (a) ITO NWs with no shell layer (b) 1D core-shell nanostructures of ITO- MoO_3 with ultrathin longitudinal shell morphology (c) EDX spectra on stem of 1D core-shell structure of ITO- MoO_3 with ultrathin longitudinal shell morphology.

CHAPTER 5. LOW-TEMPERATURE PHOTOCATALYTIC PROTONATION OF MoO_3 NANOFLOAKES WITH ALCOHOL: MECHANISM AND OPTICAL PROPERTY STUDY

5.1 Introduction

Recently, an efficient way to enhance the photocatalytic efficiency in semiconductors has been developed. Metal nanoparticles are attached to semiconductor nanostructures to employ plasmon resonances in photocatalysis [104]. Plasmon resonances are the collective oscillation of free carriers in response to the electromagnetic field of light irradiation. When the plasmon resonances are confined to the surface of metallic nanoparticles, they are called localized surface plasmon resonances (LSPRs) [105-107]. With the LSPRs excited at resonance frequency, metal nanoparticles can dramatically enhance the light absorption, light scattering, and charge separation and transfer in the semiconductors. The exact mechanism of the LSPR enhancement is still not clear. Several modes have been proposed including: (1) direct electron transfer of hot electrons from metal to the semiconductor, (2) local electromagnetic field enhancement of the carrier generation in the semiconductor, and (3) resonant energy transfer from the LSPR dipole to the electron-hole pair in the semiconductor [108]. Although it is still under investigation that under what conditions which process would dominate the enhancement through LSPR, these multiple processes provide a broad range of opportunities for the enhancement of semiconductor photocatalysis using plasmonic nanoparticles.

Intensive studies of LSPRs have been focused on noble metals, such as Au and Ag, because of their excellent chemical stability and strong light absorption in the visible region. The resonance frequency is also tunable by adjusting the size and shape of the nanoparticles [105, 107]. However, due to their high carrier density, the resonant

absorption of these metal nanoparticles only cover a narrow region in the visible range, and hence the major portion of the solar spectrum can't be fully utilized [105]. Recently, research results have demonstrated strong LSPRs in non-metal materials, i.e., heavily doped semiconductors (e.g., metal chalcogenides and metal oxides) [105-107, 109]. With their tunable carrier density by adjusting doping or stoichiometry, the resulting resonance absorption can be expanded to cover visible, near-infrared (NIR), and mid-infrared regions. Therefore, this approach opens up new opportunities for the plasmonic enhancement in solar energy utilization [109]. While most studies have been conducted on widely used conducting oxides such as indium tin oxide and aluminum-doped zinc oxide with plasmon resonances at near-infrared region,[110, 111] we will focus on transition metal oxide (TMOs, e.g., molybdenum oxide) for their visible range plasmon resonances [107, 112, 113]. The TMOs have unique properties in metal-insulator transition, high-temperature superconductivity, fast ionic transport, and colossal magnetoresistance resulting from their outer-d valence electrons [107]. They are widely employed in applications in microelectronics, quantum computing, spintronics, and energy conversion and storage [107]. With anisotropic structures and wide range of substoichiometric compositions, the LSPRs in TMO nanostructures can be finely tailored by controls in dimension and composition.

Molybdenum oxides have multiple varieties of compositions and crystalline structures, including molybdenum trioxide (MoO_3) and different substoichiometric forms, such as Mo_4O_{11} , Mo_5O_{14} , Mo_8O_{23} , and Mo_9O_{26} , etc. [114]. The most common phase of MoO_3 is $\alpha\text{-MoO}_3$ having an orthorhombic structure with strong ionic and covalent bonding within the (010) layers but weak van der Waals interactions between the (010) layers [83].

Computational calculations show the α -MoO₃ (010) surface has the lowest surface energy of 0.19-0.31 J/m², while the (100) surface has a surface energy of 0.7 J/m² [114]. No surface energy value was reported for (001) surface, but it is expected to be slightly higher than the one for (100) surface according to the crystal structure. This highly anisotropic structure makes α -MoO₃ a natural two-dimension (2D) layered material. Therefore, it is easy to form 2D nanostructures of MoO₃ with a (010) basal plane by dry[115] or wet[116] exfoliations or by direct growth using chemical vapor deposition (CVD) [83]. Here, we report the formation of MoO₃ nanoflakes using a facile liquid exfoliation of the CVD grown MoO₃ whiskers. A low-temperature protonation reaction of 2D MoO₃ nanoflakes with pure alcohol under visible light irradiation was discovered. Comprehensive materials structure characterization, optical property measurement and analysis, and photothermal study were performed to reveal and understand its reaction mechanism.

5.2 Experimental Section

5.2.1 Synthesis of MoO₃ Whisker

The synthesis of MoO₃ whiskers was performed using a home-built hot-wall CVD system based on resistance heating, which has been employed previously for the growth of other nanostructures [83, 87, 117, 118]. About 2 g of Mo powders were loaded in a quartz boat, which was placed at the center of the reaction chamber. The reaction chamber was first sealed and pumped down to ~ 20 mTorr, and then brought up to the atmosphere pressure by purging UHP (ultra-high purity) Ar. Constant flows of 10 sccm (standard cubic centimeter per minute) UHP Ar as the carrier gas and 10 sccm UHP O₂ as the reactant gas were then supplied during the synthesis. The heating temperature at the center of the reaction chamber was ramped up to 800 °C in 30 min and maintained for 120 min, followed

by a natural cooling down to room temperature. A large amount of light yellow crystals of MoO_3 whiskers was collected downstream in a temperature zone of $\sim 770^\circ\text{C} - 700^\circ\text{C}$.

5.2.2 Exfoliation

Liquid phase exfoliation method was employed to produce 2D MoO_3 nanoflakes from as-synthesized whiskers. Anhydrous isopropyl alcohol (IPA, Millipore Sigma) with extremely low H_2O content (< 50 ppm) was used as the exfoliation solvent. Pure IPA solvent and IPA- H_2O mixtures were used in the exfoliation of MoO_3 whiskers. For each exfoliation, ~ 200 mg of as-synthesized whiskers were weighted and dispersed into 20 mL solvent solution in a glass vial (VWR TraceClean 20 mL, clear). The exfoliation was carried out using an ultrasonic cleaner (Branson 1510R-MTH, Branson Ultrasonics) for 120 min. The suspension was then transferred into a polypropylene conical centrifuge tube (Falcon 50mL, Corning) and centrifuged at 6000 rpm for 30 min using a centrifuge (Hermle Labmet Z326, HERMLE Labortechnik GmbH). After the centrifuge, the top clear supernatant with MoO_3 nanoflakes was collected and divided into five glass vials (VWR screw thread vial with cap, 2 dram (8 mL)) with ~ 4 mL suspension in each vial. The steps of the material processing procedure are demonstrated in Figure 5-1.

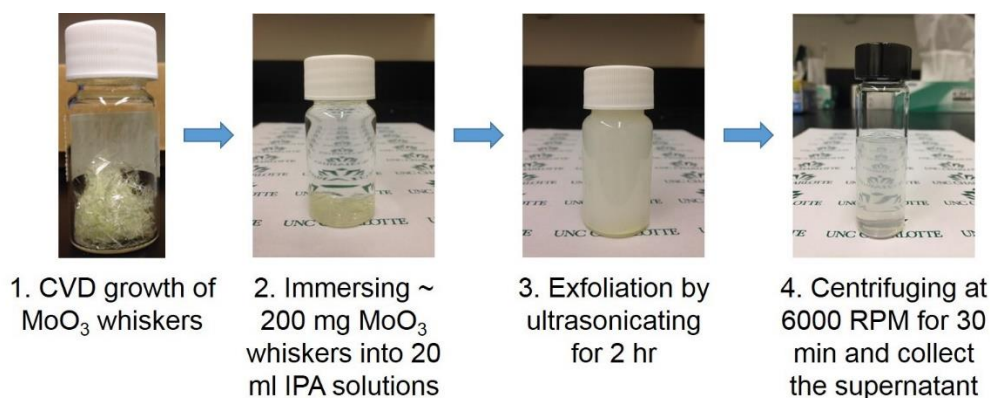


Figure 5-1. Demonstration of the steps of the liquid exfoliation process changing the CVD grown MoO_3 whiskers into MoO_3 nanoflakes suspended in IPA solutions.

For the structure characterization study, pure IPA, 70 vol% IPA-H₂O, and 50 vol% IPA-H₂O solutions, were used in exfoliation to show the effects of solution concentration on the resulting nanoflakes. In the photocatalytic experiments, study was focused to compare the performances between the MoO₃ nanoflakes produced from the 100% pure IPA and the 50 vol% IPA-H₂O solutions.

5.2.3 Light irradiation and UV-vis-NIR spectrometry

Photocatalytic experiments were realized by visible light irradiation of the exfoliated MoO₃ samples in their original exfoliation solutions. Therefore, the samples are dubbed as MoO₃-100IPA and MoO₃-50IPA thereafter in the text. An Hg-Xe lamp (operated at ~ 540W, i.e., with power supply at 30V and 18 A) with a dichroic cold beam turning mirror (Oriel 66219, 420 to 630 nm, Newport) was employed to produce light in the visible range (Figure 5-2).

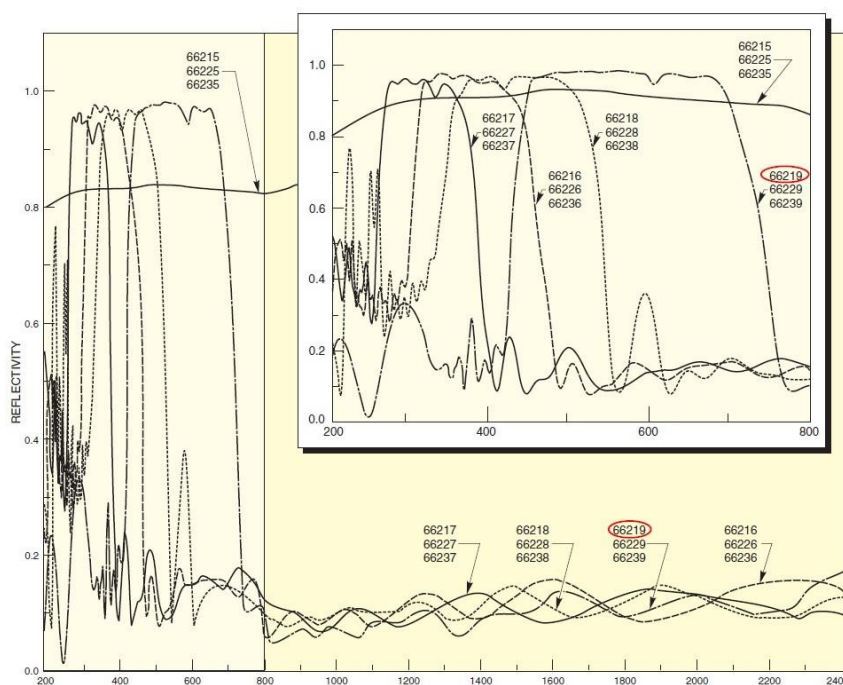


Figure 5-2. Reflectivity spectrum of the dichroic cold beam turning mirrors. Model 66219 was used to reflect the light in the visible range. Adapted from Newport product information brochure [119].

The light irradiation was performed at different time intervals from 1.5 min up to 3 h. UV-vis-NIR spectrometry (ultraviolet-visible-near infrared, Shimadzu UV-2600) covering 200-1400 nm was employed to study the change in absorbance measurement for the irradiated samples with different exposure durations. The suspension temperature during the irradiation was detected with a thermocouple probe (Omega, KTIN-116E-12). The temperature profiles were recorded first manually from the temperature reading of a temperature/process controller (Omega, CN8200-DC1-FH2), and later automatically using a temperature input device (National Instruments, USB-TC01).

5.3 Results and Discussion

5.3.1 Morphology and Structure Characterization

Figure 5-3 shows the as-synthesized MoO_3 depositions from the CVD growth. They are ribbon-like thin whiskers with widths of a few millimeters, thicknesses from tens to a few hundred microns, and lengths up to ~ 20 mm. The whisker length was only limited by the inner dimension of the reaction chamber. The MoO_3 whiskers have a light yellow color (Figure 5-3a) with shiny surfaces. Due to their thin thickness and large aspect ratio, the whiskers are extremely flexible and can be easily bended into a ball (Figure 5-3b) without breaking. Scanning electron microscopic (SEM) image (Figure 5-3c) demonstrates the whiskers are long crystals with smooth surfaces throughout the length indicating the layered structure of MoO_3 .

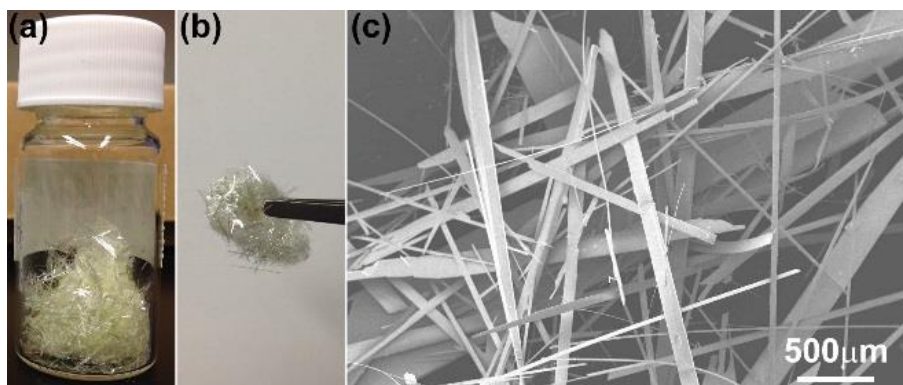


Figure 5-3. (a-b) Photos of (a) the as-synthesized MoO_3 whiskers and (b) the whiskers twisted and rolled into a ball and (c) SEM image of the whiskers.

After the liquid exfoliation in different IPA solutions, the large whiskers were exfoliated into small 2D nanoflakes suspended in the solutions. Structure characterization was performed using transmission electron microscopy (TEM). With a constant exfoliation time of 120 min, the concentration effect of the IPA solutions on the dimension of the resulting nanoflakes is obviously shown in Figure 5-4a-c. The resulting nanoflakes are rectangle-shaped with different sizes from the exfoliation solutions with different concentrations. For the 100% IPA solution, nanoflakes are tiny with edge lengths about tens nanometers to ~ 100 nm. As the solution concentration reduces to 70 vol%, the nanoflakes becomes longer with lengths about hundreds nanometers. With the 50 vol% solution, the nanoflake lengths are about a few microns. On the other hand, the width of the nanoflakes increases slightly from tens nanometers to hundreds nanometers with the decrease of the solution concentration. The effect of the exfoliation solution concentration on the dimension of the exfoliated nanoflakes can be explained by the change of the surface tension of the solutions. Study reported the exfoliation efficiency of 2D materials is highly dependent on the surface tension of the cosolvent solution and it can be finely tuned by adjusting the solution concentration [116]. Estimated from the reported data,[116, 120] the

surface tension of our exfoliation solutions changes from $\sim 21.22 \text{ mJ/m}^2$ for 100 % IPA, to $\sim 23.11 \text{ mJ/m}^2$ for 70% IPA-H₂O, and to $\sim 24.87 \text{ mJ/m}^2$ for 50% IPA-H₂O solutions, respectively. The exfoliation efficiency of MoO₃ in IPA solutions was reported to reach to its maximum when the solution surface tension was around 25-33 mJ/m^2 . During the exfoliation, the liquid-solid interaction helps to overcome the inter-layer van der Waals bonding to separate the thick whiskers into thin layers. However, as a brittle ceramic material, intra-layer cracking of MoO₃ whiskers occurs concurrently with the inter-layer separation under the ultrasonication. Therefore, with the low surface tension of the 100% IPA solution, the exfoliation efficiency is low so that the nanoflakes break into very short pieces during the slow exfoliation process. As the surface tension increases with the reduction of the IPA concentration, the enhanced exfoliation efficiency provides a faster exfoliation process producing larger nanoflakes with fewer fractures along the length.

The crystalline structure of the exfoliated MoO₃ nanoflakes was confirmed and investigated by the high-resolution TEM (HRTEM) imaging and the selected area electron diffraction (SAED). The crystal structure is found to be close to the orthorhombic α -MoO₃ phase (ICDD PDF # 04-012-8070, $a = 3.9616 \text{ \AA}$, $b = 13.8560 \text{ \AA}$, and $c = 3.6978 \text{ \AA}$). The HRTEM image (Figure 5-4d) and the corresponding SAED pattern in [010] axis (inset of Figure 5-4d) show the nanoflake has a (010) basal plane surface and two orthogonal edges along [100] and [001] respectively. The measured atomic separations are 0.4095 nm along [100] and 0.3657 nm along [001] directions, which coincide closely with the standard lattice parameters a and c from database (PDF # 04-012-8070). Use the standard data as a reference, this exfoliated nanoflake has planar lattice strains of $\varepsilon_a = 3.37\%$ and $\varepsilon_c = -1.10\%$.

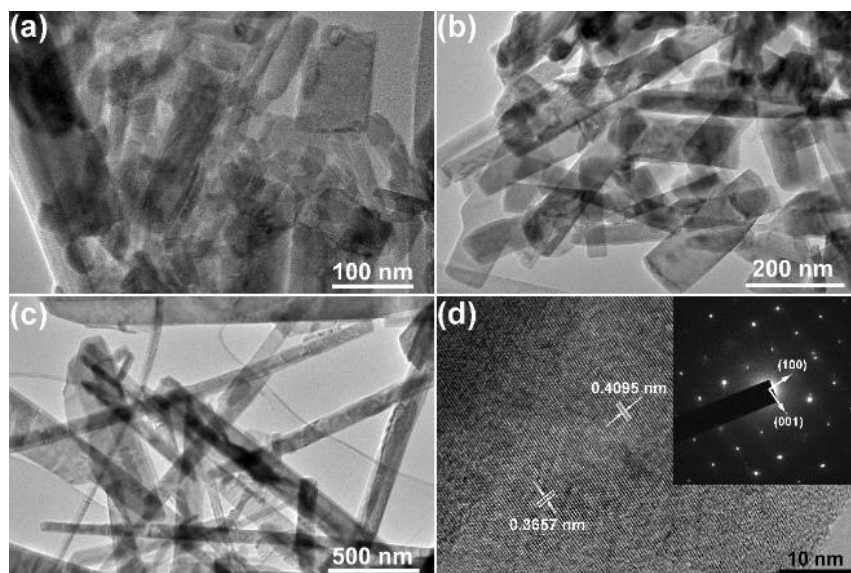


Figure 5-4. (a-c) Low magnification TEM images of the MoO₃ nanoflakes from liquid exfoliation in different IPA solutions: (a) 100% IPA, (b) 70 vol% IPA-H₂O, and (c) 50 vol% IPA-H₂O. (d) HRTEM image of a MoO₃ nanoflake and a SAED pattern (inset) showing its crystalline structure.

5.3.2 Optical Property Measurement

5.3.2.1 Photocatalytic Experiments and Optical Absorption Measurements

The photocatalytic performance and optical properties of the exfoliated MoO₃ nanoflakes in the original exfoliation solutions were studied under visible light irradiation for a variety of durations followed with the UV-vis-NIR absorption measurement. Experiments were compared between the MoO₃-50IPA (Figure 5-6a) and MoO₃-100IPA (Figure 5-6b) samples. First, both samples show a strong absorption peak at the UV region before the photocatalytic reaction (i.e. baselines in Figure 5-6a and Figure 5-6b) indicating their wide bandgaps. It is worth mentioning that after the reaction extremely large absorption spikes appeared randomly at the UV absorption peak ranges for both samples. These UV absorption spikes can be explained by the aggregation of the nanoflakes from controlled experiments as shown in Figure 5-5. The reacted suspension was set in dark for 2h and most of the spikes disappeared or diminished. The thin layer of sediment found at

the bottom of the vial indicates the settlement of the aggregated catalysts. The sediment was remixed with the solution by stirring and light ultrasonication and these spikes reappeared. These controlled experiments clearly show the reacted MoO_3 nanoflakes aggregated together forming large particles with a size comparable to the wavelength scale at UV range (i.e., several hundred nanometers). These aggregated particles suspended in the solution strongly scatter the UV light causing strong absorption spikes and the randomness of the spikes is due to their Brownian motions in the solution.

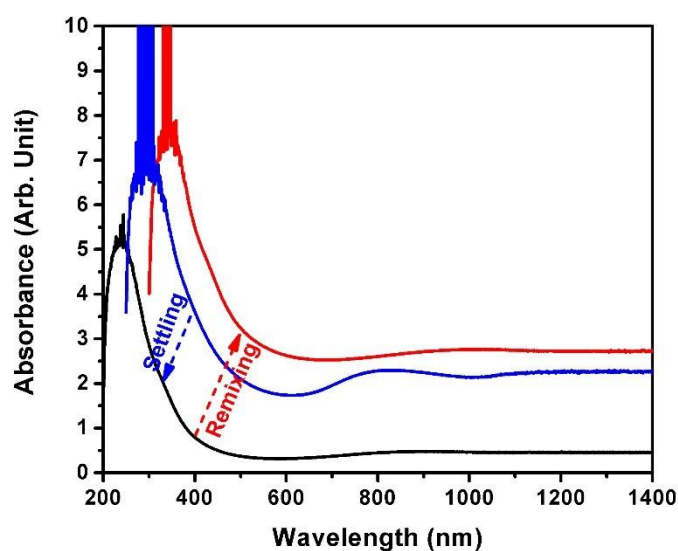
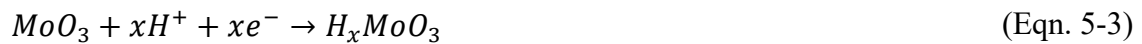


Figure 5-5. UV-vis-NIR absorbance measurement demonstrating the effects of catalysts settling and remixing in the solution: (blue) right after photocatalytic reaction, the spectrum shows many large spikes at the UV region; (black) after settling in dark for 2h, most of the spikes disappear or diminish due to the settlement of the aggregated catalysts; and (red) the spikes reappear after the sediment was remixed with the solution by stirring and light ultrasonication. The spectra are plotted with a diagonally shift for a clear view.

Furthermore, Figure 5-6a shows the MoO_3 -50IPA sample changes its color swiftly from clear transparent (baseline before the light exposure) to bright blue, dark blue, and bluish black in 1.5 min, 2.5 min and 2 h, respectively. From the corresponding UV-vis-NIR spectra, the color change of the suspension is due to the appearance of the strong optical absorption band in the visible range. The spectra also show a strong NIR absorption

band after light irradiation. The intensities of the visible and NIR absorption bands both increase quickly with the increase of the light exposure duration. This result is similar to the previous report and the appearance of the absorption band can be attributed to the formation of the quasi-metallic phases and their plasmon resonances [112, 121]. During the light irradiation, the MoO_3 nanoflakes can react with the protons from H_2O forming H_xMoO_3 bronzes, which will subsequently dissociate into $\text{MoO}_{3-x/2}$ with continuous light irradiation. Both the H_xMoO_3 bronzes and $\text{MoO}_{3-x/2}$ sub-stoichiometric oxides are quasi-metallic giving rise to the strong plasmonic absorption bands in the visible and NIR regions. The reaction steps can be formulated as follows:



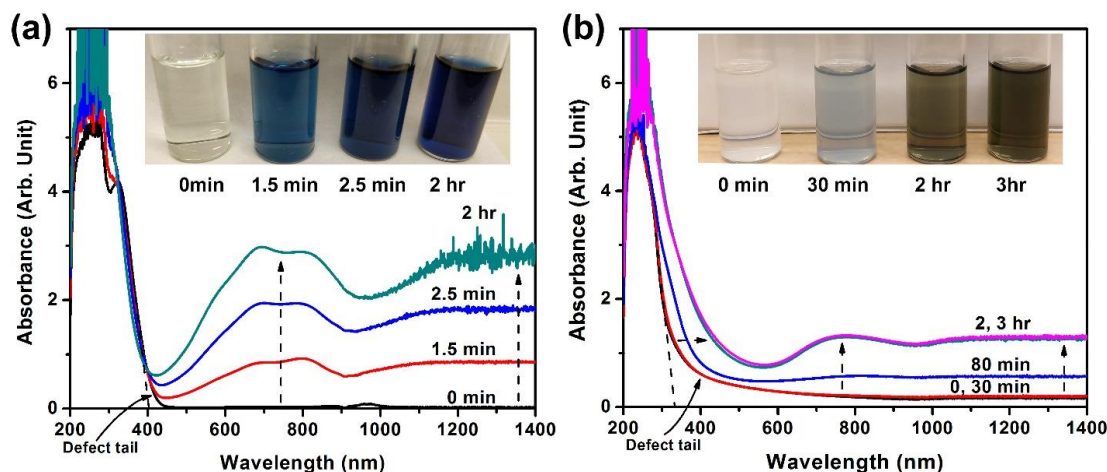


Figure 5-6. UV-vis-NIR absorbance measurement of (a) MoO₃-50IPA and (b) MoO₃-100IPA suspensions with different durations of visible light irradiation. Insets are corresponding optical photos of MoO₃ nanoflake suspensions showing color changes before and after different light exposure durations.

The more interesting observation is the color change of the MoO₃-100IPA sample under the visible light irradiation. As shown in Figure 5-6b, the suspension changes its color slowly from clear transparent to light blue, brown, and dark brown in 30 min, 2 h and 3 h, respectively. The UV-Vis-NIR spectra also show the appearance of two absorption bands in the visible and NIR regions. The absorption band ranges are similar to these of the MoO₃-50IPA sample, but their intensities increase slowly with the irradiation time showing a slower reaction rate than the one for the MoO₃-50IPA sample. However, it is well known that at low temperature the protons for the protonation of MoO₃ are solely from H₂O rather than from IPA [112]. Alcohol based solvents (e.g., methanol, ethanol, and IPA, etc.) are not able to produce protons unless they are heated to 200 °C or higher [122]. Therefore, our results indicate a significant phenomenon of low temperature protonation of MoO₃ nanoflakes with pure alcohol. It is of essential importance to explore the mechanism of this low-temperature photocatalytic protonation reaction. Hence, we characterized the band structure, defect status, and plasmonic properties of the MoO₃

nanoflakes, studied their evolutions during the photocatalytic protonation reaction, and performed thermal analysis during the reaction to unveil the reaction mechanism.

5.3.2.2 Band Structure and Bandgap Analysis

In Figure 5-6, the absorption spectra of the exfoliated MoO₃ nanoflakes show strong bandgap absorption in the UV region and clear sub-bandgap defect tails. MoO₃ is an n-type semiconductor material, while its reported band structure types and bandgap values are still debatable in the literature. Many claimed a direct allowed band transition for MoO₃ with a wide range of bandgap values. From absorption measurement on thin crystals with micron thickness, Deb derived polarization dependent bandgaps of 2.80 eV ($E_{0\perp c}$) and 2.96 eV ($E_{0\parallel c}$) related to the bound excited states based on optical absorption measurement, while photoconductivity measurement indicated a large bandgap of 3.56 eV [123]. However, Itoh et al. reported a larger bandgap of 4.1 eV for similar MoO₃ thin crystals supported by the calculated value of 3.87 eV from their DV X α calculation [124]. Other direct bandgap values have been published for MoO₃ samples with different dimension and crystallinity, such as 3.16 eV/3.27 for amorphous/crystalline thin films,[125] and 3.04 and 3.01 eV for nanobelts[126, 127]. On the other hand, some reported an indirect allowed band transition for MoO₃ with bandgap values of 3.04 eV for thin films,[128] 3.05 eV for lamellas,[129] and 2.76 eV for nanobelts confirmed by the calculated value of 2.59 eV from density functional theory calculation [130]. The discrepancies in reports reflect the nature of the complicated band structure dependence of MoO₃ on its crystallinity, stoichiometry, dimension, defect status, and measurement method. For the exfoliated MoO₃ nanoflakes in this report, absorption spectra were analyzed to estimate the optical bandgap before and after the light irradiation (Figure 5-7). The data were fitted using Tauc plot, [131, 132]

$(\alpha h\nu)^{\frac{1}{n}} \sim h\nu$, where α is the absorption coefficient, $h\nu$ is the photon energy, and n takes $\frac{1}{2}$ for direct allowed transition or 2 for indirect allowed transition. We find the direct band structure fits well for our MoO_3 nanoflake samples as shown in Figure 5-7 with $n = \frac{1}{2}$ and the analyzed results are listed in Table 5-1. It should be noted that Tauc plot fitting is not a determinate method to verify the type of a band structure, as the optical absorption measurement is sensitive to the crystalline quality, composition, various defects, dimension, doping level, and other factors. Tauc plot fitting can only be used as an extrapolation method to estimate the value of an optical bandgap based on the assumption of the transition type [133].

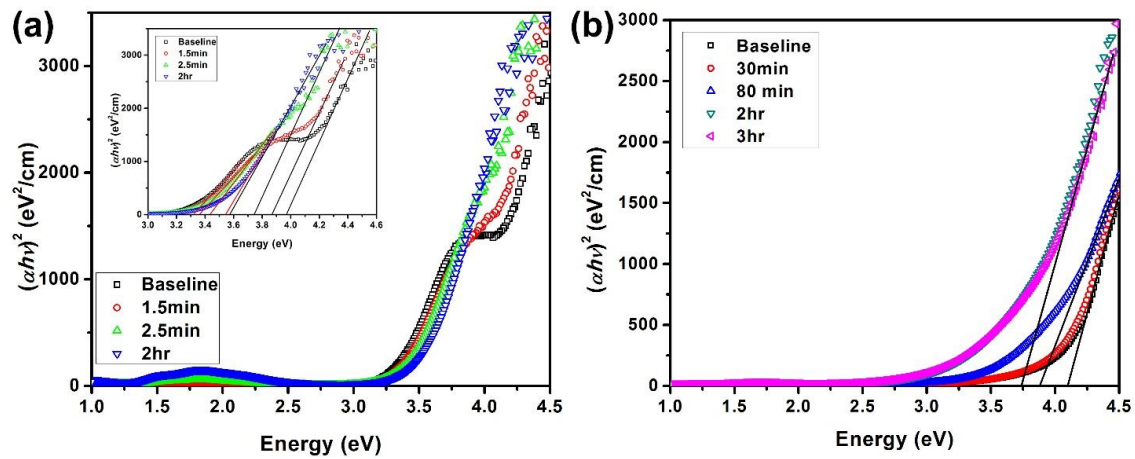


Figure 5-7. Direct bandgap fittings of (a) MoO_3 -50IPA and (b) MoO_3 -100IPA suspensions at different durations of visible light irradiation. Inset in (a) shows the fitting of exciton edges and bandgaps.

Table 5-1. List of Bandgap and exciton edge values at different irradiation durations from the direct bandgap fittings.

MoO ₃ -50IPA			MoO ₃ -100IPA	
Reaction time	Exciton edge (eV)	Bandgap (eV)	Reaction Time	Bandgap (eV)
Baseline	3.32	3.97	Baseline	4.10
1.5 min	3.36	3.87	80 min	3.88
2.5 min	3.43	3.75	3 h	3.73
2 h	3.55	3.57		

Figure 5-8 and Table 5-2 show the results from indirect Tauc plot fittings, providing much smaller bandgap values compared to these from direct bandgap fittings. Although a linear fitting region can always be found for the assumption of indirect transition, considering the onset of the band absorption and the range of sub-bandgap defect tail, a direct band structure is more reasonable for the MoO₃ samples in this report.

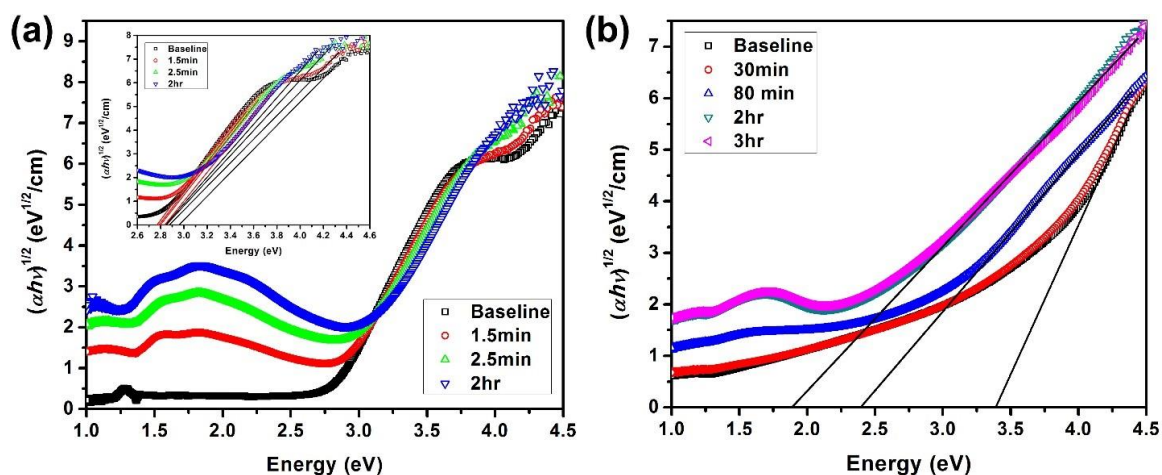


Figure 5-8. Indirect bandgap fittings of (a) MoO₃-50% IPA and (b) MoO₃-100% IPA solutions at different durations of visible light irradiation. Inset in (a) shows the fitting of exciton edges and bandgaps.

Table 5-2. List of Bandgap and exciton edge values at different irradiation durations from the indirect bandgap fittings.

MoO ₃ -50IPA			MoO ₃ -100IPA	
Reaction time	Exciton edge (eV)	Bandgap (eV)	Reaction Time	Bandgap (eV)
Baseline	2.77	2.96	Baseline	3.39
1.5 min	2.78	2.88	80 min	2.39
2.5 min	2.80	2.85	3 h	1.89
2 h	2.83	2.85		

For the MoO₃-50IPA samples, an exciton-like absorption peak is found at the onset edge of the bandgap absorption peak (Figure 5-6a and Figure 5-7a). Little literature has reported about the exciton structure of MoO₃. Deb assumed the low absorption edge was dominated by bound excited states, but didn't observe any isolated exciton absorption peak [123]. Itoh et al. attributed a small hump at around 4.05 eV as the exciton peak, with a exciton binding energy of 50 meV estimated with the bandgap of 4.10 eV [124]. The exciton absorption peak for the sample here is at around 3.84 eV (i.e., ~ 323 nm), similar to the 3.98 eV exciton peak assigned to the exfoliated MoO₃ nanosheets in a recent report [134]. The direct bandgap for the exfoliated sample before the irradiation is about 3.97 eV, resulting in a large exciton binding energy around 130 meV. With the increase of light irradiation duration up to 2 h, the bandgap has a redshift from 3.97 eV to 3.87 eV, 3.75 eV, and to 3.57 eV. The exciton peak changes slightly with its edge shifts from 3.32 eV, to 3.36 eV, 3.43 eV and to 3.55 eV. Therefore, the exciton peak of the MoO₃ nanoflakes gradually merges with the fundamental absorption peak and eventually disappears with the increase of the photocatalytic protonation reaction. The redshift of the bandgap can be explained by the increase of oxygen vacancies during the formation of H_xMoO₃ bronze and the

subsequent $\text{MoO}_{3-x/2}$ sub-stoichiometric oxide. During the reaction, Mo^{6+} is reduced to be Mo^{5+} or Mo^{4+} injecting e^- into the conduction band. The charge injection will subsequently introduce gap states in between the valence and the conduction bands narrowing the bandgap [135]. On the other hand, the blueshift and the disappearance of the exciton peak are related to two possible reasons. The first one is the change of the sub-bandgap defect tail due to the increase of oxygen vacancies accompanied with more lattice distortions. The development of the defect tail could cause exciton smearing [136]. The second one is the increase of the free carrier concentration as demonstrated by the appearance and the increase of plasmonic absorption bands. When the free carrier concentration becomes high enough, it will reduce the excitons by shielding the electron-hole interaction [137]. The properties of the defect tail and the plasmonic absorption bands will be discussed later in the text.

On the other hand, the MoO_3 -100IPA sample shows no isolated exciton peak at the edge of the bandgap absorption. The absence of the exciton peak can be attributed to its high concentration of defects, which distort the regular MoO_3 lattice. The high defect concentration is confirmed clearly by the more significant sub-bandgap defect tail (Figure 5-6b) as compared to the one for the MoO_3 -50IPA sample. For the as-exfoliated MoO_3 -100IPA sample, its strong defect tail originates from the UV region and covers over the whole visible light region (i.e., $\sim 300 \text{ nm} - 900 \text{ nm}$). The reason that the MoO_3 -100IPA sample has much higher defect concentration than the MoO_3 -50IPA sample can be explained by their dimension differences resulting from the exfoliation. As mentioned previously, the MoO_3 -100IPA nanoflakes are tiny pieces with lengths only up to $\sim 100 \text{ nm}$ much shorter than the micron-sized lengths for the MoO_3 -50IPA nanoflakes. Therefore,

the dangling bonds and vacant atoms at the edges become more significant and introduce more defect states into the materials. The exfoliation could also introduce many intra-layer cracks inside nanoflakes that induce residue stress in the lattice. From the bandgap fitting, the MoO₃-100IPA sample always has a larger bandgap than the MoO₃-50IPA sample. This blueshift of the bandgap can also be explained by their dimension-related structure differences. Liu et al. reported large bandgap shifts of MoO₃ crystals with the reduction of thickness. When thickness $t < 10$ nm, the bandgap has a significant blueshift, which can be attributed to the anisotropic in-plane strain relaxations and redistributions introduced during the thinning process using exfoliation accompanied with the formation of microcracks [138]. Our TEM analyses do show large anisotropic lattice strain of the exfoliated nanoflakes. Therefore, the blueshift of the MoO₃-100IPA sample with respect to the MoO₃-50IPA sample could indicate its higher degree of in-plane strain due to the more crack formations in the smaller nanoflakes. In future study, an in-depth analysis of the relationship between the strain status and the band structure of MoO₃ nanoflakes is required to reveal the detailed mechanism, which will be greatly useful to the bandgap tuning in 2D nanomaterials by strain engineering.

5.3.2.3 Urbach Defect Tail

We already mentioned the low energy defect tails (Figure 5-6) located at the edge of the fundamental band absorption for the exfoliated MoO₃ nanoflakes in different IPA solutions. These tails follow Urbach rule that the absorbance increases exponentially with the increase of the photon energy [123, 139]. The Urbach defect tail is a universal phenomenon for a variety of materials originating from different types of crystalline lattice disordering, such as structure disordering (vacancies, dislocations, stoichiometry, doping,

hydrogenation, etc.), temperature disordering (lattice thermal vibrations), and compositional disordering (atomic substitution in mixed crystals) [136]. For the exfoliated MoO₃ nanoflakes, oxygen vacancies and the resulting lattice distortion are the main causes contributing to the defect tails. The Urbach defect tail smears the features (e.g., exciton peaks and bandgap edge) at the edge of the bandgap absorption, and the behavior of the absorption coefficient can be described as [136]:

$$\begin{aligned} \alpha(E) &= \alpha_0 \exp \left[\frac{\beta}{KT} (E - E_0) \right] = & \text{(Eqn. 5-5)} \\ &\alpha_0 \exp \left[\frac{(E - E_0)}{E_U} \right] \\ &\alpha_0 \exp \left(\frac{-E_0}{E_U} \right) \exp \left(\frac{E}{E_U} \right) = \\ &\alpha'_0 \exp \left(\frac{E}{E_U} \right) \end{aligned}$$

where E is the photon energy, k is the Boltzmann constant, T is the temperature, β and $E_U = \frac{KT}{\beta}$ are the steepness parameter and the Urbach energy characterizing the energy width of the tail respectively, α_0 and E_0 are constants characteristic of the material, and $\alpha'_0 = \alpha_0 \exp \left(\frac{-E_0}{E_U} \right)$. In a $\ln \alpha$ - E plot, a Urbach tail appears as a linear plot with a slope of $1/E_u$ and an intercept of $\ln \alpha'_0$. It is worth mentioning that α_0 and E_0 are two bundled parameters and they can only be derived using multiple measurements at different temperatures for the same sample as all the linear extrapolations could converge at the same coordinates of $\ln \alpha_0$ and E_0 [136]. Our MoO₃-IPA samples were measured at room temperature. Figure 5-9 shows the Urbach tail fittings with the resulting β and E_u values listed in Table 5-3.

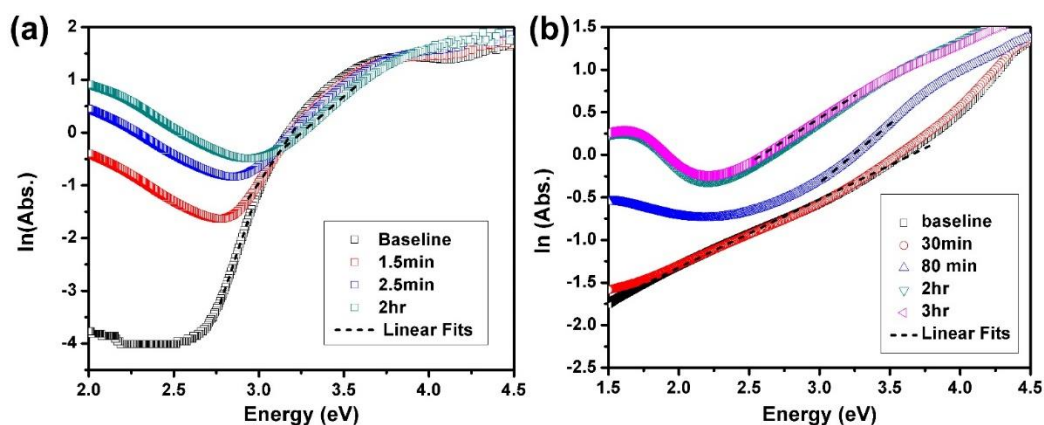


Figure 5-9. Urbach defect tail fitting for (a) MoO₃-50IPA and (b) MoO₃-100IPA samples.

The as-exfoliated MoO₃-50IPA has a steepness parameter β of 0.247 (corresponding to a tail Urbach energy E_u of 0.104 eV), similar to the values of 0.21 ($E_{0\perp c}$)/0.24 ($E_{0\parallel c}$) from Deb's measurement on MoO₃ crystals. With the light irradiation, the β value decreases and the corresponding E_u value increases with the photocatalytic reaction time, indicating the extension of the defect tails to a wider range. The tail extension can be explained by the increase of the degree of structure disordering due to the increase of oxygen vacancies during the formation of H_xMoO₃ and MoO_{3-x/2}. On the other hand, the defect tail of the as-exfoliated MoO₃-100IPA has a very broad range, as indicated by its small β of 2.06×10^{-2} and large E_u of 1.25 eV (one order different from those of the MoO₃-50IPA). This large defect tail range reflects its high degree of lattice disordering resulting from the exfoliation process, consistent with its rich defects at edges and intra-layer cracks and highly strained crystal lattice. With the photocatalytic reaction, the tail range for MoO₃-100IPA sample decreases a little as shown by the smaller E_u values. This seemingly unexpected change is due to that the effect of vacancy concentration increase during the reaction is overwhelmed by both the shift of bandgap and the appearance of the plasmonic absorption peak at the visible region. As demonstrated in Figure 5-6, the original defect

tail of the as-exfoliated MoO₃-100IPA sample covers the UV and visible regions. During the reaction, the UV end of the defect tail shifts to longer wavelength due to the redshift of the bandgap absorption, while the visible end is dominated by the plasmonic absorption peak. These changes narrow down the range of the defect tail despite of the increase of defect concentration with the reaction.

The data fitting of the Urbach defect tails can also provide information about the bandgap. A simplified model uses an approximation of $E_g \approx E_0$ [140]. Therefore, when $E = E_g$ for Eq. (5), $\ln \alpha = \ln \alpha_0$ and its value can be estimated from the plot at the edge of the bandgap absorption. However, without a sharp absorption edge for the bandgap transition, it is hard to accurately find the E_g and $\ln \alpha_0$ values. Here, we propose a method with the assumptions that at the vicinity of the bandgap edge, defect tail dominates the optical absorption below the bandgap and band transition occurs when $E \geq E_g$. Therefore, the E_g can be identified as the transition point on the plot where $\ln \alpha - E$ deviates from the linear relationship with the increase of photon energy E . In our study, the bandgaps for the MoO₃-50IPA samples are estimated to be 3.04 eV (baseline), 3.24 eV (1.5 min), and 3.59 eV (2 h) using this method. These values are close to the data from the Tauc plot fittings (Table 5-1). However, the trend of the bandgap shift with the irradiation duration is opposite to the bandgap shift from Tauc plot, but it is same to the shift of the exciton edge. This discrepancy is attributed to the presence of the exciton peak at the edge of the bandgap absorption making the estimation of E_g affected more by the exciton edge rather than the true bandgap edge. For the MoO₃-100IPA samples, the bandgaps are estimated to be 3.77 eV (baseline), 3.68 eV (80 min), and 3.37 eV (3 h). The shift has the same trend of redshift as the results from the Tauc plot fitting. This data analysis demonstrates the Urbach tail

fitting could provide an alternative method for the bandgap estimation. However, since the defect tails greatly smear the edge of the bandgap absorption together with other absorption background (such as the exciton and plasmonic peaks), it is hard to locate the accurate transition point between the defect tail and the edge of the bandgap absorption for the bandgap calculation. Therefore, this method only gives a rough bandgap estimation and it is more accurate for materials with a relatively sharp absorption edge for bandgap transition where the transition from the defect tail to the bandgap absorption is well defined.

Table 5-3. Results from Urbach defect tail fitting.

MoO ₃ -50IPA				MoO ₃ -100IPA			
Reaction time	β	E_U (eV)	E_g (eV)	Reaction Time	β	E_U (eV)	E_g (eV)
Baseline	2.47×10^{-1}	0.104	3.04	Baseline	2.06×10^{-2}	1.25	3.77
1.5 min	1.25×10^{-1}	0.206	3.24	80 min	3.56×10^{-2}	0.722	3.68
2 hr	7.10×10^{-2}	0.362	3.59	3 hr	2.72×10^{-2}	0.946	3.37

5.3.2.4 Visible and NIR plasmonic absorption peaks

As shown in Figure 5-6, after the photocatalytic reactions induced by the light irradiation, additional absorptions appear for both MoO₃ samples spanning visible and NIR light regions and their intensities increase with the irradiation duration. The absorptions have two absorption bands centered at visible and NIR regions respectively. For the MoO₃-50IPA sample, one absorption peak ranges from 450 nm to 900 nm covering the visible light region and the edge of the NIR region and another broad absorption plateau is from 900 nm to 1400 nm covering the NIR region. For the MoO₃-100IPA, the two bands are from 600 nm to 950 and from 950 nm to 1400 nm, respectively. The presence of these absorption bands is contributed to the increase of free charge carrier concentration

produced by photo-induced H^+ intercalation process. During the reaction, the photogenerated H^+ ions intercalate into the interlayer spacing of the MoO_3 crystal and bind to edge-shared and terminal oxygen atoms forming OH_2 groups. The resulting H_xMoO_3 bronze are not stable and will subsequently dissociate into substoichiometric $MoO_{3-x/2}$ oxide. The formation of H_xMoO_3 and $MoO_{3-x/2}$ reduces Mo^{6+} into Mo^{5+} (and possibly Mo^{4+}), which increases oxygen vacancies and injects e^- into the conduction band forming free charge carriers. Therefore, the visible and NIR absorption bands are plasmon resonance absorptions originating from the quasi-metallic behavior of the H_xMoO_3 and $MoO_{3-x/2}$ [121]. Similar plasmon absorption bands have been reported with MoO_3 materials. Alsaif et al. reported exfoliation solvent dependence of plasmon resonances in 2D substoichiometric molybdenum oxide nanoflakes. In the whole absorption range of 450 nm – 1500 nm, there are a low intensity visible absorption peak centered around 630-690 nm and a high intensity NIR absorption peak centered about 900-1000 nm. According to Alsaif et al., the visible peak is associated to the plasmon resonance along the thickness and the NIR peak is the plasmon resonance along the lateral dimension axis considering the aspect-ratio-dependence of the plasmon resonance of 2D materials [121]. However, Sian et al. reported on thin film sample with one visible absorption peak at about 1.75 eV (i.e., 708 nm) assigned to the charge transfer from Mo^{5+} to Mo^{6+} and one NIR peak at about 1.25 eV (i.e., 992 nm) assigned to the charge transfer from Mo^{4+} to Mo^{5+} . The different conclusions from different reports indicate the complexity of the plasmon resonance in MoO_3 samples, as it is sensitive to the free carrier density determined by the stoichiometry, layer thickness, lateral size, aspect ratio,[135] defect aggregation,[123, 125] and the possibility of coupling with polarons [128].

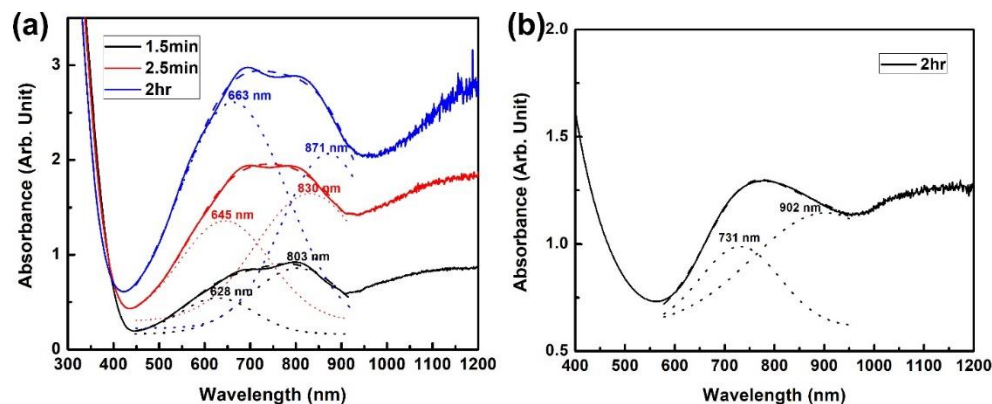


Figure 5-10. Peak fittings for the absorption bands of (a) MoO₃-50IPA sample with irradiation durations of 1.5 min, 2.5 min, and 2hr; and (b) MoO₃-100IPA sample with irradiation duration of 2hr.

According to the Mie-Gans theory, the plasmon resonance frequency is

$$\omega_p = \sqrt{\frac{Ne^2}{\epsilon_0 m_e}} \quad (\text{Eqn. 5-6})$$

where N is the free charge carrier density, e is the electron charge, ϵ_0 is the vacuum permittivity, and m_e is the effective electron mass [107, 112]. In our study (Figure 5-6 and Figure 5-10), the visible and NIR absorption bands are separated far apart by a deep valley, which might be attributed to the non-uniformity of the sample composition from the photocatalytic reaction. As there are multiple phases of MoO_{3-x/2} with quasi-metallic properties,[121] our nanoflake samples may have two groups of components with a large difference in composition. The one with larger x values has more reduced Mo ions yields larger free carrier densities and higher plasmon frequencies, while another (low x values) provides smaller free carrier densities and hence lower plasmon frequencies. The visible absorption peak also shows features of multiple peaks and the data fitting is shown in Figure 5-10. Two visible peaks are identified and Figure 5-10a demonstrates their

evolutions for the MoO₃-50IPA sample with the irradiation time. The short wavelength peak (Peak 1) has a peak center shift from 628 nm, to 645 nm, and to 663 nm with the irradiation time increases from 1.5 min, to 2.5 min, and to 2 h; while the long wavelength peak (Peak 2) shifts from 803 nm, 830 nm, 871 nm. At first glance, these two peaks have a redshift in position with the increase of the absorption intensity. This redshift[112] could be caused by the lateral size reduction[121] of the nanoflakes during the reaction. However, a closer look of their intensity evolution shows a different trend. Initially, Peak 1 has a lower intensity than Peak 2 at irradiation of 1.5 min. With the increase of the irradiation time, both peaks increase their intensities, but Peak 1 increases faster. Eventually, the intensity of Peak 1 surpasses the intensity of Peak 2 at irradiation of 2 h. Therefore, as the overall intensity of the visible absorption band increases with the irradiation duration, the absorption has a blueshift from Peak 2 (NIR edge) to Peak 1 (center of visible region). This phenomenon matches well with the reaction kinetics. With the reaction continues, more MoO₃ nanoflakes are converted into substoichiometric forms resulting in the intensity increases for both Peak 1 and Peak 2; and more oxygen vacancies are produced in the reduced nanoflakes with higher carrier density leading to transition from Peak 2 to Peak 1 with the increase of plasmon resonance frequency according to Eq. 6. For MoO₃-100IPA (Figure 5-10b), peak fitting is performed only on the data at the irradiation time of 2 h, below which the absorption intensity is too low for peak fitting. Compared to the MoO₃-50IPA sample, its overall visible absorption band moves more toward to the NIR band and the two fitting peaks also shifts to longer wavelengths at 731 nm and 902 nm, respectively. These results are all coincident with the slow reaction rate for the MoO₃-100IPA sample, resulting in low amount of reduced MoO₃ and low concentration of oxygen vacancies.

5.3.3. Mechanism Discussion and Photothermal Analysis

Despite of its low reaction rate, it is important to explore the mechanism of the low-temperature photocatalytic protonation of 2D MoO_3 nanoflakes with 100% IPA. During the photocatalytic reactions, no intentional heating was employed. As it is known that IPA and other alcohol solvents are not capable to provide protons for the reaction unless they are heated to at least 200 °C,[112, 122] suspension temperature was monitored during the reaction. A series of photothermal analyses were performed together with the absorbance measurement to reveal the heating effect from the light irradiation and to clarify the true reaction temperature for the observed protonation of MoO_3 nanoflakes with pure IPA to occur.

The suspension temperatures were first monitored under continuous light irradiation up to 2 h for pure IPA, MoO_3 -50IPA, and MoO_3 -100IPA solutions. As shown in Figure 5-11a, the temperature of the pure IPA solution increases to a plateau in a few minutes and stabilizes at about 34°C, revealing the background heating effects from the light absorption of the IPA solution and glass vial, and convection heat transfer through air. The equilibrium temperature results from the balance between the heat input from the light source and the heat loss to the ambient environment. One major way of heat loss is the slow evaporation of the IPA solution inside the sealed glass vial as the container is half-full with the liquid. For the MoO_3 -50IPA sample, the suspension temperature increases steadily and reaches a higher equilibrium temperature around 44 °C accompanied with a quick change of the suspension color (Figure 5-6a inset). The higher equilibrium temperature is due to the enhanced light absorption from the readily photocatalytic reaction between MoO_3 and H_2O as described by Eq. 1-4. On the other hand, the MoO_3 -100IPA

samples shows a unique two-plateau temperature profile. Its temperature first reaches to the first plateau around 35 °C slightly higher than the one for the pure IPA solution because of the additional light absorption from the MoO₃ nanoflakes. This temperature keeps stable until about 45 min and starts to increase slowly to the second temperature plateau around 44 °C similar to the one for MoO₃-50IPA. A slow color change of the suspension (Figure 5-6b inset) occurs concomitantly with the temperature transition from the first plateau to the second one. This result confirms the photocatalytic protonation reaction could happen between MoO₃ and pure IPA at a low temperature below 50° C.

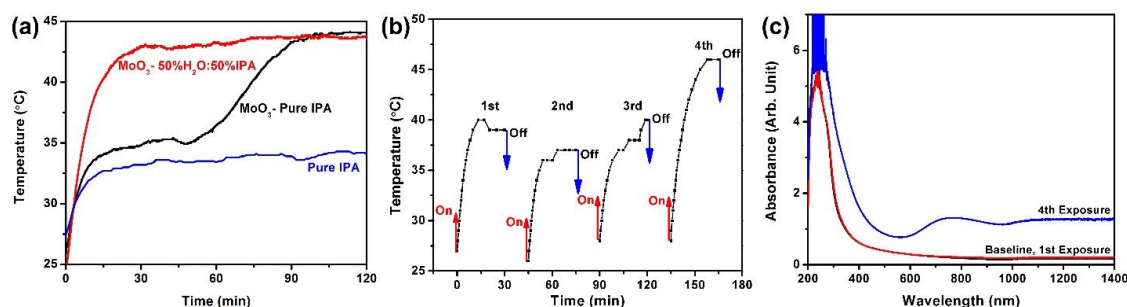


Figure 5-11. (a) Temperature profiles of different solutions during continuous light irradiation, and (b-c) repeating experiments of 30 min light irradiation with 15 min interval on a MoO₃-100IPA sample: (b) temperature profile and (c) corresponding UV-vis-NIR absorption measurements.

To show the effect of the suspension temperature on the reaction, repeating irradiation experiments were carried out on the MoO₃-100IPA suspension with an irradiation time of 30 min followed by a 15 min interval. As shown in Figure 5-11b, the temperature profile repeats for the first two cycles that the suspension temperature reaches to the first plateau with light irradiation on and cools to about room temperature with light off during the intervals. However, in the 3rd cycle, the temperature reaches the first plateau and quickly surpasses it indicating the starting of the photocatalytic reaction. In the 4th cycle, the temperature directly increases to the temperature of the second plateau without

any delay at the first plateau. The suspension had no noticeable color change after the first three cycles of light irradiation, while obvious color change from transparent to dark brown was observed after the 4th cycle irradiation. Absorbance measurement (Figure 5-11c) shows the suspension after the 4th cycle of irradiation has similar light absorption features like the 2 h irradiation sample in Figure 5-6b. From above experiments, we can conclude the reaction can occur at low temperatures slightly above room temperature with the assistance of the photothermal heating of the suspension. When the suspension reaches around 34 °C, reaction takes place at a very slow rate causing the “waiting time” at the first plateau, until a small amount of reduced bronzes or oxides were produced. After that, the suspension temperature keeps increasing to the second plateau to further facilitate the reaction. It should be noted that the suspension temperature varies from sample to sample, mainly due to the small variations of the suspension volume, power fluctuation of the light source, and location change of the sample under light beam. Therefore, the resulting temperatures for the first and second plateaus could have a temperature range of a few degree Celsius. To tell the exact effects of heating and light irradiation in this reaction, a series of experiments with different heating and light exposure conditions were performed on MoO₃-100IPA samples.

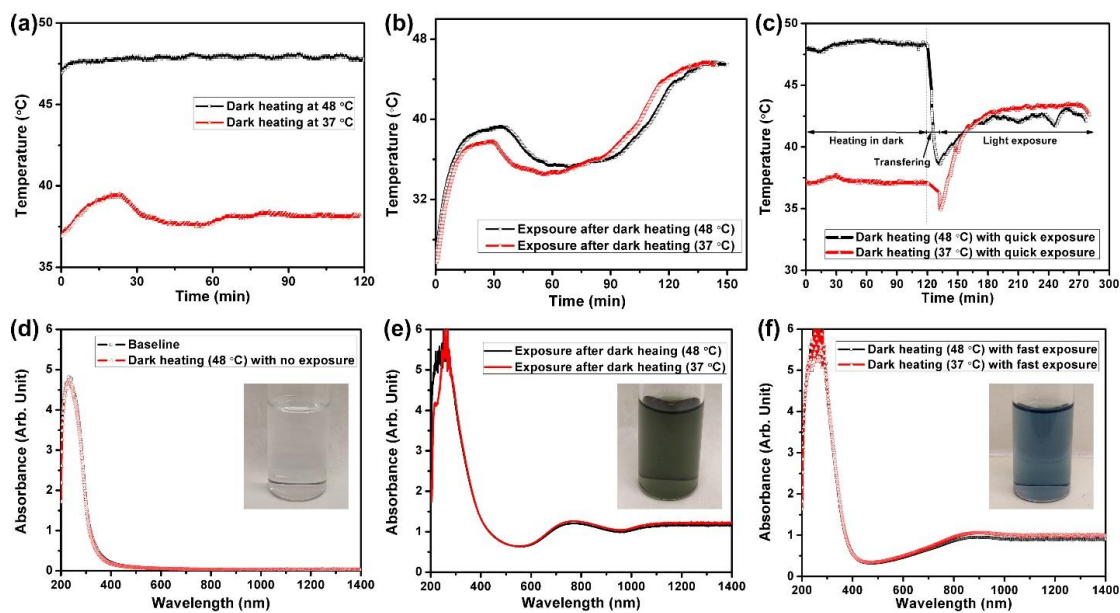
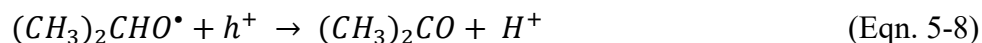
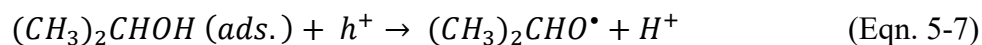


Figure 5-12. Temperature profiles (a-c) and corresponding UV-vis-NIR absorption measurements (d-f) of different heating and light exposure conditions for MoO₃-100IPA samples: (a, d) dark heating at two plateau temperatures, (b, e) samples from (a,d) having light irradiation for 2.5 hr, and (c, f) dark heating at two plateau temperatures followed by immediate light exposure of 2.5 hr. Insets show typical photographs of the resulting suspensions.

First, the suspensions were heated in dark for about 2 h at 37 °C and 48 °C, slightly higher than the two plateau temperatures to accommodate possible variations in plateau temperatures (Figure 5-12a). No reaction happened as the resulting suspensions were still transparent and absorbance spectrum after the heating was same as the one before the heating (Figure 5-12d) without additional absorption peaks. This result indicates the MoO₃-IPA reaction could not occur by heating without the light irradiation. Subsequently, the same samples were exposed to the light irradiation for 2.5 h starting from room temperature (Figure 5-12b). Both samples show similar two-plateau temperature profiles as the one in Figure 5-11a. The reaction occurred as confirmed by the suspension color change, as well as by the presence of additional visible and NIR absorption bands in the absorption measurements (Figure 5-12e). This result confirms the previous heating in dark did not

change any photocatalytic behaviors of the suspensions. The third experiment was to heat the suspensions in dark followed by an immediate light exposure. As shown by the temperature profiles (Figure 5-12c), both suspensions have a temperature drop during the transition from dark heating to light exposure. The suspension temperatures increase quickly with the light exposure and directly reach the temperature of the second temperature plateau. Both suspensions changed their color to dark blue with corresponding absorption bands appeared in the absorbance measurement (Figure 5-12f). No “waiting time” at the temperature of the first plateau. This result confirms the effect of the heating in facilitating the photocatalytic reaction.

According to the above structure characterization, the optical measurement and analysis, and the photothermal study, the detailed process of the low-temperature photocatalytic protonation of MoO_3 nanoflakes with pure IPA can be revealed clearly. The reaction is initiated by the light absorption of the MoO_3 nanoflakes. Although the as-exfoliated MoO_3 nanoflakes have a wide bandgap with strong absorption only in the UV region (Figure 5-6), the defect tail resulting from the oxygen vacancies allows weak absorption of visible light creating photogenerated electrons and holes (Eqn. 5-1). In addition, the dichroic mirror used to produce visible light cannot totally remove the UV light (Figure 5-2). Therefore, small amount of UV absorption could also contribute to the initialization of the reaction. The reaction between MoO_3 and H_2O follows Eq. 2-4, as H_2O is easy to provide protons at room temperature. For the pure alcohol solvents like IPA, literature[141] reported following reaction steps:



For the MoO₃ nanoflakes, the edges of (100) surface have rich Mo atoms with a coordination vacancy,[114] which could act like Lewis acid sites to induce above reactions (Eq. 7-8) [141]. The H^+ can react with e^- forming hydrogen atoms, which can either form H₂ molecules or intercalate into MoO₃ forming bronze and substoichiometric oxide (Eq. 3-4). Contradictory to the common knowledge that alcoholic solvents (e.g., methanol, ethanol, and IPA, etc.) require high heating temperature (more than ~200 °C) to generate protons for the reaction,[122] Pichat et al. reported room temperature photoassisted formation of H_xMoO₃ bronze with alcohol. They reported that the suspension of MoO₃ powders in IPA or methanol turned rapidly to a deep dark blue color upon UV exposure with the formation of H_xMoO₃ bronze and small amount of H₂, while the suspension of MoO₃ in water had much less pronounced color change and turned to a grayish blue color [141]. This observation is opposite to our study demonstrated in Figure 5-6 and other literature reports [112, 121]. According to our photothermal study, we conclude the photocatalytic reaction rate of MoO₃ and alcohol at room temperature is too slow to occur, but it can be expedited with a low temperature heating from the photothermal heating effect. With the continuous visible light exposure, the background photothermal heating from the solution and container could heat the suspension slightly above room temperature (~ 34 °C). At this temperature, the reaction could happen at very slow rate such that a “waiting time” is required to produce noticeable amount of reduced bronze and oxide. Once H_xMoO₃ or MoO_{3-x/2} appeared, the suspension temperature will increase rapidly due to the enhanced photothermal effect from their strong visible light absorption

and the photocatalytic reaction will be greatly expedited with a quick color change. Therefore, the protonation reaction between MoO_3 and pure alcohol under visible light irradiation can be enhanced with photothermal heating at a low temperature higher than $\sim 34^\circ\text{C}$. It deserves to mention the first temperature plateau in our experiment for MoO_3 -100IPA is due to the balance between background photothermal heating and heat loss of IPA evaporation inside the container. If the suspension is fully loaded in the glass vial to reduce the evaporation effect, its temperature could rise directly beyond 34°C and enhance the reaction efficiently. Therefore, without additional heating, the low temperature photocatalytic reaction between MoO_3 nanoflakes and pure alcohol is realized with visible light irradiation. This mechanism could be applied for other photocatalytic processes of MoO_3 nanostructures to improve their efficiency in utilizing the solar energy.

As for the discrepancies of our study with Pichat's report,[141] it is possibly due to the differences in materials quality and experiment conditions. Pichat et al. used the MoO_3 powders prepared from the decomposition of MoO_2Cl_2 in oxygen ambient. Their MoO_3 powders may have quite different crystalline quality, defect status, and optical properties from our MoO_3 nanoflakes from the liquid exfoliation of CVD grown whiskers. They employed UV illumination rather than the visible light in our study. It could be possible their MoO_3 -alcohol suspension was photothermally heated to a temperature high enough to promote the reaction. However, it is still hard to explain why the MoO_3 - H_2O reaction is less significant than the MoO_3 -alcohol reaction in their report. It is important to mention that our study show the experiment is very sensitive to the H_2O content. All the MoO_3 -100IPA samples reported were prepared using freshly grown MoO_3 whiskers and anhydrous IPA with less than 50 ppm H_2O transferred from septum-sealed bottles to avoid

possible moisture absorption from air. The samples were also exfoliated and centrifuged in tightly sealed vials in dark to avoid moisture and possible light exposure before the photocatalytic reaction. It was found the experiment results were not consistent if the sample had small amount of H₂O content inside. The suspension could have a quick but light color change followed by bleaching with particle precipitations. However, detailed discussion on this phenomenon is beyond the scope of this report and it needs future investigation in detail.

CHAPTER 6. SUMMARY AND CONCLUSION

In summary, we report a low-temperature protonation reaction of 2D MoO_3 nanoflakes with pure alcohol under visible light irradiation. In contrast with the classic concept of the high protonation temperature more than 200 °C for MoO_3 with pure alcohols, we find the suspension temperature was below 50°C throughout the photocatalytic protonation of nanoflakes with IPA, one type of alcohol solvents. Using a scalable liquid exfoliation method, MoO_3 nanoflakes were produced by using different alcohol-water solutions. The resulting nanomaterials have different dimensions and defect structures tailorable by the mixing ratio of the solutions, as shown by the materials structure characterization and optical property measurement. Combined with the photothermal study, the detailed reaction mechanism for the low-temperature protonation was revealed. Sub-bandgap defects provide the visible light absorption to initialize the reaction under the visible light irradiation. The usually slow reaction is expedited by the photothermal heating to achieve evident reaction rate without providing any additional heating. The low-temperature reaction has a great potential to produce substoichiometric semiconductors with tunable plasmonic behaviors at low cost. The reaction mechanism can be extended to a variety of photocatalytic processes of MoO_3 nanostructures, with enhanced efficiencies to harvest and convert solar energy into chemical energies.

Also, during the first part of this dissertation (chapter 2) we focused on synthesizing 1D MoO_3 nanostructures by utilizing an alkali metal-based catalyst. The major drawback of currently used metal catalysts is their high temperature reaction with target materials, producing intermetallic compounds and contamination, which negatively affects the

overall electrical and optical properties of the synthesized nanostructures. Through the CVD technique, the catalytic effects of sodium hydroxide on the growth morphologies of MoO_3 were explored and the results were discussed based on two main growth mechanisms called vapor-solid (VS) and vapor-liquid-solid (VLS). The growth resulted in different morphologies (*e.g.*, rectangular fork-end nanoplates, long nano/micro-belts, and microtowers). Thick and dense growth of MoO_3 semi-circle microplates were normally observed for non-catalytically affected areas. By applying 0.01 M catalytic NaOH droplets, formations of long triangle nanobelts, rounded and fork-end rectangular microplates of molybdenum trioxide appeared. Growth morphology-dependence on the distance from the catalytic droplet was studied in detail in respect to droplet boundaries and at different temperature zones. Considering the potential applications of long nanobelts as they interconnect in integrated nanoscale device, we mostly focused on carefully controlling growth conditions to improve growth density and uniformity of synthesized nanobelts across the substrate. For this purpose, additional catalyst sources were deposited on separate substrates and were placed at different locations near the target location. Growth density of long nanobelts substantially improved, which is mainly due to the additional source of catalyst. The length of nanobelts further increased from a few hundred microns to a few millimeters. Finally, the growth density and uniformity was further increased when no catalytic droplet was deposited on the target substrate. The best growth conditions were obtained when both target and catalytic substrates were placed side-by-side with no catalytic droplet on the target substrate. Highly uniform millimeter long nanobelts were synthesized across the entire substrate.

For the second part of this research (chapter 3) work we focused on exploring low temperature growth of 1D MoO_3 nanostructures to obtain high density and uniform rectangular nanoribbons. The chemical vapor deposition (CVD) method was utilized to synthesize one-dimensional nanostructures of $\alpha\text{-MoO}_3$ in the form of nanoribbons. Morphology, crystal structure, and chemical composition of the synthesized nanoribbons were investigated in detail while altering several growth parameters. For example, the effects of growth time, oxygen flow, type (powder vs whiskers), temperature, and amount of the growth source were carefully monitored and growth mechanisms were studied within the different temperature zones. The effects of change in growth parameters on altering morphology of synthesized nanoribbons were carefully studied. Optimum growth conditions were established through detailed study of growth parameters such as temperature (800°C vs 600°C), type (powder vs whiskers) and amount (small 3-12 mg vs large 25-100 mg) amount of growth sources, location of source and target substrate. The resulting growth morphologies were discussed within three different heating zones of high, medium, and low temperatures. High density and uniform growth of $\alpha\text{-MoO}_3$ rectangular nanoribbons (sharp edges) with the length ranging from 7 to 10 μm , typical thickness of 60-130 nm, and width around 350-800 nm was successfully synthesized at the relatively low temperature of $350\text{-}550^\circ\text{C}$ with a minimum amount of source materials (as low as 6 mg). Uniform and high-density growth of rectangular MoO_3 nanoribbons was achieved with a growth source as low as 3 milligrams.

In chapter four of this research study we proposed a promising design of 1D core-shell nanostructures to achieve multiple functions. The nano-cable heterostructures are 1D core-shell nanostructures composed of semiconductor hetero-shells, MoO_3 and transparent

conductive oxide (TCO) cores of tin doped indium oxide (ITO). It is essential to employ optimum growth parameters to successfully synthesize ITO nanowires (NWs) as the core structure. For this purpose, we have fully investigated the effects of (1) Au catalyst patterning, (2) different oxygen flow rates, (3) different Ar flow rates, and (4) employing thermal insulators (to provide a uniform growth heating zone), on morphology change of grown ITO NWs on different substrates (SiO_2/Si and ITO/glass). We have demonstrated the synthesis of 1D heterostructures of ITO/ MoO_3 core-shell structures through a multi-step CVD process. Growth of ITO NWs on both SiO_2/Si and ITO/glass substrates were studied in detail by discussing the growth results at different temperature zones while altering growth parameters such as thickness of Au catalytic film and rate of carrier/reactant gases (O_2 and Ar). The optimum growth condition for ITO NWs on SiO_2/Si was identified with a deposition of 10 nm Au catalytic film, running 0.1 sccm oxygen reactant gas, and within the temperature zone 750-800°C. For growth on ITO/glass substrates, optimum growth was observed at a temperature zone of 700-750°C while employing thermal isolators at both sides of the reaction chamber, substantially improving the growth uniformity. Also, by placing the ITO/glass substrate at the upstream side of the reaction chamber, ITO NWs with a diameter 150 nm were grown at a temperature of 585°C while no carrier gas (Ar) was introduced to the reaction chamber.

Growth mechanisms of ITO NWs was discussed for specific temperature zones (high to low) inside the CVD reaction chamber. After successful growth of ITO NWs, shell layer materials (MoO_3) were deposited on the ITO core by altering different growth parameters. Optimum conditions for deposition of shell material on synthesized ITO NWs were obtained at temperature zone 550-585°C (downstream side) and 550-650°C (upstream

side) while carrier and reactant gases were set at 10/ 2.5 sccm and 0/2 sccm, respectively. Deposition of shell materials on ITO NWs led to three distinguished morphologies of longitudinal, transverse, and needle shaped structures. It was concluded that ultra-thin (50 nm) 1D core-shell nanostructures (ITO/MoO₃) were successfully synthesized. Under this condition, as-synthesized ITO NWs were fully covered with a thin layer of shell materials.

REFERENCES

1. Dattoli, E.N. and W. Lu, ITO nanowires and nanoparticles for transparent films. *Mrs Bulletin*, 2011. 36(10): p. 782-788.
2. Chen, Y., et al., Single-crystalline orthorhombic molybdenum oxide nanobelts: synthesis and photocatalytic properties. *CrystEngComm*, 2010. 12(11): p. 3740-3747.
3. Moss, R.H., et al., The next generation of scenarios for climate change research and assessment. *Nature*, 2010. 463(7282): p. 747-56.
4. Hughes, J.D., Energy: A reality check on the shale revolution. *Nature*, 2013. 494(7437): p. 307-8.
5. Hernández-Moro, J., J.M. Martínez-Duart, and R. Guerrero-Lemus, Main parameters influencing present solar electricity costs and their evolution (2012–2050). *Journal of Renewable and Sustainable Energy*, 2013. 5(2): p. 023112.
6. Razykov, T.M., et al., Solar photovoltaic electricity: Current status and future prospects. *Solar Energy*, 2011. 85(8): p. 1580-1608.
7. Norris, D.J. and E.S. Aydil, Getting Moore from Solar Cells. *Science*, 2012. 338(6107): p. 625-626.
8. Pan, H., Principles on design and fabrication of nanomaterials as photocatalysts for water-splitting. *Renewable and Sustainable Energy Reviews*, 2016. 57: p. 584-601.
9. Chen, H.M., et al., Nano-architecture and material designs for water splitting photoelectrodes. *Chemical Society Reviews*, 2012. 41(17): p. 5654-5671.
10. van de Krol, R., Y. Liang, and J. Schoonman, Solar hydrogen production with nanostructured metal oxides. *Journal of Materials Chemistry*, 2008. 18(20): p. 2311-2320.
11. Atwater, H.A. and A. Polman, Plasmonics for improved photovoltaic devices. *Nat Mater*, 2010. 9(3): p. 205-213.
12. Gratzel, M., Photoelectrochemical cells. *Nature*, 2001. 414(6861): p. 338-344.
13. Contents: *Adv. Mater.* 23/2007. *Advanced Materials*, 2007. 19(23): p. 4091-4101.
14. Kudo, A. and Y. Miseki, Heterogeneous photocatalyst materials for water splitting. *Chemical Society Reviews*, 2009. 38(1): p. 253-278.
15. Fujishima, A. and K. Honda, Electrochemical Photolysis of Water at a Semiconductor Electrode. *Nature*, 1972. 238(5358): p. 37-38.
16. Bhatt, M.D. and J.S. Lee, Recent theoretical progress in the development of photoanode materials for solar water splitting photoelectrochemical cells. *Journal of Materials Chemistry A*, 2015. 3(20): p. 10632-10659.

17. Rodriguez, I., et al., Solar energy harvesting in photoelectrochemical solar cells. *Journal of Materials Chemistry*, 2007. 17(30): p. 3205-3209.
18. Stefano Fabris, M.B. Water splitting for energy storage. Available from: https://sites.google.com/site/piccininsimone/research_projects/h2o_split.
19. Chen, Y.W., et al., Atomic layer-deposited tunnel oxide stabilizes silicon photoanodes for water oxidation. *Nat Mater*, 2011. 10(7): p. 539-544.
20. Mor, G.K., et al., Enhanced Photocleavage of Water Using Titania Nanotube Arrays. *Nano Letters*, 2005. 5(1): p. 191-195.
21. Pan, J., et al., On the True Photoreactivity Order of {001}, {010}, Facets of Anatase TiO₂ Crystals. *Angewandte Chemie International Edition*, 2011. 50(9): p. 2133-2137.
22. Cho, I.S., et al., Branched TiO₂ Nanorods for Photoelectrochemical Hydrogen Production. *Nano Letters*, 2011. 11(11): p. 4978-4984.
23. Asahi, R., et al., Visible-Light Photocatalysis in Nitrogen-Doped Titanium Oxides. *Science*, 2001. 293(5528): p. 269-271.
24. Irie, H., Y. Watanabe, and K. Hashimoto, Nitrogen-Concentration Dependence on Photocatalytic Activity of TiO₂-xN_x powders. *The Journal of Physical Chemistry B*, 2003. 107(23): p. 5483-5486.
25. Liu, G., et al., Titania-based photocatalysts-crystal growth, doping and heterostructuring. *Journal of Materials Chemistry*, 2010. 20(5): p. 831-843.
26. Wang, P., et al., Stable New Sensitizer with Improved Light Harvesting for Nanocrystalline Dye-Sensitized Solar Cells. *Advanced Materials*, 2004. 16(20): p. 1806-1811.
27. Wolcott, A., et al., Synthesis and Characterization of ultrathin WO₃ Nanodisks Utilizing Long-Chain Poly(ethylene glycol). *The Journal of Physical Chemistry B*, 2006. 110(50): p. 25288-25296.
28. Sivula, K., F. Le Formal, and M. Grätzel, Solar Water Splitting: Progress Using Hematite (α -Fe₂O₃) Photoelectrodes. *ChemSusChem*, 2011. 4(4): p. 432-449.
29. Kanan, M.W. and D.G. Nocera, In Situ Formation of an Oxygen-Evolving Catalyst in Neutral Water Containing Phosphate and Co²⁺. *Science*, 2008. 321(5892): p. 1072-1075.
30. Steinmiller, E.M.P. and K.-S. Choi, Photochemical deposition of cobalt-based oxygen evolving catalyst on a semiconductor photoanode for solar oxygen production. *Proceedings of the National Academy of Sciences*, 2009. 106(49): p. 20633-20636.
31. Dasgupta, N.P., et al., 25th Anniversary Article: Semiconductor Nanowires Synthesis, Characterization, and Applications. *Advanced Materials*, 2014. 26(14): p. 2137-2184.

32. Weng, B., et al., One-dimensional nanostructure based materials for versatile photocatalytic applications. *Rsc Advances*, 2014. 4(25): p. 12685-12700.
33. Zhang, Y., et al., Transforming CdS into an efficient visible light photocatalyst for selective oxidation of saturated primary C–H bonds under ambient conditions. *Chemical Science*, 2012. 3(9): p. 2812-2822.
34. Yao, J., K. Hashimoto, and A. Fujishima, Photochromism induced in an electrolytically pretreated MoO₃ thin film by visible light. *Nature*, 1992. 355(6361): p. 624.
35. Yang, Y., et al., Microstructures of electrochromic MoO₃ thin films colored by injection of different cations. *The Journal of Physical Chemistry B*, 1998. 102(47): p. 9392-9396.
36. Molina-Mendoza, A.J., et al., Centimeter-scale synthesis of ultrathin layered MoO₃ by van der Waals epitaxy. *Chemistry of Materials*, 2016. 28(11): p. 4042-4051.
37. Muralidhara, K. and P. Misra, A Study on the Surface Properties of Transition Metal Oxides. *International Journal of Scientific Research and Management*, 2014. 2(12).
38. Li, N., et al., Open circuit voltage enhancement due to reduced dark current in small molecule photovoltaic cells. *Applied Physics Letters*, 2009. 94(2): p. 13.
39. Wang, M., et al., Thickness dependence of the MoO₃ blocking layers on ZnO nanorod-inverted organic photovoltaic devices. *Applied physics letters*, 2011. 98(10): p. 55.
40. Shakir, I., et al., Structural and electrochemical characterization of α -MoO₃ nanorod-based electrochemical energy storage devices. *Electrochimica Acta*, 2010. 56(1): p. 376-380.
41. Liang, R., H. Cao, and D. Qian, MoO₃ nanowires as electrochemical pseudocapacitor materials. *Chemical Communications*, 2011. 47(37): p. 10305-10307.
42. Ibrahim, M.A., et al., Direct conversion of multilayer molybdenum trioxide to nanorods as multifunctional electrodes in lithium-ion batteries. *Nanoscale*, 2014. 6(10): p. 5484-5490.
43. Zhuang, Z., et al., Synthesis and electrochemical behaviors of α -MoO₃ nanobelts/carbon nanotubes composites for lithium ion batteries. *Journal of Wuhan University of Technology-Mater. Sci. Ed.*, 2018. 33(1): p. 73-77.
44. Li, J. and X. Liu, Fabrication and enhanced electrochemical properties of α -MoO₃ nanobelts using dodecylbenzenesulfonic acid as both reactant and surfactant. *CrystEngComm*, 2014. 16(2): p. 184-190.
45. Balendhran, S., et al., Two-dimensional molybdenum trioxide and dichalcogenides. *Advanced Functional Materials*, 2013. 23(32): p. 3952-3970.

46. Slawinski, W.A., et al., A novel polytype - the stacking fault based gamma-MoO₃ nanobelts. *Acta Crystallographica Section B-Structural Science Crystal Engineering and Materials*, 2016. 72: p. 201-208.
47. Quevedo-Lopez, M., et al., Enhancement of the photochromic and thermochromic properties of molybdenum oxide thin films by a cadmium sulfide underlayer. *Journal of Materials Science: Materials in Electronics*, 2000. 11(2): p. 151-155.
48. Beydaghyan, G., M. Boudreau, and P. Ashrit, Optical properties and electrochromic response of nanostructured molybdenum trioxide films. *Journal of Materials Research*, 2011. 26(1): p. 55-61.
49. Chernova, N.A., et al., Layered vanadium and molybdenum oxides: batteries and electrochromics. *Journal of Materials Chemistry*, 2009. 19(17): p. 2526-2552.
50. Gesheva, K., A. Szekeres, and T. Ivanova, Optical properties of chemical vapor deposited thin films of molybdenum and tungsten based metal oxides. *Solar energy Materials and Solar cells*, 2003. 76(4): p. 563-576.
51. Hsu, C.-S., et al., Electrochromic properties of nanocrystalline MoO₃ thin films. *Thin Solid Films*, 2008. 516(15): p. 4839-4844.
52. Guerfi, A., R. Paynter, and L.H. Dao, Characterization and stability of electrochromic MoO₃ thin films prepared by electrodeposition. *Journal of The Electrochemical Society*, 1995. 142(10): p. 3457-3464.
53. Phuruangrat, A., et al., Electrochemical hydrogen evolution over MoO₃ nanowires produced by microwave-assisted hydrothermal reaction. *Electrochemistry Communications*, 2009. 11(9): p. 1740-1743.
54. Chithambararaj, A., et al., Flower-like hierarchical h-MoO₃: new findings of efficient visible light driven nano photocatalyst for methylene blue degradation. *Catalysis Science & Technology*, 2013. 3(5): p. 1405-1414.
55. Taurino, A.M., et al., Synthesis, electrical characterization, and gas sensing properties of molybdenum oxide nanorods. *Applied physics letters*, 2006. 88(15): p. 152111.
56. Chang, T.-Y., Y.-W. Cheng, and P.-T. Lee, Electrical characteristics of an organic bistable device using an Al/Alq₃/nanostructured MoO₃/Alq₃/p+-Si structure. *Applied Physics Letters*, 2010. 96(4): p. 16.
57. Lou, X.W. and H.C. Zeng, Hydrothermal synthesis of α -MoO₃ nanorods via acidification of ammonium heptamolybdate tetrahydrate. *Chemistry of materials*, 2002. 14(11): p. 4781-4789.
58. Satishkumar, B., et al., Synthesis of metal oxide nanorods using carbon nanotubes as templates. *Journal of Materials Chemistry*, 2000. 10(9): p. 2115-2119.
59. Li, Y. and Y. Bando, Quasi-aligned MoO₃ nanotubes grown on Ta substrate. *Chemical physics letters*, 2002. 364(5-6): p. 484-488.

60. Liu, T., Y. Xie, and B. Chu, Use of block copolymer micelles on formation of hollow MoO₃ nanospheres. *Langmuir*, 2000. 16(23): p. 9015-9022.
61. Antonelli, D.M. and M. Trudeau, Phase changes and electronic properties in toroidal mesoporous molybdenum oxides. *Angewandte Chemie International Edition*, 1999. 38(10): p. 1471-1475.
62. Li, Y., et al., Field emission from MoO₃ nanobelts. *Applied Physics Letters*, 2002. 81(26): p. 5048-5050.
63. Patzke, G.R., et al., One-step synthesis of submicrometer fibers of MoO₃. *Chemistry of materials*, 2004. 16(6): p. 1126-1134.
64. Li, X.-L., J.-F. Liu, and Y.-D. Li, Low-temperature synthesis of large-scale single-crystal molybdenum trioxide (MoO₃) nanobelts. *Applied physics letters*, 2002. 81(25): p. 4832-4834.
65. Rabalais, J.W., R.J. Colton, and A.M. Guzman, Trapped electrons in substoichiometric MoO₃ observed by X-ray electron spectroscopy. *Chemical Physics Letters*, 1974. 29(1): p. 131-133.
66. Buono-Core, G., et al., Growth and characterization of molybdenum oxide thin films prepared by photochemical metal–organic deposition (PMOD). *Polyhedron*, 2010. 29(6): p. 1551-1554.
67. Fleisch, T. and G. Mains, An XPS study of the UV reduction and photochromism of MoO₃ and WO₃. *The Journal of Chemical Physics*, 1982. 76(2): p. 780-786.
68. Medrano, M., et al., State of the art on high-temperature thermal energy storage for power generation. Part 2—Case studies. *Renewable and Sustainable Energy Reviews*, 2010. 14(1): p. 56-72.
69. Sha, X., et al., Hydrogen Absorption and Diffusion in Bulk α -MoO₃. *The Journal of Physical Chemistry C*, 2009. 113(26): p. 11399-11407.
70. Ou, J.Z., et al., In situ Raman spectroscopy of H₂ gas interaction with layered MoO₃. *The Journal of Physical Chemistry C*, 2011. 115(21): p. 10757-10763.
71. Varshney, V., et al., MD simulations of molybdenum disulphide (MoS₂): Force-field parameterization and thermal transport behavior. *Computational Materials Science*, 2010. 48(1): p. 101-108.
72. Kim, J.-Y., et al., Thermal and electronic properties of exfoliated metal chalcogenides. *Bulletin of the Korean Chemical Society*, 2010. 31(11): p. 3225-3227.
73. Wagner, R.S. and W.C. Ellis, Vapor-Liquid-Solid Mechanism Of Single Crystal Growth. Vol. 4. 1964. 89-90.
74. Choi, H.-J., Vapor–Liquid–Solid Growth of Semiconductor Nanowires, in *Semiconductor Nanostructures for Optoelectronic Devices: Processing*,

- Characterization and Applications, G.-C. Yi, Editor. 2012, Springer Berlin Heidelberg: Berlin, Heidelberg. p. 1-36.
75. Dattoli, E.N., The Electrical Characteristics and Device Applications of Metal Oxide Nanowires, in *Electrical Engineering*. 2010, The University of Michigan.
 76. Redwing, J.M., X. Miao, and X. Li, Vapor-Liquid-Solid Growth of Semiconductor Nanowires, in *Handbook of Crystal Growth (Second Edition)*, T.F. Kuech, Editor. 2015, North-Holland: Boston. p. 399-439.
 77. Kamins, T.I., et al., Ti-catalyzed Si nanowires by chemical vapor deposition: Microscopy and growth mechanisms. *Journal of Applied Physics*, 2001. 89(2): p. 1008-1016.
 78. K. K. Lew, J.R., Growth characteristics of silicon nanowires synthesized by vapor-liquid-solid growth in nanoporous alumina templates. *Journal of Crystal Growth*, 2003.
 79. H. Huang, M., et al., Catalytic Growth of Zinc Oxide Nanowires by Vapor Transport. Vol. 13. 2001. 113-116.
 80. Allen, J.E., et al., High-resolution detection of Au catalyst atoms in Si nanowires. *Nature Nanotechnology*, 2008. 3(3): p. 168-173.
 81. Wang, Y.W., et al., Epitaxial growth of silicon nanowires using an aluminium catalyst. *Nature Nanotechnology*, 2006. 1(3): p. 186-189.
 82. Ke, Y., et al., Fabrication and Electrical Properties of Si Nanowires Synthesized by Al Catalyzed Vapor-Liquid-Solid Growth. *Nano Letters*, 2009. 9(12): p. 4494-4499.
 83. Sheng, T., et al., New growth modes of molybdenum oxide layered 1D structures using alternative catalysts: transverse mode vs. axial mode. *CrystEngComm*, 2015. 17(5): p. 1139-1150.
 84. Yu, H.K. and J.L. Lee, Growth mechanism of metal-oxide nanowires synthesized by electron beam evaporation: A self-catalytic vapor-liquid-solid process. *Scientific Reports*, 2014. 4.
 85. Hoermann, F., Beitrag zur Kenntnis der Molybdate und Wolframate. Die binären Systeme: $\text{Li}_3\text{MoO}_4\text{-MoO}_3$, $\text{Na}_2\text{MoO}_4\text{-MoO}_3$, $\text{K}_3\text{MoO}_4\text{-MoO}_3$, $\text{Li}_2\text{WO}_4\text{-WO}_3$, $\text{Na}_2\text{WO}_4\text{-WO}_3$, $\text{K}_2\text{WO}_4\text{-WO}_3$, $\text{Li}_2\text{MoO}_4\text{-Na}_2\text{MoO}_4$, $\text{Li}_2\text{WO}_4\text{-Na}_2\text{WO}_4$, $\text{Li}_2\text{MoO}_4\text{-K}_2\text{MoO}_4$. Vol. 177. 2004. 145-186.
 86. Subannajui, K., et al., ZnO Nanowire Growth: A Deeper Understanding Based on Simulations and Controlled Oxygen Experiments. *Crystal Growth & Design*, 2010. 10(4): p. 1585-1589.
 87. Zhang, H.T., et al., Selective growth of tungsten oxide nanowires via a vapor-solid process. *Journal of Vacuum Science & Technology B*, 2010. 28(2): p. 310-315.

88. Xiao, F.X., et al., One-Dimensional Hybrid Nanostructures for Heterogeneous Photocatalysis and Photoelectrocatalysis. *Small*, 2015. 11(18): p. 2115-2131.
89. Lee, S., et al., Transparent-conducting-oxide nanowire arrays for efficient photoelectrochemical energy conversion. *Nanoscale*, 2014. 6(15): p. 8649-8655.
90. Yeh Yee, K., et al., Low-temperature synthesis of indium tin oxide nanowires as the transparent electrodes for organic light emitting devices. *Nanotechnology*, 2012. 23(2): p. 025706.
91. Dong, H.B., et al., Indium Tin Oxide Nanowires Grown by One-Step Thermal Evaporation-Deposition Process at Low Temperature. *Journal of Nanoscience and Nanotechnology*, 2013. 13(2): p. 1300-1303.
92. Chen, Y.Q., et al., Synthesis of tin-doped indium oxide nanowires by self-catalytic VLS growth. *Journal of Physics D: Applied Physics*, 2004. 37(23): p. 3319.
93. Li, L., et al., Controlled synthesis of tin-doped indium oxide (ITO) nanowires. *Journal of Crystal Growth*, 2015. 413: p. 31-36.
94. Wan, J. Sun, and H. Liu, Semiconducting Oxide Nanowires: Growth, Doping and Device applications, in *Nanowires - Implementations and Applications*. 2011.
95. Kumar, R.R., et al., Low temperature VLS growth of ITO nanowires by electron beam evaporation method. *Materials Research Express*, 2014. 1(3): p. 035008.
96. Beaudry, A.L., et al., Flux Engineering for Indium Tin Oxide Nanotree Crystal Alignment and Height-Dependent Branch Orientation. *Crystal Growth & Design*, 2013. 13(1): p. 212-219.
97. Li, S.Q., R.P.H. Chang, and L.E. Ocola, TCO Nanostructures as building blocks for nanophotonic devices in the infrared, in *Plasmonics: Metallic Nanostructures and Their Optical Properties* Xi, M.I. Stockman, Editor. 2013, Spie-Int Soc Optical Engineering: Bellingham.
98. Steinmann, P. and J.M.R. Weaver, Fabrication of sub-5 nm gaps between metallic electrodes using conventional lithographic techniques. *Journal of Vacuum Science & Technology B*, 2004. 22(6): p. 3178-3181.
99. Terauchi, M., et al., A new grating X-ray spectrometer for 2-4 keV enabling a separate observation of In-L beta and Sn-L alpha emissions of indium tin oxide. *Microscopy*, 2013. 62(3): p. 391-395.
100. Meng, G., et al., Impact of Preferential Indium Nucleation on Electrical Conductivity of Vapor-Liquid-Solid Grown Indium-Tin Oxide Nanowires. *Journal of the American Chemical Society*, 2013. 135(18): p. 7033-7038.
101. Lide, D.R., *CRC Handbook of Chemistry and Physics* 2003.
102. Kumar, R.R., et al., Low temperature and self catalytic growth of ultrafine ITO nanowires by electron beam evaporation method and their optical and electrical properties. *Materials Research Bulletin*, 2014. 52: p. 167-176.

103. O'Dwyer, C. and C. Sotomayor Torres, Epitaxial growth of an antireflective, conductive, graded index ITO nanowire layer. *Frontiers in Physics*, 2013. 1.
104. Linic, S., P. Christopher, and D.B. Ingram, Plasmonic-metal nanostructures for efficient conversion of solar to chemical energy. *Nature Materials*, 2011. 10(12): p. 911-921.
105. Clavero, C., Plasmon-induced hot-electron generation at nanoparticle/metal-oxide interfaces for photovoltaic and photocatalytic devices. *Nature Photonics*, 2014. 8(2): p. 95-103.
106. Smith, J.G., J.A. Fauchaux, and P.K. Jain, Plasmon resonances for solar energy harvesting: A mechanistic outlook. *Nano Today*, 2015. 10(1): p. 67-80.
107. Manthiram, K. and A.P. Alivisatos, Tunable Localized Surface Plasmon Resonances in Tungsten Oxide Nanocrystals. *Journal of the American Chemical Society*, 2012. 134(9): p. 3995-3998.
108. Cushing, S.K., et al., Photocatalytic Activity Enhanced by Plasmonic Resonant Energy Transfer from Metal to Semiconductor. *Journal of the American Chemical Society*, 2012. 134(36): p. 15033-15041.
109. Mattox, T.M., et al., Chemical Control of Plasmons in Metal Chalcogenide and Metal Oxide Nanostructures. *Advanced Materials*, 2015. 27(38): p. 5830-5837.
110. West, P.R., et al., Searching for better plasmonic materials. *Laser & Photonics Reviews*, 2010. 4(6): p. 795-808.
111. Naik, G.V., J. Kim, and A. Boltasseva, Oxides and nitrides as alternative plasmonic materials in the optical range. *Optical Materials Express*, 2011. 1(6): p. 1090-1099.
112. Alsaif, M.M.Y.A., et al., Tunable Plasmon Resonances in Two-Dimensional Molybdenum Oxide Nanoflakes. *Advanced Materials*, 2014. 26(23): p. 3931-3937.
113. Cheng, H., et al., A Plasmonic Molybdenum Oxide Hybrid with Reversible Tunability for Visible-Light-Enhanced Catalytic Reactions. *Advanced Materials*, 2015. 27(31): p. 4616-4621.
114. Papakondylis, A. and P. Sautet, Ab Initio Study of the Structure of the α -MoO₃ Solid and Study of the Adsorption of H₂O and CO Molecules on Its (100) Surface. *The Journal of Physical Chemistry*, 1996. 100(25): p. 10681-10688.
115. Kalantar-zadeh, K., et al., Synthesis of nanometre-thick MoO₃ sheets. *Nanoscale*, 2010. 2(3): p. 429-433.
116. Halim, U., et al., A rational design of cosolvent exfoliation of layered materials by directly probing liquid–solid interaction. *Nature Communications*, 2013. 4: p. 2213.
117. Sheng, T., et al., Growth of ultra-long sodium tungsten oxide and tungsten oxide nanowires: Effects of impurity and residue deposition. *Journal of Crystal Growth*, 2014. 395: p. 61-67.

118. Sheng, T. and H. Zhang. Scalable seeded growth of tungsten oxide nanowires for energy applications. in High-capacity Optical Networks and Emerging/Enabling Technologies (HONET), 2014 11th Annual. 2014.
119. ; Available from: * <http://assets.newport.com/pdfs/e5426.pdf>, last visited December 13, 2018. .
120. Vazquez, G., E. Alvarez, and J.M. Navaza, Surface Tension of Alcohol Water + Water from 20 to 50 .degree.C. Journal of Chemical & Engineering Data, 1995. 40(3): p. 611-614.
121. Alsaif, M., et al., Exfoliation Solvent Dependent Plasmon Resonances in Two-Dimensional Sub-Stoichiometric Molybdenum Oxide Nanoflakes. Acs Applied Materials & Interfaces, 2016. 8(5): p. 3482-3493.
122. Smith, R.L. and G.S. Rohrer, The protonation of MoO₃ during the partial oxidation of alcohols. Journal of Catalysis, 1998. 173(1): p. 219-228.
123. Deb, S.K., Physical Properties of a Transition Metal Oxide - Optical and Photoelectric Properties of Singel Crystal and Thin Film Molybdenum Trioxide. Proceedings of the Royal Society of London Series a-Mathematical and Physical Sciences, 1968. 304(1477): p. 211-&.
124. Itoh, M., K. Hayakawa, and S. Oishi, Optical properties and electronic structures of layered MoO₃ single crystals. Journal of Physics-Condensed Matter, 2001. 13(31): p. 6853-6864.
125. Sian, T.S. and G.B. Reddy, Optical, structural and photoelectron spectroscopic studies on amorphous and crystalline molybdenum oxide thin films. Solar Energy Materials and Solar Cells, 2004. 82(3): p. 375-386.
126. Chu, W.G., et al., Direct thermal oxidization evaporation growth, structure, and optical properties of single-crystalline nanobelts of molybdenum trioxide. Journal of Materials Research, 2007. 22(6): p. 1609-1617.
127. Siciliano, T., et al., Characteristics of molybdenum trioxide nanobelts prepared by thermal evaporation technique. Materials Chemistry and Physics, 2009. 114(2-3): p. 687-691.
128. Hussain, Z., Optical and electrochromic properties of heated and annealed MoO₃ thin films. Journal of Materials Research, 2001. 16(9): p. 2695-2708.
129. Zhao, Y., et al., Preparation Of MoO₃ nanostructures and their optical properties. Journal of Physics-Condensed Matter, 2003. 15(35): p. L547-L552.
130. Zheng, L., et al., Novel Metastable Hexagonal MoO₃ Nanobelts: Synthesis, Photochromic, and Electrochromic Properties. Chemistry of Materials, 2009. 21(23): p. 5681-5690.
131. Tauc, J., Optical properties and electronic structure of amorphous Ge and Si. Materials Research Bulletin, 1968. 3(1): p. 37-46.

132. Davis, E.A. and N.F. Mott, Conduction in non-crystalline systems V. Conductivity, optical absorption and photoconductivity in amorphous semiconductors. *The Philosophical Magazine: A Journal of Theoretical Experimental and Applied Physics*, 1970. 22(179): p. 0903-0922.
133. Chen, Z., E. Miller, and H.N. Dinh, Chapter 5 UV-Vis Spectroscopy, in *Photoelectrochemical Water Splitting - Standards, Experimental Methods, and Protocols*. 2013, Springer: New York
134. Liu, H.F., et al., Aqueous and mechanical exfoliation, unique properties, and theoretical understanding of MoO₃ nanosheets made from free-standing alpha-MoO₃ crystals: Raman mode softening and absorption edge blue shift. *Nano Research*, 2018. 11(3): p. 1193-1203.
135. Balendhran, S., et al., Enhanced Charge Carrier Mobility in Two-Dimensional High Dielectric Molybdenum Oxide. *Advanced Materials*, 2013. 25(1): p. 109-114.
136. Studenyak, I., M. Kranjčec, and M. Kurik, Urbach Rule in Solid State Physics. *International Journal of Optics and Applications*, 2014. 4(3): p. 76-83.
137. Amirtharaj, P.M. and D.G. Seiler, Chapter 36 Optical Properties of Semiconductors in *Handbook of Optics*, M. Bass, et al., Editors. 1995, McGRAW-HILL: New York.
138. Liu, H.F., et al., Huge Absorption Edge Blue shifts of Layered alpha-MoO₃ Crystals upon Thickness Reduction Approaching 2D Nanosheets. *Journal of Physical Chemistry C*, 2018. 122(22): p. 12122-12130.
139. Urbach, F., The Long-Wavelength Edge of Photographic Sensitivity and of the Electronic Absorption of Solids. *Physical Review*, 1953. 92(5): p. 1324-1324.
140. Jean, J., et al., Radiative Efficiency Limit with Band Tailing Exceeds 30% for Quantum Dot Solar Cells. *ACS Energy Letters*, 2017. 2(11): p. 2616-2624.
141. Pichat, P., C. Hoang Van, and C. Hoang Van, Room temperature photoassisted formation of hydrogen-molybdenum bronzes with an alcohol as a hydrogen source. *The Journal of Physical Chemistry*, 1988. 92(2): p. 467-470.